


2012

Evaluation of crack signals in cylindrical structures using eddy current nondestructive evaluation theory

Hui Xie
Iowa State University

Follow this and additional works at: <https://lib.dr.iastate.edu/etd>

 Part of the [Applied Mathematics Commons](#), [Electrical and Electronics Commons](#), and the [Electromagnetics and Photonics Commons](#)

Recommended Citation

Xie, Hui, "Evaluation of crack signals in cylindrical structures using eddy current nondestructive evaluation theory" (2012). *Graduate Theses and Dissertations*. 12749.
<https://lib.dr.iastate.edu/etd/12749>

This Dissertation is brought to you for free and open access by the Iowa State University Capstones, Theses and Dissertations at Iowa State University Digital Repository. It has been accepted for inclusion in Graduate Theses and Dissertations by an authorized administrator of Iowa State University Digital Repository. For more information, please contact digirep@iastate.edu.

**Evaluation of crack signals in cylindrical structures
using eddy current nondestructive evaluation theory**

by

Hui Xie

A dissertation submitted to the graduate faculty
in partial fulfillment of the requirements for the degree of
DOCTOR OF PHILOSOPHY

Major: Electrical Engineering

Program of Study Committee:

John R. Bowler, Co-major Professor

Jiming Song, Co-major Professor

Nicola Bowler

Jaeyoun Kim

Ronald A. Roberts

Jue Yan

Iowa State University

Ames, Iowa

2012

Copyright © Hui Xie, 2012. All rights reserved.

DEDICATION

In memory of Qing-Yun Zhang, my grandma,

A generous spirit who taught me how to be a real man,

And for Xiao-Cui Wang and Hu-Liang Xie, my great parents,

Who brought me up with their hard work in the past thirty years.

TABLE OF CONTENTS

LIST OF TABLES	viii
LIST OF FIGURES	ix
ACKNOWLEDGEMENTS	xiv
ABSTRACT	xv
CHAPTER 1. INTRODUCTION	1
1.1 From Simple to Complex	2
1.2 Keep Everything Connected	4
1.3 Organization	5
CHAPTER 2. OVERVIEW	6
2.1 Introduction to Eddy Current Nondestructive Evaluation	6
2.2 Electromagnetic and Mathematical Backgrounds	8
2.2.1 Maxwell's Equations in Quasistatic Regime	8
2.2.2 Constitutive Relations in Conductors	9
2.2.3 Boundary Conditions	10
2.2.4 Auxiliary Vector Potentials	10
2.2.5 Skin Effect and Skin Depth	12
2.2.6 Reciprocity Theorem	13
2.2.7 Truncated Region Eigenfunction Expansion Method	14
2.3 Introduction to the EC NDE Problems	15
2.4 Statement of the Problem	17

CHAPTER 3. LITERATURE REVIEW	20
3.1 Analytical Methods	20
3.1.1 Modeling of Incident Field	21
3.1.2 Modeling of Probe-Crack Interaction	22
3.1.3 Thin-Skin Theory	23
3.2 Numerical Methods	23
3.2.1 Finite Element Method	24
3.2.2 Method of Moments	25
3.3 Modeling in Cylindrical Coordinates	26
CHAPTER 4. COIL IMPEDANCE CHANGE DUE TO CRACKS IN A	
BOREHOLE	28
4.1 Introduction	28
4.2 Formulation	30
4.2.1 Scalar Decomposition	30
4.2.2 Dyadic Green's Function	31
4.2.3 Electric Field Integral Equation	33
4.3 Incident Field Distribution	35
4.4 Scalar Green's Function	36
4.4.1 Scalar Green's Function for a Point Source in a Borehole	39
4.4.2 Transmission and Reflection Inside a Borehole	41
4.5 Flaw Theory and Crack Model	43
4.5.1 Narrow Crack and Ideal Crack	43
4.5.2 Transverse and Longitudinal Cracks	44
4.6 Volume Element Method and Numerical Algorithm	44
4.6.1 Singular Matrix Elements	46
4.6.2 Reflection Matrix Elements	46
4.7 Numerical Implementation	48
4.7.1 Integral of Unbounded Domain Kernel	49
4.7.2 Calculation under Limited Bit Length	49

4.7.3	Recurrence Algorithm	51
4.8	Series Convergence Issues	53
4.9	Results	55
4.9.1	Cracks in Half-Space Conductor	55
4.9.2	Dipole Density Distribution over Crack Surface	58
4.9.3	Transverse and Longitudinal Cracks around a Borehole	58
4.10	Summary	59
CHAPTER 5. COIL IMPEDANCE CHANGE DUE TO CRACKS IN A		
TUBE		63
5.1	Introduction	64
5.2	Transmission and Reflection due to Single Cylindrical Interface	64
5.2.1	Transmission and Reflection for an Outgoing Wave	65
5.2.2	Transmission and Reflection for an Incoming Wave	68
5.3	Transmission and Reflection due to Multiple Cylindrical Interfaces	70
5.3.1	Source Located inside a Tube	71
5.3.2	Source Located outside a Tube	72
5.4	Incident Field in an Infinitely Long Tube	74
5.5	Green's Function for a Point Source in a Tube	74
5.6	Reflection Matrix Element for a Longitudinal Crack	76
5.7	Experimental Measurements and Results	78
5.7.1	Through-Thickness Crack in Thin Plate	78
5.7.2	Experimental Configuration	79
5.7.3	Measurement Procedure	82
5.7.4	Dipole Density over Crack Surface	86
5.7.5	Through-Wall Notch in a Tube	86
5.8	Summary	87
CHAPTER 6. COILS AT THE OPENING OF A BOREHOLE IN A CON-		
DUCTOR		93

6.1	Introduction	93
6.2	Formulation	95
6.2.1	Formal Solution	97
6.2.2	Continuity at the Radial Interface	101
6.2.3	Impedance Change near a Borehole Opening	102
6.3	Incident Field Calculation	104
6.4	Discussion on the Ill-Conditioned Matrices	105
6.5	Numerical Algorithm for Complex Eigenvalue Calculation	106
6.5.1	Complex Eigenvalues	106
6.5.2	Newton-Raphson Method	107
6.5.3	Lyness Algorithm	109
6.6	Results	110
6.6.1	Coil Impedance Change at Borehole Opening	110
6.6.2	Current Distribution around a Borehole Edge	114
6.7	Summary	116
CHAPTER 7. COIL IMPEDANCE CHANGE DUE TO CORNER CRACKS		118
7.1	Introduction	118
7.2	Scalar Green's Function for a Half Space	120
7.3	Point Source around the Opening of a Borehole	122
7.4	Dyadic Green's Function for a Longitudinal Crack	128
7.5	Discussion and Summary	128
CHAPTER 8. CONCLUSION		130
APPENDIX A. USEFUL MATHEMATICAL FORMULAS IN CYLINDRICAL COORDINATE SYSTEM		132
APPENDIX B. BOBBIN COIL ABOVE A HALF-SPACE CONDUCTOR		134
APPENDIX C. COIL IMPEDANCE CHANGE DUE TO CRACKS IN A HALF-SPACE CONDUCTOR		140
APPENDIX D. COILS INSIDE A BOREHOLE		142

APPENDIX E. BOUNDARY INTEGRAL EQUATION FOR EDDY-CURRENT PROBLEMS WITH DIRICHLET BOUNDARY CONDITION	145
BIBLIOGRAPHY	161
BIOGRAPHICAL SKETCH	174

LIST OF TABLES

Table 4.1	Parameters of test experiment for a rotary coil inside borehole.	35
Table 4.2	Summary of the truncated boundary conditions at $z = 0$ and $z = h$. . .	37
Table 4.3	Parameters of test experiment for a bobbin coil above a half-space conductor.	56
Table 5.1	Parameters of test experiment for a bobbin coil above a thin plate. . .	79
Table 5.2	Parameters of test experiment for a rotary coil inside the tube.	83
Table 6.1	Coil and borehole parameters for a coil around the opening of a borehole.	111
Table E.1	Number of unknowns computed in five infinite-domain cases.	158

LIST OF FIGURES

Figure 1.1	The structure of this dissertation and corresponding chapters.	4
Figure 2.1	Wave behavior inside a conductor and the relationship between skin depth and the wave length.	13
Figure 2.2	Schematic of a typical eddy-current nondestructive problem.	15
Figure 2.3	Definitions of coil impedance and its change.	16
Figure 2.4	Impedance plane diagram for a bobbin coil above a half-space conductor.	17
Figure 2.5	Two-layer aircraft structure with cracks emanating from a fastener hole.	18
Figure 4.1	A rotary coil inside a boerhole in the presence of a longitudinal crack.	29
Figure 4.2	Incident field at the plane $\phi = 0^\circ$ due to a rotary coil inside a boerhole in the absence of cracks.	36
Figure 4.3	A point source in a truncated borehole region.	38
Figure 4.4	The meaning of truncation boundary conditions.	39
Figure 4.5	A point source in a truncated homogeneous conductive region.	40
Figure 4.6	Volume elements for modeling a transverse open crack and a longitudinal one.	47
Figure 4.7	The order of magnitude for the terms in the double summation involved in the reflection matrix element calculation.	54
Figure 4.8	Bobbin coil above conductive half space with a slot.	56
Figure 4.9	Change in coil resistance and coil reactance due to the slot as a function of coil-center position for the experimental configuration described in Table 4.3.	57

Figure 4.10	The distribution of electric current dipole density over crack surface for a longitudinal crack around the borehole.	58
Figure 4.11	A rotary coil inside borehole with a longitudinal crack.	59
Figure 4.12	Change in coil resistance and coil reactance due to the transverse crack as a function of coil-center position for the experimental configuration described in Fig. 4.2 and Table 4.1.	60
Figure 4.13	Change in coil resistance and coil reactance due to the longitudinal crack as a function of coil-center position for the experimental configuration described in Fig. 4.2 and Table 4.1.	61
Figure 5.1	A rotary coil insides a tube in the presence of a through-wall longitudinal notch.	64
Figure 5.2	Transmission and reflection of an outgoing wave.	66
Figure 5.3	Transmission and reflection of an incoming wave.	68
Figure 5.4	Transmission and reflection of an outgoing wave inside a tube.	70
Figure 5.5	Transmission and reflection of an incoming wave outside a tube.	72
Figure 5.6	A point source located between the walls of a tube.	75
Figure 5.7	Coil resistance change and reactance change due to a notch as a function of coil center position at a fixed frequency of 1 kHz.	80
Figure 5.8	Coil resistance change and reactance change due to a notch as a function of coil center position at a fixed frequency of 1 kHz.	81
Figure 5.9	A rotary pancake coil inside a tube.	82
Figure 5.10	Experimental configuration used to measure the coil impedance change due to the notch in a tube.	83
Figure 5.11	Normalized resistance change and reactance change of a rotary coil inside an unflawed tube as a function of frequency.	85
Figure 5.12	Normalized impedance change of a rotary coil inside an unflawed tube as a function of frequency on the impedance plane.	86
Figure 5.13	Electric current dipole density over a through-wall notch in a tube.	87

Figure 5.14	Change in coil resistance and coil reactance due to the longitudinal notch as a function of coil center position at frequency 25 kHz.	88
Figure 5.15	Change in coil resistance and coil reactance due to the longitudinal notch as a function of coil center position at frequency 50 kHz.	89
Figure 5.16	Change in coil resistance and coil reactance due to the longitudinal notch as a function of coil center position at frequency 100 kHz.	90
Figure 5.17	Change in coil resistance and coil reactance due to the longitudinal notch as a function of coil center position at frequency 150 kHz.	91
Figure 5.18	Change in coil resistance and coil reactance due to the longitudinal notch as a function of coil center position at frequency 200 kHz.	92
Figure 6.1	A rotary coil at the opening of a borehole.	94
Figure 6.2	A rotary coil at the opening of a borehole in a conductor.	96
Figure 6.3	The spectrum of complex eigenvalues.	100
Figure 6.4	Two kinds of modes are supported in the truncated half space.	100
Figure 6.5	A differential bobbin coil at the opening of a borehole in a conductor.	103
Figure 6.6	The phase of the function $f(z) = z$ on the complex plane.	107
Figure 6.7	The order of magnitude of the function $1/ f(z) $ and the phase of function $f(z)$ for the eigenvalue problem discussed in this chapter.	108
Figure 6.8	Coil resistance change and reactance change of a rotary coil as a function of the axial position.	112
Figure 6.9	Variation of the normalized resistance change and reactance change of an bobbin coil as a function of the axial position with respect to the edge of the borehole opening at a fixed frequency 10 kHz.	113
Figure 6.10	Normalized impedance plane plot for a differential probe around the edge of borehole at four different frequencies, 1 kHz, 5 kHz, 10 kHz, and 20 kHz.	114
Figure 6.11	Amplitude contours of azimuthal component of eddy-current density for three coil positions at the $\phi = 0^\circ$ plane: 9.35 mm, 0 mm, and -9.35 mm.	115

Figure 6.12	Amplitude contours of radial and axial component of eddy-current density at the $\phi = 0^\circ$ plane.	116
Figure 7.1	A rotary pancake coil is used to inspect a crack near the opening of a borehole.	119
Figure 7.2	A point source in a truncated half space.	121
Figure 7.3	A point source around the opening of a borehole.	123
Figure B.1	Equipotential lines of the magnetic vector potential, \mathbf{A} on a plane passing through the axis of the filament.	136
Figure B.2	Magnetic field of a coil with rectangular cross section in free space. . .	137
Figure B.3	Distribution of eddy-current density for a cylindrical coil above a half space.	139
Figure D.1	A rotary coil inside a borehole.	142
Figure E.1	Schematic configuration of the surface crack problems with uniform applied field.	148
Figure E.2	Normal derivative of the scattered field on the plane surface for a perpendicular crack ($\theta = 0^\circ$) with depth $d = 4\delta$	150
Figure E.3	Absolute error in the normalized surface impedance on the plane surface for different truncated length l ($d = 4\delta$, $\theta = 0^\circ$).	152
Figure E.4	Normalized surface impedance on the crack surface for a perpendicular crack with depth $d = 4\delta$	153
Figure E.5	Normalized surface impedance over the crack surface for a crack with $d = 3\delta$ and $\theta = 30^\circ$	154
Figure E.6	Comparison of results from Kahn and the proposed BIE for the normalized surface impedance on the plane surface: $d = 3\delta$ and $\theta = 30^\circ$	155
Figure E.7	Normalized surface impedance on both crack surface and plane surface for a v-groove crack with depth $D = 2\delta$ and half-opening $F = 0.25\delta$. .	156

Figure E.8	Comparison of numerical result and analytical solution for the normalized surface impedance on both crack surface and cylinder surface $d = a = 1\delta$	157
Figure E.9	Normalized surface impedance of cases with $d = 8\delta$, $\theta = 45^\circ$ and $d = \delta$, $\theta = 45^\circ$	159

ACKNOWLEDGEMENTS

I would like to take this opportunity to express my thanks to those who helped me with various aspects of conducting research and the writing of this dissertation.

First and foremost, I would like to thank to Dr. John Bowler and Dr. Jiming Song, my advisors, for their guidance, patience and support throughout my research and study at Iowa State University. Their insights and words of encouragement have inspired me a lot in my research projects. What I have learned from them is not only fundamental and advanced electromagnetic theories, but also the way to study new knowledges; what I have learned from them is not only the methods to solve some specific research problems, but also the ideas to identify and analyze the problems; what I have learned from them is not only how to do good research, but also how to be a honest and responsible scholar.

Besides, I would like to thank Dr. Nicola Bowler, my committee member and the instructor of course EE588X in 2008, who introduced me this interesting research area, eddy current nondestructive evaluation. I would like to thank Dr. James Evans and Dr. Jue Yan, who served as minor the representatives in my committee. I would also like to thank Dr. Jaeyoun Kim and Dr. Ronald Roberts, the other two committee members, for their patience and many valuable suggestions during my graduate study.

I would like to say thanks to my colleagues, Dr. Fu-Gang Hu, Dr. Sidharath Jain, Yi Lu and Sa Li, for their help on my study and life at Iowa State University.

Special thanks also to my family, Xiu-Qin Xie and Li Wang, and my friends, Tao Liu, Jian Li, Yong-Gang He, Ping Ren, Kai Zhang, Yu Liu and Dr. Yifen Liu, for their endless spiritual support and encouragement to pursue my dream.

ABSTRACT

The modeling of eddy current (EC) problems is not only helpful for the probe design and the interpretation of measurement data, but also essential to the corresponding inverse problems. In order to deal with high conductivity and low operating frequency, the conventional pure numerical methods require large memory and long computing time to accurately solve EC problems. In this dissertation, semi-analytical approaches are presented to efficiently solve a series of EC problems in cylindrical polar coordinates.

By applying the truncation in an unbounded domain, the fields are expanded into a linear combination of the eigenfunctions. Each eigenfunction belongs to different eigenvalue. The expansion coefficients are determined by the continuity conditions at the interface between different regions. For a given coil source, the semi-analytic solution of the fields in an unflawed conductor can be obtained using this method.

The electromagnetic fields are expressed in terms of transverse electric and transverse magnetic modes. At a circularly cylindrical interface, these two modes are coupled with each other. The coupling is considered in the borehole and tube problems. Then the concept is further extended into the borehole opening problem, in which the coupling between different eigenmodes is added.

A well-developed crack model is used to solve the crack problems and estimate the impedance change of an induction coil due to a thin crack in conductors. The thin crack is equivalent to an electric current dipole source distributed over the crack region. An electric integral equation is constructed to solve this equivalent source, and the coil impedance change is predicted. The dyadic Green's kernel, which is required in the integral equation, is derived for different structures.

Special numerical implementations are proposed to deal with the issues arising in our program to make sure the calculation is accurate and the computational cost is small. The con-

vergence of the series expansion is discussed. Methods used to compute the eigenvalues are also investigated. Predictions of the probe signals show a good agreement with experimental measurements in several examples. Compared to numerical methods, the approach is much faster to get the results with same accuracy.

CHAPTER 1. INTRODUCTION

It has been about three years since I started to think about the organization of my dissertation. When I went to the library, I noticed that there were a lot of dissertations that had not been checked out for a long time, especially those related to engineering and technology. At that time, I told myself that I should try to write a better dissertation. It is clear that we are in an age where the knowledge is rapidly developed and a specific research field could be out of date pretty soon. Besides this, the topic of a dissertation might be so narrow that only a few people would be interested in it. I would like to try a different way to write my dissertation and make more people feel it useful, even after a long time. Here is what resulted from these thoughts.

As a graduate student, I keep warning myself that I should always do something meaningful for myself and the others, even for our whole society. It is easy to lose the big picture when we are buried in the details of a work, especially when we struggle in our trivial research projects. Sometimes people make the same mistake several times and sometimes people keep doing repeated work just because they get used to it. We do the same thing in our research work and I believe there must be some books which teach people to avoid such behaviors and make ourselves more productive. However, those suggestions always seem to be too impractical for our own research work.

On the other hand, during my graduate study, all the dissertations I read just present their own specific research work. They neither talk about the methodology used in their research, nor give us a clear picture about the logic to their research work. For me, it is important to know how they thought when they did their work, even though it might be just a simple logic or idea. It is important because it could introduce us a new approach to tackle the similar problems in another work; it is important because it could help us relate those abstract concepts

in methodology and philosophy with our specific research so that we could make sure our logic is well organized; it is important because it might remind us an approach that we missed before. If we indicate our original logical relationship of the research work inside dissertations, it would be more or less useful for the others, even for people who work in different research areas. If everybody could do so, I believe our scientific society would benefit a lot. I don't want my dissertation to become one of those that have never been borrowed in the library. Therefore, I will present my research ideas over here.

Some of the ideas are originally from my advisors, Dr. John Bowler and Dr. Jiming Song. They inspired me a lot during our weekly discussions. The credits should be given to them. During my graduate study, they did not just teach me 'what, how and why', they also taught me how to think when I encountered a new problem and how to make sure my work is correct and reasonable, i.e. the logical relationship of my thoughts. They are important guidance in my research, although they are not creative viewpoints at all. This is another reason why I discuss them in front of other chapters. I hope this could help readers understand my dissertation. I am trying to demonstrate these thoughts from a rather macroscopic perspective, not cover too many details. After all, I am supposed to present my own research work in this dissertation. The contents of the research projects are started from Chapter 2.

1.1 From Simple to Complex

For a complex problem, we can reduce it into several simple models which focus on the different aspects of the whole model, then grasp the fundamental principles by investigating those simple models and finally solve the complex problem through combining the principles learned from the simple models. Although this idea is pretty straightforward, it might be neglected by people because it seems to take longer time to solve the whole project in this way. As a matter of fact, it is the other way around and this approach is always an efficient strategy. It helps us to concentrate on one specific issue each time and build the complex system step by step to make sure we can have a good understanding of the complex model. It is also much easier to locate the 'bugs' with this approach. Besides this, we can verify the final complete model by reducing it to those simpler problems which have been solved before. In fact, people

widely use this approach to design and analysis very-large-scale integrated (VLSI) circuit. I used this approach through my research in which we tried to find the semi-analytical solution of the wave interaction with a complex geometrical model.

The ultimate objective of my research project is to estimate the impedance change of an eddy-current coil due to a thin crack around a rivet in a layered structure. The detailed description will be given later. As mentioned before, the difficulty comes from the wave interaction with this complicated geometrical structure. The model actually involves wave interactions with layered structure, borehole structure and conical structure. All of those structures are actually fundamental and primary topics in the electromagnetic research and they all play important roles in different applications, such as well logging interpretation, microwave circuit design, and scattering from rough surface. In my work, the wave interaction with an infinitely long borehole without other factors was investigated first, and then an infinitely long tube, an extension of the borehole model, was solved. Finally the opening of a borehole was considered, in which layered structure was added into the borehole model. The more complicated the geometry is, the more difficult the problem becomes. The structure of my dissertation is shown in Fig. 1.1. The complexity increases from the bottom to the top.

For each geometry, the coil response due to a thin crack is estimated. In order to solve the crack problems, the field for the same geometry in the presence of cracks is required in our method. We refer to this field as incident field. This is quite similar to the ideas to calculate the scattering field using equivalent theorem in electromagnetic theories. Thus, we actually solve two types of problem for each geometry, incident field and coil response due to cracks. They are not independent to each other. The way to find the incident field can be transplanted to derive the Green's function for a point source in the same geometry, which is used to get the coil signal due to cracks. The crack problem is more difficult than the incident field calculation, which means the problem is also getting complicated from left to right in Fig. 1.1. Thus, coil response due to a crack around a borehole corner, which is the most difficult one among those problems, is discussed at the end of my dissertation.

	Incident Field	Crack Response
Borehole Edge	Chapter 6	Chapter 7
Tube	Chapter 5	Chapter 5
Borehole	Appendix D	Chapter 4
Half Space	Appendix B	Appendix C
Coil in Air	Appendix B	

Figure 1.1: The structure of this dissertation and corresponding chapters. The shadow indicates the difficulty and complexity of the problems. The darker color means a more complicated problem.

1.2 Keep Everything Connected

My research work is mainly about electromagnetic simulation in eddy-current nondestructive evaluation. Theoretical models are formulated based on the physical principles, then a computer code is written from the formulation and finally the models are verified by comparing simulation results from the code with experiment measurements. Apparently, physical model, mathematical formulation and computer code have their own rules to follow. Numerical accuracy issues never show up when we think about the model and formulation. The formulation might have to be changed to different form to overcome some numerical issues. However, for a good research work, these three aspects should be related to each other on all the levels. Debugging code might take us a long time and we will waste lots of time on running some useless codes if we are not careful enough. A good practice I learned is to keep the relationship between codes and theories in mind while we are analyzing the simulation results. It could save us an enormous amount of time and effort if we have a clear picture about our code and its relation with the physical model. When I wrote the program for the tube problem in Fig. 1.1,

I tried to do the work in this way. This idea did help me a lot. I tested and verified my code by setting the outer radius of the tube model to a relatively large number. Therefore, the results should get close to those calculated from borehole geometry. Meanwhile, the reflection matrix also approaches to the one in the borehole calculation, so does the incident field. It makes code debugging become easier. This is also an important difference between scientific programming and the software application programming.

1.3 Organization

The dissertation is organized as follows. Chapter 2 introduces fundamental concepts used in eddy current nondestructive evaluation and backgrounds of my research projects. Chapter 3 presents a literature review on general EC NDE problems. Special attention is paid to the problems solved in cylindrical polar coordinates. Chapter 4 presents a theoretical model used to predict the probe signal due to cracks in a infinitely long borehole with the aid of method of moments. Numerical implementation is studied to accelerate the algorithm. Series convergence issue is also discussed in this chapter. The model is extended to a tube problem in Chapter 5. Transmission and reflection coefficients due to a multi-layered structure are derived. Incident field of a coil near a borehole corner is solved in Chapter 6. Methods used to compute eigenvalues from a complex transcendental equation are discussed. Impedance change and eddy-current distribution are calculated as a function of the coil position. In Chapter 7, coil response due to a crack around the opening of a borehole is considered. Conclusions are given in Chapter 8. Necessary mathematical formulas used in this dissertation are summarized in Appendix A. Incident field calculation and coil response estimation of a bobbin coil above a half-space conductor are derived in Appendixes B and C, respectively. The eddy-current distribution due to a rotary coil inside a borehole is provided in Appendix D. A paper related to boundary element method in two dimensional eddy current problems is given in Appendix E for reference.

CHAPTER 2. OVERVIEW

Nondestructive Evaluation (NDE) is an interdisciplinary field concerned with the study of analysis and measurement technologies for the quantitative characterization of materials, tissues and structures by noninvasive means. Acoustic, ultrasonic, radiographic, thermographic, electromagnetic, optic, and visual inspections are employed to probe interior structure or characterize subsurface features of the object. It plays an important role in noninvasive medical diagnosis, security screening, and manufacturing process control, as well as the traditional NDE areas of flaw detection, structural health monitoring, and materials characterization.

Compared with other NDE methods, eddy-current nondestructive evaluation (EC NDE) is an effective approach to detect flaws in conductors and inspect the characterization of conductive materials. It has wide applications in material, aerospace, petroleum, nuclear, and manufacturing industries. In order to formulate and solve the problems involving wave interaction with conductors, traditional electromagnetic theories are needed. However, there are some special properties for EC NDE problems. In this chapter, those electromagnetic and mathematical fundamentals used in this dissertation are summarized for reference.

2.1 Introduction to Eddy Current Nondestructive Evaluation

According to Faraday's law, electromotive forces (EMFs) are induced in a conductor by a time-varying magnetic field. These electromotive forces give rise to the circulating flows of electrons, or currents, within the body of the conductor and the current flows are called eddy currents, which is also referred to as Foucault current. Eddy current was first observed by a French physicist, François Arago in 1824 even though the complete explanation was given by Michael Faraday in 1831. Like all other electric current, eddy currents generate heat as well as

electromagnetic forces. The induction heating can be used for metallurgical treatment, welding and melting furnaces. The electromagnetic forces have applications in linear induction motors, eddy-current brake, and the flow of molten metals.

When an alternating current (AC) flows in a coil in close proximity to a conductor, the magnetic field of the coil will induce eddy currents in that conductor. Lenz's law tells us the direction of the current flow is such that the induced magnetic field produced by the eddy currents will oppose the change in the original magnetic field. Consequently, the secondary induced magnetic field generated by the eddy currents will affect the loading on the coil and thus its impedance. Therefore, the variations of these eddy currents can be monitored by measuring impedance changes from the coil. Variations in the electrical conductivity, magnetic permeability, homogeneity of the conductor or the presence of any flaws, cracks, and corrosion inside the conductor, will cause a change in eddy currents and corresponding impedance change of the coil. This is the basic principle of eddy-current nondestructive evaluation.

The early use of eddy currents to detect differences in conductivity, magnetic permeability, and temperature was initiated by E. Hughes in 1879. The first eddy-current instruments was developed by H. Knerr, C. Farrow, T. Zuschlag, and Fr. F. Foerster from 1935 to 1940 [1]. Since then, EC NDE has been widely used in the aerospace, nuclear, and manufacturing industries for inspecting properties of the conductive material and detecting flaws in metallic components at relatively low frequency. One of the most interesting examples is the counterfeit coin detection in vending machines. A coin rolls past a stationary magnet, and the induced eddy current slows its speed. The strength of the eddy currents, and thus the retardation, depends on the conductivity of the coin's metal. Counterfeit coins are slowed to a different degree than genuine coins, and then they are sent into the rejection slot.

Theoretical modeling of EC NDE problems can be utilized for the coil design, operating frequency selection, interpretation of inspection data and even for estimating flaw size and its geometry. Cylindrical structures, such as bolt hole, cylinder, and tube, are most commonly used metallic components in various industries and cracks frequently occur in those components. Cylindrical surface is a critical region where cracks can initiate in the components under stress. Thus, it is necessary to study the modeling of EC NDE problems in cylindrical polar

coordinates.

2.2 Electromagnetic and Mathematical Backgrounds

This section presents fundamental electromagnetic theories used in this dissertation. Mathematical methods are also discussed for the subsequent derivation. We will focus on the eddy-current problems, electromagnetic fields in close proximity to conductors at low frequencies.

2.2.1 Maxwell's Equations in Quasistatic Regime

Like all other electromagnetic phenomena, EC NDE problems are governed by Maxwell's equations. In this dissertation, we only consider configurations which involve conductors with high conductivity instead of dielectrics and these conductors could be magnetic material. Comparing to scattering problems due to dielectrics, the operating frequency of EC problems is relatively low (usually less than 10 MHz) and it turns out that the displacement current $\partial\mathbf{D}/\partial t$, can be neglected in the calculation [2]. Therefore, for EC problems, Maxwell's equations have a slightly different form [3],

$$\nabla \times \mathbf{E}(\mathbf{r}, t) = -\frac{\partial}{\partial t}\mathbf{B}(\mathbf{r}, t), \quad (2.1)$$

$$\nabla \times \mathbf{H}(\mathbf{r}, t) = \mathbf{J}(\mathbf{r}, t), \quad (2.2)$$

$$\nabla \cdot \mathbf{D}(\mathbf{r}, t) = \rho(\mathbf{r}, t) \quad (2.3)$$

$$\nabla \cdot \mathbf{B}(\mathbf{r}, t) = 0, \quad (2.4)$$

where $\mathbf{E}(\mathbf{r}, t)$ is the electric field intensity (V/m), $\mathbf{H}(\mathbf{r}, t)$ is the magnetic field intensity (A/m), $\mathbf{D}(\mathbf{r}, t)$ is the electric flux density (C/m²), $\mathbf{B}(\mathbf{r}, t)$ is the magnetic flux density (Wb/m²), $\mathbf{J}(\mathbf{r}, t)$ is the current density (A/m²), and $\rho(\mathbf{r}, t)$ is the electric charge density (C/m³). All the fields are functions of position in space, \mathbf{r} and time, t . Equations (2.1)–(2.4) are well-known Faraday's law, Ampère's law and Gauss' law, respectively.

For a time-harmonic field with certain angular frequency ω , we can, in general, relate the instantaneous field to their phasor form by

$$\mathbf{E}(\mathbf{r}, t) = \text{Re} \{ \mathbf{E}(\mathbf{r})e^{-j\omega t} \}, \quad (2.5)$$

where $\text{Re}\{\cdot\}$ denotes the real part of a complex quantity. $e^{-i\omega t}$ is the time convention used to denote the time harmonic dependence and ω is the angular frequency. With this notation, Maxwell's equations can be expressed in terms of phasor form

$$\nabla \times \mathbf{E}(\mathbf{r}) = i\omega\mathbf{B}(\mathbf{r}), \quad (2.6)$$

$$\nabla \times \mathbf{H}(\mathbf{r}) = \mathbf{J}(\mathbf{r}), \quad (2.7)$$

$$\nabla \cdot \mathbf{D}(\mathbf{r}) = \rho(\mathbf{r}) \quad (2.8)$$

$$\nabla \cdot \mathbf{B}(\mathbf{r}) = 0. \quad (2.9)$$

From now on, the phasor form is adopted through this dissertation. In other words, we only discuss time-harmonic solution here.

The conservation law for current density can be derived from Ampère's law by taking the divergence of (2.7)

$$\nabla \cdot \mathbf{J}(\mathbf{r}) = \nabla \cdot \nabla \times \mathbf{H}(\mathbf{r}) = 0. \quad (2.10)$$

This implies eddy current is irrotational inside a conductor. We could imagine the flow of eddy current inside a conductor as the water flow inside a river.

From the Ampère's law (2.2) and Gauss' law (2.4), it looks like we are solving magneto-static problems. One should keep in mind that the magnetic field produced by a coil has to be time-varying in order to induce eddy current inside the conductor. That's why people use the term 'quasi-static', instead of 'static' [2].

2.2.2 Constitutive Relations in Conductors

Constitutive relations provide the macroscopic relations between the flux and corresponding field. For a homogeneous isotropic conductor,

$$\mathbf{B} = \mu\mathbf{H}, \quad (2.11)$$

$$\mathbf{J} = \sigma\mathbf{E}, \quad (2.12)$$

where scalars, μ and σ are the permeability and conductivity of the conductor, respectively.

The conductor could be inhomogeneous, nonlinear, anisotropic or dispersive media. In those

cases, μ and σ have other forms, such as tensor form for anisotropic conductors or a function of frequency for a dispersive conductor. Normally, cracks in a conductor are considered as air-filled gap which is nonconductive. As we mentioned before, electric flux density $\mathbf{D} = \epsilon\mathbf{E}$ will not be considered due to the low frequency and high conductivity.

2.2.3 Boundary Conditions

For a interface separating two regions, such as the interface between conductors and air, the boundary conditions are as follows

$$[\mathbf{E}_t] = 0, \quad (2.13)$$

$$[\mathbf{H}_t] = \mathbf{J}_s, \quad (2.14)$$

$$[B_n] = 0, \quad (2.15)$$

where subscript t denotes the tangential components and n denotes the normal component of a field. Operator $[\cdot]$ stands for the jump of the quantity at the interface. If the media have finite conductivities, surface current density, \mathbf{J}_s vanishes and (2.14) is simplified to

$$[\mathbf{H}_t] = 0. \quad (2.16)$$

If one region is a conductor and another one is free space, the normal component of current density inside the conductor vanishes at the surface because displacement current is neglected in the nonconductive region. Thus, we have that

$$J_n = 0. \quad (2.17)$$

This boundary condition can be used to describe the behavior of eddy-current flow in the presence of nonconductive cracks, which is like the water flow around an object inside the river. However, surface charge is still at the conductor surface. In fact, charges are not conserved in the quasistatic regime.

2.2.4 Auxiliary Vector Potentials

As mentioned in Section 2.2.1, the electromagnetic vector fields satisfy Maxwell's equations. In order to solve the fields for a three-dimensional problem, it is more convenient to introduce

auxiliary potentials. Based on the fact that the divergence of a curl is zero, $\nabla \cdot (\nabla \times \mathbf{A}) = 0$, the magnetic vector potential \mathbf{A} is defined as

$$\mathbf{B} = \nabla \times \mathbf{A}, \quad (2.18)$$

and the electric field can be written as

$$\mathbf{E} = \omega \mathbf{A} - \nabla \phi, \quad (2.19)$$

where electric scalar potential ϕ could be any scalar function because $\nabla \times \nabla \phi = 0$. The electric scalar potential is uniquely determined by a suitable condition, which is so called gauge condition. There are different definitions of gauge condition. For example, Lorentz gauge is defined as

$$\nabla \cdot \mathbf{A} = \mu \sigma \phi. \quad (2.20)$$

Similarly, the electric vector potential \mathbf{T} and the electric field have the relationship

$$\mathbf{J} = \nabla \times \mathbf{T}, \quad (2.21)$$

and the corresponding magnetic field can be written as

$$\mathbf{H} = \mathbf{T} - \nabla \Omega, \quad (2.22)$$

where Ω is the magnetic scalar potential and it is determined by a gauge condition. There are some other formulations based on alternative potentials used to describe EC problems in numerical approach. Detailed discussion and analysis about the vector potentials are given in [4, 5].

Another pair of useful scalar potentials are the transverse electric (TE) and transverse magnetic (TM) scalar potentials. A solenoidal (divergence free) vector field can be split into two parts, solenoidal and irrotational parts, and we can introduce the second-order vector potential (SOVP) \mathbf{W} as

$$\mathbf{A} = \nabla \times \mathbf{W}, \quad (2.23)$$

where \mathbf{W} has the following form

$$\mathbf{W} = \mathbf{u}W_a + \mathbf{u} \times \nabla W_b. \quad (2.24)$$

Here, W_a is the transverse electric scalar potential and W_b is the transverse magnetic scalar potential with respect to the direction \mathbf{u} . With an appropriate choice of unit vector \mathbf{u} , these two scalar quantities, W_a and W_b can be separated and a general solution for each potential can be constructed with the separation of variables method for some simple geometrical shapes in Cartesian coordinates. However, it is difficult to do that in curvilinear coordinate systems, such as cylindrical and spherical coordinates, in which some components are coupled because of the boundary conditions at the curved surface. The detailed discussion is given in Chapter 4.

2.2.5 Skin Effect and Skin Depth

It is well known that an uniform plane wave propagating along \mathbf{r} direction can be written as $e^{i\mathbf{k}\cdot\mathbf{r}}$. The wave number \mathbf{k} , which is normally solved from Maxwell's equations, could be a real number for wave propagation or a complex vector for both attenuation and propagation. Skin depth is a critical parameter when we are talking about EC problems, in which the attenuation is significant. The skin depth is defined as the distance that the fields must travel in a conductor to reduce its magnitude to $e^{-1} = 36.8\%$ [3]. For a good conductor, the skin depth can be easily derived from the behavior of an uniform plane wave in an unbounded lossy medium under the assumption that

$$\left(\frac{\sigma}{\omega\epsilon}\right)^2 \gg 1. \quad (2.25)$$

With this assumption, the wave number is approximated as

$$k^2 \approx i\omega\mu\sigma \quad \text{and} \quad k = \pm\sqrt{\frac{\omega\mu\sigma}{2}}(1+i). \quad (2.26)$$

Substituting k back into the plane wave form, skin depth δ can be calculated according to the definition

$$\delta = \sqrt{\frac{2}{\omega\mu\sigma}}. \quad (2.27)$$

It is interesting to notice that the corresponding wave length λ in the conductor is

$$\lambda = 2\pi\delta, \quad (2.28)$$

which means a wave length is roughly six times longer than the skin depth, Fig. 2.1.

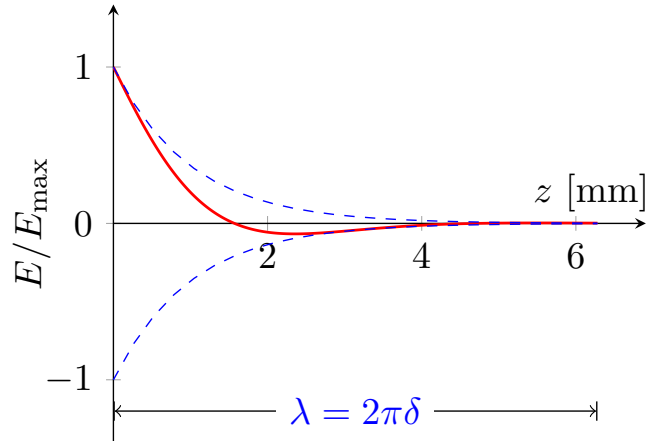


Figure 2.1: Wave behavior inside a conductor and the relationship between skin depth and the wave length. A snapshot of the electrical field inside a half-space conductor. The skin depth is $\delta = 1$ mm. The dash line shows the magnitude change of the wave in the conductor.

Skin depth is associated with a phenomenon called skin effect, which is the tendency of an alternating current to distribute itself within a conductor with the current density being largest near the surface of the conductor. According to (2.27), skin depth is inversely proportional to the square root of the angular frequency. As the operating frequency increases, the eddy current density induced in a conductor will be confined to an increasingly thin layer near the conductor surface. This is the reason why the operating frequency in EC NDE can not be too high.

Skin effect is also one of the reasons why EC problems are difficult in general. The exponentially decreasing fields would easily cause numerical trouble while we are using numerical approaches to solve the problem. It is different from typical scattering problems where the field doesn't vary dramatically. In EC problems, one has to consider the numerical accuracy and other issues.

2.2.6 Reciprocity Theorem

Reciprocity theorem is frequently used for the EC problems, in which there are always two sources existing, the current source in the coil and the induced current in the conductor. In our theoretical model, the coil impedance change is always derived based on this theorem.

Reciprocity theorem states that the reaction between a current source and the resulting electric field is unchanged if one interchanges the points where the current is placed and where the field is measured [3]

$$\nabla \cdot (\mathbf{E}_1 \times \mathbf{H}_2 - \mathbf{E}_2 \times \mathbf{H}_1) = 0, \quad (2.29)$$

where subscripts 1 and 2 denote the fields due to two sets of sources.

2.2.7 Truncated Region Eigenfunction Expansion Method

In general, there are three methods used to solve Maxwell's equations, analytical methods, approximation methods, and numerical methods. The method we adopted is actually a combination of analytical method and numerical method, which is called semi-analytical method.

In these classical methods, analytical solution is accurate and fast, but it is only accessible for some simple symmetrical two-dimensional structures, such as a half-space problem, an infinitely long cylinder, or a sphere. Although it is difficult to get an analytical solution for the electromagnetic problems with complicated geometry, truncated region eigenfunction expansion (TREE) method provides a practical way to deal with some of them and it keeps the advantages of analytical methods. In a TREE method, domain truncation is typically applied to a domain dimension that is infinite according to the original problem definition. Limits are imposed in the infinite spatial dimension by adding artificial boundaries and forcing the solution to be a given value there. Only certain discrete eigenmodes can be supported within the truncated region. The analysis of a shielded microstrip line is an example of such consideration.

The solution in a truncated dimension can be expressed as a series expansion of eigenfunctions rather than as an integral over the whole spectrum and these eigenfunctions correspond to the different eigenvalues. In order to get an approximate solution to the original problem, the imposed boundaries should have little or no influence on the final solution we concern. Normally, this method gives rise to errors but these errors can be made as small as desired by adjusting the location of the imposed boundaries.

Several boundary conditions can be used as truncation boundaries in electromagnetic problems, such as perfect electric conductor (PEC), perfect magnetic conductor (PMC), and perfect matched layer (PML). For a specific problem, we should choose the ones which make the so-

lution much simpler. The functions over a truncated domain generally can be expanded into periodic functions due to the truncation boundary conditions. The truncation boundary conditions should be chosen to make the expanded function as smooth as possible so that the discontinuity of the expansion could be avoided.

In this dissertation, TREE method is applied to all the structures, even for some simple cases which could be solved without truncation. As we discussed in Section 1.1, the reason is that we hope our method can be extended from simple geometrical shapes to the complex models, so that a complex problem can be reduced to the simple ones for the validation. The consistency of using TREE method makes the extension possible.

2.3 Introduction to the EC NDE Problems

A schematic of a typical EC NDE problem is shown in Fig. 2.2. A coil, which generates original magnetic field, induces eddy currents in a conductive test-piece in the presence of flaws or cracks. The coil is driven by a time-harmonic voltage and the impedance of the coil is measured by an impedance analyzer, which is not shown in the figure. When the coil is isolated from any conductor, we annotate the impedance as Z_0 and ideally it should be pure induction, imaginary number, if we neglect the wire resistance, as shown in the left part of Fig. 2.3. The coil impedance changes to Z in the presence of the test-piece but without the cracks, the middle of Fig. 2.3, and to Z_c with the cracks, the right part of Fig. 2.3. The impedance change is defined as $\Delta Z = Z - Z_0$ for the cases in the absence of cracks and $\Delta Z_c = Z_c - Z$ for the cases in the presence of cracks. The difference due to the conductor or the cracks could be observed

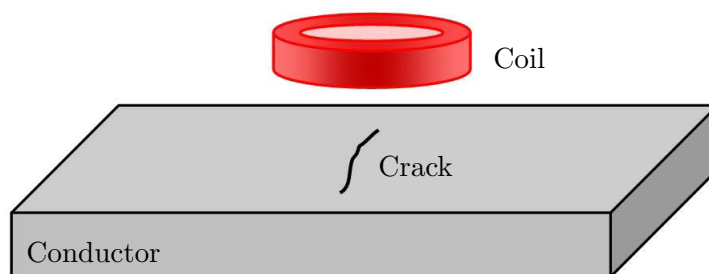


Figure 2.2: Schematic of a typical eddy-current nondestructive problem. A bobbin coil above a conductive plate with a surface-breaking crack.

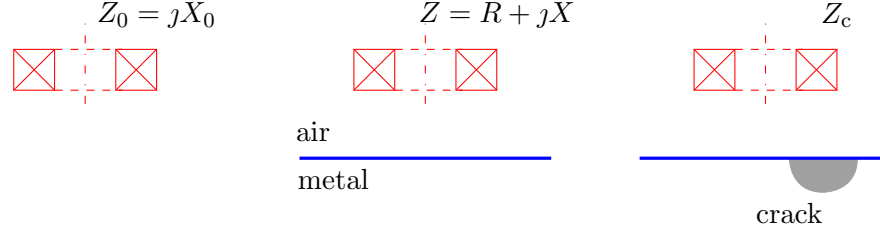


Figure 2.3: Definitions of coil impedance and its change. The coil impedance change is defined as $\Delta Z = Z - Z_0$ for the cases in the absence of cracks and $\Delta Z_c = Z_c - Z$ for the cases in the presence of cracks.

from ΔZ or ΔZ_c .

Normally the coil impedance is normalized with respect to the reactance of the isolated coil, X_0 , and plotted on the impedance plane diagram. The normalized coil impedance for a bobbin coil above a half-space conductor are plotted in Fig. 4.3. The solid lines show the coil impedance as a function of frequency for different coil lift-offs. The dashed lines represent the coil impedance as a function of lift-off for different frequencies. As the lift-off increases or the frequency decreases, the impedance tends towards to the coil impedance in air, which is called ‘air point’. The dotted line shows the coil impedance on the impedance plane due to a crack in the conductor.

The impedance can be derived from the definition of the electromagnetic power. Combining with reciprocity theorem (2.29), the impedance change of a coil due to a crack in a conductor can be written as [6]

$$\Delta Z_c = \frac{1}{I^2} \oint_S \mathbf{n} \cdot \left(\mathbf{E}^{(s)} \times \mathbf{H}^{(0)} - \mathbf{E}^{(0)} \times \mathbf{H}^{(s)} \right) dS, \quad (2.30)$$

where the superscript (0) denotes the fields without cracks, the superscript (s) denotes the ones with cracks and I is the magnitude of the coil current. The integration surface, S , could be any surface enclosing the crack. This formula not only can be used to find the impedance change due to crack, ΔZ_c , but also can be used for any inhomogeneous part of the geometry, even the impedance change from the conductor itself, ΔZ . For the calculation of coil impedance change in the absence of cracks, ΔZ , the integration surface becomes the surface enclosing the conductor. In that case, superscript (0) denotes the field in the absence of the conductor and the superscript (s) represents the fields in the presence of the conductor. Alternatively,

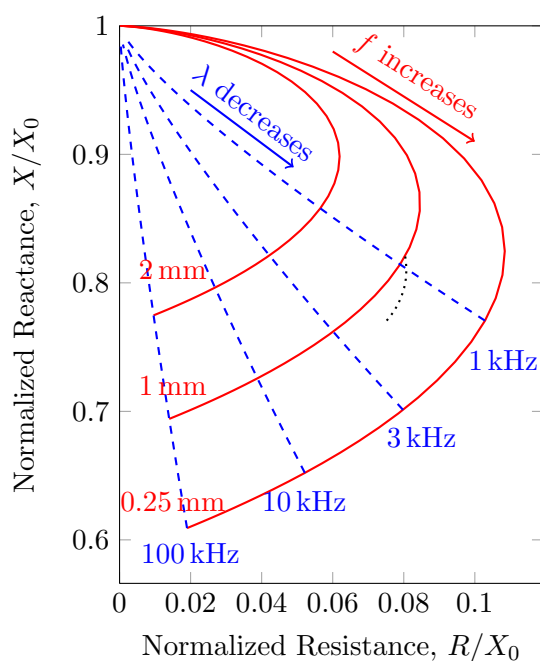


Figure 2.4: Impedance plane diagram for a bobbin coil above a half-space conductor. The coil size and the conductivity of the test-piece are listed in Table 4.3. Solid lines represent the complex impedance of the probe as a function of frequency. Dash lines represent the impedance as a function of coil lift-off, λ . The dotted line represents the coil impedance due to a crack.

the crack can be regarded as an equivalent electric dipole source and we can derive another expression for the coil impedance change through reciprocity theorem. The detailed discussion is provided in Section 4.2.3.

As mentioned before, skin effect could bring some numerical trouble in EC calculation. Compared to the typical scattering problems, another difference is that the coil is normally pretty close to the test-piece. Therefore, the far-field scattering theory used in other electromagnetic applications, such as antenna simulation, could not be applied to the EC problems. Normally, the near-field interaction is more complicated.

2.4 Statement of the Problem

In recent years, many in service aircrafts have exceeded their design lives and the maintenance of these aging aircraft structures becomes a worldwide issue. One of the most important

issues in aeronautic inspection is to detect embedded cracks located in the fastened structures. The fatigue cracks can initiate at corroded rivet holes and the location of crack initiation depends upon the local stress distribution. These fatigue cracks must be detected and repaired before they lead to catastrophic failure. The demand for a fast, low cost and reliable monitoring system to ensure the functionality of the crack detection in such structures is increasing. A three-dimensional electromagnetic model for eddy current fastened structures inspection is needed to meet this demand [7, 8, 9, 10, 11].

As shown in Fig. 2.5, the cracks around a rivet is actually a complex structure and a systematic approach has to be built to solve this problem. First of all, the model is simplified as cracks around a borehole in the layered conductors. The structure of corner cracks at the borehole opening considered as the further simplification. Finally, the problem is reduced to the cracks inside a infinitely long borehole in a conductor. All of these problems include cylindrical structures, such as bolt hole, cylinder or tube. Therefore, the study of EC NDE problems in cylindrical polar coordinates becomes an important subject. For each problem, the modeling of EC NDE involves two related configurations:

- *Incident field for the structure in the absence of cracks:* The first parts solves the problems with basic conductive geometries in the absence of cracks. The solution can be used not only for the incident field in the probe-defect interaction, but also for the characterization of the conductor with the same structure.

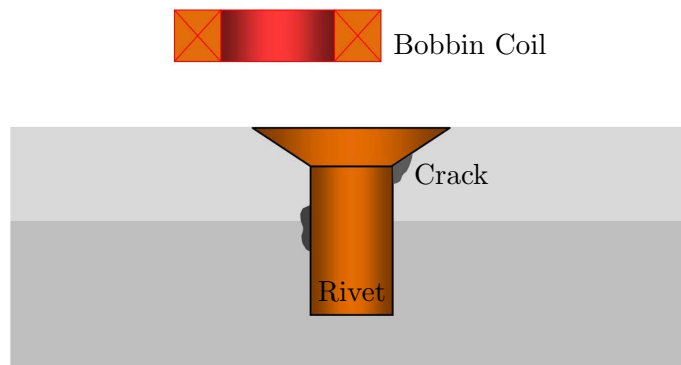


Figure 2.5: Two-layer aircraft structure with cracks emanating from a fastener hole.

- *Probe signal due to cracks in a conductor:* The probe-defect interaction is considered in this part. In general, the cracks are modeled as air-filled gap with given shape and it is equivalent to a secondary source. Then the Green's function is derived for a singular source in the similar structure. Finally, the coil impedance is calculated using volume integral method.

Although we have not completely solved the fastened structure yet, the systematic approach used in this research has already provided us a good understanding of the final problem. The models of cracks in the infinitely long borehole and tube have been finished and the result shows a good agreement compared with experimental measurements. The incident field of a coil around the opening of a borehole has also been solved using the same method. Finally, the coil signal due to a corner crack near the opening of a borehole is discussed.

It is worth mentioning that our approach can be easily extended into other cylindrical configurations, such as oil pipeline in petroleum industry and nuclear reactors in the nuclear power stations.

CHAPTER 3. LITERATURE REVIEW

Like other electromagnetic problems, EC NDE problems can be solved using either analytical methods, approximation methods, or numerical methods. For a problem with simple geometrical configuration, analytical solution may be written into a closed form with an integral expression. With the TREE method, semi-analytical solution may be available for some more complicated problems. Appropriate approximation, such as thin-skin theory, can be applied to certain special problems, in which analytical solution can not be found. On the other hand, numerical methods are more flexible and can handle more special and complicated configurations. However, because of the skin effect in quasi-static regime, it requires a large amount of unknowns and usually takes long time to compute, even for some simple structures.

A brief literature review about EC NDE problems is given in this chapter. Especially, a survey of EC problems in cylindrical coordinate system is also summarized. Other topics in EC NDE, such as inversion, imaging and reconstruction is not covered here. We will focus on the forward problems and the electromagnetic approaches to present the fundamental theory development in EC NDE.

3.1 Analytical Methods

In this section, analytical methods for the incident field calculation are discussed first. Then the modeling of flawed test-piece is considered. Again, it should be noticed that the solution of the unflawed test-piece can be used as the incident field for the probe-flaw interaction modeling. In addition, some of these methods could be extended to derive the Green's function from the same structure with cracks, which is a critical step to find the coil signal due to cracks in our theoretical models.

3.1.1 Modeling of Incident Field

Two classical axially symmetric probe-conductor problems were first solved by Dodd and Deeds with the closed-form solutions in 1968 [12]. One was for a rectangular cross-section coil (bobbin coil) above a semi-infinite conducting slab covered with another uniform conductor layer and another one was for a rectangular coil encircling an infinitely long circular conductive rod with uniform metal coating. This paper developed an important analytical method to analyze the real EC problems. The essential point was to work out the magnetic vector potential of a circular filament and then derive the coil field by using the superposition principle. Later the same idea was applied to other symmetrical configurations, such as multilayer plates solved by Burke et al. [13, 14, 15], concentric spherical shells by Luquire et al. [16, 17], and coaxial cylinders by Dodd et al. [18, 19].

The theory of eddy currents induced by a non-symmetric coil above a conducting half space was proposed by Beissener and Sablik in 1984 [20]. That was a generalization of the work from Dodd and Deeds for axisymmetric current sources. The effect of coil orientation on the eddy-current distribution was also demonstrated in that work. Impedance of a horizontal coil (or tangent coil, the axis of the coil is parallel to the conductor surface) above a half-space conductor was derived by Burke [21]. A thin-skin approximation and a closed-form solution of this problem were presented in that work. The mutual impedance of air-cored coils located above a conductive plate was considered by Burke and Ibrahim in 2004 [22]. The results for different orientation of the individual coil were discussed. Theodoulidis derived a closed-form expression for a cylindrical eddy-current probe coil located with an arbitrary tilt angle above a conductive half space [23]. This work helps us to understand the noise in eddy-current surface inspection due to an unexpected tilt of the probe.

There was some work related to ferrite-cored probes. A model of an axisymmetric probe coil with a cylindrical ferrite core in the presence of a layered conducting half space was developed with the aid of radial truncation by Theodoulidis [24, 25].

Eddy-current induction in an uniaxially anisotropic plate, where the axis of uniaxial anisotropy was lying in a plane parallel to the surface of the plate, was another interesting work done by

Burke [26]. In this approach, the fields were expressed in terms of Hertzian potentials, which is similar to SOVP. The half-space problem involving both electrical anisotropy and magnetic anisotropy was derived by Zhou and Dover in 1998 [27]. This method can be extended to the layered electromagnetic induction problems.

TREE method was widely applied to EC problems in the past decades [28]. Using this method, series expansion for simple configurations were presented by Theodoulidis in 2005 [29]. Problems with complicated geometrical configuration in Cartesian coordinates, such as right-angled wedge [30, 31] and edge of conductive plate [32], have also been solved by Bowler and Theodoulidis.

3.1.2 Modeling of Probe-Crack Interaction

Except a few cases with simple two-dimensional configuration, such as semi-infinite crack with a sharp tip, square corner [33], and infinite long cylinder containing a radial surface crack [34] solved by Kahn and Spal et al., it is impossible to get a closed-form solution for the crack problems, especially for the three dimensional configurations. Electromagnetic methods for EC problems were summarized by Kriezis et al. in 1992 [5], Lewis [35], and Auld and Moulder in 1999 [6].

Compared to the closed form, semi-analytical solution is accessible for more general crack problems. For instance, eddy current interaction with cracks in a thin plate which thickness is small compared with the skin depth was presented by Burke in 1988 [36]. In general, a semi-analytical solution has to be obtained more or less with the aid of approximation, from physical model to mathematical calculation. For example, perturbation method was applied to the low-frequency EC analysis by Harfield [37] and a long coil with a slot in a conductive plate was solved with TREE method by Theodoulidis and Bowler in 2005 [38].

One of the most important crack models is the ideal crack, which has infinitesimal thickness but forms a perfect barrier to eddy currents. By considering continuity boundary conditions, the ideal crack can be represented by an equivalent secondary source consisting of a layer of current dipole directed normal to the crack surface as stated by Bowler [39, 40]. The equivalent surface source could be found by the method of moments using Green's function. The model

can be extended to the volumetric flaw and volume integral formulation by Bowler et al. [41]. It turns out this is an accurate and efficient method to estimate the coil response due to cracks. Comparison of two boundary integral formulations based on electric field and magnetic vector potential were also discussed by Bowler et al. in 1997 [42].

3.1.3 Thin-Skin Theory

At high frequency, induced eddy current can be thought of as occupying a relatively thin layer near the surface of a test-piece because of the skin depth is much less than the relevant dimension of the surface defect. Within thin-skin limit, it is possible to solve the impedance change of a coil due to surface-breaking cracks [43, 44], long cracks [45, 46, 47], semi-elliptical, and epicyclic cracks [48] in a half-space conductor.

3.2 Numerical Methods

Ideally, a good numerical method could manipulate any structure regardless of geometrical complexity, homogeneity and type of coils. It could also be designed to compute the incident field for a specific structure. For example, some numerical methods are developed especially for the structures involving ferrite cores. A model of a three-dimensional axisymmetric probe coil with a linear isotropic ferrite core in the presence of a conducting half space was developed by Sabbagh using the method of moments [49]. In that model, a volume integral equation based on the magnetic induction field and the induced magnetization was introduced. Any arbitrarily shaped bodies-of-revolution, such as the E-shaped core (cup-core) and the coil with truncated ferrite cylinder could be solved with this model. The field calculation for single- or multilayer coaxial cylindrical shells of infinite length with an arbitrarily oriented inside source were solved using electric vector potential and the magnetic scalar potential by Antonopoulos et al. [50]. Another simulation code, which can handle ferrite core, was developed with a rigorous volume integral formulation based on the dyadic Green's functions by Buvat et al. [51]. This model was fast because it had the advantage that only the ferrite core needs to be discretized and not the entire space.

Typically a numerical approach involves the following four basic steps.

1. Definition of the problem region.
2. Formulation of the specific fields or potentials over the defined region.
3. Derivation of matrix equations whose solution gives numerically an approximate field.
4. Solution of the matrix equations and post-processing.

For a given problem, different formulations could be derived based on the choice of the fields as unknown variables. Comparison between different sets of potentials used in numerical methods was given by Nakata et al. in 1988 [52] and Kriezis et al. in 1992 [5].

Three most fundamental numerical approaches are finite difference method (FDM), finite element method (FEM), and method of moments (MoM). In order to obtain correct solution using FDM, it requires fine mesh structure and a large number of unknowns in EC NDE problems because of skin effect. FDM is not as widely used today as in the past, thus we only discuss the other two methods here.

3.2.1 Finite Element Method

Finite element method is an extension of the Rayleigh-Ritz technique by constructing coordinate functions whose linear combinations approximate the unknown solutions. An appropriate variational formulation can be chosen to set up a system of sparse matrix equations for two dimensional done by Ptchelintsev and de Halleux [53] and three dimensional EC problems by Badics et al. [54, 55]. FEM has the same issue as FDM. It requires a large number of unknowns to solve the problem, which dramatically increases the computational cost. In order to overcome this difficulty, an efficient techniques of solving matrix equations for two dimensional finite element analysis was proposed by Nakata et al. [56]. The use of nodal finite element in FEM may have difficulties when applied to highly permeable and sharp corner. Comparison for formulations of edge finite elements based on different vector and potentials unknowns was provided by Biro in 1999 [57].

3.2.2 Method of Moments

Method of moments is one kind of weighted residual methods. Green's functions have to be derived based on the choice of equivalent sources. Then an integral equation is set up to form the matrix equation from which the equivalent sources can be obtained. Compared to FDM and FEM, MoM does not require to discretize the whole solution domain if the specific Green's function is available. Thus, the computational cost can be reduced a lot.

Green's function is a critical part for the MoM. Therefore, appropriate Green's functions with relatively small solution domain were derived for specific configurations, such as a half-space conductor by Bowler [58] and a long tube by Barlow [59]. The time-domain Green's functions for a transient field solution were sought in EC problems for a half space [60], a plate [61] or a half space with injected currents at the surface [62] by Bowler et al.

For a flaw inside a conductor, the solution is available by using volume integral formulation. A summary was given by Mckirdy [63]. The method to calculate EC pattern in a planar layered conductor affected by a localized inhomogeneity of an arbitrary geometry was developed with a full-wave vector domain integral formulation by Reis et al. [64].

Boundary element method (BEM) is also an efficient way to deal with EC problems. It is applicable for two dimensional problems done by Kahn et al. [65, 66] and flaw detection in three dimensions done by Dezhi et al. [67]. Boundary integral can be derived based on electric and magnetic fields [68, 69] or different vector potentials [70, 71]. Boundary integral vector potential formulation with weak singularity kernel has also been developed by Yoshida [72]. Impedance boundary condition was utilized to analyze eddy current far away from the edge of conductor by Ishibashi [73]. An improvement of the ideal crack model taking into account the inclination, the conductance, and the low thickness of the crack was presented by Beltrame [74]. Fast multipole method has also been introduced to accelerate the BEM calculation in two-dimensional EC problems by Yang and Song [75, 76]. An improved boundary integral equation (BIE) is developed for the EC problems with Dirichlet boundary condition by Xie and Song et al. [77].

3.3 Modeling in Cylindrical Coordinates

Conductive half space and plate are two typical EC problems that people have solved during the 1990s. The reason is that it is easy to separate three scalar components of a vector representation in Cartesian coordinates. However, there are also considerable problems involving cylindrical geometrical configurations. Thus, the work related to the modeling in cylindrical coordinate system is summarized in this section.

With Fourier transform, longitudinal components in a conductive shell of infinite length and finite thickness with a straight current filament source was formulated by Gong et al. [78]. The solution of an arbitrary current distribution placed outside an infinitely long non-magnetic conductive cylinder was discussed by Grimberg et al. in 1997 [79] and the method was extended to a multi-layer conductive cylinder in 1999 [80].

Second-order magnetic vector potential was used to represent eddy-current distribution inside a long conducting cylinder excited by a saddle shaped coil by Theodoulidis et al. [81]. Using the similar method, a model of Wobbin coil inside a conductive tube was established in 2002 [82]. Eddy-current induction by an horizontal coil inside a long cylindrical bolthole was examined using the same idea by Burke and Theodoulidis [83]. Force and eddy current in a solid conducting cylinder due to an eccentric circular current loop was considered by Sakaji in 2000 [84]. Other examples, in which the SOVP is applied, include impedance calculation of curved rectangular spiral coils wrapped around a long conductive cylinder [85], detection of long cracks in steel using a spiral coil [86], a bobbin coil inside a conductive tube with eccentric walls [87], and coil around conductive sphere [88] by Burke, Skarlatos, and Theodoulidis et al.

TREE method is quite useful for cylindrical problems, such as eddy currents in a cylindrical conducting rod of finite length due to a coaxial encircling coil [89], the modeling of ferrite-cored probes [25], finite length layered rod [90, 91], the end effect in tube testing with bobbin coils [92], and coils inside a borehole [93]. The case of a coil at the opening of a borehole in a conductor has also been solved using this method by Theodoulidis and Bowler in 2008 [94]. However, in that work, the location of the coil has to be constrained to the borehole region due to the axial truncation and boundary conditions have to be matched at the surface of borehole.

Field expressions also can be further simplified with different truncation boundary conditions.

Volume integral method is also widely used in cylindrical problems. Grimberg et al. modeled the inner-eddy-current transducer with rotating magnetic field using volume integral method [95, 96]. Skarlatos et al. proposed a volume integral equation formulation for the modeling of ferromagnetic tubes [97].

In practice, not all the computer codes work well for the impedance calculation due to cracks in cylindrical objects because of convergence and accuracy issues. Most of them are slow and not efficient when they encounter the cylindrical problems. It is necessary to derive the formulation and design the code exclusively for cylindrical structures. Three dimensional bounded flaw in a metal tube was discussed by Monebhurrun et al. using a typical scattering formulation [98]. Thin-skin model was introduced to solve cracks in borehole by Burke [99]. For tubes with large radius, Chen et al. used the crack model with a finite-thickness plate to approximate cracks in steam generator tube [100]. The traditional approach dealing with the electric field scattering from layered cylinders is a possible way to solve above issues [101], but it does not take any advantage of eddy-current problems. Therefore, a systematic work which can efficiently tackle cylindrical problems is needed.

CHAPTER 4. COIL IMPEDANCE CHANGE DUE TO CRACKS IN A BOREHOLE

As mentioned in Chapter 2, cracks in cylindrical holes are the fundamental and important EC NDE problems. This chapter develops the theoretical and computational model of eddy-current coil signals due to a surface crack near a circular cylindrical hole. The surface crack is represented by an electric current dipole layer and an electric field integral formulation with a dyadic Green's kernel for the electric field in this cylindrical structure is developed. Numerical implementation is also discussed. Three specific examples are considered to validate our theoretical model. Comparison between prediction and experimental measurement shows a close agreement. This work has been published on IEEE Transactions on Magnetics in 2012 [102].

In order to apply TREE method to this problem, the infinitely long borehole is truncated in the axial direction and all the analytical solutions, including Green's function and the incident field, are expressed in terms of series. However, the integral-form solution for this special geometry is also viable due to the single circularly cylindrical boundary. The reason why we truncate the domain is to make the solution consistent with later chapters in which the truncation is necessary for the more complicated geometrical structure.

4.1 Introduction

We consider a surface crack in a cylindrical hole, as shown in Fig. 4.1. Assume the conductor has linear and homogeneous material properties apart from the flaw region, Ω . The permeability of the conductor is $\mu = \mu_0\mu_r$, where μ_0 is the permeability of free space. At the crack, the conductivity $\sigma(\mathbf{r})$ differs from that of the host conductivity σ_0 . The radius of the borehole is

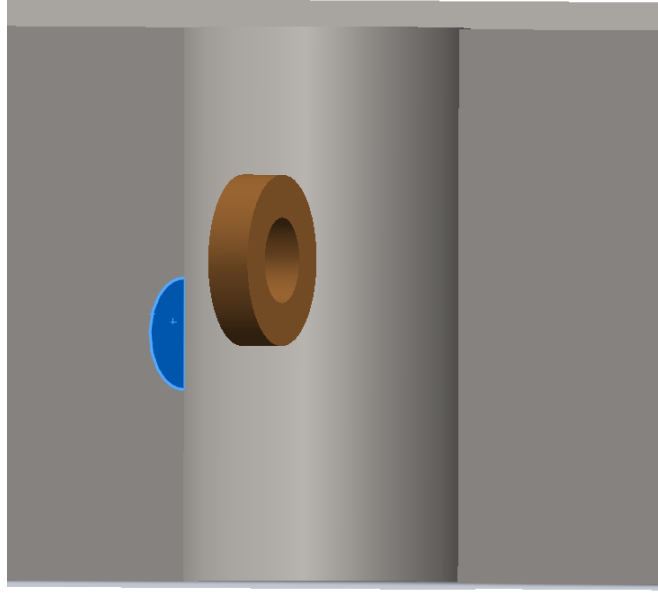


Figure 4.1: A rotary coil inside a boerhole in the presence of a longitudinal crack. The axis of the coil is perpendicular to the axis of the borehole.

b. The coil carries a current varying as the real part of $Ie^{-i\omega t}$.

The electric and magnetic fields inside the conductor and the flaw region satisfy Faraday's law (2.6) and Ampère's law (2.7), which are rewritten as

$$\nabla \times \mathbf{E}(\mathbf{r}) = i\omega\mu\mathbf{H}(\mathbf{r}), \quad (4.1)$$

$$\nabla \times \mathbf{H}(\mathbf{r}) = \sigma(\mathbf{r})\mathbf{E}(\mathbf{r}), \quad (4.2)$$

where the relationship $\mathbf{J} = \sigma\mathbf{E}$ has been substituted into the (2.7). Here, $\sigma(\mathbf{r})$ is σ_0 for (\mathbf{r}) at the conductive region and it becomes zero for (\mathbf{r}) at the crack region. The incident fields, i.e. the fields in the absence of cracks also satisfy the similar equations with homogeneous conductivity σ_0 , including the crack region,

$$\nabla \times \mathbf{E}^{(0)}(\mathbf{r}) = i\omega\mu\mathbf{H}^{(0)}(\mathbf{r}), \quad (4.3)$$

$$\nabla \times \mathbf{H}^{(0)}(\mathbf{r}) = \sigma_0\mathbf{E}^{(0)}(\mathbf{r}). \quad (4.4)$$

We will discuss these two problems separately. Let's consider the crack problem first.

4.2 Formulation

In the presence of an incident field, the field change comes from the inhomogeneity of the conductivity at the crack region. We define the induced electric dipole as

$$\mathbf{P}(\mathbf{r}) = [\sigma(\mathbf{r}) - \sigma_0]\mathbf{E}(\mathbf{r}). \quad (4.5)$$

This induced electric dipole is only non-zero at the crack region. With this definition, the Ampère's law becomes

$$\nabla \times \mathbf{H}(\mathbf{r}) = \sigma_0\mathbf{E}(\mathbf{r}) + \mathbf{P}(\mathbf{r}). \quad (4.6)$$

Taking the curl of both sides of (4.6) and substituting (4.1) into the right side, we have that

$$\nabla \times \nabla \times \mathbf{H} - k^2\mathbf{H} = \nabla \times \mathbf{P}, \quad (4.7)$$

where k is wave number and $k^2 = \omega\mu\sigma_0$. Taking the curl of both sides of (4.1) and combining it with (4.6), we find the electric field satisfies

$$\nabla \times \nabla \times \mathbf{E} - k^2\mathbf{E} = \omega\mu\mathbf{P}. \quad (4.8)$$

Considering (4.7) and (4.8) together, the induced electric dipole is actually equivalent to a local source which causes a field change from the incident field. Thus, the problem of finding the fields due to a crack is the same as the one of finding the electric current dipole density, \mathbf{P} .

4.2.1 Scalar Decomposition

The benefits of using scalar potentials has been discussed in Section 2.2.4. Here, because the magnetic field is divergence free, we can express it in terms of TE and TM potentials

$$\mathbf{H} = \nabla \times \nabla \times (\hat{z}W_a) + k^2\nabla \times (\hat{z}W_b), \quad (4.9)$$

over the whole solution domain and \hat{z} is the unit vector in the axial direction. From (4.7), we can write that

$$(\nabla^2 + k^2)\mathbf{H} = -\nabla \times \mathbf{P}. \quad (4.10)$$

By substituting (4.9) into (4.7), we get

$$(\nabla^2 + k^2) [\nabla \times \nabla \times (\hat{z}W_a) + k^2\nabla \times (\hat{z}W_b)] = -\nabla \times \mathbf{P}. \quad (4.11)$$

Taking the dot product of the left-hand side of (4.11) with \hat{z} , we have that

$$\begin{aligned}
& \hat{z} \cdot (\nabla^2 + k^2) [\nabla \times \nabla \times (\hat{z}W_a) + k^2 \nabla \times (\hat{z}W_b)] \\
&= (\nabla^2 + k^2) \hat{z} \cdot [\nabla \times \nabla \times (\hat{z}W_a) + k^2 \nabla \times (\hat{z}W_b)] \\
&= (\nabla^2 + k^2) \hat{z} \cdot \nabla \times \nabla \times (\hat{z}W_a) \\
&= -(\nabla^2 + k^2) \nabla_t^2 W_a
\end{aligned} \tag{4.12}$$

where $\nabla_t \equiv \nabla - \hat{z}\partial/\partial z$ and the transverse Laplace operator is defined as $\nabla_t^2 = \nabla^2 - \partial^2/\partial z^2$. On the other hand, by forming the cross product with \hat{z} and then taking the transverse divergence, $\nabla_t \cdot \hat{z} \times$ of the left-hand side of (4.11), we find that the TM potential, W_b satisfies

$$\begin{aligned}
& \nabla_t \cdot \hat{z} \times (\nabla^2 + k^2) [\nabla \times \nabla \times (\hat{z}W_a) + k^2 \nabla \times (\hat{z}W_b)] \\
&= (\nabla^2 + k^2) \nabla_t \cdot \hat{z} \times \left[\left(-\hat{z}\nabla_t^2 + \frac{\partial}{\partial z} \nabla_t \right) W_a + k^2 \nabla \times (\hat{z}W_b) \right] \\
&= (\nabla^2 + k^2) \nabla_t \cdot \left[-\frac{\partial}{\partial z} (\hat{z} \times \nabla_t W_a) + k^2 \nabla_t W_b \right] \\
&= k^2 (\nabla^2 + k^2) \nabla_t^2 W_b,
\end{aligned} \tag{4.13}$$

with $\nabla_t \cdot (\hat{z} \times \mathbf{Q}) = -\hat{z} \cdot (\nabla \times \mathbf{Q})$, we can write that

$$(\nabla^2 + k^2) \nabla_t^2 \begin{bmatrix} W_a \\ W_b \end{bmatrix} = \begin{bmatrix} \hat{z} \cdot \nabla \times \mathbf{P} \\ \hat{z} \cdot \nabla \times \nabla \times \mathbf{P}/k^2 \end{bmatrix}, \tag{4.14}$$

Some operator identities used in above derivations are given in Appendix A. The transverse Laplace operator, ∇_t^2 in (4.14) makes this equation different from a general Helmholtz equation. This is an important fact for the scalar potentials in EC problems.

4.2.2 Dyadic Green's Function

TE and TM modes are coupled with each other in this problem due to the continuity of the tangential fields at the cylindrical boundary. The flaw field can be found by constructing a dyadic kernel from scalar Green's functions and using the kernel in an electric field integral equation to determine the dipole source. We start by defining the scalar Green's function as

$$(\nabla^2 + k^2) \begin{bmatrix} G_{aa} & G_{ab} \\ G_{ba} & G_{bb} \end{bmatrix} = - \begin{bmatrix} 1 & 0 \\ 0 & 1 \end{bmatrix} \delta(\mathbf{r} - \mathbf{r}'). \tag{4.15}$$

The subscripts, a and b denote the modal character of the field and the source respectively. For example, G_{ab} represents the TE field migrating from the borehole interface originating at a TM source. Thus, the mode coupling is taken into account by including the terms G_{ab} and G_{ba} in this matrix form. In addition, a set of functions $U_{ij}(\mathbf{r}|\mathbf{r}')$ is defined as

$$G_{ij}(\mathbf{r}|\mathbf{r}') = -\nabla_t^2 U_{ij}(\mathbf{r}|\mathbf{r}') \quad i, j = a, b \quad (4.16)$$

where $(\mathbf{r}|\mathbf{r}')$ is Dirac delta function. Therefore, $U_{ij}(\mathbf{r}|\mathbf{r}')$ can be identified as the TE/TM potential due to a TE/TM point source.

In a conductor without any boundaries, there is no coupling between these two modes and a formal solution of (4.15) could be obtained using the fundamental solution of a scalar Helmholtz equation. We can write the solution as

$$G_0(\mathbf{r}|\mathbf{r}') = \frac{e^{ik|\mathbf{r}-\mathbf{r}'|}}{4\pi|\mathbf{r}-\mathbf{r}'|}, \quad (4.17)$$

where $G_0(\mathbf{r}|\mathbf{r}')$ is the Green's function in an unbounded space. A related function $U_0(\mathbf{r}|\mathbf{r}')$ is defined such that

$$G_0(\mathbf{r}|\mathbf{r}') = -\nabla_t^2 U_0(\mathbf{r}|\mathbf{r}'). \quad (4.18)$$

With the borehole boundary, additional fields due to the reflection has to be considered. Thus, we can write a set of dedicated Green's functions in (4.15) for the borehole problem as the sum of a singular part and a regular part as follows

$$G_{ij}(\mathbf{r}|\mathbf{r}') = \delta_{ij}G_0(\mathbf{r}|\mathbf{r}') + G_{ij}^{(\Gamma)}(\mathbf{r}|\mathbf{r}') \quad i, j = a, b \quad (4.19)$$

where δ_{ij} denote the Kronecker delta function with $\delta_{aa} = \delta_{bb} = 1$ and zero otherwise. The reflection parts from the borehole interface are considered in terms $G_{ij}^{(\Gamma)}$.

From (4.14), (4.16), (4.18), and (4.19), TE and TM potentials over the crack region are given by

$$\begin{bmatrix} W_a \\ W_b \end{bmatrix} = \int_{\Omega} \begin{bmatrix} U_0 + U_{aa} & U_{ab} \\ U_{ba} & U_0 + U_{bb} \end{bmatrix} \begin{bmatrix} \hat{z} \cdot \nabla' \times \mathbf{P} \\ \hat{z} \cdot \nabla' \times \nabla' \times \mathbf{P}/k^2 \end{bmatrix} d\mathbf{r}', \quad (4.20)$$

where the integrations are defined over the crack region Ω . Integrating (4.20) by parts gives

$$W_a(\mathbf{r}) = \int_{\Omega} \left\{ \nabla' \times [\hat{z}(U_0 + U_{aa})] + \frac{1}{k^2} \nabla' \times \nabla' \times [\hat{z}U_{ab}] \right\} \cdot \mathbf{P} \, d\mathbf{r}', \quad (4.21)$$

$$W_b(\mathbf{r}) = \int_{\Omega} \left\{ \nabla' \times [\hat{z}U_{ba}] + \frac{1}{k^2} \nabla' \times \nabla' \times [\hat{z}(U_0 + U_{bb})] \right\} \cdot \mathbf{P} \, d\mathbf{r}'. \quad (4.22)$$

With specific functions U_{ij} $i, j = a, b$, the potentials can be calculated for a given electric current dipole density and these expressions can be used to construct a dyadic kernel for an electric field integral equation as follows.

4.2.3 Electric Field Integral Equation

An air-filled crack in a conductor forms a barrier to the eddy current, as stated in (2.17). This boundary condition is applied to the electric field to form an integral equation. Therefore, an expression for the electric field is needed for the calculation. The relationship between electric field and the dipole source is given in (4.8), and we can regard $i\omega\mu\mathbf{P}$ as the source term. In order to derive the integral equation from (4.8), a formal solution of the electric field can be written as

$$\mathbf{E}(\mathbf{r}) = \mathbf{E}^{(0)}(\mathbf{r}) + i\omega\mu \int_{\Omega} \mathcal{G}(\mathbf{r}|\mathbf{r}') \cdot \mathbf{P}(\mathbf{r}') \, d\mathbf{r}', \quad (4.23)$$

where $\mathbf{E}^{(0)}$ is the incident electric field in the absence of the crack and it could be solved from (4.3) and (4.4). The dyadic Green's function, $\mathcal{G}(\mathbf{r}|\mathbf{r}')$, satisfies

$$\nabla \times \nabla \times \mathcal{G}(\mathbf{r}|\mathbf{r}') - k^2 \mathcal{G}(\mathbf{r}|\mathbf{r}') = \mathcal{I}\delta(\mathbf{r} - \mathbf{r}'), \quad (4.24)$$

with the borehole geometry.

In general, the dyadic Green's function can be expressed as the sum of a singular unbounded domain term in the absence of any boundaries, plus a regular term that accounts for the interaction of the primary field with conductor boundaries [103]. Here, as with the scalar Green's functions in (4.19), the dyadic kernel for an infinite borehole is written as the sum of the unbounded domain kernel and a reflection term representing the field migration from the borehole surface

$$\mathcal{G}(\mathbf{r}|\mathbf{r}') = \mathcal{G}^{(0)}(\mathbf{r}|\mathbf{r}') + \mathcal{G}^{(\Gamma)}(\mathbf{r}|\mathbf{r}'), \quad (4.25)$$

where the dyadic Green's kernel in an unbounded domain is

$$\mathcal{G}^{(0)}(\mathbf{r}|\mathbf{r}') = \left(\mathcal{I} + \frac{1}{k^2} \nabla \nabla \right) G_0(\mathbf{r}|\mathbf{r}'), \quad (4.26)$$

with $G_0(\mathbf{r}|\mathbf{r}')$ given by (4.17) [103].

Dyadic identities provided in Appendix A can be used to derive the dyadic Green's function via the scalar decomposition of the fields. Substituting (4.22) into (4.2) and (4.9), one can identify the two terms in (4.25) as follows

$$\mathcal{G}^{(0)}(\mathbf{r}|\mathbf{r}') = - \left(\mathcal{I} + \frac{1}{k^2} \nabla \nabla \right) \nabla_t^2 U_0(\mathbf{r}|\mathbf{r}'), \quad (4.27)$$

and

$$\begin{aligned} \mathcal{G}^{(\Gamma)}(\mathbf{r}|\mathbf{r}') &= (\nabla \times \hat{z})(\nabla' \times \hat{z})U_{aa}(\mathbf{r}|\mathbf{r}') + \frac{1}{k^2}(\nabla \times \hat{z})(\nabla' \times \nabla' \times \hat{z})U_{ab}(\mathbf{r}|\mathbf{r}') \\ &+ (\nabla \times \nabla \times \hat{z})(\nabla' \times \hat{z})U_{ba}(\mathbf{r}|\mathbf{r}') + \frac{1}{k^2}(\nabla \times \nabla \times \hat{z})(\nabla' \times \nabla' \times \hat{z})U_{bb}(\mathbf{r}|\mathbf{r}'). \end{aligned} \quad (4.28)$$

A general discussion is also given in [104].

Once the electric field is obtained from (4.23), the eddy current inside the conductor can be found as $\mathbf{J} = \sigma_0 \mathbf{E}$. For an air-filled crack in the conductor, the eddy current can not flow across the interface. We can applied this boundary condition at the crack interface and the final electric field integral equation is given by

$$J_n^{(0)}(\mathbf{r}) + k^2 \int_{\Omega} \hat{n} \cdot \mathcal{G}(\mathbf{r}|\mathbf{r}') \cdot \mathbf{P} \, d\mathbf{r}' = 0, \quad (4.29)$$

where \mathbf{r} is on the surface of the crack and \hat{n} is an unit vector normal to the crack surface.

As mentioned before, the coil signal due to the crack is measured in practical applications. By applying reciprocity theorem to the scattered field at the primary source and the incident field at the equivalent source (the induced current dipole density at the flaw) [41], the coil impedance change due to a crack is given by

$$\Delta Z_c = -\frac{1}{I^2} \int_{\Omega} \mathbf{E}^{(0)}(\mathbf{r}) \cdot \mathbf{P}(\mathbf{r}) \, d\mathbf{r}. \quad (4.30)$$

Once the incident field and the dipole density are calculated, we could get the coil impedance change using (4.30).

4.3 Incident Field Distribution

As discussed in the last section, the incident field is required in (4.29) and (4.30) to get the coil impedance change due to cracks. The calculation of the incident coil field in the presence of a borehole, $\mathbf{E}^{(0)}(\mathbf{r})$, has been presented in an integral form by Burke and Theodoulidis [83] and a series form by Theodoulidis and Bowler [93]. The derivations are also given in Appendix D for supplementation. In our program, a bobbin coil and a rotary coil are considered. Rotary coils have larger response for a longitudinal crack and are more useful in EC NDE applications. Thus, we will focus on the rotary coils in the following discussion.

A contour plot of the incident field at the plane $\phi = 0^\circ$ is shown in Fig. 4.2. The parameters of the coil size are listed in Table 4.1. In this figure, the coil excitation frequency is 1 kHz and the center of the rotary coil is at $z = 0$ and the borehole interface is located at $\rho = 12.5$ mm.

Table 4.1: Parameters of test experiment for a rotary coil inside borehole. The configuration is shown in Fig. 4.3.

Coil	
Inner radius (r_1)	1.53 mm
Outer radius (r_2)	3.92 mm
Length (ℓ)	1.04 mm
Number of turns (N)	305
Lift-off ($b - x_2$)	0.73 mm
Test Specimen	
Borehole radius (b)	12.5 mm
Conductivity (σ)	23.05 MS/m
Relative permeability (μ_r)	1
Transverse Notch	
Circumferential notch	5.0 mm rad.
Width (w)	0.130 mm
Longitudinal Notch	
Semi-elliptical axial notch	5.0×15.0 mm ²
Width (w)	0.130 mm
Other Parameters	
Frequency (f)	40 kHz
Skin depth at 40 kHz (δ)	0.524 mm
Isolated coil inductance (L)	462.0 μ H

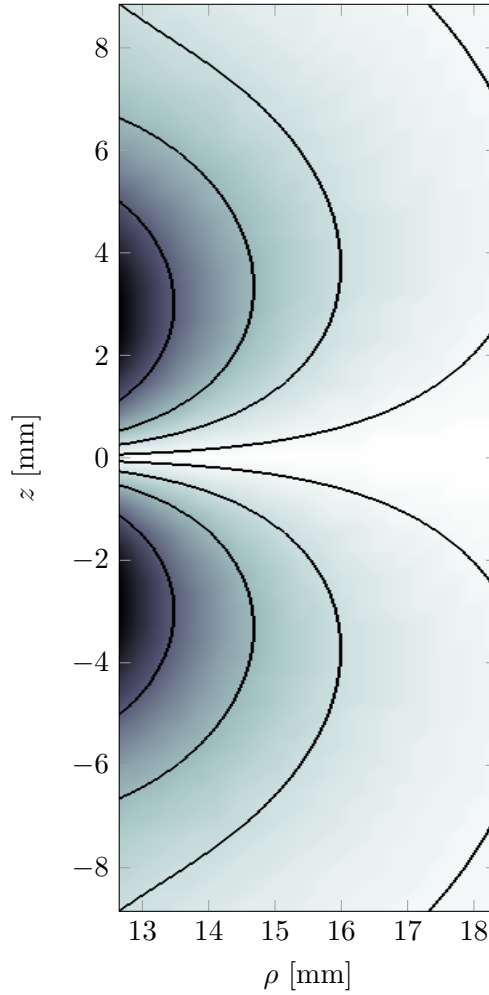


Figure 4.2: Incident field at the plane $\phi = 0^\circ$ due to a rotary coil inside a boerhole in the absence of cracks, the parameters are listed in Table 4.1. The operating frequency is 1 kHz.

4.4 Scalar Green's Function

To complete the solution and find the electric current dipole density, the scalar Green's function $G_{ij}(\mathbf{r}|\mathbf{r}')$ defined in (4.15) and its related functions $U(\mathbf{r}|\mathbf{r}')$ defined in (4.16) are sought for a cylindrical borehole with corresponding boundary conditions in this section. For the scalar functions expressed in cylindrical polar coordinates, Fourier series representation is used in the azimuthal direction due to the periodicity of 2π . TREE method is used here to derive the scalar Green's function. The whole domain is truncated in the axial direction at the surface $z = 0$ and $z = h$, where h is the truncation length. We impose the truncation boundary

condition that the tangential electric field is zero (PEC boundary condition) at $z = 0$ and the tangential magnetic field is zero (PMC boundary condition) at $z = h$. These truncation boundary conditions, which are used through this dissertation, are summarized in Table 4.2. The axial direction, \hat{z} is chosen as the normal direction.

Assume a point source located at P in the conductor, Fig. 4.3. For the region $\rho < \rho'$, the magnetic field has a scalar representation like

$$\mathbf{H} = \nabla \times \nabla \times (\hat{z}W_a) + k^2 \nabla \times (\hat{z}W_b), \quad (4.31)$$

and, in this region, the electric field can be expressed as

$$\mathbf{E} = \omega\mu[\nabla \times (\hat{z}W_a) + \nabla \times \nabla \times (\hat{z}W_b)]. \quad (4.32)$$

Both the scalar potentials satisfy Helmholtz equation

$$(\nabla^2 + k^2)W = 0, \quad (4.33)$$

in the conductive region for $b < \rho < \rho'$ and Laplace equation

$$\nabla^2 W = 0, \quad (4.34)$$

in the borehole for $\rho < b$. Analytical solution can be found in each region by using the method of separation of variables.

With the axial truncation, the function can be extended into a periodic function and the Fourier series expansion respect to the axial direction \hat{z} , is performed. The PEC truncation boundary condition means the TE potential is zero at $z = 0$, while the PMC truncation condition means the derivative of the TE potential respective to z is zero at $z = h$. With this property, the truncation boundary conditions we imposed are actually equivalent to that we

Table 4.2: Summary of the truncated boundary conditions at $z = 0$ and $z = h$.

Truncation Plane	Field Condition	Boundary Condition
$z = 0$	$\hat{z} \times \mathbf{E} = 0$	$W_a = 0, \frac{\partial W_b}{\partial z} = 0$
$z = h$	$\hat{z} \times \mathbf{H} = 0$	$\frac{\partial W_a}{\partial z} = 0, W_b = 0$

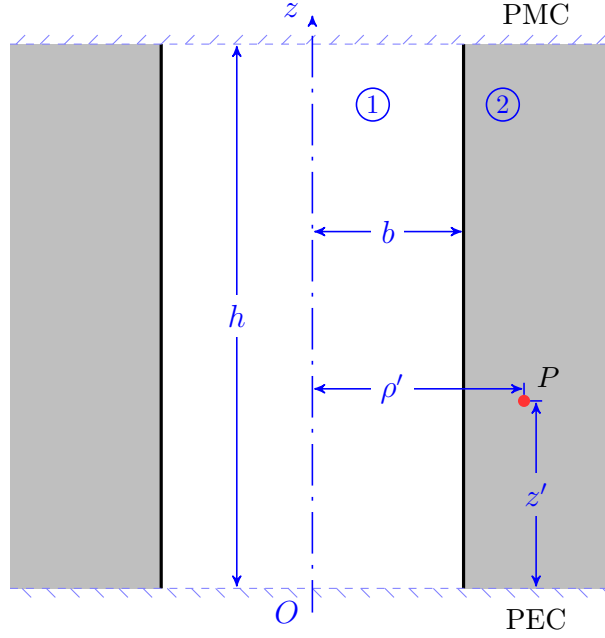


Figure 4.3: A point source in a truncated borehole region. The whole domain is truncated in the axial direction at the surface $z = 0$ with PEC truncation boundary condition and at $z = h$ with PMC truncation boundary condition.

extend the function within the region $0 \leq z \leq h$ into a smooth periodic function and apply the Fourier series expansion to this periodic function. Therefore, the sine functions with certain periods form a complete set to express the TE potential in the axial direction. The first three sine functions in this set and their expansions are plotted in Fig. 4.4. It is easy to see the period of these functions should be $\pi/2h$, $3\pi/2h$, $5\pi/2h$, and so on.

With Fourier series expansion in the azimuthal and axial directions, all the scalar Green's functions corresponding to the TE potential can be written as

$$G_a(\mathbf{r}|\mathbf{r}') = \frac{1}{\pi h} \sum_{m=-\infty}^{\infty} e^{im(\phi-\phi')} \sum_{i=1}^{\infty} \tilde{G}_0(\rho, \rho', m, \kappa_i) \sin(\kappa_i z) \sin(\kappa_i z'), \quad (4.35)$$

where eigenvalues $\kappa_i = (2i - 1)\pi/2h$ ($i = 1, 2, 3, \dots$) to match the truncation conditions. The Green's function for the TM potential has the similar form except a cosine function is used to satisfy truncation conditions in the axial direction

$$G_b(\mathbf{r}|\mathbf{r}') = \frac{1}{\pi h} \sum_{m=-\infty}^{\infty} e^{im(\phi-\phi')} \sum_{i=1}^{\infty} \tilde{G}_0(\rho, \rho', m, \kappa_i) \cos(\kappa_i z) \cos(\kappa_i z'). \quad (4.36)$$

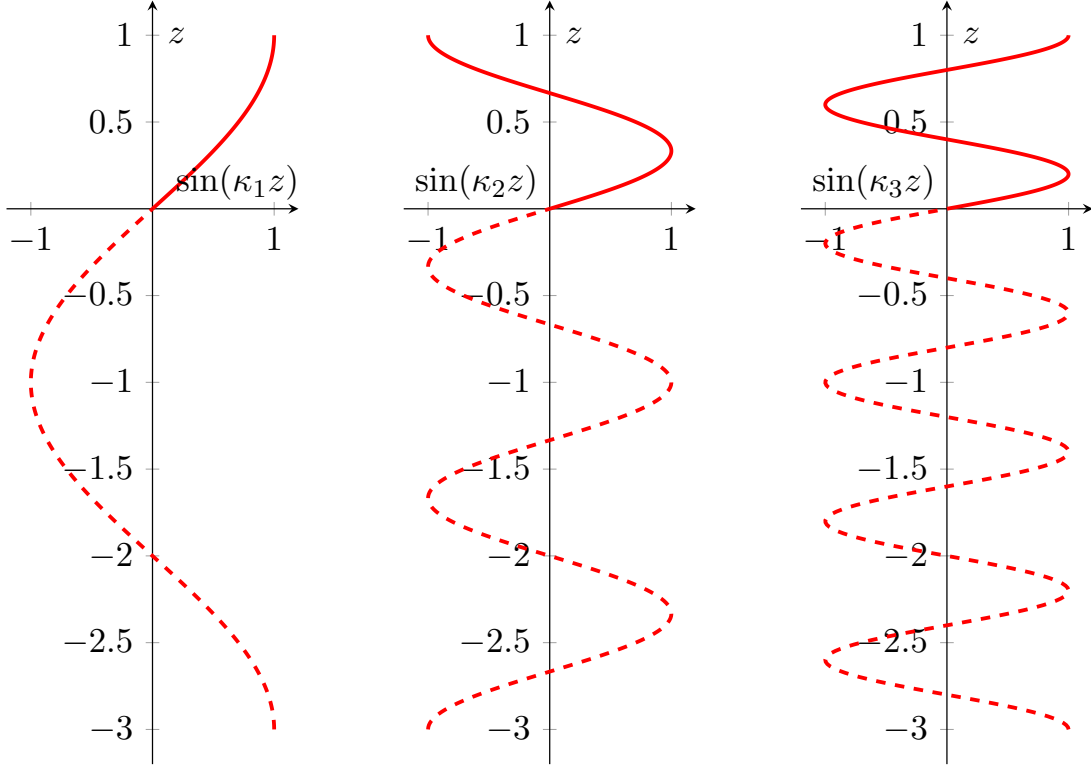


Figure 4.4: The meaning of truncation boundary conditions. Here, the PEC and PMC truncation boundary conditions are applied at $z = 0$ and $z = 1$, respectively. Eigenvalues $\kappa_i = (2i - 1)\pi/2$ where $i = 1, 2, 3, \dots$

For simplicity, we drop this double summation form for the time being and use the Fourier series expansion form \tilde{G} in the following discussion.

4.4.1 Scalar Green's Function for a Point Source in a Borehole

Let's first consider a singular source point in a homogeneous conductive domain, Fig. 4.5. There is no coupling between TE and TM potentials in this case and the dyadic Green's function is reduced to two separate scalar Green's functions. Substituting (4.35) into (4.15), the Fourier transform of the unbounded Green's function $\tilde{G}_0(\rho, \rho', m, \kappa_i)$ satisfies

$$\frac{1}{\rho} \frac{\partial}{\partial \rho} \left(\rho \frac{\partial \tilde{G}_0}{\partial \rho} \right) - \left(\gamma_i^2 + \frac{m^2}{\rho^2} \right) \tilde{G}_0 = -\frac{1}{\rho} \delta(\rho - \rho'), \quad (4.37)$$

where $\gamma_i^2 = \kappa_i^2 - k^2$ and the solution is given by

$$\tilde{G}_0(\rho, \rho', m, \kappa_i) = I_m(\gamma_i \rho_{<}) K_m(\gamma_i \rho_{>}), \quad (4.38)$$

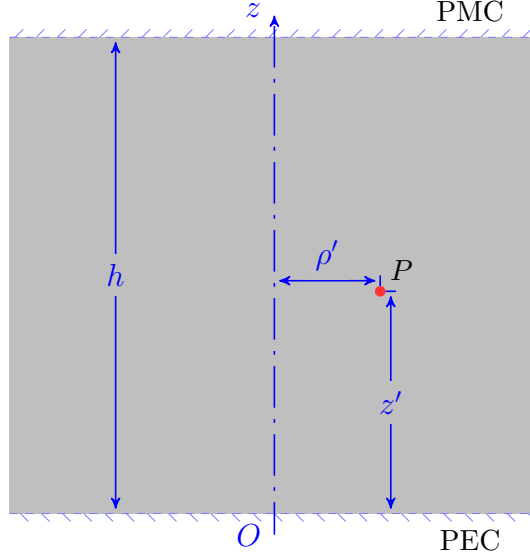


Figure 4.5: A point source in a truncated homogeneous conductive region, $0 \leq z \leq h$. The truncation boundary conditions are the same as before.

with $\rho_{<} = \min(\rho, \rho')$ and $\rho_{>} = \max(\rho, \rho')$ [105]. $I_m(z)$ is the modified Bessel function of the first kind and $K_m(z)$ is the modified Bessel function of the second kind. The index m is corresponding to the order of the modified Bessel function or the period in the azimuthal direction and the index i is related to the modes in the axial direction. For simplicity, let's also drop the subscript i from κ_i and γ_i for now.

As mentioned in (4.19), the Fourier domain kernels for a point source in the conductive region surrounding a circular hole takes the form

$$\tilde{G}_{ij}(\rho, \rho', m, \kappa) = \delta_{ij} \tilde{G}_0(\rho, \rho', m, \kappa) + \tilde{G}_{ij}^{(\Gamma)}(\rho, \rho', m, \kappa). \quad (4.39)$$

The field migrating outwardly from the surface of the borehole is represented by

$$\tilde{G}_{ij}^{(\Gamma)}(\rho, \rho', m, \kappa) = \Gamma_{ij}(m, \gamma) K_m(\gamma \rho) K_m(\gamma \rho'), \quad i, j = a, b \quad (4.40)$$

where $\Gamma_{ij}(m, \gamma)$ are the reflection coefficients characterizing the boundary conditions on the circularly cylindrical surface and they can be found using the following standard method by matching the boundary conditions at the cylindrical surface.

4.4.2 Transmission and Reflection Inside a Borehole

For the truncated borehole, the tangential fields on both sides of the borehole interface have to be considered together to match the continuity of the tangential electric and magnetic fields. In the following derivation, the superscript (0) is used to represent the incident field, Fig. 4.3. The coefficients representing the fields inside borehole are denoted by the superscript (1) and the quantities associated with the reflection from the borehole surface are denoted by the superscript (2). According to (4.16), the functions $\tilde{U}_{ij}(\rho, \rho', m, \kappa)$ in the conductive region can be written as

$$\tilde{U}_{ij}(\rho, \rho', m, \kappa) = \delta_{ij} \tilde{U}_{ij}^{(0)}(\rho, \rho', m, \kappa) + \tilde{U}_{ij}^{(2)}(\rho, \rho', m, \kappa), \quad i, j = a, b \quad (4.41)$$

where

$$\tilde{U}_{aa}^{(0)} = \tilde{U}_{bb}^{(0)} = -\frac{1}{\gamma^2} \tilde{G}_0 = -\frac{1}{\gamma^2} I_m(\gamma\rho) K_m(\gamma\rho'), \quad (4.42)$$

and

$$\tilde{U}_{ij}^{(2)} = -\frac{1}{\gamma^2} \tilde{G}_{ij}^{(\Gamma)} = -\frac{1}{\gamma^2} \Gamma_{ij}(m, \gamma) K_m(\gamma\rho) K_m(\gamma\rho'). \quad (4.43)$$

Inside the borehole, \tilde{U}_{ij} has the form

$$\tilde{U}_{ij}^{(1)}(\rho, \rho', m, \kappa) = T_{ij}(m, \gamma) I_m(\kappa\rho) K_m(\gamma\rho'), \quad (4.44)$$

where $T_{ij}(m, \gamma)$ is the transmission coefficients due to the interface. Let's define the vector and matrix form, such as

$$\tilde{\mathbf{U}} = \begin{bmatrix} \tilde{U}_a \\ \tilde{U}_b \end{bmatrix} = \begin{bmatrix} \tilde{U}_{aa} + \tilde{U}_{ab} \\ \tilde{U}_{ba} + \tilde{U}_{bb} \end{bmatrix}, \quad (4.45)$$

and

$$\mathbf{\Gamma}_m = \begin{bmatrix} \Gamma_{aa} & \Gamma_{ab} \\ \Gamma_{ba} & \Gamma_{bb} \end{bmatrix}. \quad (4.46)$$

Coefficients in (4.41) and (4.44) are then related as

$$\tilde{\mathbf{U}}^{(1)} = \mathbf{\Gamma}_m \tilde{\mathbf{U}}^{(0)}, \quad (4.47)$$

and

$$\tilde{\mathbf{U}}^{(1)} = \mathbf{\Gamma}_m \tilde{\mathbf{U}}^{(0)}. \quad (4.48)$$

Similarly, the coupling between the TE and TM modes have been included as the off-diagonal elements in the reflection matrix. The transmission and reflection coefficient matrices, \mathbf{T}_m and $\mathbf{\Gamma}_m$, can be solved by applying the continuity of the tangential fields on $\rho = b$. The continuity conditions of the axial and the azimuthal components of electric and magnetic fields are given by

$$\kappa^2 \tilde{\mathbf{U}}^{(1)} \Big|_{\rho=b^-} = \gamma^2 \mathbf{I}_\mu \tilde{\mathbf{U}}^{(2)} \Big|_{\rho=b^+} \quad (4.49)$$

$$\begin{bmatrix} \frac{im}{b} \partial_z & 0 \\ \partial_\rho & -\frac{im}{b} \partial_z \end{bmatrix} \tilde{\mathbf{U}}^{(1)} \Big|_{\rho=b^-} = \mathbf{I}_\mu \begin{bmatrix} \frac{im}{b} \partial_z & -k^2 \partial_\rho \\ \partial_\rho & -\frac{im}{b} \partial_z \end{bmatrix} \tilde{\mathbf{U}}^{(2)} \Big|_{\rho=b^+} \quad (4.50)$$

where $\mathbf{I}_\mu = \begin{bmatrix} 1 & 0 \\ 0 & \mu_r \end{bmatrix}$ and the equations are derived from the continuity of the tangential fields in terms of TE and TM potentials. The tangential components are derived from (4.31) and (4.32). From (4.49) and (4.50), it is clear that the TE and TM modes are coupled at the borehole interface for nonzero order mode ($m \neq 0$). The following notations are used in the our solution

$$\Lambda_m(x) = \frac{x I'_m(x)}{I_m(x)}, \quad M_m(x) = \frac{x K'_m(x)}{K_m(x)}, \quad (4.51)$$

and we have that

$$\Lambda_m(x) - M_m(x) = \frac{1}{I_m(x) K_m(x)}. \quad (4.52)$$

Solving equations (4.49) and (4.50), we find

$$\begin{aligned} \Gamma_{aa}(m, \gamma) &= -\frac{I_m(\gamma b)}{K_m(\gamma b)} \Delta_m^{-1} \{ \mu_r k^2 m^2 - M_m(\gamma b) [\mu_r \kappa^2 \Lambda_m(\gamma b) - \gamma^2 \Lambda_m(\kappa b)] \}, \\ \Gamma_{bb}(m, \gamma) &= -\frac{I_m(\gamma b)}{K_m(\gamma b)} \Delta_m^{-1} \{ \mu_r k^2 m^2 - \Lambda_m(\gamma b) [\mu_r \kappa^2 M_m(\gamma b) - \gamma^2 \Lambda_m(\kappa b)] \}, \\ \Gamma_{ab}(m, \gamma) &= -\frac{i \mu_r \kappa m k^2}{[K_m(\gamma b)]^2} \Delta_m^{-1}, \quad \Gamma_{ba}(m, \gamma) = -\Gamma_{ab}(m, \gamma) / k^2, \end{aligned} \quad (4.53)$$

where

$$\Delta_m = \mu_r k^2 m^2 - M_m(\gamma b) [\mu_r \kappa^2 M_m(\gamma b) - \gamma^2 \Lambda_m(\kappa b)]. \quad (4.54)$$

By substituting the reflection coefficients in (4.53) back to (4.40), we complete the derivation of the scalar Green's function and the dyadic kernel in (4.23).

4.5 Flaw Theory and Crack Model

Narrow surface crack is a typical simulation model used in EC NDE problems. For a narrow crack, the component of the dipole density normal to the crack surface is dominant. Thus, it is reasonable and efficient to only compute this component. In this section, transverse and longitudinal cracks are introduced as two examples to validate the formulation derived before.

4.5.1 Narrow Crack and Ideal Crack

For a general flaw, the electric field integral equation (4.29) can be solved numerically using volume element method. However, for a parallel sided narrow crack, the component normal to the crack surface dominates and the transverse components can be neglected. Thus, the electric current dipole density can be written as

$$\mathbf{P}(\mathbf{r}) \cong \hat{n}P(\mathbf{r}), \quad (4.55)$$

where \hat{n} is normal to the crack surface. Then the integral equation (4.29) is reduced to

$$J_n^{(0)}(\mathbf{r}) + k^2 \int_{\Omega} G_{nn}(\mathbf{r}|\mathbf{r}')P(\mathbf{r}) d\mathbf{r}' = 0, \quad (4.56)$$

for the points on the outside surface of a crack that is impenetrable and the kernel is one component of the dyadic Green's function

$$G_{nn}(\mathbf{r}|\mathbf{r}') = \hat{n} \cdot \mathcal{G}(\mathbf{r}|\mathbf{r}') \cdot \hat{n}. \quad (4.57)$$

Now the problem simply becomes the calculation of a dipole density over a crack surface using volume element method. We only need to define the problem domain over the crack region, which means a significant reduction of the computational cost. The same thing happens for an ideal crack which is a surface crack with infinitesimal thickness and a surface dipole density is defined as

$$\mathbf{P}(\mathbf{r}) = \hat{n}\delta_n P(\mathbf{r}). \quad (4.58)$$

Here, we examine both transverse and longitudinal cracks in a borehole and refer to both ideal and open cracks in the our discussion. The transverse crack is a crack which surface is perpendicular to the axial direction, because the axial direction has been chosen as the

longitudinal direction in above derivation. The longitudinal crack, as shown in Fig. 4.1, means the crack which surface is parallel to the radial and axial directions.

4.5.2 Transverse and Longitudinal Cracks

For a transverse crack, the crack surface is normal to the axial direction with $\hat{n} = \hat{z}$ and the component of the tensor kernel required for the calculation is $G_{zz}(\mathbf{r}|\mathbf{r}')$. Also, only the axial component of the incident field is needed. As the expression of the dyadic Green's function in (4.25), this kernel can be divided into two parts, unbounded domain part from (4.27),

$$G_{zz}^{(0)}(\mathbf{r}|\mathbf{r}') = \left(1 + \frac{1}{k^2} \frac{\partial^2}{\partial z^2}\right) G_0(\mathbf{r}|\mathbf{r}'), \quad (4.59)$$

and the reflection part from (4.28)

$$G_{zz}^{(\Gamma)}(\mathbf{r}|\mathbf{r}') = -\frac{1}{k^2} \nabla_t'^2 G_{bb}^{(\Gamma)}(\mathbf{r}|\mathbf{r}') = \frac{1}{k^2} \nabla_t^2 \nabla_t'^2 U_{bb}^{(\Gamma)}(\mathbf{r}|\mathbf{r}'). \quad (4.60)$$

For a longitudinal crack, the crack surface is normal to the azimuthal direction with $\hat{n} = \hat{\phi}$. The component of tensor kernel required for the calculation, $G_{\phi\phi}(\mathbf{r}|\mathbf{r}')$, can be written as

$$G_{\phi\phi}^{(0)}(\mathbf{r}|\mathbf{r}') = \left(1 + \frac{1}{k^2 \rho^2} \frac{\partial^2}{\partial \phi^2}\right), \quad (4.61)$$

for the unbounded domain part and

$$G_{\phi\phi}^{(\Gamma)}(\mathbf{r}|\mathbf{r}') = \frac{\partial^2 U_{aa}}{\partial \rho \partial \rho'} - \frac{1}{k^2 \rho'} \frac{\partial^3 U_{ab}}{\partial \rho \partial \phi' \partial z'} - \frac{1}{\rho} \frac{\partial^3 U_{ba}}{\partial \phi \partial z \partial \rho'} + \frac{1}{k^2 \rho \rho'} \frac{\partial^4 U_{bb}}{\partial \phi \partial z \partial \phi' \partial z'}, \quad (4.62)$$

for the reflection part. We only have to consider the azimuthal component of the incident field $J_\phi^{(0)}(\mathbf{r})$ in (4.56).

With appropriate discretization procedure, the dipole density over a crack region can be expressed in terms of linear combination of the given basis function and the volume element method can be applied to a specific problem. Final results of the coil impedance change can be obtained numerically.

4.6 Volume Element Method and Numerical Algorithm

Consider the crack problem described above with the integral equation (4.56). The crack region is divided into cubic volume elements. Pulse basis function in cylindrical polar coordi-

nates is used to describe the dipole density over each cell [106]. An approximated solution for $P(\mathbf{r})$ can be written as

$$P(\mathbf{r}) \approx \sum_{l=1}^L p_l f_l(\mathbf{r}), \quad (4.63)$$

where pulse function $f_l(\mathbf{r})$ is defined as

$$f_l(\mathbf{r}) = \begin{cases} 1 & \text{if } \mathbf{r} \in \text{cell } l \\ 0 & \text{otherwise} \end{cases} \quad (4.64)$$

Substituting (4.63) into (4.56), we have that

$$k^2 \sum_{l=1}^L p_l \int_{\Omega_l} G_{nn}(\mathbf{r}|\mathbf{r}') d\mathbf{r}' = -J_n^{(0)}(\mathbf{r}). \quad (4.65)$$

With point-matching (collocation) method on the crack surface, a system of matrix equations with L unknown coefficients p_l is obtained as

$$[\mathbf{M}][\mathbf{p}] = -[\mathbf{J}], \quad (4.66)$$

where $[\mathbf{p}]$ and $[\mathbf{J}]$ are column vectors and the element in matrix $[\mathbf{M}]$ is

$$M_{jl} = k^2 \int_{\Omega_l} G_{nn}(\mathbf{r}_j|\mathbf{r}') d\mathbf{r}'. \quad (4.67)$$

Once the matrix equations, (4.66) are constructed, the dipole density can be solved by using standard matrix solver. To simplify the thin-crack problem, only one element is used in the normal direction \hat{n} and (4.67) is calculated over all the volume elements. Notice that the testing point \mathbf{r}_j is located on the outside surface of each cell, not at center. For an ideal crack, the volume integral is reduced to the surface integral and the testing point is at the center of the cell.

Finally, the impedance change of a coil due to a crack in (4.30) is approximated as

$$\Delta Z_c = -\frac{1}{\sigma_0 I^2} [\mathbf{J}]^T \cdot [\mathbf{P}], \quad (4.68)$$

where superscript T means the transpose of \mathbf{J} . The calculation of the matrix elements, M_{jl} for the transverse and longitudinal cracks are described as follows. As derived in Section 4.5.2, the Green's function includes two parts, singular term and reflection term. The matrix elements are evaluated through the integrals for these two parts separately.

4.6.1 Singular Matrix Elements

The matrix element due to a singular source in unbounded domain is calculated first. Special attention has to be paid on the diagonal element computation in which the integral over the singular point is evaluated because of the hyper singularity. Integrals over the singular term can be written as

$$M_{jl}^{(0)} = \int_{\Omega_l} \left(k^2 + \frac{\partial^2}{\partial n'^2} \right) G_0(\mathbf{r}_j|\mathbf{r}') \, d\mathbf{r}', \quad (4.69)$$

where n' represents the coordinate normal to the crack surface. Because $G_0(\mathbf{r}|\mathbf{r}')$ is the solution of the scalar Helmholtz equation, we can transform the singular integrand by using

$$\left(k^2 + \frac{\partial^2}{\partial n'^2} \right) G_0(\mathbf{r}_j|\mathbf{r}') = -\nabla_\tau'^2 G_0(\mathbf{r}_j|\mathbf{r}'). \quad (4.70)$$

Here the subscript τ denotes the components of the differential operator tangential to a surface of constant n . For a transverse crack, for example, this surface is a plane in which z is a constant whereas for an axial crack, the crack face is in a plane of constant ϕ . Using the identity $\nabla_\tau'^2 = \nabla_\tau' \cdot \nabla_\tau'$ to transform the Laplacian operator and applying Gauss divergence theorem, we can express the singular element as a path integral

$$M_{jl}^{(0)} = - \oint_{C_l} \hat{\tau} \cdot \nabla_\tau' G_0(\mathbf{r}_j|\mathbf{r}') \, d\ell', \quad (4.71)$$

where C_l is the path bordering the surface of the cell l . The details about the numerical evaluation of the integral over the singular term are discussed in Section 4.6.1. Next, we present the integral over the reflection part.

4.6.2 Reflection Matrix Elements

The reflection matrix element is calculated from the integral of the Green's kernel in Section 4.5.2 over the cells. The reflection matrix elements for the transverse and longitudinal cracks are presented as follows.

4.6.2.1 Reflection matrix elements for transverse cracks

A single element of a transverse crack in cylindrical polar coordinates is shown in Fig. 4.6 (a). The cell is expanded from ρ_1 to ρ_2 in the radial direction, from $\phi_c + \Delta\phi/2$ to $\phi_c - \Delta\phi/2$

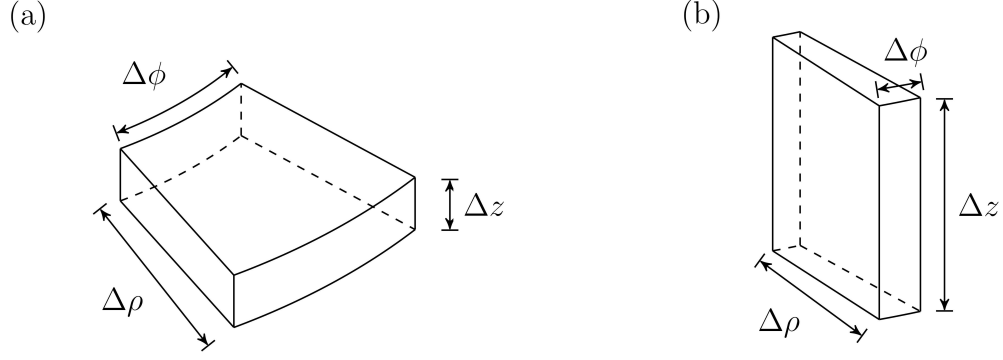


Figure 4.6: Volume elements for modeling (a) a transverse open crack and (b) a longitudinal one.

in the azimuthal direction, and from $z_c - \Delta z/2$ to $z_c + \Delta z/2$ in the axial direction with small Δz . For a transverse crack, Fourier transform of the reflection part in the Green's function is given by (4.60) and (4.40)

$$\tilde{G}_{zz}^{(\Gamma)}(\rho, \rho', m, \kappa_i) = -\frac{\gamma_i^2}{k^2} \Gamma_{bb}(m, \gamma_i) K_m(\gamma_i \rho) K_m(\gamma_i \rho'). \quad (4.72)$$

From (4.67) and (4.35), the integral over a transverse element can be written as

$$\begin{aligned} M^{(\Gamma)} &= k^2 \int_{z_c - \Delta z/2}^{z_c + \Delta z/2} \int_{\phi_c - \Delta \phi/2}^{\phi_c + \Delta \phi/2} \int_{\rho_1}^{\rho_2} \rho' G_{zz}^{(\Gamma)} d\rho' d\phi' dz' \\ &= -\frac{4}{\pi h} \sum_{m=0}^{\infty} \frac{\epsilon_m}{m} \cos[m(\phi - \phi_c)] \sin \frac{m \Delta \phi}{2} \\ &\quad \times \sum_{i=1}^{\infty} \frac{1}{\kappa_i} \Gamma_{bb}(m, \gamma_i) g_{1,m}(\gamma_i \rho_1, \gamma_i \rho_2) K_m(\gamma_i \rho) \cos(\kappa_i z) \cos(\kappa_i z_c) \sin \frac{\kappa_i \Delta z}{2}, \end{aligned} \quad (4.73)$$

where $\epsilon_0 = 1$ and $\epsilon_m = 2$ for $m = 1, 2, \dots$ and the function $g_{\mu,m}$ is defined as

$$g_{\mu,m} = \int_0^z \rho^\mu K_m(\rho) d\rho. \quad (4.74)$$

For conciseness we write $g_{\mu,m}(\rho_1, \rho_2) = g_{\mu,m}(\rho_2) - g_{\mu,m}(\rho_1)$. The detailed evaluation is given in Section 4.7.

In the case of an ideal transverse crack, a similar expression can be derived except the difference on the integral over variable z .

4.6.2.2 Reflection matrix elements for longitudinal cracks

For a longitudinal crack, Fourier transform of the reflection part in the Green's function is given by (4.40) and (4.62) as

$$\begin{aligned} & \tilde{G}_{\phi\phi}^{(\Gamma)}(\rho, \rho', m, \kappa_i) \\ &= -\Gamma_{aa}(m, \gamma_i)K'_m(\gamma_i\rho)K'_m(\gamma_i\rho') - \frac{1}{k^2} \frac{m^2\kappa_i^2}{\rho\rho'\gamma_i^2} \Gamma_{bb}(m, \gamma_i)K_m(\gamma_i\rho)K_m(\gamma_i\rho') \\ & \quad - \frac{im\kappa_i}{\gamma_i} \Gamma_{ba}(m, \gamma_i) \left[\frac{1}{\rho} K_m(\gamma_i\rho)K'_m(\gamma_i\rho') + \frac{1}{\rho'} K'_m(\gamma_i\rho)K_m(\gamma_i\rho') \right]. \end{aligned} \quad (4.75)$$

For an open crack, the integration over the crack opening with small $\rho\Delta\phi$ can be written as

$$\begin{aligned} M^{(\Gamma)} &= k^2 \int_{z_c-\Delta z/2}^{z_c+\Delta z/2} \int_{\phi_c-\Delta\phi/2}^{\phi_c+\Delta\phi/2} \int_{\rho_1}^{\rho_2} \rho' G_{\phi\phi}^{(\Gamma)} d\rho' d\phi' dz' \\ &= -\frac{4}{\pi h} \sum_{m=0}^{\infty} \frac{\epsilon_m}{m} \cos[m(\phi - \phi_c)] \sin \frac{m\Delta\phi}{2} \\ & \quad \times \sum_{i=1}^{\infty} \sin(\kappa_i z) \sin(\kappa_i z_c) \sin \frac{\kappa_i \Delta z}{2} \int_{\rho_1}^{\rho_2} \rho' \tilde{G}_{\phi\phi}^{(\Gamma)} d\rho', \end{aligned} \quad (4.76)$$

where the integral over ρ has the form

$$\begin{aligned} & \int_{\rho_1}^{\rho_2} \rho' \tilde{G}_{\phi\phi}^{(\Gamma)} d\rho' \\ &= \frac{k^2}{\gamma_i^2} \Gamma_{aa}(m, \gamma_i) K'_m(\gamma_i\rho) h_m(\gamma_i\rho_1, \gamma_i\rho_2) + \frac{m^2\kappa_i^2}{\rho\gamma_i^3} \Gamma_{bb}(m, \gamma_i) K_m(\gamma_i\rho) g_{0,m}(\gamma_i\rho_1, \gamma_i\rho_2) \\ & \quad + \frac{im\kappa_i k^2}{\gamma_i^2} \Gamma_{ba}(m, \gamma_i) \left[\frac{1}{\rho\gamma_i} K_m(\gamma_i\rho) h_m(\gamma_i\rho_1, \gamma_i\rho_2) + K'_m(\gamma_i\rho) g_{0,m}(\gamma_i\rho_1, \gamma_i\rho_1) \right]. \end{aligned} \quad (4.77)$$

For an ideal crack, the reflection matrix element is slightly different because the integration over radial direction becomes $d\rho'$ instead of $\rho' d\rho'$.

This completes the matrix element calculation in the volume element method for transverse and longitudinal cracks near a borehole.

4.7 Numerical Implementation

In this section, we discuss the program implementation based on the formulation derived before. Even though the idea and formulation are pretty clear, there are still some other issues that have to be considered in the program implementation and numerical calculations. From

(4.73) and (4.76), each matrix element involves a double summation over infinite number of orders and modes. In numerical calculations, the summation has to be truncated to a certain number. In order to get correct numerical results, we have to make sure this double summation is convergent and the truncation of the series will not effect the accuracy of the final results in the calculation. It turns out that careless implementation could affect the execution of the program a lot. Either we can not get convergent results, or it might take long time to solve the whole problem. We limit our discussion based on the implementation from MATLAB¹. The ideas could be extended to other computer languages. Three important factors on the code implementation are discussed as follows.

4.7.1 Integral of Unbounded Domain Kernel

For the singular matrix element calculation in (4.69), the double integral in (4.71) could be realized using 'quad2d' function. For the off-diagonal elements, a single-point evaluation of the integral is accurate enough if the observation point \mathbf{r}_j is a few skin depth away from the source cell Ω_j . For the observation points near a given source cell, the log-like Gaussian quadrature [107] and the 'quad2d' function are used together to ensure the accuracy and the speed of the triple integral over a source cell.

4.7.2 Calculation under Limited Bit Length

There is a double summation involved in the reflection matrix element calculation. We have to make sure those matrix elements completely convergent so that the final results are correct. In other words, we need to keep enough orders and modes to get an accurate matrix element in (4.73) and (4.76), especially for the diagonal elements. The theory requires a large amount of calculation over modified Bessel functions and their integrals, which are included in the reflection coefficient calculation and the matrix element evaluation.

For numerical calculation, all the algorithms have to be executed within the limited computation range. In MATLAB, the data is stored in a double precision floating-point format. Typically the numerical range is from 10^{-308} to 10^{308} . Take the computation of the modified

¹MALTAB is a registered trademark of The MathWorks, Inc., 24 Prime Park Way, Natick, MA 01760, USA.

Bessel function $I_m(\gamma_i b)$ as an example. For given order m and large radius b , the function $I_m(\gamma_i b)$ will increase exponentially when we increase the magnitude of γ_i and it is easy to reach the limit 10^{308} . Similarly, for a large parameter γ_i , only a quite small range of b can be covered if the calculation is implemented under the limited bit length. It implies the convergence over the higher modes γ_i might not be accessible and the final results might be completely wrong. This is true for a borehole with a large radius.

In order to avoid this issue, we need a better numerical implementation in which the modified Bessel functions can be obtained for a large argument and a large order simultaneously. The fact is that the final result of the matrix element is always a reasonable number, neither too small nor too big. By observing (4.73) and (4.76), we propose a new implementation in which two functions with different trends are combined together so that the calculation will always be within a reasonable numerical range. Instead of calculating those Bessel functions separately, the combined functions are always treated together. This is not only efficient but also important because an appropriate arrangement brings extra benefits in the calculation. Take the reflection kernel of a transverse crack (4.73) as an example. The following two functions are implemented in the code

$$I_m(\gamma_i b)K_m(\gamma_i \rho) \quad \text{and} \quad g_{1,m}(\gamma_i \rho_1, \gamma_i \rho_2)/K_m(\gamma_i b), \quad (4.78)$$

where the ratio, $I_m(\gamma_i b)/K_m(\gamma_i b)$ has been separated from the reflection coefficient $\Gamma_{bb}(m, \gamma_i)$ so that the rest part of $\Gamma_{bb}(m, \gamma_i)$ also has a small variation. It should be stressed that we evaluate the combination of the two functions together, not the functions individually at any time. Now the problem becomes how to evaluate those combined functions for a large range of orders and modes. The difficulty is that there is no such internal functions to calculate the desired combination of those modified Bessel functions, let alone integral of the modified Bessel functions. The recurrence relations [108]

$$I_{m+1}(z) = -\frac{2m}{z}I_m(z) + I_{m-1}(z), \quad (4.79)$$

$$K_{m+1}(z) = \frac{2m}{z}K_m(z) + K_{m-1}(z), \quad (4.80)$$

provide us a good clue for the high-order calculation, but it can not be directly used here. The different arguments, b and ρ in (4.78), make the problem even serious. In order to solve those

problems, a new recurrence algorithm is introduced.

4.7.3 Recurrence Algorithm

The recurrence algorithm should to be able to deal with extreme cases, such as the problem of a borehole with a large radius in which the series convergence quite slowly. In order to do this efficiently, there are two fundamental functions have to be calculated first, which are

$$\frac{I_m(z)}{I_{m-1}(z)} \quad \text{and} \quad \frac{K_m(z)}{K_{m+1}(z)}. \quad (4.81)$$

Recurrence relations (4.83) and (4.80) can be rewritten as

$$\frac{I_{m+1}(z)}{I_m(z)} = -\frac{2m}{z} + \frac{I_{m-1}(z)}{I_m(z)}, \quad (4.82)$$

$$\frac{K_{m+1}(z)}{K_m(z)} = \frac{2m}{z} + \frac{K_{m-1}(z)}{K_m(z)}. \quad (4.83)$$

Once the ratio of the modified Bessel functions of the first two orders ($m = 0$ and 1) are given, the ratio of the high orders can be efficiently calculated from these recurrence relations. We don't need to calculate the modified Bessel functions of high orders separately. However, the three-term linear recurrence relation (4.82) is unstable for the upward recurrence. In other words, the roundoff error would increase as the higher-order terms are calculated and finally swallow the whole significant digits. Therefore, the upward calculation is no practical use for the calculation of the ratio $I_{m+1}(z)/I_m(z)$. Pincherle's theorem can be used to analysis the stability of recurrence relation [109]. However, the recurrence relation (4.82) is stable for the downward recurrence. Thus, we can start any seed values from the highest-order term and generate low-order terms based on this recurrence. If there is a way to normalize all the sequences to the correct values, then this algorithm becomes a practical method to evaluate the ratio. This method is called Miller's algorithm. The following normalization formula for $I_m(z)$ is adopted in our code [108]

$$1 = I_0(z) - 2I_2(z) + 2I_4(z) - 2I_6(z) + \dots . \quad (4.84)$$

Rearranging the terms, we have that

$$[1 - I_0(z)]/I_1(z) = [-2I_2(z) + 2I_4(z) - 2I_6(z) + \dots]/I_1(z), \quad (4.85)$$

where the right-hand side is computed with downward recurrence and finally the whole sequence is normalized by the exact value $[1 - I_0(z)]/I_1(z)$. The procedure is similar to the calculation of a single Bessel function [109]. With the Miller's algorithm, the high-order terms could be generated pretty fast without affecting the accuracy. By using the identities

$$\frac{I'_m(z)}{I_m(z)} = \frac{1}{2} \frac{I_{m-1}(z) + I_{m+1}(z)}{I_m(z)} = \frac{1}{2} \left(1 \Big/ \frac{I_m(z)}{I_{m-1}(z)} + \frac{I_{m+1}(z)}{I_m(z)} \right), \quad (4.86)$$

$$\frac{K'_m(z)}{K_m(z)} = -\frac{1}{2} \frac{K_{m-1}(z) + K_{m+1}(z)}{K_m(z)} = -\frac{1}{2} \left(\frac{K_{m-1}(z)}{K_m(z)} + 1 \Big/ \frac{K_m(z)}{K_{m+1}(z)} \right), \quad (4.87)$$

the reflection coefficients can be evaluated directly based on above ratio functions.

Once the ratio of the modified Bessel functions for the same argument $\gamma_i b$ is formed, the recurrence relations of combined functions can be easily derived from (4.82) and (4.83). Two typical derivations are given here as examples. Let's consider $I_m(z)K_m(w)$ first. With recurrence relation (4.83), we can write that

$$\begin{aligned} & I_{m+1}(z)K_{m+1}(w) \\ &= I_{m+1}(z) \left[\frac{2m}{w} K_m(w) + K_{m-1}(w) \right] \\ &= \frac{2m}{w} I_m(z)K_m(w) \frac{I_{m+1}(z)}{I_m(z)} + I_{m-1}(z)K_{m-1}(w) \frac{K_{m+1}(z)}{K_{m-1}(z)}, \end{aligned} \quad (4.88)$$

where

$$\frac{K_{m+1}(z)}{K_{m-1}(z)} = 1 \Big/ \left[\frac{K_{m-1}(z)}{K_m(z)} \frac{K_m(z)}{K_{m+1}(z)} \right]. \quad (4.89)$$

The function $I_m(z)K_m(w)$ for the whole orders can be generated with this recurrence as long as the function $I_0(z)K_0(w)$ and $I_1(z)K_1(w)$ are given.

A more difficult case is that combined functions involving the integral of the modified Bessel function $g_{\mu,m}$. The integral itself has the recurrence relation

$$g_{\mu,m+1}(w) = -\frac{2mw^\mu}{m-\mu} K_m(w) + \frac{\mu+m}{\mu-m} g_{\mu,m-1}(w). \quad (4.90)$$

So the recurrence relation for the function $g_{\mu,m}(z)/K_m(w)$ can be written as

$$\frac{g_{\mu,m+1}(w)}{K_{m+1}(z)} = -\frac{2mw^\mu}{m-\mu} \frac{K_m(w)}{K_m(z)} \frac{K_m(z)}{K_{m+1}(z)} - \frac{\mu+m}{\mu-m} \frac{g_{\mu,m-1}(w)}{K_{m-1}(z)} \frac{K_{m-1}(z)}{K_{m+1}(z)}, \quad (4.91)$$

where $K_m(w)/K_m(z)$ requires one more recurrence relation which can be easily derived in the same way.

Now the only trouble left is to evaluate all the functions for the zeroth and first order. The internal function is suitable for those functions with a small argument. For argument $|z| \gg 1$, asymptotic forms of the modified Bessel functions are

$$I_m(z) \approx \frac{e^z}{\sqrt{2\pi z}} \left\{ 1 - \frac{4m^2 - 1}{8z} + \frac{(4m^2 - 1)(4m^2 - 9)}{2!(8z)^2} - \dots \right\}, \quad (4.92)$$

$$K_m(z) \approx \sqrt{\frac{\pi}{2z}} e^{-z} \left\{ 1 + \frac{4m^2 - 1}{8z} + \frac{(4m^2 - 1)(4m^2 - 9)}{2!(8z)^2} + \dots \right\}. \quad (4.93)$$

Applying these two asymptotic approximations to the combined functions with large arguments, a good estimation can be made even with a few terms. For example, the approximation

$$I_m(z)K_m(w) \approx \frac{e^{z-w}}{2\sqrt{zw}} \left(1 - \frac{4m^2 - 1}{8z} \right) \left(1 + \frac{4m^2 - 1}{8w} \right), \quad (4.94)$$

gives the first order approximation for $m = 0, 1$. Now, the reflection matrix element could be evaluated with high speed and high accuracy using this approach. Another advantage of this algorithm is that it is suitable to use better data structure in the program, which takes less memory while we evaluate the matrix element.

4.8 Series Convergence Issues

In our approach, the calculation of the reflection matrix element takes the most time. Series convergence is an important issue which determines the total computational cost, including CPU time and memory requirement. The singular term has a slow convergence and hypersingular term has a super slow convergence. For the reflection matrix element, a typical distribution of the terms in the double summation is shown in Fig. 4.7. The color shows the order of magnitude for each term. The slow convergence indicates that large orders and modes of the terms are required. In general, it is possible to solve the convergence issue using some extrapolation methods.

Mathematically, the summation of the first n -term series forms a sequence and it can be accelerated using a sequence transformation. Most of the transformation methods are constructed by an extrapolation with linear or non-linear mapping. The original slowly convergent sequence is transformed to a new one which is assumed to have a faster convergence. General methods can be applied to any series, such as Euler transformation, Shanks' transformation,

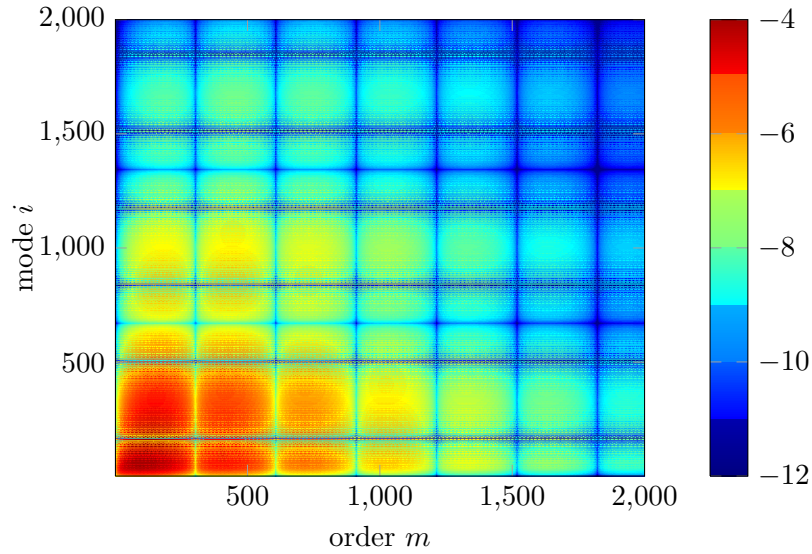


Figure 4.7: The order of magnitude for the terms in the double summation involved in the reflection matrix element calculation.

Wynn's ϵ -algorithm, Chebyshev-Toeplitz Algorithm, and Θ -algorithm. The details concerning the behavior of those transformation can be found in [110]. On the other hand, specific methods are available for certain types of series and they usually work better than the general methods. Examples of such methods are method of average, Poisson transformation, Ewald's transformation, method of exponentials, and Kummer's transformation. Some of them have been applied to many other electromagnetic problems, like scattering from dielectrics. The basic principle and comparison of these specific methods are given by Kinayman and Aksun [111]. Other methods, such as mid-point summation [112] and summation-by-parts [113], also have a good performance on some electromagnetic problems. In our case, the technique has to be able to deal with a double summation, or even a triple one later, for a large range of argument where the coefficients might not have a closed-form. Unfortunately, most of above methods only have a little action to our problems and some of them even do not work.

For the physical model, the singular source point and its image can be subtracted from the matrix element and the remainder convergence pretty fast. This approach works well for the coil above a half-space conductor. Nonetheless, it is not easy to find the image term for

a point source around cylindrical structure. Asymptotic approximation might be used as an approximation of the image term, but there is no well-developed approach to address the similar problem as we know.

The generalized pencil of function (GPOF) method is a possible way to deal with this issue [114]. Combining with the evaluation of sommerfeld type integrals and the concept of discrete complex images, the GPOF method has been used to accelerate the computation of the eddy-current inspection of narrow cracks in a half-space conductor [115, 116].

4.9 Results

In order to validate the physical modeling and numerical implementation, the predictions of the coil impedance change are compared to experimental measurements. As a special case, the coil impedance change due to a rectangular slot in a half-space conductor is examined first by making the borehole radius large enough so that the borehole can be approximate as a half space. Experiments of the transverse and longitudinal surface cracks around boreholes are examined later.

4.9.1 Cracks in Half-Space Conductor

The world federation of NDE centers provides several benchmark problems including the impedance change of a bobbin coil due to a slot inside a half-space conductor. As mentioned before, the program and the theory are designed to relate to each other. Thus, this well-known benchmark problem was used to verify our borehole solution first before any further experimental work. This saved us lots of work. The bobbin coil above an aluminum alloy plate with a rectangular slot is considered according to the team workshop problem 15 by Burke [117]. The experimental arrangement and the problem are presented in Fig. 4.8 [117]. The coil is scanned along the length of the slot. Both the frequency and the coil lift-off are fixed and coil impedance change ΔZ_c was measured as a function of coil center position. The parameters for this test experiment are listed in Table 4.3. Here, this problem is approximated as a rotary coil inside a borehole with a pretty large radius. As shown in Fig. 4.9, the predicted coil impedance change due to the same size crack is calculated and agrees with experimental measurements.

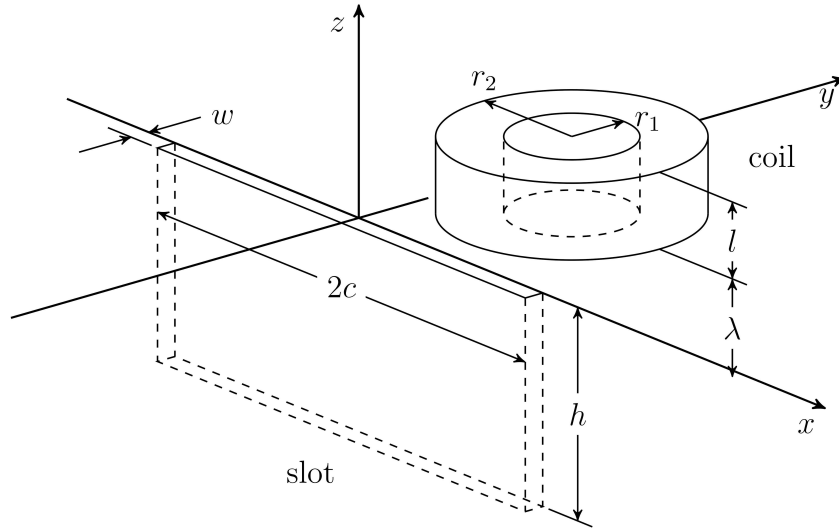
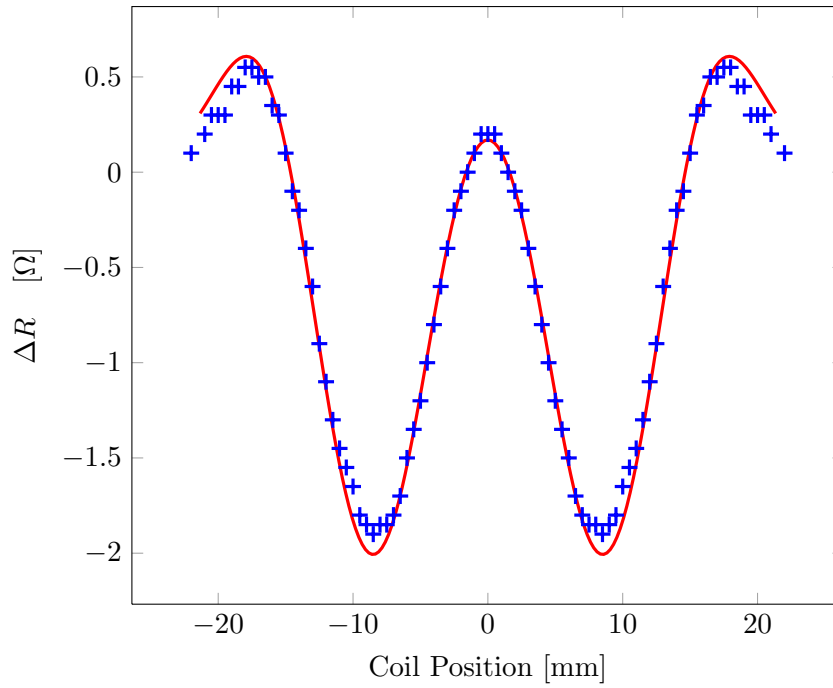


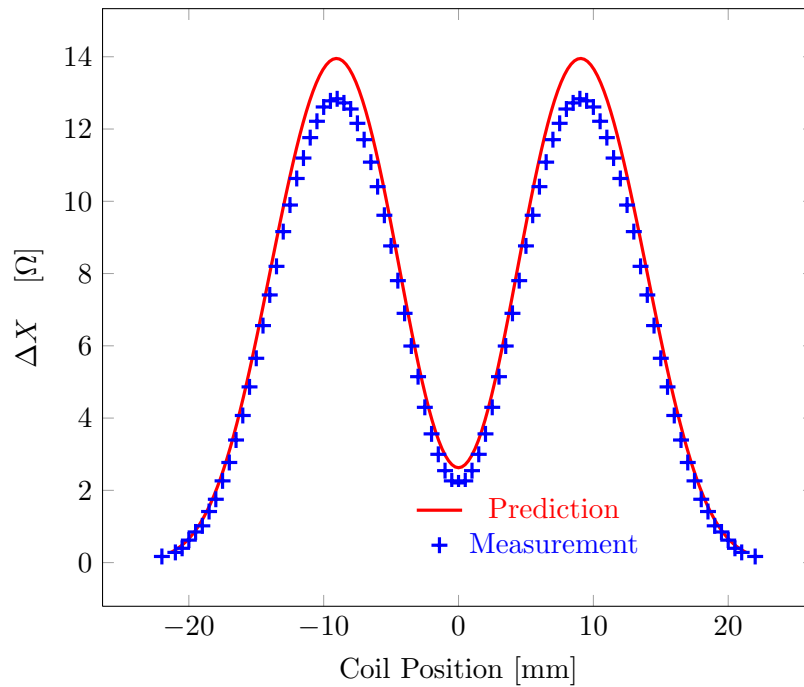
Figure 4.8: Bobbin coil above conductive half space with a slot. The coil and slot parameters are given in Table 4.3.

Table 4.3: Parameters of test experiment for a bobbin coil above a half-space conductor. The configuration is shown in Fig. 4.8.

Coil	
Inner radius (r_1)	6.15 ± 0.05 mm
Outer radius (r_2)	12.4 ± 0.05 mm
Length (ℓ)	6.15 ± 0.1 mm
Number of turns (N)	3790
Lift-off (λ)	0.88 mm
Test Specimen	
Conductivity (σ)	$3.06 \pm 0.02 \times 10^7$ S/m
Thickness	12.22 ± 0.02 mm
Defect	
Length ($2c$)	12.60 ± 0.02 mm
Depth (h)	5.00 ± 0.05 mm
Width (w)	0.28 ± 0.01 mm
Other Parameters	
Frequency (f)	900 Hz
Skin depth at 900 Hz (δ)	3.03 mm
Isolated coil inductance (L)	221.8 ± 0.04 mH



(a)



(b)

Figure 4.9: Change in (a) coil resistance, ΔR and (b) coil reactance, ΔX due to the slot as a function of coil-center position for the experimental configuration described in Table 4.3. The numerical result (*solid line*) and experimental data (+) are shown for comparison.

4.9.2 Dipole Density Distribution over Crack Surface

The electric current dipole distribution is plotted to verify the result. Figure 4.10 shows the electric current dipole distribution over the crack surface calculated from (4.66) for an open longitudinal crack around borehole. The details of the parameters are given later. According to the definition in (4.5), the current dipole should be zero along the boundary of the conductor. This is confirmed in the result.

Experiments have also been carried out to test the predictions of coil impedance due to cracks around a borehole using two aluminum alloy specimens by my colleague, Yuan Ji at Center of NDE, Iowa State University. The parameters for the experiment are listed in Table 4.1. There is a semi-elliptical transverse notch cut in a test-piece and a similar longitudinal notch in another test-piece, Fig. 4.11.

4.9.3 Transverse and Longitudinal Cracks around a Borehole

Although most coil dimensions were measured using a microscope to an accuracy of $20\ \mu\text{m}$,

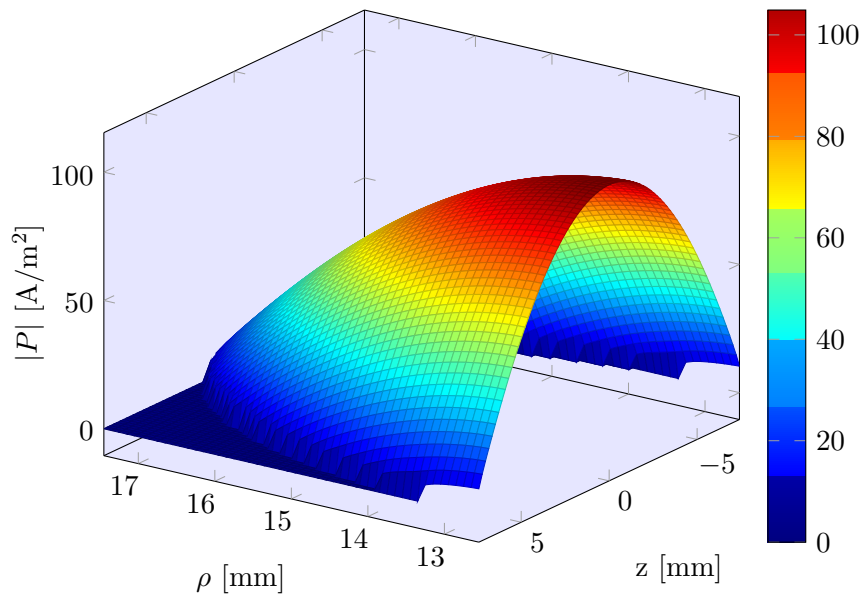


Figure 4.10: The distribution of electric current dipole density over crack surface for a longitudinal crack around the borehole.

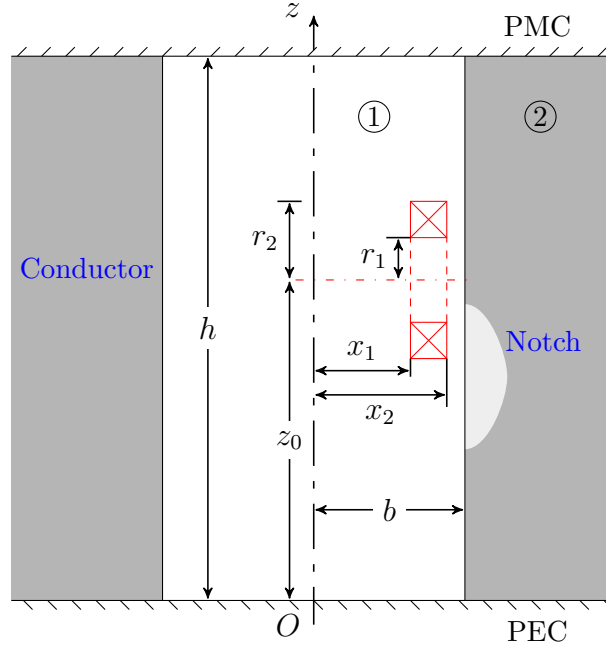


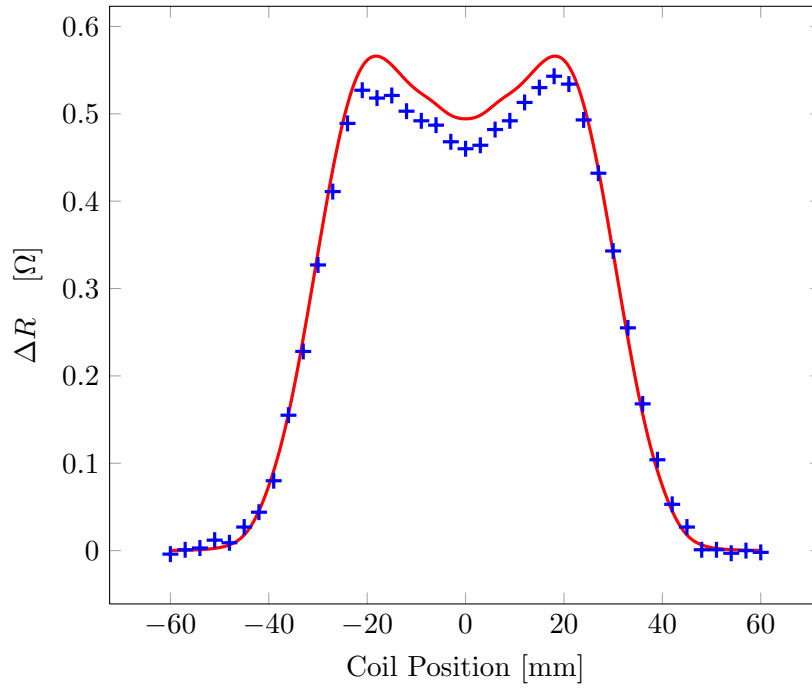
Figure 4.11: A rotary coil inside borehole with a longitudinal crack. The coil and crack parameters are given in Table 4.1.

the lift off of the coil was difficult to measure directly. It was determined by parameter fitting to multi-frequency coil impedance measurements inside a borehole. Coil impedance measurements and their variation with position are made with Agilent 4294A impedance analyzer and a four axis (x , y , z , and ϕ) computer controlled precision scanner.

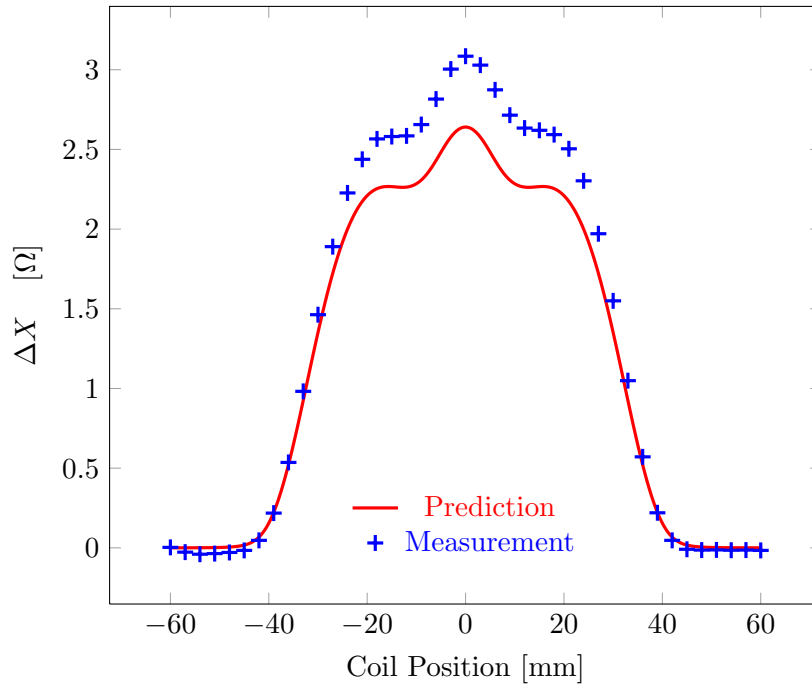
A comparison of impedance predictions with measurement is shown in Fig. 4.12 for the transverse crack and Fig. 4.13 for the longitudinal crack at 40 kHz. The error was due to the uncertainties of the dimension measurements, such as lift-off and the notch opening. Tilt of the coil is another factor which might affect the measurement.

4.10 Summary

A crack model is developed for the interaction of an induction coil with a crack near a borehole in a conductor. Equivalent current dipole is used to represent a thin crack as a secondary source in the conductor. A volume integral equation is set up to calculate this equivalent source through a dyadic Green's kernel. The kernel is derived based on a point

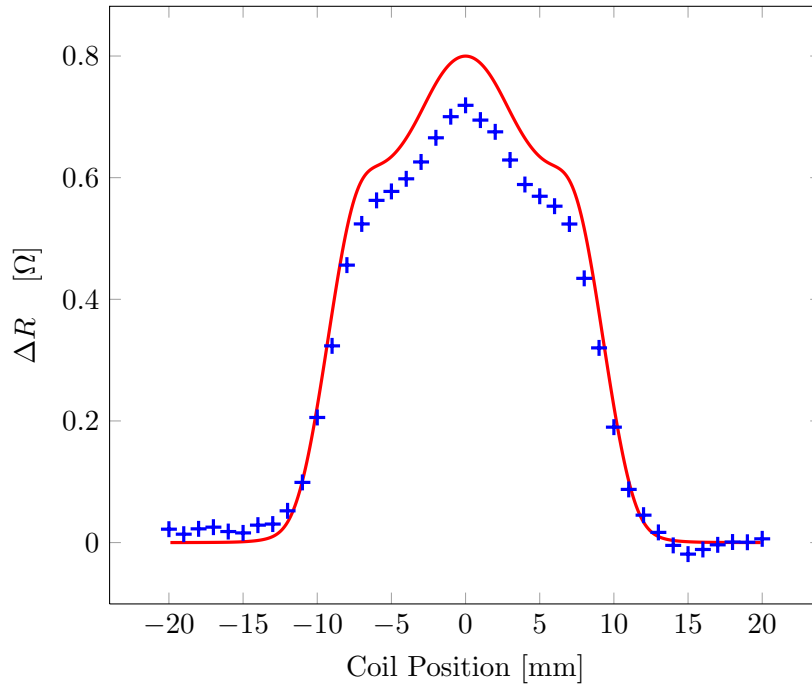


(a)

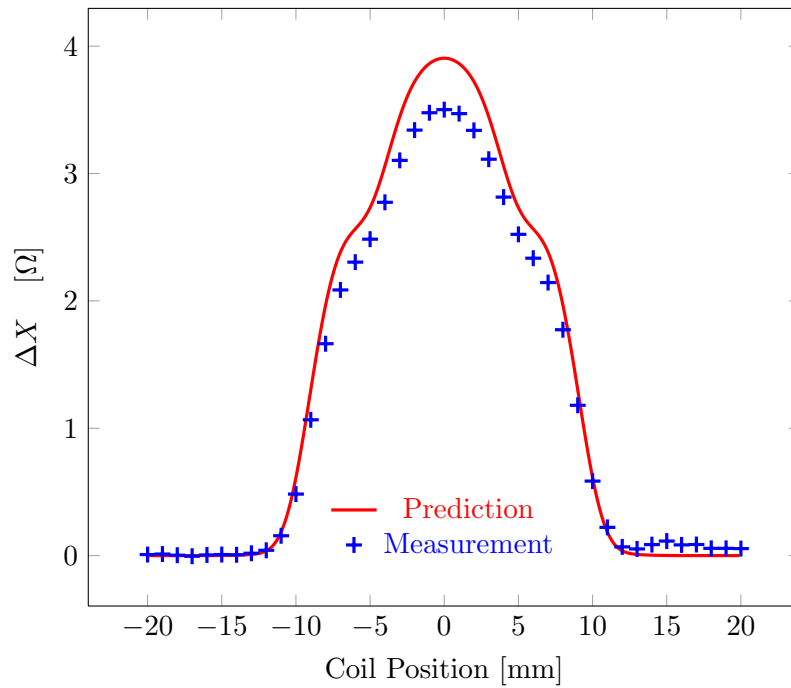


(b)

Figure 4.12: Change in (a) coil resistance, ΔR and (b) coil reactance, ΔX due to the transverse crack as a function of coil-center position for the experimental configuration described in Fig. 4.2 and Table 4.1. The numerical result (*solid line*) and experimental measurement (+) are shown for comparison.



(a)



(b)

Figure 4.13: Change in (a) coil resistance, ΔR and (b) coil reactance, ΔX due to the longitudinal crack as a function of coil-center position for the experimental configuration described in Fig. 4.2 and Table 4.1. The numerical result (*solid line*) and experimental measurement (+) are shown for comparison.

source in the borehole. The fields are decomposed as TE and TM modes. These two modes are coupled in this problem due to the boundary conditions at the cylindrical interface. The Green's kernel is expressed as the sum of a singular unbounded domain term, plus a regular term due to the material boundaries. The coil impedance is determined from the dipole source and incident field.

Numerical issues are discussed to make sure the program implementation is correct, fast, and accurate. Algorithms are proposed to deal with the calculation of Bessel functions in the formulation. Series convergence is also considered.

The crack model is validated first by calculating the coil impedance change due to a crack in a half-space conductor. The approximation is made by assigning a large radius to the borehole model. Good agreement is obtained. The code shows good performance in this harsh case. Predictions of a transverse crack and a longitudinal crack in the borehole are also validated by comparing with experimental measurements.

CHAPTER 5. COIL IMPEDANCE CHANGE DUE TO CRACKS IN A TUBE

Cylindrical layered structure, such as optical fibers in the high-speed network and pipelines in the petroleum transportation, plays an important role in the engineering and manufacturing industry. In this chapter, the theoretical model for coil signal due to cracks in a conductive tube is presented.

The study of electromagnetic waves in cylindrical layered structure can be extended from the cases with a single interface like the borehole model discussed in the last chapter. With reflection coefficients obtained for single interface, the transmission and reflection coefficients due to multiple circularly cylindrical boundaries are considered in the tube model. TE and TM modes are coupled at cylindrical borehole surface due to continuity boundary conditions. The reflection and transmission coefficients are expressed as a two-by-two matrix form to describe this coupling and self-interaction. For the tube problem, this concept is further extended by introducing the total reflection and transmission coefficients due to multiple cylindrical interfaces obtained with certain matrices operations. The fundamental ideas, which have been presented by Chew [118], are used in our derivation. In Chew's work, the scattering problems are the main concern and the axial components of the electric and magnetic fields, E_z and H_z are used to characterize vector fields and the coupling, instead of scalar TE and TM potentials we used before. TE and TM modes have different meaning in that book. In this chapter, we will emphasize the issues related to EC problems and its difference from the typical scattering problems.

Like discussed in Chapter 4, the same truncation scheme is used here for consistency, which means the domain of the infinitely long tube is truncated in the axial direction with two different truncation boundary conditions and the solution is expressed in terms of series. Again, two by

two matrix is used to represent the interaction between TE and TM modes here.

5.1 Introduction

In this chapter, a through-wall crack in an infinitely long tube is considered. The impedance change of an arbitrary coil due to the crack is derived, Fig. 5.1. We assume that the conductor has the linear material properties with conductivity σ_0 and the permeability of free space, μ_0 .

The crack model stated in Chapter 4 is still valid for the tube structure. However, the reflection coefficients have to be modified by considering multiple reflections in a tube due to multiple cylindrical interfaces. Hence, the matrix element in volume element method is changed. We start by formulating the total transmission and reflection coefficients first, then the matrix elements in crack problems are re-derived. Finally, numerical results are compared with experimental measurements to validate the tube model.

5.2 Transmission and Reflection due to Single Cylindrical Interface

For a source outside a borehole structure, the transmission and reflection coefficients are derived in Section 4.4 to get the Green's function. Transmission and reflection coefficients for

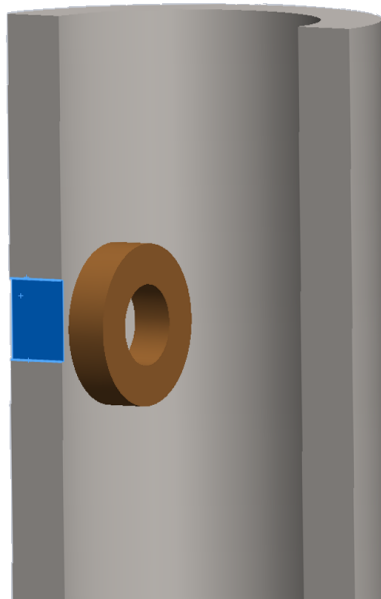


Figure 5.1: A rotary coil insider a tube in the presence of a through-wall longitudinal notch.

a source inside a borehole are formulated in Appendix D to obtain the incident field for the borehole configuration. To extend these cases to more general purpose, the medium inside borehole with any material is re-formulated first. The fields are expressed in terms of scalar TE and TM potentials and these two potential satisfy Helmholtz equation

$$(\nabla^2 + k^2)W = 0. \quad (5.1)$$

The Fourier series expansion are used in the azimuthal and axial directions

$$W_a = \sum_{m=-\infty}^{\infty} e^{im\phi} \sum_{s=1}^{\infty} \tilde{W}_{am} \sin(\kappa_s z), \quad (5.2)$$

and

$$W_b = \sum_{m=-\infty}^{\infty} e^{im\phi} \sum_{s=1}^{\infty} \tilde{W}_{bm} \cos(\kappa_s z), \quad (5.3)$$

where eigenvalues are given by

$$\kappa_s = (2s - 1)\pi/2h \quad s = 1, 2, 3, \dots \quad (5.4)$$

In (5.2) and (5.3), the Fourier series \tilde{W}_m satisfy the Bessel equation

$$\frac{1}{\rho} \frac{\partial}{\partial \rho} \left(\rho \frac{\partial \tilde{W}_m}{\partial \rho} \right) - \left(\gamma_s^2 + \frac{m^2}{\rho^2} \right) \tilde{W}_m = 0 \quad (5.5)$$

with $\gamma_s^2 = \kappa_s^2 - k^2$. For the following derivation, we will use the Fourier transform of the scalar potentials, \tilde{W}_{am} and \tilde{W}_{bm} to represent the fields and the mode index s will be dropped to avoid a conflict with the region index i .

The region inside the borehole is designated as region 1, and the region outside the borehole is named as region 2. Assume the conductivity and permeability in region i are σ_i and μ_i , with $i = 1, 2$. The interface is located at $\rho = b$ between region 1 and 2. We derive the transmission and reflection due to this cylindrical interface based on the location of the source. In other words, an outgoing wave incidence and an incoming wave incidence are considered separately.

5.2.1 Transmission and Reflection for an Outgoing Wave

For a source inside region 1, Fig. 5.2, an outgoing wave is incident on a circularly cylindrical interface, the Fourier transform of TE and TM fields between the source and the cylindrical

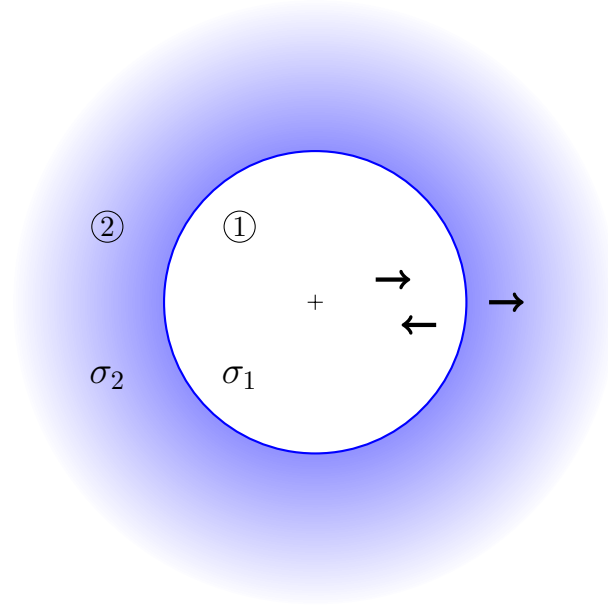


Figure 5.2: Transmission and reflection of an outgoing wave. The arrows represent components of the field that migrate from the source, migrate from the boundary back towards the source, and transmitted into the outside of borehole.

boundary $\rho = b$ can be expressed as

$$\begin{bmatrix} \tilde{W}_{am}^{(1)} \\ \tilde{W}_{bm}^{(1)} \end{bmatrix} = \begin{bmatrix} K_m(\gamma_1\rho) \mathbf{I} + \frac{I_m(\gamma_1\rho)}{I_m(\gamma_1b)} \mathbf{\Gamma}_{21} \\ K_m(\gamma_1b) \end{bmatrix} \cdot \mathbf{a}_{1m}, \quad (5.6)$$

and Fourier transform of the potentials in region 2 has the form

$$\begin{bmatrix} \tilde{W}_{am}^{(2)} \\ \tilde{W}_{bm}^{(2)} \end{bmatrix} = \frac{K_m(\gamma_2\rho)}{K_m(\gamma_2b)} \mathbf{T}_{21} \cdot \mathbf{a}_{1m}, \quad (5.7)$$

where \mathbf{a}_1 is the coefficient which is determined by the source inside region 1 and \mathbf{I} is two-by-two identity matrix. Here, $\gamma_i^2 = \kappa^2 - k_i^2$ with $i = 1, 2$ for two regions and k_i is zero for a nonconductive region. The two-by-two matrix $\mathbf{\Gamma}_{21}$ represents the reflection matrix due to the outgoing source in region 1. Similar to (4.46), its diagonal terms denote the self-interaction of the modes and the off-diagonal terms denote the coupling from TE mode to TM mode or the one from TM mode to TE mode.

In (5.6) and (5.7), we prefer to make explicit the additional geometric factors, $\frac{K_m(\gamma_1\rho)}{K_m(\gamma_1b)}$ and $\frac{I_m(\gamma_1\rho)}{I_m(\gamma_1b)}$, which it seems best to separate from the transmission and reflection matrices.

This becomes important from the program's point of view and it is helpful in the numerical calculation.

Given TE and TM potentials, the electric and magnetic fields can be derived from (4.31) and (4.32). The z -components of electric and magnetic fields can be expressed as

$$\begin{bmatrix} \tilde{H}_{zm}^{(i)} \\ \tilde{E}_{zm}^{(i)}/\omega \end{bmatrix} = \gamma_i^2 \mathbf{I}_{\mu i} \begin{bmatrix} \tilde{W}_a^{(i)} \\ \tilde{W}_b^{(i)} \end{bmatrix}, \quad (5.8)$$

and the ϕ -components have the form

$$\begin{bmatrix} \tilde{H}_{\phi m}^{(i)} \\ \tilde{E}_{\phi m}^{(i)}/\omega \end{bmatrix} = \mathbf{I}_{\mu i} \begin{bmatrix} im\kappa/b & -k_i^2 \partial_\rho \\ \partial_\rho & im\kappa/b \end{bmatrix} \begin{bmatrix} \tilde{W}_a^{(i)} \\ \tilde{W}_b^{(i)} \end{bmatrix}, \quad (5.9)$$

where the notation $\mathbf{I}_{\mu i}$ is defined as

$$\mathbf{I}_{\mu i} = \begin{bmatrix} 1 & 0 \\ 0 & \mu_i \end{bmatrix}.$$

At the borehole boundary $\rho = b$, the continuity conditions of tangential electric and magnetic fields yield

$$\gamma_1^2 \mathbf{I}_{\mu 1} [\mathbf{I} + \mathbf{\Gamma}_{21}] = \gamma_2^2 \mathbf{I}_{\mu 2} \mathbf{T}_{21}, \quad (5.10)$$

$$\mathbf{I}_{\mu 1} [\mathbf{M}_m(\gamma_1 b) + \mathbf{\Lambda}_m(\gamma_1 b) \mathbf{\Gamma}_{21}] = \mathbf{I}_{\mu 2} \mathbf{M}_m(\gamma_2 b) \mathbf{T}_{21} \quad (5.11)$$

where the functions $\mathbf{M}(\gamma_i \rho)$ and $\mathbf{\Lambda}(\gamma_i \rho)$ are defined as

$$\mathbf{B}_m(\gamma_i \rho) = \begin{bmatrix} im\kappa & -k_i^2 B_m(\gamma_i \rho) \\ B_m(\gamma_i \rho) & im\kappa \end{bmatrix}. \quad (5.12)$$

and functions $M(x)$ or $\Lambda(x)$ are defined in (4.51). From (5.10), we have

$$\gamma_2^2 \mathbf{T}_{21} = \gamma_1^2 \mathbf{I}_{\mu 2}^{-1} \mathbf{I}_{\mu 1} [\mathbf{I} + \mathbf{\Gamma}_{21}], \quad (5.13)$$

where $\mathbf{I}_{\mu 2}^{-1}$ represents the inverse of matrix $\mathbf{I}_{\mu 2}$. Multiplying (5.11) with γ_2^2 and substituting $\gamma_2^2 \mathbf{T}_{21}$ into the equation, the reflection coefficients can be solved from

$$\begin{aligned} & - \left[\gamma_1^2 \mathbf{I}_{\mu 2} \mathbf{M}_m(\gamma_2 b) \mathbf{I}_{\mu 2}^{-1} \mathbf{I}_{\mu 1} - \gamma_2^2 \mathbf{I}_{\mu 1} \mathbf{\Lambda}_m(\gamma_1 b) \right] \mathbf{\Gamma}_{21} \\ & = \gamma_1^2 \mathbf{I}_{\mu 2} \mathbf{M}_m(\gamma_2 b) \mathbf{I}_{\mu 2}^{-1} \mathbf{I}_{\mu 1} - \gamma_2^2 \mathbf{I}_{\mu 1} \mathbf{M}_m(\gamma_1 b) \end{aligned} \quad (5.14)$$

and the result is

$$\mathbf{\Gamma}_{21} = \gamma_2^2 \mathbf{Q}_{21}^{-1} \mathbf{I}_{\mu 1} [\mathbf{\Lambda}_m(\gamma_1 b) - \mathbf{M}_m(\gamma_1 b)] - \mathbf{I}, \quad (5.15)$$

where

$$\mathbf{Q}_{21} = - \left[\gamma_1^2 \mathbf{I}_{\mu 2} \mathbf{M}_m(\gamma_2 b) \mathbf{I}_{\mu 2}^{-1} \mathbf{I}_{\mu 1} - \gamma_2^2 \mathbf{I}_{\mu 1} \mathbf{\Lambda}_m(\gamma_1 b) \right], \quad (5.16)$$

and

$$\mathbf{\Lambda}_m(\gamma_1 b) - \mathbf{M}_m(\gamma_1 b) = \frac{1}{I_m(\gamma_1 b) K_m(\gamma_1 b)} \begin{bmatrix} 0 & -k_1^2 \\ 1 & 0 \end{bmatrix}.$$

Meanwhile, the transmission coefficients can be obtained from (5.13) and (5.15)

$$\mathbf{T}_{21} = \gamma_1^2 \mathbf{I}_{\mu 2}^{-1} \mathbf{I}_{\mu 1} \mathbf{Q}_{21}^{-1} \mathbf{I}_{\mu 1} [\mathbf{\Lambda}_m(\gamma_1 b) - \mathbf{M}_m(\gamma_1 b)]. \quad (5.17)$$

Equations (5.15) and (5.17) give the transmission and reflection matrices for an outgoing wave corresponding to the order m and mode κ .

5.2.2 Transmission and Reflection for an Incoming Wave

For a source located outside the borehole interface, it is equivalent to an incoming wave is incident on a cylindrical boundary, Fig. 5.3. Fourier transform of the potentials in region 1 ($\rho < b$) can be written as

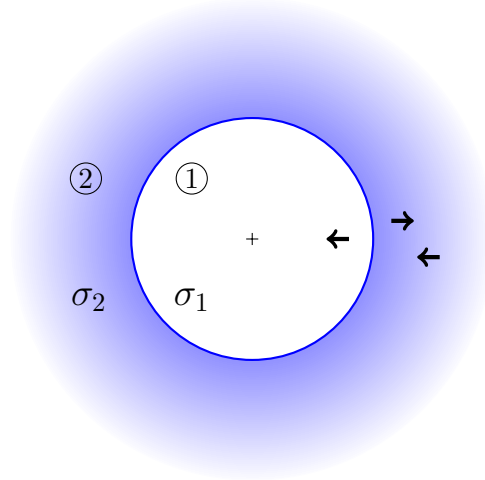


Figure 5.3: Transmission and reflection of an incoming wave. The arrows represent components of the field that migrate from the source, migrate from the boundary back towards the source, and transmitted through the interface into the borehole.

$$\begin{bmatrix} \tilde{W}_{am}^{(1)} \\ \tilde{W}_{bm}^{(1)} \end{bmatrix} = \frac{I_m(\gamma_1 \rho)}{I_m(\gamma_1 b)} \mathbf{T}_{12} \cdot \mathbf{a}_{2m}, \quad (5.18)$$

and Fourier transform of the potentials inbetween the boundary and the source in region 2 has the form

$$\begin{bmatrix} \tilde{W}_{am}^{(2)} \\ \tilde{W}_{bm}^{(2)} \end{bmatrix} = \left[\frac{I_m(\gamma_2 \rho)}{I_m(\gamma_2 b)} \mathbf{I} + \frac{K_m(\gamma_2 \rho)}{K_m(\gamma_2 b)} \mathbf{\Gamma}_{12} \right] \cdot \mathbf{a}_{2m}. \quad (5.19)$$

Here, transmission and reflection matrices have the same meaning as those for the source in region 1.

Similarly, the continuity conditions at $\rho = b$ can be used to obtain the following matrix equations

$$\gamma_1^2 \mathbf{I}_{\mu 1} \mathbf{T}_{12} = \gamma_2^2 \mathbf{I}_{\mu 2} [\mathbf{I} + \mathbf{\Gamma}_{12}], \quad (5.20)$$

$$\mathbf{I}_{\mu 1} \mathbf{\Lambda}_m(\gamma_1 b) \mathbf{T}_{12} = \mathbf{I}_{\mu 2} [\mathbf{\Lambda}_m(\gamma_2 b) + \mathbf{M}_m(\gamma_2 b) \mathbf{\Gamma}_{12}]. \quad (5.21)$$

From (5.20), we have

$$\gamma_1^2 \mathbf{T}_{12} = \gamma_2^2 \mathbf{I}_{\mu 1}^{-1} \mathbf{I}_{\mu 2} [\mathbf{I} + \mathbf{\Gamma}_{12}]. \quad (5.22)$$

Multiplying (5.21) with γ_1^2 and substituting $\gamma_1^2 \mathbf{T}_{12}$ into the equation, the reflection matrix can be solved from the following equation

$$\begin{aligned} & - \left[\gamma_2^2 \mathbf{I}_{\mu 1} \mathbf{\Lambda}_m(\gamma_1 b) \mathbf{I}_{\mu 1}^{-1} \mathbf{I}_{\mu 2} - \gamma_1^2 \mathbf{I}_{\mu 2} \mathbf{M}_m(\gamma_2 b) \right] \mathbf{\Gamma}_{12} \\ & = \gamma_2^2 \mathbf{I}_{\mu 1} \mathbf{\Lambda}_m(\gamma_1 b) \mathbf{I}_{\mu 1}^{-1} \mathbf{I}_{\mu 2} - \gamma_1^2 \mathbf{I}_{\mu 2} \mathbf{\Lambda}_m(\gamma_2 b), \end{aligned} \quad (5.23)$$

and the reflection matrix is given by

$$\mathbf{\Gamma}_{12} = \gamma_1^2 \mathbf{Q}_{12}^{-1} \mathbf{I}_{\mu 2} [\mathbf{\Lambda}_m(\gamma_2 b) - \mathbf{M}_m(\gamma_2 b)] - \mathbf{I}, \quad (5.24)$$

where

$$\mathbf{Q}_{12} = \gamma_2^2 \mathbf{I}_{\mu 1} \mathbf{\Lambda}_m(\gamma_1 b) \mathbf{I}_{\mu 1}^{-1} \mathbf{I}_{\mu 2} - \gamma_1^2 \mathbf{I}_{\mu 2} \mathbf{M}_m(\gamma_2 b). \quad (5.25)$$

Then the transmission coefficient is obtained by substituting (5.24) into (5.22)

$$\mathbf{T}_{12} = \gamma_2^2 \mathbf{I}_{\mu 1}^{-1} \mathbf{I}_{\mu 2} \mathbf{Q}_{12}^{-1} \mathbf{I}_{\mu 2} [\mathbf{\Lambda}_m(\gamma_2 b) - \mathbf{M}_m(\gamma_2 b)]. \quad (5.26)$$

The transmission and reflection matrices for an incoming wave incidence with a given order m and mode κ are obtained in (5.24) and (5.26).

For an axially symmetric case where only zeroth-order solution ($m = 0$) is required, TE and TM modes are decoupled. The off-diagonal terms of $\mathbf{\Gamma}$ and \mathbf{T} become zero. If the medium in region 1 is free space, the transmission and reflection matrices are reduced to those derived in Chapter 4 and Appendix D. With above solutions for a single cylindrical interface, the more complicated problems with multiple cylindrical interfaces can be set up as follows.

5.3 Transmission and Reflection due to Multiple Cylindrical Interfaces

Now let's consider the derivation of transmission and reflection matrices due to multilayered medium. The tube is a simplest case with three media and two interfaces. The tube model can be directly extended to other multilayered structures. Therefore, we only discuss the tube problem here. The basic idea is similar to the theory for the transmission and reflection of multiple planar interfaces [3]. We designate the regions from the inside to the outside as region 1, 2, and 3. The interface between region 1 and 2 is at $\rho = a$ and the interface between region 2 and 3 is located at $\rho = b$, Fig. 5.4.

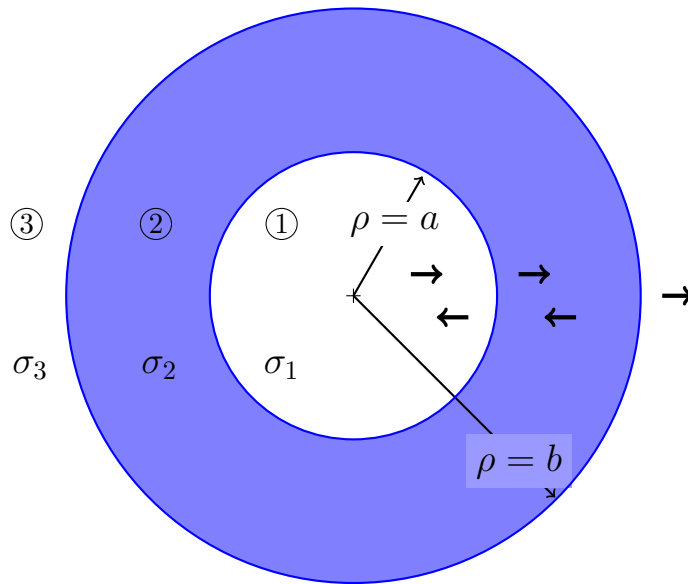


Figure 5.4: Transmission and reflection of an outgoing wave inside a tube.

5.3.1 Source Located inside a Tube

For a source located in region 1, an outgoing wave incident on the tube, the Fourier transform of total field in region 1 can be written as

$$\begin{bmatrix} \tilde{W}_{am}^{(1)} \\ \tilde{W}_{bm}^{(1)} \end{bmatrix} = \left[\frac{K_m(\gamma_1 \rho)}{K_m(\gamma_1 a)} \mathbf{I} + \frac{I_m(\gamma_1 \rho)}{I_m(\gamma_1 a)} \tilde{\mathbf{\Gamma}}_{21} \right] \cdot \mathbf{a}_{1m}, \quad (5.27)$$

where the tilde sign on the reflection matrix, such as $\tilde{\mathbf{\Gamma}}_{21}$, represents a generalized total reflection matrix which will be determined later. Fourier transform of the fields in region 2 has the form

$$\begin{bmatrix} \tilde{W}_{am}^{(2)} \\ \tilde{W}_{bm}^{(2)} \end{bmatrix} = \left[\frac{K_m(\gamma_2 \rho)}{K_m(\gamma_2 b)} \mathbf{I} + \frac{I_m(\gamma_2 \rho)}{I_m(\gamma_2 b)} \mathbf{\Gamma}_{32} \right] \cdot \mathbf{a}_{2m}, \quad (5.28)$$

where $\mathbf{\Gamma}_{32}$ is the reflection matrix representing the reflected fields migrating from the interface $\rho = b$ due to a source between region 2 and region 3 derived and its definition is given in the last two sections. The vector \mathbf{a}_{2m} is an unknown vector to be determined and it represents the total outgoing field in region 2. Moreover, Fourier transform of the fields in region 3 is given by

$$\begin{bmatrix} \tilde{W}_{am}^{(3)} \\ \tilde{W}_{bm}^{(3)} \end{bmatrix} = \frac{K_m(\gamma_3 \rho)}{K_m(\gamma_3 b)} \mathbf{a}_{3m}, \quad (5.29)$$

where \mathbf{a}_{3m} is the second unknown vector in this problem.

At the interface $\rho = a$, the outgoing field in region 2 consists of two parts, the transmission of an outgoing wave in region 1 and the reflection of the outgoing wave itself in region 2. Therefore, we have

$$\frac{\mathbf{a}_{2m}}{K_m(\gamma_2 b)} = \frac{K_m(\gamma_1 a)}{K_m(\gamma_2 a)} \mathbf{T}_{21} \cdot \frac{\mathbf{a}_{1m}}{K_m(\gamma_1 a)} + \frac{I_m(\gamma_2 a)}{K_m(\gamma_2 a)} \mathbf{\Gamma}_{12} \cdot \frac{K_m(\gamma_2 b)}{I_m(\gamma_2 b)} \mathbf{\Gamma}_{32} \cdot \frac{\mathbf{a}_{2m}}{K_m(\gamma_2 b)}. \quad (5.30)$$

From (5.30), \mathbf{a}_{2m} can be expressed as

$$\mathbf{a}_{2m} = \frac{K_m(\gamma_2 b)}{K_m(\gamma_2 a)} \left(\mathbf{I} - \frac{I_m(\gamma_2 a) K_m(\gamma_2 b)}{I_m(\gamma_2 b) K_m(\gamma_2 a)} \mathbf{\Gamma}_{12} \cdot \mathbf{\Gamma}_{32} \right)^{-1} \cdot \mathbf{T}_{21} \cdot \mathbf{a}_{1m}. \quad (5.31)$$

In addition, the incoming wave in region 1 comes from the reflection of the outgoing wave in region 1 and the transmission of an incoming wave in region 2. So, at $\rho = a$, we have that

$$\frac{1}{I_m(\gamma_1 a)} \tilde{\mathbf{\Gamma}}_{21} \cdot \mathbf{a}_{1m} = \frac{K_m(\gamma_1 a)}{I_m(\gamma_1 a)} \mathbf{\Gamma}_{21} \cdot \frac{\mathbf{a}_{1m}}{K_m(\gamma_1 a)} + \frac{I_m(\gamma_2 a)}{I_m(\gamma_1 a)} \mathbf{T}_{12} \cdot \frac{K_m(\gamma_2 b)}{I_m(\gamma_2 b)} \mathbf{\Gamma}_{32} \cdot \frac{\mathbf{a}_{2m}}{K_m(\gamma_2 b)}. \quad (5.32)$$

Substituting (5.31) into (5.32), we get the total reflection matrix

$$\tilde{\mathbf{T}}_{21} = \mathbf{\Gamma}_{21} + \frac{I_m(\gamma_2 a) K_m(\gamma_2 b)}{I_m(\gamma_2 b) K_m(\gamma_2 a)} \mathbf{\Gamma}_{12} \cdot \mathbf{\Gamma}_{32} \cdot \left(\mathbf{I} - \frac{I_m(\gamma_2 a) K_m(\gamma_2 b)}{I_m(\gamma_2 b) K_m(\gamma_2 a)} \mathbf{\Gamma}_{12} \cdot \mathbf{\Gamma}_{32} \right)^{-1} \cdot \mathbf{T}_{21}. \quad (5.33)$$

All the transmission and reflection matrices in (5.33) are defined in the previous sections. If there is another extra layer presented outside region 3, all we need to do is to modify the terms related to reflection matrix, $\mathbf{\Gamma}_{32}$ with corresponding total the reflection matrix, $\tilde{\mathbf{\Gamma}}_{32}$. Finally, the reflection matrix for any multilayered structure could be derived iteratively using (5.33).

5.3.2 Source Located outside a Tube

Similarly, for a source located in region 3, Fig. 5.5, Fourier transform of the total fields in region 1 is

$$\begin{bmatrix} \tilde{W}_{am}^{(1)} \\ \tilde{W}_{bm}^{(1)} \end{bmatrix} = \frac{I_m(\gamma_1 \rho)}{I_m(\gamma_1 a)} \mathbf{a}_{1m}, \quad (5.34)$$

and Fourier transform of the fields in region 2 can be written as

$$\begin{bmatrix} \tilde{W}_{am}^{(2)} \\ \tilde{W}_{bm}^{(2)} \end{bmatrix} = \left[\frac{K_m(\gamma_2 \rho)}{K_m(\gamma_2 a)} \mathbf{\Gamma}_{12} + \frac{I_m(\gamma_2 \rho)}{I_m(\gamma_2 a)} \mathbf{I} \right] \cdot \mathbf{a}_{2m}. \quad (5.35)$$

Finally, Fourier transform of the fields in region 3 is,

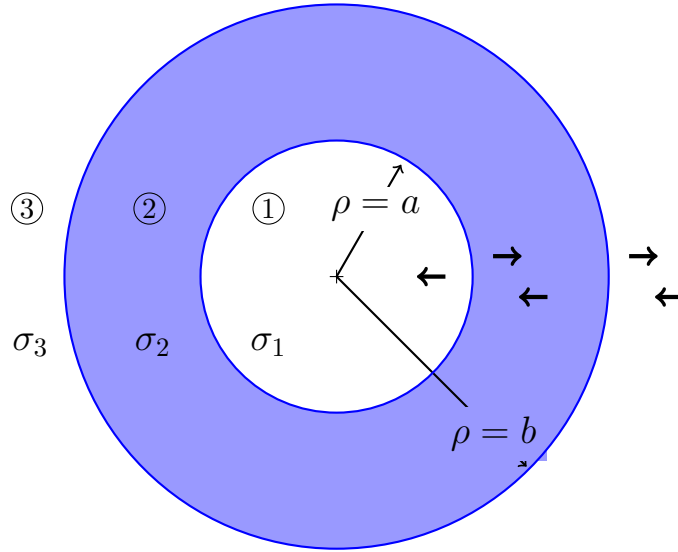


Figure 5.5: Transmission and reflection of an incoming wave outside a tube.

$$\begin{bmatrix} \tilde{W}_{am}^{(3)} \\ \tilde{W}_{bm}^{(3)} \end{bmatrix} = \begin{bmatrix} K_m(\gamma_3\rho) \\ K_m(\gamma_3b) \end{bmatrix} \tilde{\Gamma}_{23} + \frac{I_m(\gamma_3\rho)}{I_m(\gamma_3b)} \mathbf{I} \cdot \mathbf{a}_{3m}. \quad (5.36)$$

where $\tilde{\Gamma}_{23}$ is the total reflection matrix. In this case, vector \mathbf{a}_{3m} represents the source field and vectors \mathbf{a}_{1m} and \mathbf{a}_{2m} are unknown coefficients for the incoming fields in each region.

The same approach is used to derive the reflection matrix $\tilde{\Gamma}_{23}$. At the interface $\rho = b$, we have

$$\frac{\mathbf{a}_{2m}}{I_m(\gamma_2a)} = \frac{I_m(\gamma_3b)}{I_m(\gamma_2b)} \mathbf{T}_{23} \cdot \frac{\mathbf{a}_{3m}}{I_m(\gamma_3b)} + \frac{K_m(\gamma_2b)}{I_m(\gamma_2b)} \mathbf{T}_{32} \cdot \frac{I_m(\gamma_2a)}{K_m(\gamma_2a)} \mathbf{T}_{12} \cdot \frac{\mathbf{a}_{2m}}{I_m(\gamma_2a)}. \quad (5.37)$$

The incoming fields in region 2 come from the transmission of the incoming field in region 3 and the reflection of the incoming fields in region 2 and it could be solved from (5.37) as

$$\mathbf{a}_{2m} = \frac{I_m(\gamma_2a)}{I_m(\gamma_2b)} \left(\mathbf{I} - \frac{I_m(\gamma_2a)K_m(\gamma_2b)}{I_m(\gamma_2b)K_m(\gamma_2a)} \mathbf{T}_{32} \cdot \mathbf{T}_{12} \right)^{-1} \cdot \mathbf{T}_{23} \cdot \mathbf{a}_{3m}. \quad (5.38)$$

The reflection wave in region 3 can be solved from

$$\frac{1}{K_m(\gamma_3b)} \tilde{\Gamma}_{23} \cdot \mathbf{a}_{3m} = \frac{I_m(\gamma_3b)}{K_m(\gamma_3b)} \mathbf{T}_{23} \cdot \frac{\mathbf{a}_{3m}}{I_m(\gamma_3b)} + \frac{K_m(\gamma_2b)}{K_m(\gamma_3b)} \mathbf{T}_{32} \cdot \frac{I_m(\gamma_2a)}{K_m(\gamma_2a)} \mathbf{T}_{12} \cdot \frac{\mathbf{a}_{2m}}{I_m(\gamma_2a)}. \quad (5.39)$$

This means the outgoing wave in region 3 is a consequence of the transmission of the outgoing wave in region 2 and the reflection of the incoming wave in region 3. Substituting (5.38) into (5.39), we obtain the total reflection matrix for a source in region 3

$$\tilde{\Gamma}_{23} = \mathbf{T}_{23} + \frac{I_m(\gamma_2a)K_m(\gamma_2b)}{I_m(\gamma_2b)K_m(\gamma_2a)} \mathbf{T}_{32} \cdot \mathbf{T}_{12} \cdot \left(\mathbf{I} - \frac{I_m(\gamma_2a)K_m(\gamma_2b)}{I_m(\gamma_2b)K_m(\gamma_2a)} \mathbf{T}_{32} \cdot \mathbf{T}_{12} \right)^{-1} \cdot \mathbf{T}_{23}. \quad (5.40)$$

Equation (5.40) can be extended for multiple layered structure by modifying the reflection matrix \mathbf{T}_{12} . The results presented here are similar to those in Chew's work [118]. Some normalizing factors are introduced in our formulation to prevent the numerical overflows in the calculation.

With the total reflection matrices derived in (5.33) and (5.40), the incident fields due an eddy-current coil inside or outside a tube can be obtained by replacing the original reflection coefficients for the borehole case. If we make the conductivity σ_3 equals to σ_2 in the calculation, or extend the outer radius of the tube, b to the infinite, the transmission and reflection matrices become the ones for a single cylindrical interface.

5.4 Incident Field in an Infinitely Long Tube

The incident field calculation for a rotary coil inside a borehole is provided in Appendix D. With the total reflection derived from the previous section, the incident field for a rotary coil inside a tube can be easily obtained by replacing the transmission and reflection coefficients in (D.5) and (D.10) with the corresponding terms in (5.33). In this chapter, we introduced different geometric factor in our TE and TM potential definitions. That's the only difference we need to modify from the borehole model when we calculate the incident field calculation.

The impedance change due to the tube can be also derived from the original form of the impedance change of a coil inside borehole (D.7) and it is given by

$$\begin{aligned}\Delta Z &= \frac{i\omega\pi h}{\mu_0 I^2} \sum_{m=-\infty}^{\infty} \sum_{i=1}^{\infty} \kappa_i^2 \frac{a_{1a}}{K_m(\kappa_i a)} \frac{K_m(\kappa_i a)}{I_m(\kappa_i a)} \tilde{\Gamma}_{21}^{aa} \frac{a_{1a}}{K_m(\kappa_i a)} \\ &= \frac{i\omega\pi h}{\mu_0 I^2} \sum_{m=-\infty}^{\infty} \sum_{i=1}^{\infty} \frac{\kappa_i^2 \tilde{\Gamma}_{21}^{aa} a_{1a}^2}{I_m(\kappa_i a) K_m(\kappa_i a)}\end{aligned}\quad (5.41)$$

where a_{1a} is the TE component of the source coefficient \mathbf{a}_{1m} and $C_{mi}^{(0)}$ in (D.7) is equivalent to $\frac{a_{1a}}{K_m(\kappa_i a)}$ here.

5.5 Green's Function for a Point Source in a Tube

Now, Let's consider a point source embedded in walls of a tube, Fig. 5.6. The corresponding TE/TM potentials can also be represented as a two-by-two Green's function matrix whose Fourier space representation takes form

$$\tilde{\mathbf{G}}(\rho, \rho', m) = I_m(\gamma\rho<)K_m(\gamma\rho>)\mathbf{I} + K_m(\gamma\rho)\mathbf{A}_m + I_m(\gamma\rho)\mathbf{B}_m, \quad (5.42)$$

where the first term $I_m(\gamma\rho<)K_m(\gamma\rho>)\mathbf{I}$ is from the Green's function in a homogeneous unbounded conductor. The other two terms represent the migration from inner and outer interfaces and the coefficient matrices, \mathbf{A}_m and \mathbf{B}_m , can be expressed as

$$\mathbf{B}_m = \frac{K_m(\gamma b)}{I_m(\gamma b)} \mathbf{\Gamma}_{32} [I_m(\gamma\rho')\mathbf{I} + \mathbf{A}_m], \quad (5.43)$$

at $\rho = b$, and

$$\mathbf{A}_m = \frac{I_m(\gamma a)}{K_m(\gamma a)} \mathbf{\Gamma}_{12} [K_m(\gamma\rho')\mathbf{I} + \mathbf{B}_m], \quad (5.44)$$

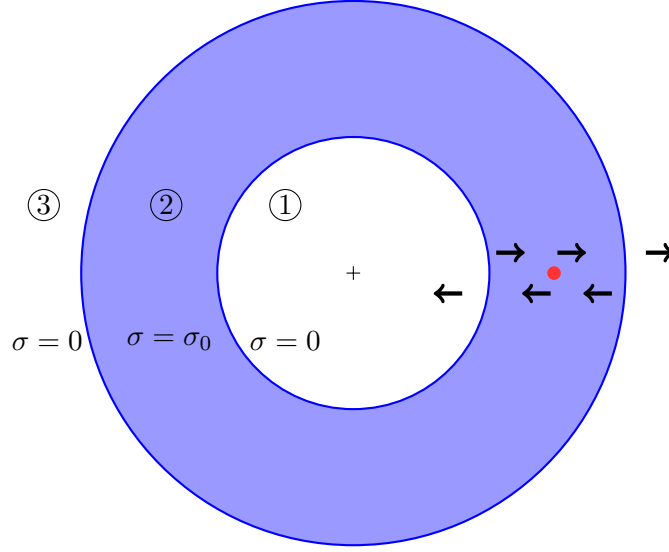


Figure 5.6: A point source located between the walls of a tube. The conductivity of the tube is σ_0 .

at $\rho = a$.

From (5.43) and (5.44), one can solve \mathbf{A}_m and \mathbf{B}_m as

$$\mathbf{A}_m = \frac{I_m(\gamma a)}{K_m(\gamma a)} \mathbf{Q}_+ \Gamma_{12} \left[K_m(\gamma \rho') \mathbf{I} + \frac{K_m(\gamma b)}{I_m(\gamma b)} I_m(\gamma \rho') \Gamma_{32} \right], \quad (5.45)$$

$$\mathbf{B}_m = \frac{K_m(\gamma b)}{I_m(\gamma b)} \mathbf{Q}_- \Gamma_{32} \left[I_m(\gamma \rho') \mathbf{I} + \frac{I_m(\gamma a)}{K_m(\gamma a)} K_m(\gamma \rho') \Gamma_{12} \right], \quad (5.46)$$

where

$$\mathbf{Q}_+ = \left[\mathbf{I} - \frac{I_m(\gamma a) K_m(\gamma b)}{I_m(\gamma b) K_m(\gamma a)} \Gamma_{12} \Gamma_{32} \right]^{-1}, \quad (5.47)$$

and

$$\mathbf{Q}_- = \left[\mathbf{I} - \frac{I_m(\gamma a) K_m(\gamma b)}{I_m(\gamma b) K_m(\gamma a)} \Gamma_{32} \Gamma_{12} \right]^{-1}. \quad (5.48)$$

\mathbf{Q}_+ and \mathbf{Q}_- are related to each other as

$$\mathbf{Q}_- \Gamma_{32} = \Gamma_{32} \mathbf{Q}_+, \quad (5.49)$$

and

$$\mathbf{Q}_+ \Gamma_{12} = \Gamma_{12} \mathbf{Q}_-. \quad (5.50)$$

Therefore, we can write that

$$\mathbf{I} + \frac{I_m(\gamma a) K_m(\gamma b)}{I_m(\gamma b) K_m(\gamma a)} \Gamma_{12} \mathbf{Q}_- \Gamma_{32} = \mathbf{Q}_+, \quad (5.51)$$

and

$$\mathbf{I} + \frac{I_m(\gamma a)K_m(\gamma b)}{I_m(\gamma b)K_m(\gamma a)}\mathbf{\Gamma}_{32}\mathbf{Q}_+\mathbf{\Gamma}_{12} = \mathbf{Q}_-. \quad (5.52)$$

Substituting (5.45) and (5.46) into (5.42), with above relations, Fourier transform of the Green's function can be written as

$$\tilde{\mathbf{G}}(\rho, \rho', m) = \left[K_m(\gamma\rho)\mathbf{I} + \frac{K_m(\gamma b)}{I_m(\gamma b)}I_m(\gamma\rho)\mathbf{\Gamma}_{32} \right] \cdot \mathbf{Q}_+ \cdot \left[I_m(\gamma\rho')\mathbf{I} + \frac{I_m(\gamma a)}{K_m(\gamma a)}K_m(\gamma\rho')\mathbf{\Gamma}_{12} \right], \quad (5.53)$$

for $\rho > \rho'$ and

$$\tilde{\mathbf{G}}(\rho, \rho', m) = \left[I_m(\gamma\rho)\mathbf{I} + \frac{I_m(\gamma a)}{K_m(\gamma a)}K_m(\gamma\rho)\mathbf{\Gamma}_{12} \right] \cdot \mathbf{Q}_- \cdot \left[K_m(\gamma\rho')\mathbf{I} + \frac{K_m(\gamma b)}{I_m(\gamma b)}I_m(\gamma\rho')\mathbf{\Gamma}_{32} \right], \quad (5.54)$$

for $\rho < \rho'$.

The regular terms in (5.42) are then given by

$$\begin{aligned} & \tilde{\mathbf{G}}^{(\Gamma)}(\rho, \rho', m) \\ &= K_m(\gamma\rho)\mathbf{A}_m + I_m(\gamma\rho)\mathbf{B}_m \\ &= K_m(\gamma\rho')\frac{I_m(\gamma a)}{K_m(\gamma a)}\left[K_m(\gamma\rho)\mathbf{I} + I_m(\gamma\rho)\frac{K_m(\gamma b)}{I_m(\gamma b)}\mathbf{\Gamma}_{32} \right]\mathbf{Q}_+\mathbf{\Gamma}_{12} \\ & \quad + I_m(\gamma\rho')\frac{K_m(\gamma b)}{I_m(\gamma b)}\left[I_m(\gamma\rho)\mathbf{I} + K_m(\gamma\rho)\frac{I_m(\gamma a)}{K_m(\gamma a)}\mathbf{\Gamma}_{12} \right]\mathbf{Q}_-\mathbf{\Gamma}_{32}. \end{aligned} \quad (5.55)$$

Compared to the borehole problem, the singular part in an unbounded domain is the same as that in the borehole model but the reflection part is changed to (5.55). This completes derivation of the Green's function for a point source in a tube.

5.6 Reflection Matrix Element for a Longitudinal Crack

With the scalar Green's function derived in the previous section, the function \mathbf{U} due to a point source in a tube is similar to that in (4.46) and it has the form

$$\mathbf{U}(\mathbf{r}|\mathbf{r}') = \begin{bmatrix} U_a \\ U_b \end{bmatrix} = \frac{1}{\pi h} \sum_{m=-\infty}^{\infty} e^{zm(\phi-\phi')} \sum_{s=1}^{\infty} \begin{bmatrix} \sin(\kappa_s z) & 0 \\ 0 & \cos(\kappa_s z) \end{bmatrix} \begin{bmatrix} \tilde{U}_{aa} & \tilde{U}_{ab} \\ \tilde{U}_{ba} & \tilde{U}_{bb} \end{bmatrix} \begin{bmatrix} \sin(\kappa_s z') \\ \cos(\kappa_s z') \end{bmatrix}, \quad (5.56)$$

where

$$\begin{bmatrix} \tilde{U}_{aa} & \tilde{U}_{ab} \\ \tilde{U}_{ba} & \tilde{U}_{bb} \end{bmatrix} = -\frac{1}{\gamma_s^2} \begin{bmatrix} \tilde{G}_{aa} & \tilde{G}_{ab} \\ \tilde{G}_{ba} & \tilde{G}_{bb} \end{bmatrix}. \quad (5.57)$$

The reflection part of the dyadic Green's function in (4.28) can be rewritten into matrix form as

$$\mathcal{G}^{(\Gamma)}(\mathbf{r}|\mathbf{r}') = \begin{bmatrix} \nabla \times \hat{z} \\ \nabla \times \nabla \times \hat{z} \end{bmatrix}^T \begin{bmatrix} U_{aa} & U_{ab} \\ U_{ba} & U_{bb} \end{bmatrix} \begin{bmatrix} \nabla' \times \hat{z} \\ \frac{1}{k^2} \nabla' \times \nabla' \times \hat{z} \end{bmatrix}, \quad (5.58)$$

where the superscript T is the transpose operator.

The crack model is the same as we used in the borehole problem. In order to solve the current dipole density over the crack region, the kernel, $G_{nn}(\mathbf{r}|\mathbf{r}')$ is needed in the volume integral method. We will only discuss a longitudinal crack in a tube here. For the longitudinal crack, the integral kernel related to the reflection part of the dyadic Green's function can be obtained as

$$\begin{aligned} & G_{\phi\phi}^{(\Gamma)}(\mathbf{r}|\mathbf{r}') \\ &= \hat{\phi} \cdot \mathcal{G}^{(\Gamma)}(\mathbf{r}|\mathbf{r}') \cdot \hat{\phi} \\ &= -\frac{1}{\pi h} \sum_{m=-\infty}^{\infty} e^{im(\phi-\phi')} \sum_{s=1}^{\infty} \frac{\sin(\kappa_s z) \sin(\kappa_s z')}{\gamma_s^2} \begin{bmatrix} \frac{\partial}{\partial \rho} \\ im\kappa_s \\ \rho \end{bmatrix}^T \tilde{\mathbf{G}}^{(\Gamma)}(\rho, \rho', m) \begin{bmatrix} \frac{\partial}{\partial \rho'} \\ -im\kappa_s \\ k^2 \rho' \end{bmatrix}, \end{aligned} \quad (5.59)$$

where the Fourier representation of the reflection part of the Green's function $\tilde{\mathbf{G}}^{(\Gamma)}(\rho, \rho', m)$ is given in (5.55).

Finally, the reflection matrix element is derived based on volume integral over the source cell l has the form

$$M_{jl}^{(\Gamma)} = k^2 \int_{z_c - \Delta z/2}^{z_c + \Delta z/2} \int_{\phi_c - \Delta \phi/2}^{\phi_c + \Delta \phi/2} \int_{\rho_1}^{\rho_2} \rho' G_{\phi\phi}^{(\Gamma)}(\mathbf{r}_j|\mathbf{r}') d\rho' d\phi' dz',$$

where the integral over ϕ' gives

$$\int_{-\Delta \phi/2}^{\Delta \phi/2} e^{-im\phi'} d\phi' = \Delta \phi \operatorname{sinc}\left(\frac{m\Delta \phi}{2}\right), \quad (5.60)$$

and the integral over z' gives

$$\int_{z_c - \frac{\Delta z}{2}}^{z_c + \frac{\Delta z}{2}} \sin(uz') dz' = \Delta z \sin(uz_c) \operatorname{sinc}\left(u \frac{\Delta z}{2}\right). \quad (5.61)$$

The integral over variable ρ' , $\int_{\rho_1}^{\rho_2} \rho' \tilde{G}_{\phi\phi}^{(\Gamma)} d\rho'$, is cumbersome but the derivation is straightforward and similar to those given in the borehole case. Therefore, they will not list them here.

The matrix element related to the unbounded domain Green's function is the same as that in (4.61). Using the volume element method, the impedance change of a coil due to a crack in a tube can be obtained. Next, the numerical results and experimental validations are presented.

5.7 Experimental Measurements and Results

In this section, the coil impedance change due to a through-wall crack in a tube is tested. The results are compared with the plate cases for an extreme case with large radius. A well controlled experiment is also presented to validate our crack calculation. Good agreement is obtained between theoretical predictions and measurement data.

The numerical techniques used in the borehole model has also been applied to the tube code for the matrix element calculation. We examine a special case with the large radius first. The singular matrix elements are calculated using MATLAB internal integral function with log-like Gaussian quadrature and the reflection matrix elements are evaluated using the recurrence algorithm in Section 4.7.

5.7.1 Through-Thickness Crack in Thin Plate

Through-thickness cracks in a thin plate has been well developed by Burke et al. [36, 13]. A bobbin coil above a brass plate is used to measure the coil impedance change due to a slot in the thin plate as a function of the coil position. All the parameters are listed in Table 5.1.

Here, we use our tube model to approximate this problem by putting a rotary coil inside a tube with a large inner radius, $a = 200$ mm. Two cases with slot length 44.4 mm and 101 mm are validated here. As shown in Figs. 5.7 and 5.8, the predicted coil impedance change due to the slot with the same size in the tube is calculated and compared with the measurement for a slot in a thin plate. The numerical results show a reasonable agreement with the measurement data.

Next, coil impedance change due a through-wall notch in a tube is considered. The experiment is presented first and then predictions are compared with measurements.

Table 5.1: Parameters of test experiment for a bobbin coil above a thin plate. The configuration is similar to Fig. 4.8.

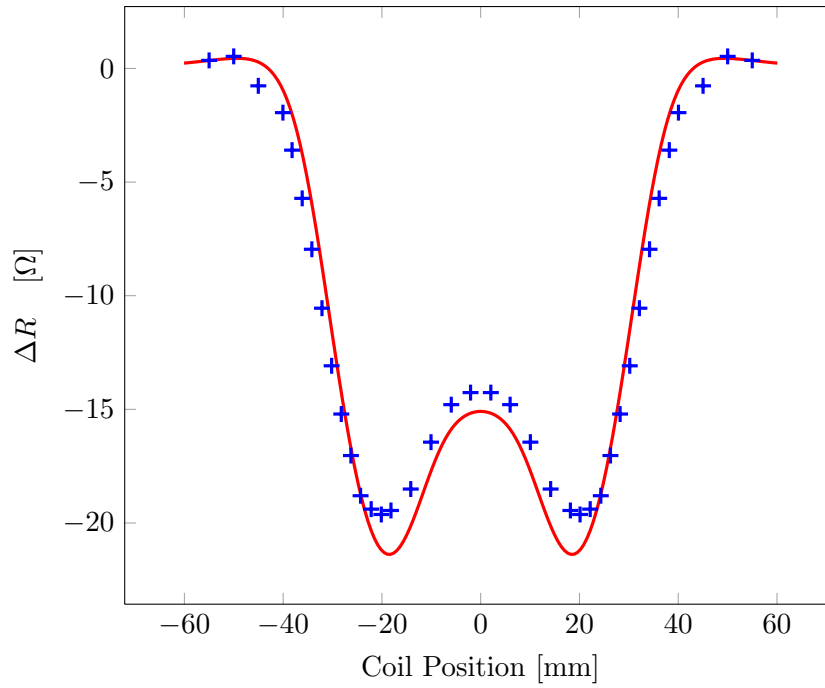
Coil	
Inner radius (r_1)	9.33 mm
Outer radius (r_2)	18.04 mm
Height (ℓ)	10.05 mm
Lift-off (λ)	1.87 mm
Number of turns (N)	1910
Test Specimen	
Plate height (h)	0.90 ± 0.01 mm
Conductivity (σ)	16.42 MS/m
Relative permeability (μ_r)	1
Through-Thickness Cracks	
Length ($2c$)	44.4 mm, 101 mm
Height (h)	0.90 ± 0.01 mm
Width (w)	0.3 mm
Other Parameters	
Frequency (f)	1 kHz
Isolated DC coil inductance (L_0)	$84.2 \mu\text{H}$
Isolated DC resistance (R_0)	260Ω

5.7.2 Experimental Configuration

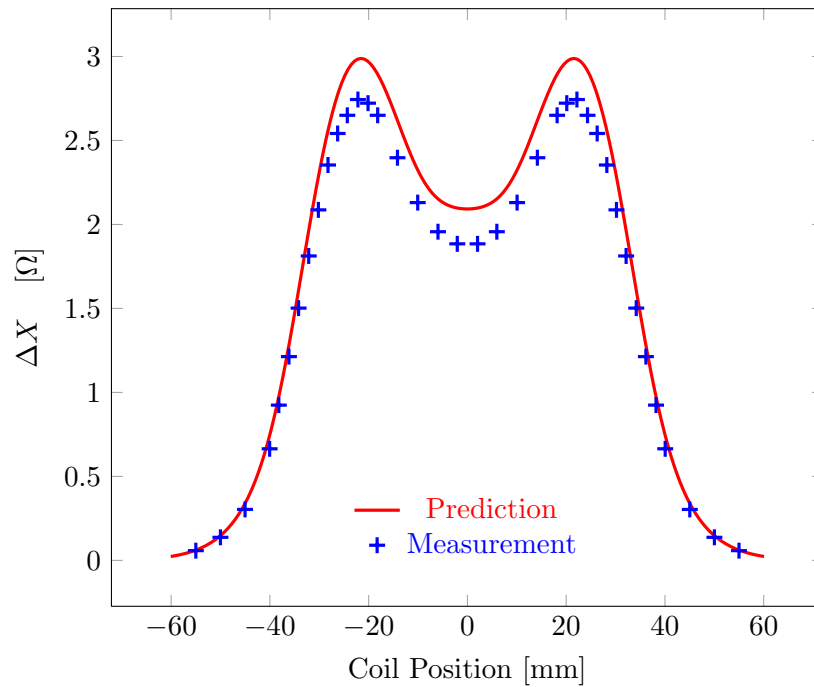
The experimental work was done by my colleague, Yuan Ji at Center for NDE, Iowa State University. This work has been submitted as a benchmark problem to the world federation of NDE. In this benchmark problem, we measured the impedance of a pancake coil due to a longitudinal through-wall notch inside a tube. Besides other parameters measured in the experiment, coil lift-off and tube conductivity can not be measured directly and they were determined based on the multifrequency impedance data with the theoretical model. All the measurement data have been corrected to remove the parasitic capacitance effects.

We have carried out a controlled experiment to acquire eddy current impedance measurements using a rotary pancake coil interacting with a longitudinal through-wall notch in an inconel 600 tube. The data provides a means of testing theoretical and computational models that predict the variation in the coil impedance with position due to the presence of the notch or crack. Figure 5.9 shows the schematic diagram of the coil in the tube.

The tube has the permeability of free space ($\mu_r = 1$). Its inner diameter is 16.64 ± 0.025 mm,

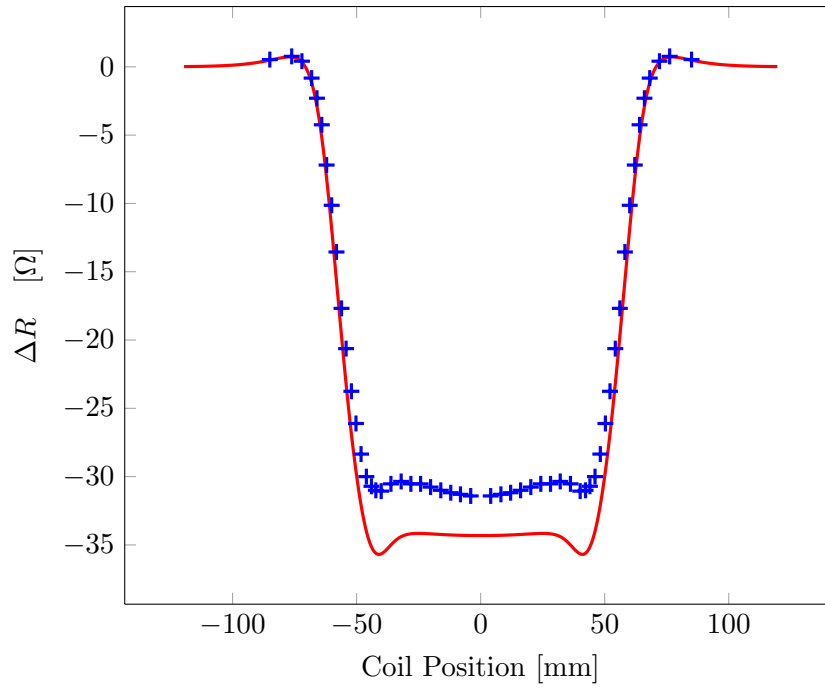


(a)

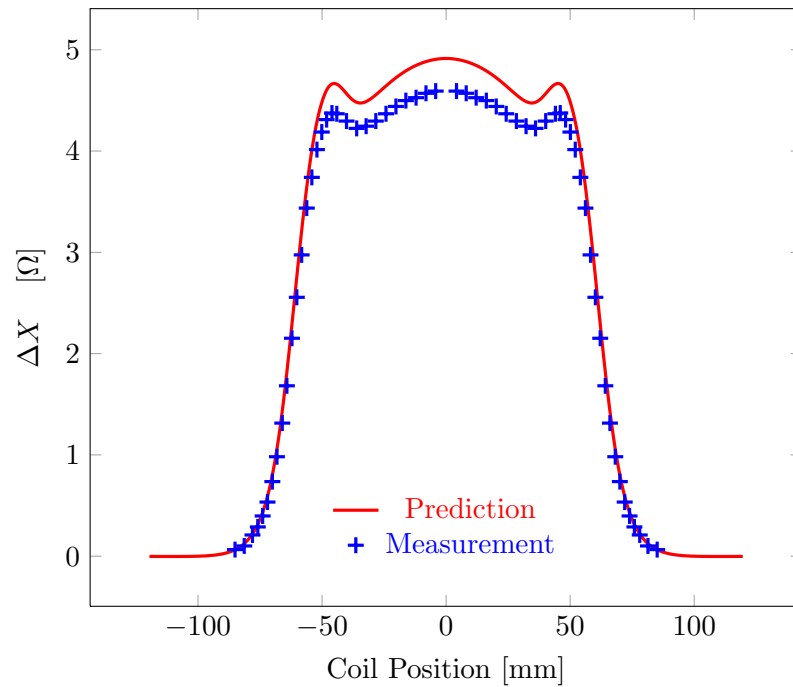


(b)

Figure 5.7: Coil resistance change (a) and reactance change (b) due to a notch as a function of coil center position at a fixed frequency of 1 kHz. The slot length is 44.4 mm. The numerical result (*solid line*) and the experimental measurements (+) are shown for comparison.



(a)



(b)

Figure 5.8: Coil resistance change (a) and reactance change (b) due to a notch as a function of coil center position at a fixed frequency of 1 kHz. The slot length is 101 mm. The numerical result (*solid line*) and the experimental measurements (+) are shown for comparison.

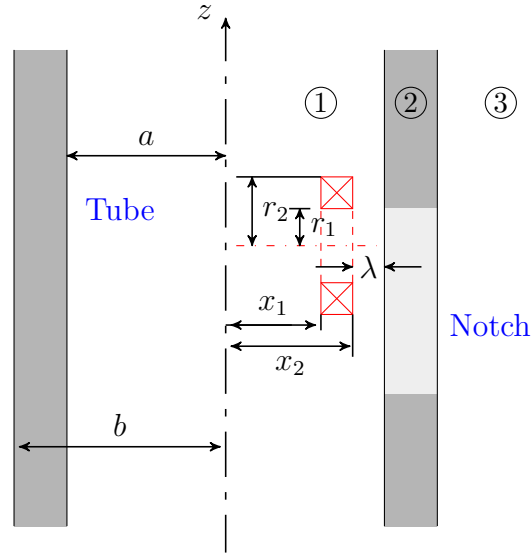


Figure 5.9: A rotary pancake coil inside a tube.

and the outer diameter 18.99 ± 0.025 mm. The probe is an air-cored eddy-current coil with a rectangular cross section, Fig. 5.9. Coil parameters are listed in Table 5.2. The longitudinal through-wall air-filled notch is a straight slit cut along at a plane through the tube axis with a length of 12.20 mm, the depth is 100% of the tube wall thickness, and the width of the opening is $85 \mu\text{m}$.

Other important parameters, including the conductivity of the tube, the coil lift-off ($\lambda = b - x_2$, in the notation illustrated in Fig. 5.9, and the coil operating frequencies are given in the following section.

5.7.3 Measurement Procedure

Measurements were carried out with the tube supported on a platform which was mounted on three motion stages, Fig. 5.10. From the bottom up, these were a 5 micron resolution xy -stage, a rotary stage and a manually adjusted tilt stage. A set-up procedure ensures that the tube axis and rotary stages have a common axis in line with the z -axis motion stage for the probe. Care over alignment and the fact that the coil mount is a close sliding fit in the tube ensure that the coil is scanned parallel to the inner surface of the tube and variations in the critical lift-off parameter, λ , are minimized.

Table 5.2: Parameters of test experiment for a rotary coil inside the tube. The configuration is shown in Fig. 5.9.

Coil	
Inner radius (r_1)	1.529 ± 0.004 mm
Outer radius (r_2)	3.918 ± 0.003 mm
Height ($\ell = x_2 - x_1$)	1.044 ± 0.005 mm
Lift-off (λ)	1.235 mm
Number of turns (N)	305
Test Specimen	
Tube inner diameter ($2a$)	16.64 ± 0.025 mm
Tube outer diameter ($2b$)	18.99 ± 0.025 mm
Conductivity (σ)	0.84 MS/m
Relative permeability (μ_r)	1
Longitudinal Notch	
Through-wall notch	1.175×12.20 mm ²
Width (w)	0.085 mm
Other Parameters	
Skin depth at 100 kHz (δ)	1.7365 mm
Isolated DC coil inductance (L_0)	465 μ H
Isolated coil resistance (R_0)	19.00 Ω

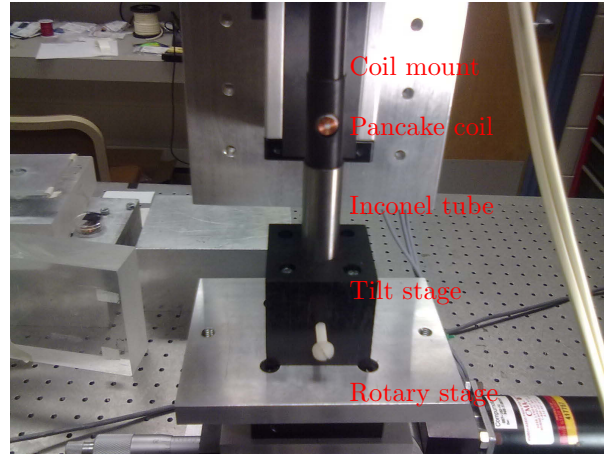
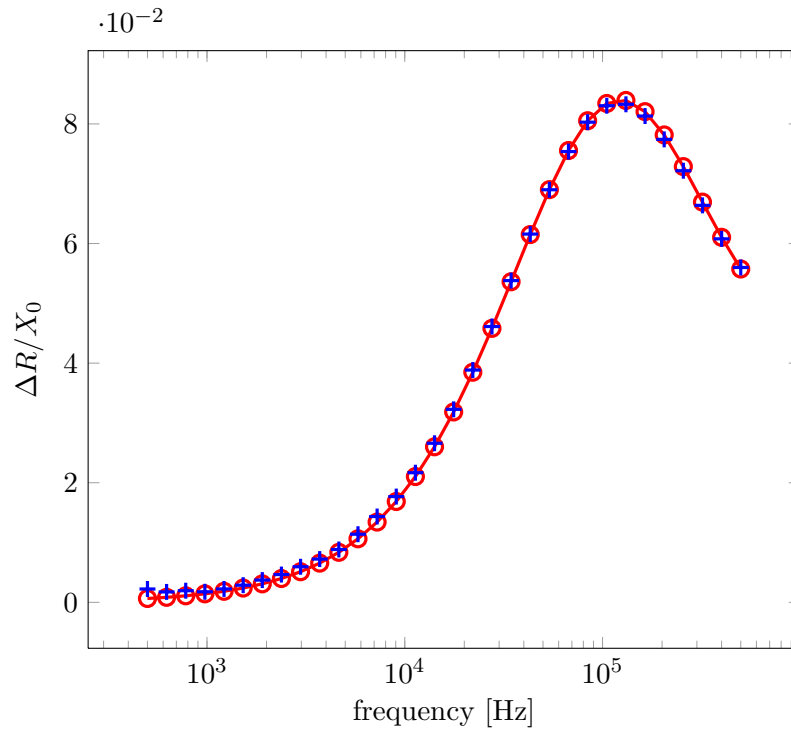


Figure 5.10: Experimental configuration used to measure the coil impedance change due to the notch in a tube.

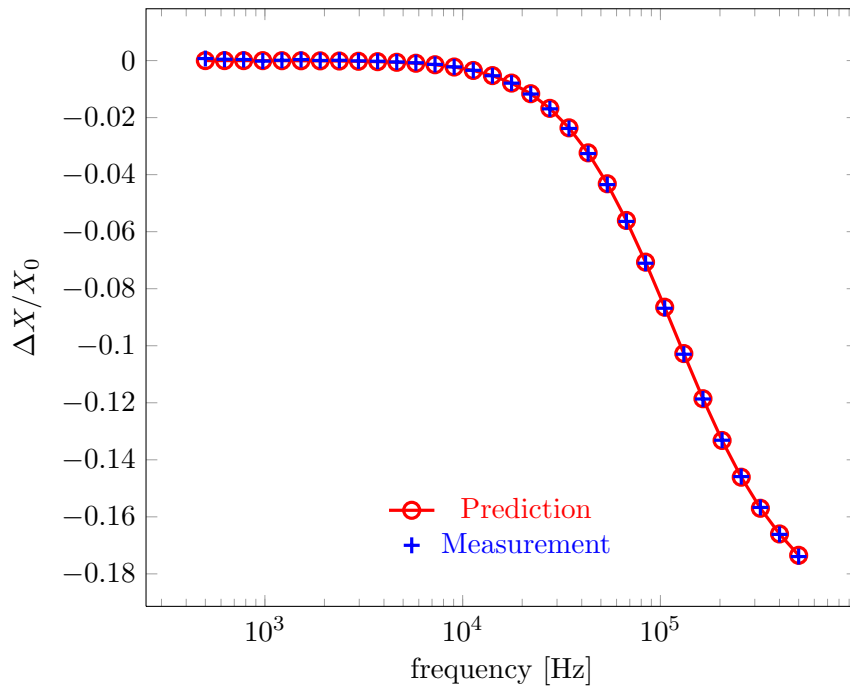
Direct measurement of lift-off using for example a traveling microscope may be possible but in earlier benchmark studies the lift-off parameter has been deduced from multi-frequency eddy current coil impedance measurements [119] using model-based estimates of the probe response on an unflawed region of the conductor fitted to the experimental data by varying the lift-off. This approach is likely to be more reliable than a direct measurement and also reveals the effects of shunt capacitance in the probe circuit as the experimental results depart from idealized capacitance-free model predictions at high frequency. Knowledge of the shunt capacitance can then be used to correct the measurement data for its effect on the flaw signals [119].

Estimating the conductivity of the tube could be done using an eddy current conductivity meter but the instruments are inaccurate for samples that are not flat. Instead one can use the multifrequency impedance data provided here to determine both lift-off and tube conductivity. The coil impedance in air was measured first over a frequency range 0.5 kHz to 500 kHz. Then the impedance due to the unflawed tube was measured over the same frequency range by putting the probe at points far away from cracks. Ideally, the impedance change due to the unflawed tube could be obtained by simply subtracting impedance in air from the one inside tube. In practice, parasitic shunt capacitance has a noticeable effect on the coil impedance at high frequencies but a correction has been applied to the data as in [119]. Finally, the effective value of coil lift-off and tube conductivity have been determined by fitting the measurement data with the calculation based on the theoretical model for a rotary coil inside the tube [83, 93, 118]. Figure 5.11 shows the multifrequency impedance data from both theoretical calculation and the corrected measurement data. We also plotted the same data on the impedance plane as shown in Fig. 5.12. In our theoretical model, the effective value of coil lift-off is 1.235 mm and the tube conductivity is 0.84 MS/m.

The coil impedance change due to the crack was measured as the z -coordinate of the coil was varied incrementally as it passed symmetrically over the notch. The scan was carried out at 25 kHz, 50 kHz, 100 kHz, 150 kHz, and 200 kHz, respectively. Again, the measurement data have been corrected for capacitance effects [119] and the background signals have also been removed from the corrected data to leave only the impedance due to the notch.



(a)



(b)

Figure 5.11: Normalized resistance change (a) and reactance change (b) of a rotary coil inside an unflawed tube as a function of frequency. Both the theoretical result (o) and the corrected measurement data (+) are plotted.

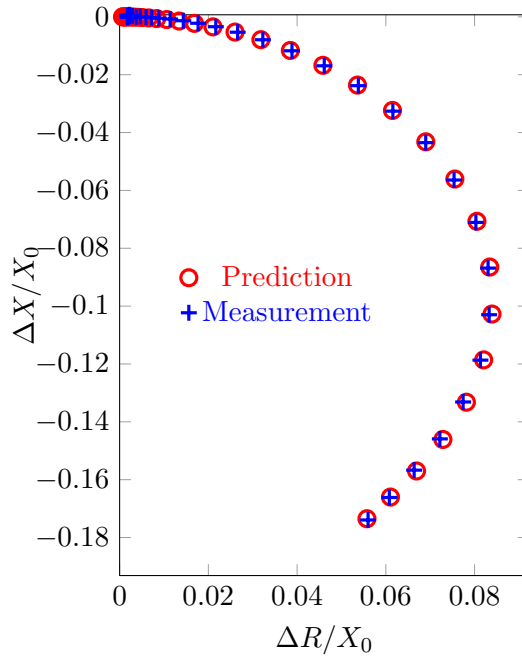


Figure 5.12: Normalized impedance change of a rotary coil inside an unflawed tube as a function of frequency on the impedance plane. Both the theoretical result (○) and the corrected measurement data (+) are plotted.

5.7.4 Dipole Density over Crack Surface

The electric current dipole distribution is also plotted here to verify our result. Figure 5.13 shows the electric current dipole distribution over the crack surface calculated from (4.66) for a through-wall longitudinal notch in a tube with the parameters listed in Table 5.2.

5.7.5 Through-Wall Notch in a Tube

The theoretical prediction of the through-wall notch in the tube mentioned before has been calculated at five different frequencies. It only takes a few minutes to do the calculation for each frequency. The results are presented in Figs. 5.14–5.18. All the notch measurement data, including both resistance change and reactance change, are also plotted in Figs. 5.14–5.18 for reference.

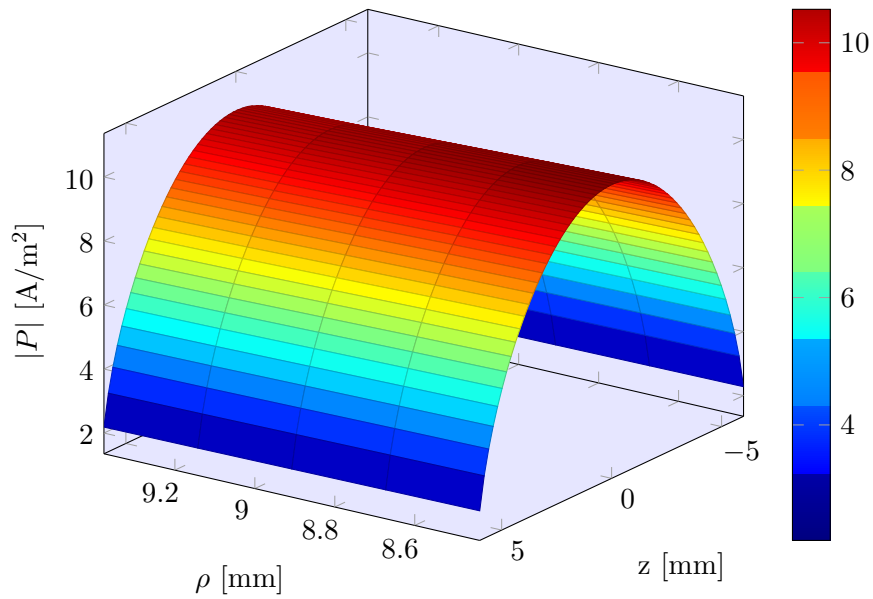
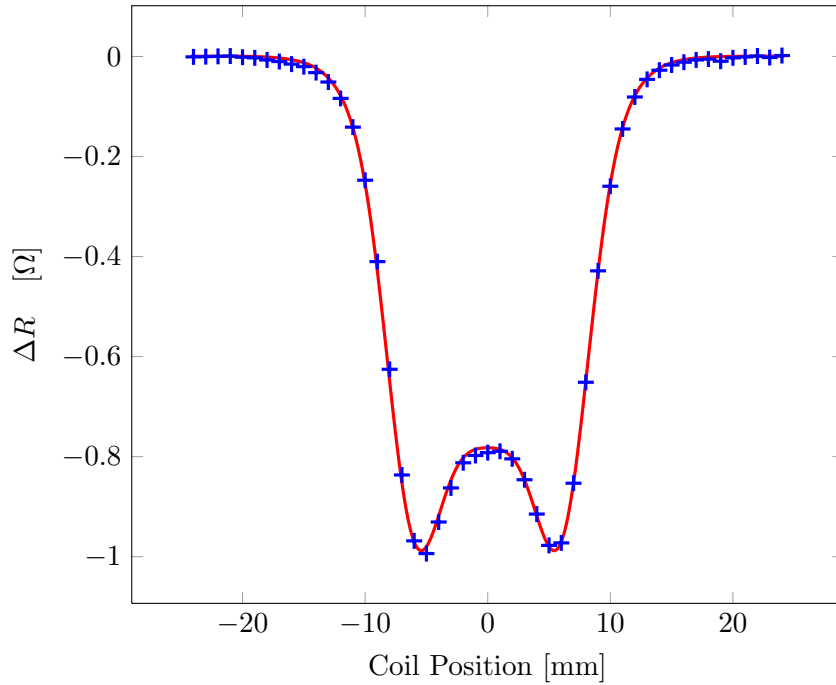


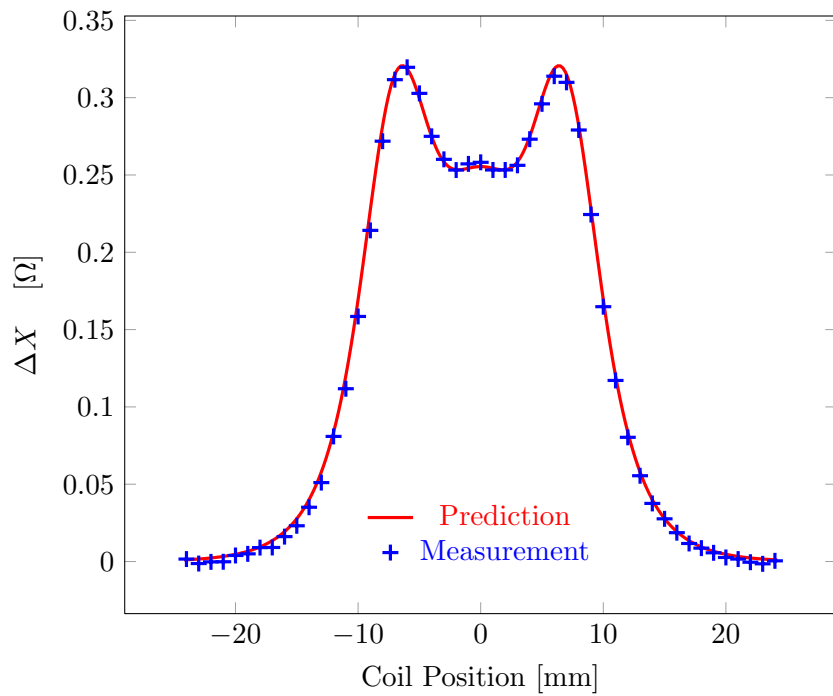
Figure 5.13: Electric current dipole density over a through-wall notch in a tube.

5.8 Summary

The crack model presented in Chapter 4 is extended to the model for a crack in a tube. This is achieved by considering the multiple reflection due to the multilayered structure. To prevent the numerical overflows in the calculation, some normalizing factors are introduced in our formulation. The interaction between TE and TM modes are considered in the matrix expression. The theoretical model is validated with the plate problems. A comparison of impedance predictions and measurements shows good agreement for a through-wall notch in the tube at multiple operating frequencies. In both cases, the program shows good performance. The calculation only takes a few minutes.

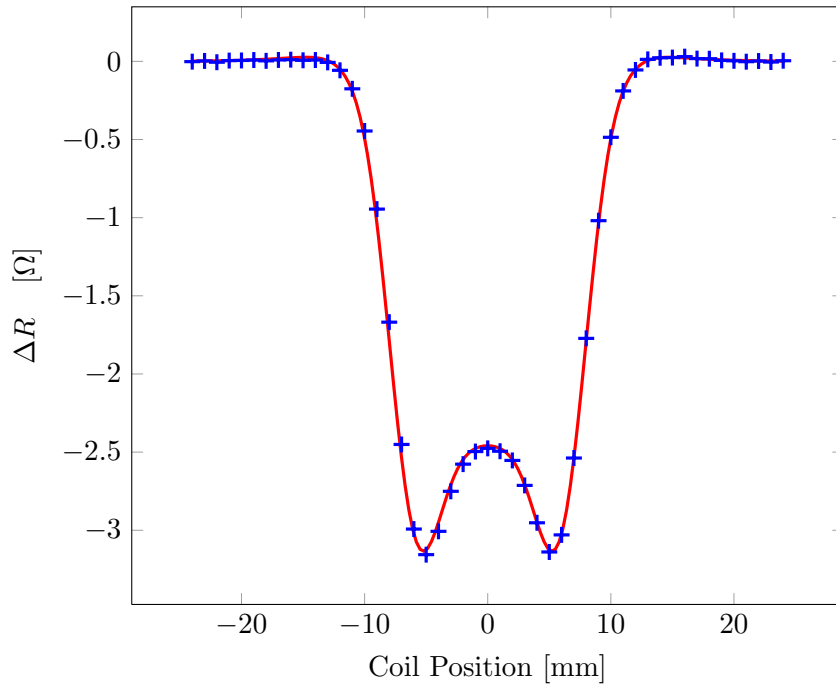


(a)

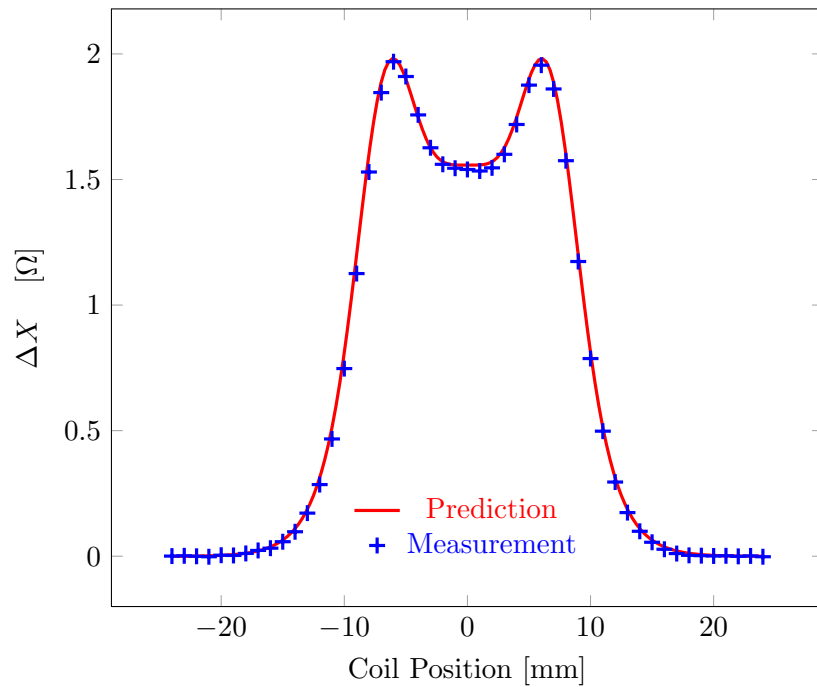


(b)

Figure 5.14: Change in (a) coil resistance, ΔR and (b) coil reactance, ΔX due to the longitudinal notch as a function of coil center position at frequency 25 kHz.

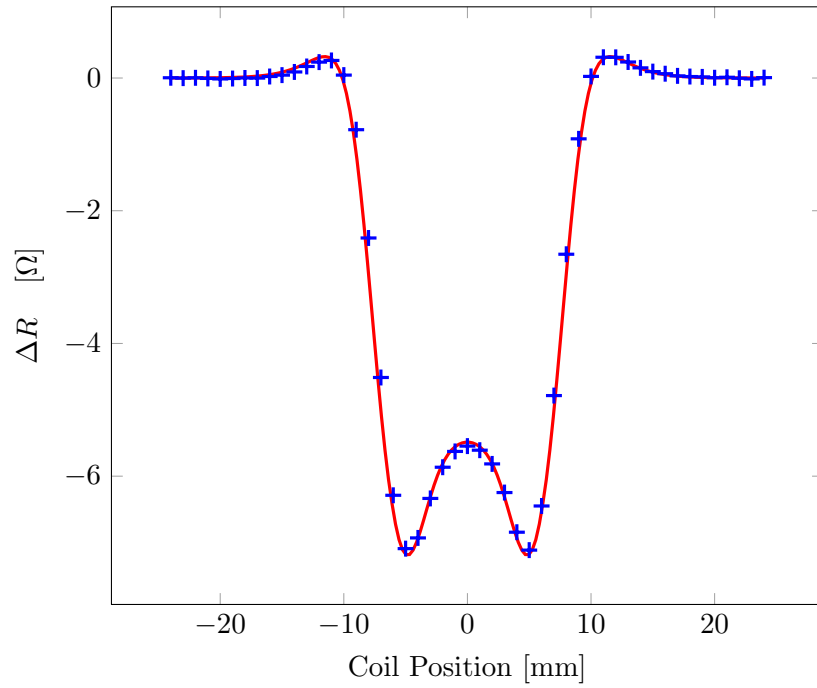


(a)

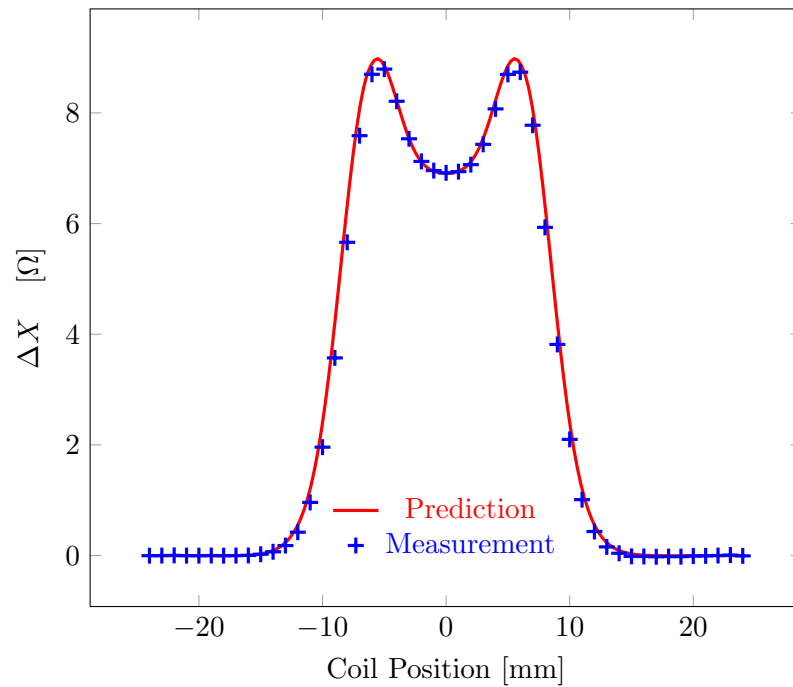


(b)

Figure 5.15: Change in (a) coil resistance, ΔR and (b) coil reactance, ΔX due to the longitudinal notch as a function of coil center position at frequency 50 kHz.

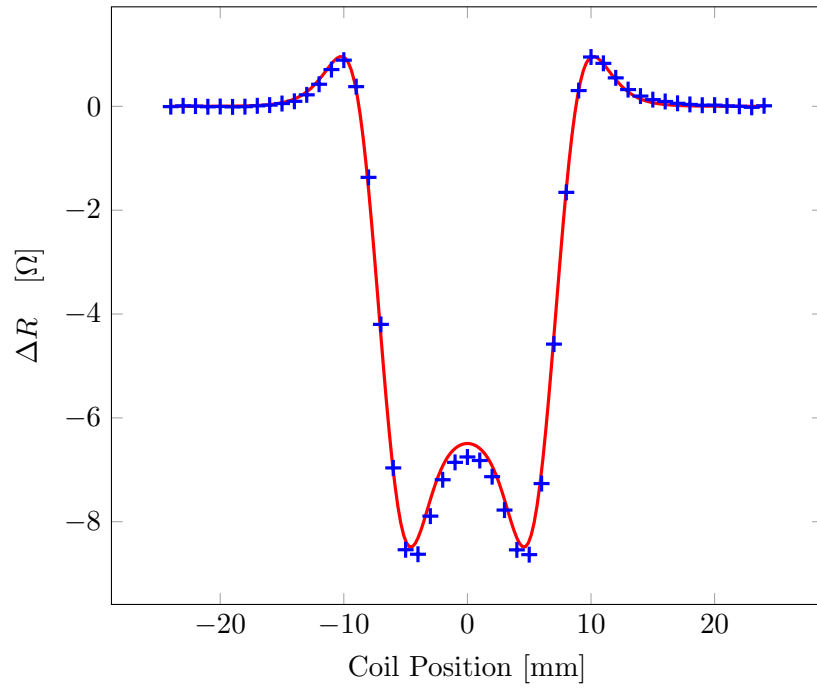


(a)

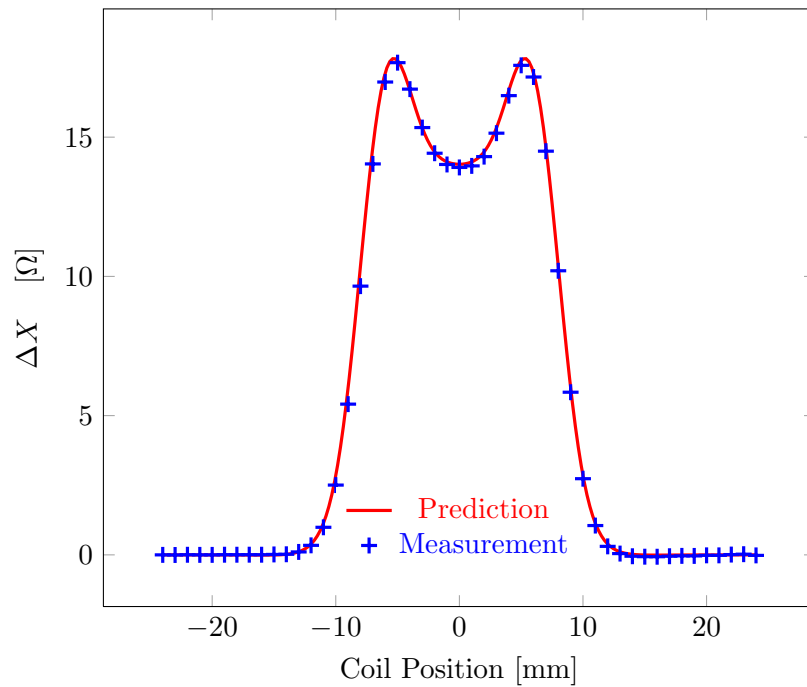


(b)

Figure 5.16: Change in (a) coil resistance, ΔR and (b) coil reactance, ΔX due to the longitudinal notch as a function of coil center position at frequency 100 kHz.

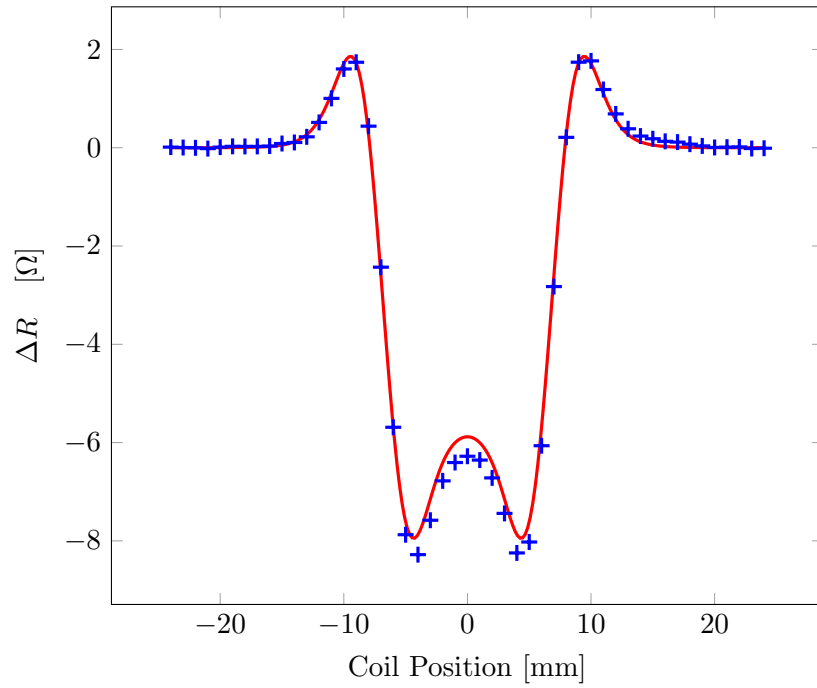


(a)

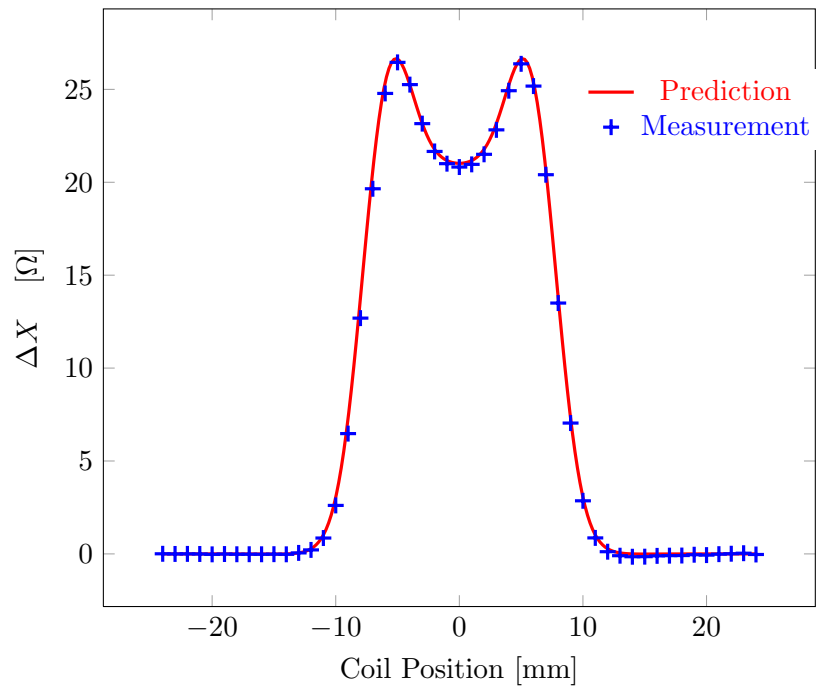


(b)

Figure 5.17: Change in (a) coil resistance, ΔR and (b) coil reactance, ΔX due to the longitudinal notch as a function of coil center position at frequency 150 kHz.



(a)



(b)

Figure 5.18: Change in (a) coil resistance, ΔR and (b) coil reactance, ΔX due to the longitudinal notch as a function of coil center position at frequency 200 kHz.

CHAPTER 6. COILS AT THE OPENING OF A BOREHOLE IN A CONDUCTOR

In this chapter, we estimate the impedance changes of coils at the opening of a borehole in a conductor and compute the induced eddy currents adjacent to the crack free edge as the incident field for the crack calculation. There is no closed-form analytical solution for this problem, and TREE method is applied. The solution representing the coil field at the edge of the hole is expanded into series form. Matrix equations are derived to solve for the expansion coefficients. The difficulty of this problem is that boundary conditions have to be satisfied at two surfaces which intersect with each other. The result shows this approach is accurate and computationally efficient. Theodoulidis and Bowler have solved the coil impedance change with the same approach [94]. An improved model is presented to remove the zero order terms from the earlier model and thereby simplify the analysis. This approach can be further extended to a coil in a hole through a plate and other layered structures.

6.1 Introduction

The edge of a borehole is a critical region because the cracks in a conductor commonly occur around stress concentrations at the edges. Here, the interaction of an eddy-current coil with the opening of a borehole in a half-space conductor is considered. Our analysis provides a foundation for tackling the more complicated problem of a countersunk hole [7, 9].

Both the coil impedance change and the incident field due to a coil around the borehole opening are calculated. According to the model for ideal or narrow cracks using volume integral method, this work can be viewed as a part in the process of evaluating the crack signal, the incident field calculation. In addition, the approach presented here can be extended to derive an

appropriate Green's function for the electric field generated by a singular electric dipole source near the borehole opening, which is the critical step for the crack modeling via an integral equation formulation. This approach is presented in the next chapter. It also can be adapted for the related problem of calculating the fields, such as a coil inside a hole through a planar layered structure.

We consider an induction coil at the opening of a semi-infinite borehole in a conductor, Fig. 6.1. For this problem, there is no closed-form solution, but an approximate analytical solution can be found by applying the TREE method. Here, the domain of the borehole problem is truncated in the axial direction of a cylindrical polar coordinate system. As discussed before, we expand the axial dependence in terms of Fourier series. However, the eigenvalues, which represent the eigenmodes supported by the truncated structure, don't have simple forms as before because of the non-uniform domain in the axial direction. The expansion coefficients are determined from a system of matrix equations derived using the continuity conditions of the field at the radial interface defined by extending the surface of the hole over the entire vertical length of the domain. This problem can be also solved by numerical methods. Compared to the general numerical methods, such as finite element method and method of moments, our

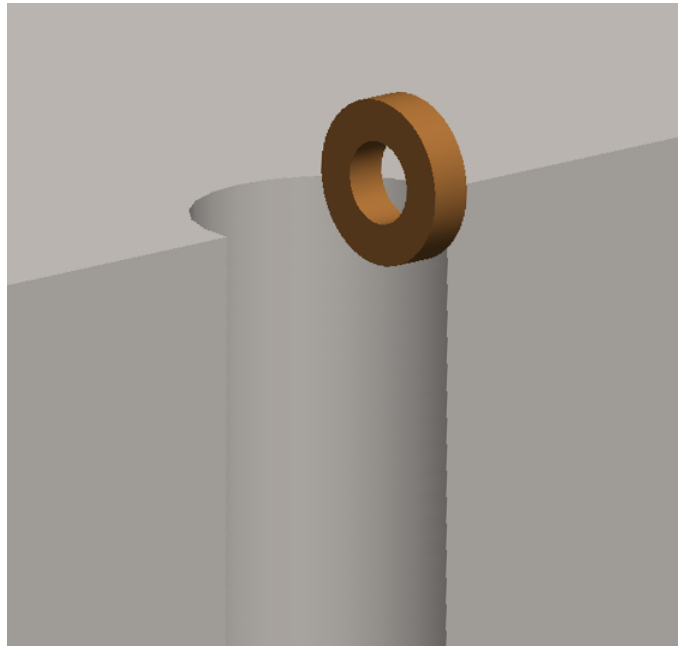


Figure 6.1: A rotary coil at the opening of a borehole.

approach is computationally efficient and the accuracy of the results can be easily controlled [29].

The impedance change due to a rotary coil at the edge of a hole can be calculated by matching the modes across the cylindrical interface between different regions of the problem. We eliminate the zero order expansion in [94] by applying different truncation boundary conditions in the method presented in this chapter. As a result, the solution is simplified and the computation efficiency is improved. Due to the exponential decay of the eddy current inside the conductor, this problem is potentially ill-conditioned. In our method, however, a boundary condition at the borehole surface is used to overcome this difficulty. On the other hand, because of the limited precision of the calculation, the effect of the numerical overflow has to be avoided by normalizing the expansion coefficients to restrict their numerical range. The normalization is also helpful to ameliorate the potential problems with ill-conditioned matrices.

Here we examine the calculation of the field of an arbitrary coil carrying a current varying as the real part of $Ie^{-\omega t}$ in a cylindrical hole within a domain which is finite in the axial direction, Fig. 6.1. The electromagnetic fields at the edge of the hole are derived and the change in coil impedance is calculated. Expressions for both bobbin coil and rotary coil are discussed.

6.2 Formulation

The initially infinite domain problem is truncated in the axial direction to limit the axial coordinate range to $0 \leq z \leq h$, Fig. 6.2. By locating the coil sufficiently far from the upper and lower boundaries, the truncation error can be set at a tolerable level. Instead of the magnetic field, the magnetic flux density is expressed in terms of scalar potentials

$$\mathbf{B} = \nabla \times \nabla \times (\hat{z}W_a) + k^2 \nabla \times (\hat{z}W_b), \quad (6.1)$$

where $k^2 = \omega\mu_0\sigma$. The electric field is given by

$$\mathbf{E} = \omega [\nabla \times \hat{z}(W_a) + \nabla \times \nabla \times \hat{z}(W_b)]. \quad (6.2)$$

Both For the conductive region, both of the potentials satisfy the Helmholtz equation

$$(\nabla^2 + k^2)W = 0. \quad (6.3)$$

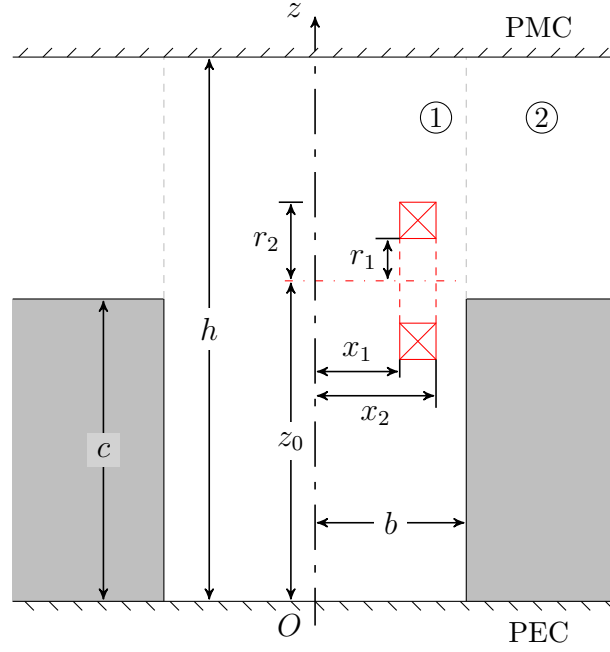


Figure 6.2: A rotary coil at the opening of a borehole in a conductor.

Equation (6.3) is reduced to the Laplace equation for the nonconductive region for which $k = 0$.

The same Fourier series representation with respect to the azimuthal angle is used here

$$W(\rho, \phi, z) = \sum_{m=-\infty}^{\infty} \tilde{W}_m(\rho, z) e^{im\phi}. \quad (6.4)$$

For convenience, in this chapter, we redefine the scalar potentials as

$$\psi_m = \frac{\partial \tilde{W}_{am}}{\partial z}, \quad \text{and} \quad \varphi_m = k^2 \tilde{W}_{bm} \quad (6.5)$$

to represent the TE and TM modes, respectively. According to (6.1) and Appendix A, the components of the magnetic field are given by

$$\tilde{B}_{\rho m} = \frac{\partial \psi_m}{\partial \rho} + \frac{im}{\rho} \varphi_m, \quad (6.6)$$

$$\tilde{B}_{\phi m} = \frac{im}{\rho} \psi_m - \frac{\partial \varphi_m}{\partial \rho}, \quad (6.7)$$

$$\tilde{B}_{zm} = \frac{\partial \psi_m}{\partial z} + k^2 \tilde{W}_{am}. \quad (6.8)$$

In the nonconductive region $\mathbf{B} = \nabla \psi$.

6.2.1 Formal Solution

By using the separation of variables method, Fourier transform of the solution in (6.3), $\tilde{W}_m(\rho, z)$ can be written as a product of two functions, $g_m(\rho)$ and $f_m(z)$. For the conductive region, these functions have the form

$$\begin{aligned} g_m(\rho) &= A_m(\kappa)I_m(v\rho) + B_m(\kappa)K_m(v\rho), \\ f_m(z) &= C_m(\kappa)\sin(\kappa z) + D_m(\kappa)\cos(\kappa z), \end{aligned} \quad (6.9)$$

where variables, κ and v have the relationship

$$v^2 = \kappa^2 - k^2. \quad (6.10)$$

The unknown coefficients, $A_m(\kappa)$, $B_m(\kappa)$, $C_m(\kappa)$ and $D_m(\kappa)$ are determined by applying the boundary conditions at the interface between region 1 and region 2.

In general, the zero order term

$$(A_0\rho^m + B_0\rho^{-m}) [C_0 \sinh(kz) + D_0 \cosh(kz)],$$

should be included for a complete solution. For the nonconductive regions, we have the similar solution to those in (6.9) and (6.10) with $\kappa = v$, but the zero order term has the form

$$(A_0\rho^m + B_0\rho^{-m}) (C_0 + D_0z).$$

As we discussed in Chapter 2, the solution for an infinite region can be represented as an integral over a continuous spectra [118]. Because of the truncation in the axial direction, however, the solution $\tilde{W}_m(\rho, z)$ is expressed as a summation, rather than an integral, with u having discrete values. With truncation conditions at boundaries $z = 0$ and $z = h$, the field solution within $0 \leq z \leq h$ is represented as a periodic function in the axial direction. The series expression is equivalent to the Fourier series transform of this periodic function, as shown in Fig. 4.4.

The zero order term is needed if we impose the same conditions on these two boundaries. However, it can be eliminated if two different truncation conditions are imposed on the boundaries. As before, we impose PEC condition at $z = 0$ and PMC condition at $z = h$. It follows from the latter condition that the normal component of the magnetic flux density at the boundary $z = 0$ is zero.

We construct a formal solution for each homogeneous region first based on the general solution given in (6.9). The superscript (0) and (1) represent the source field in the absence of conductors and the field due to induced current, respectively. The total field in region 1 is the superposition of these two parts. For the region 2, $\rho > b$ ($0 \leq z \leq h$), the fields are denoted by the superscript (2). Continuity conditions are then applied to determine the unknown expansion coefficients at the radial interface. Finally the results are obtained from the prescribed source coefficient for a given coil.

The transformed TE and TM potentials that satisfy both the Helmholtz equation and the truncation boundary conditions at $z = 0$ and $z = h$ are formulated as follows. In region 1, the transformed TE source potential outside the outer radial limit of the of the probe coil, $\rho_c < \rho \leq b$ can be written as

$$\psi_m^{(0)}(\rho, z) = \sum_{i=1}^{\infty} \frac{K_m(\kappa_i \rho)}{K_m(\kappa_i b)} \cos(\kappa_i z) C_{mi}^{(0)}, \quad (6.11)$$

where the normalizing factor $K_m(u_i b)$ is used to simplify the expressions for the matrix equations derived from the continuity properties of the field at the radial boundary $\rho = b$. The coefficients, $C_{mi}^{(0)}$ are prescribed for a given source coil current. The transformed TE potential due to induced current has the form

$$\psi_m^{(1)}(\rho, z) = \sum_{i=1}^{\infty} \frac{I_m(\kappa_i \rho)}{I_m(\kappa_i b)} \cos(\kappa_i z) C_{mi}^{(1)}. \quad (6.12)$$

The cosine function in (6.11) and (6.12) ensures that $B_z = 0$ at $z = 0$. Putting $\kappa_i = (2i-1)\pi/2h$, $i = 1, 2, \dots$ ensures that $\psi_m = 0$ and $\partial\psi_m/\partial\rho = 0$ at $z = h$.

For region 2 ($\rho \geq b$), the transformed TE potential can be written as

$$\psi_m^{(2)}(\rho, z) = \begin{cases} \sum_{i=1}^{\infty} \frac{K_m(v_i \rho)}{K_m(v_i b)} \frac{\cos(\alpha_i z)}{\cos(\alpha_i c)} C_{mi}^{(2)}, & 0 \leq z \leq c \\ \sum_{i=1}^{\infty} \frac{K_m(v_i \rho)}{K_m(v_i b)} \frac{\sin[v_i(h-z)]}{\sin[v_i(h-c)]} C_{mi}^{(2)}, & c \leq z \leq h \end{cases} \quad (6.13)$$

where the eigenvalues v_i and α_i satisfy

$$v_i^2 = \alpha_i^2 - k^2. \quad (6.14)$$

It is clear that (6.13) and (6.14) satisfy the truncation boundary conditions and the normalizing factors containing c ensure the continuity of the tangential magnetic field at the interface $z = c$.

Again, the factor $K_m(v_i b)$ is used to simplify the matrix equation. Applying the continuity of the normal magnetic flux density, B_z , at $z = c$ for region 2, from (6.13) we have that

$$\frac{\cos[v_i(h-c)]}{\sin[v_i(h-c)]} = \frac{v_i \sin(\alpha_i c)}{\alpha_i \cos(\alpha_i c)}. \quad (6.15)$$

We can find the complex eigenvalues v_i and α_i by solving this complex transcendental equation with (6.14). For a given ratio c/h , it is only necessary to compute these eigenvalues once since the equation is independent of m . Discussions of the root finding algorithm will be given later. The eigenvalues α_i consist of two branches, Fig. 6.3. Because v_i and α_i are complex numbers, the z dependence of the field in (6.13) becomes exponentially large when the eigenvalue α_i is increased with i . Factors containing c are used to normalize the sine or cosine functions, which prevents numerical overflow and makes the coefficient matrix, which will be defined later, well-conditioned.

The two branches of the eigenvalues in Fig. 6.3 represent two kinds of modes existing in the truncated half space. This is similar to the modes supported by the shielded microstrip. As shown in Fig. 6.4, the first type is related to the modes supported without the PMC truncation boundary condition on the top. The wave in the air decays as the region goes to infinite far away from the conductor. The second type is corresponding to the case where the PEC truncation condition is removed and the field in the air oscillates due to the existence of the truncation boundary at $z = h$. With this explanation, the initial guess of the eigenvalues q_i can be started from two limiting cases. We will discuss the details in Section 6.5.1.

For the conductive region, we also need Fourier transform of the TM potential and it can be written as

$$\varphi_m(\rho, z) = \sum_{i=1}^{\infty} \frac{K_m(\gamma_i \rho)}{K_m(\gamma_i b)} \cos(\beta_i z) D_{mi}, \quad 0 \leq z \leq c \quad (6.16)$$

where $\gamma_i^2 = \beta_i^2 - k^2$. Letting $\beta_i = (2i-1)\pi/2c$ ensures that the normal component of the current at the horizontal surface of the conductor, approached from within it, is zero. The zero order term which corresponds to a transverse electric and magnetic (TEM) mode, must vanish due to the continuity of H_ϕ at $z = c$ ($\rho \geq b$).

This completes the formal stage of the development and the continuity requirements at the horizontal plane, $z = c$, are all satisfied. Each term in the formal solution represents a

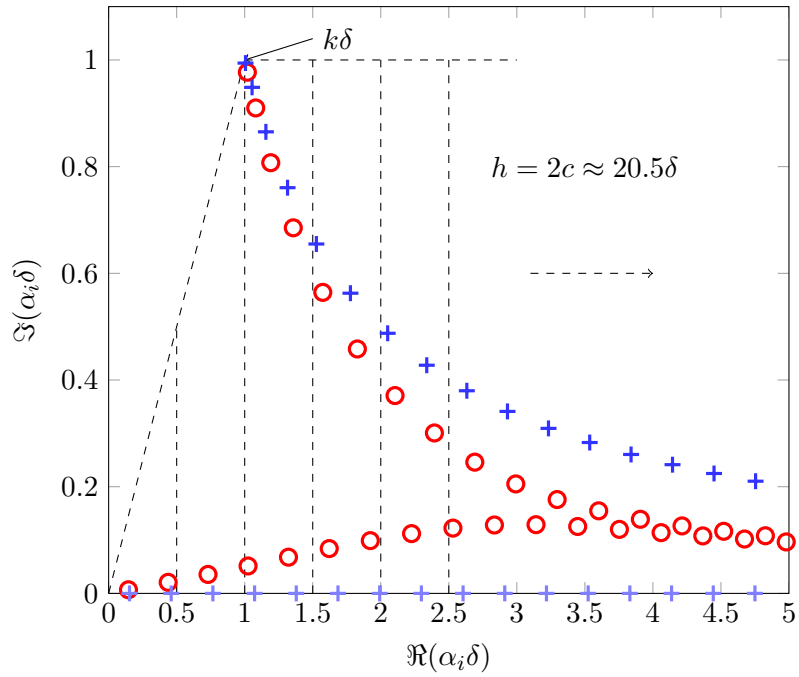


Figure 6.3: The spectrum of complex eigenvalues, α_i for $c = h/2$ (o). The eigenvalues in two extreme cases for a homogeneous domain with truncation length $h/2$ are also plotted (+). All the values are normalized by multiplying the skin depth δ .

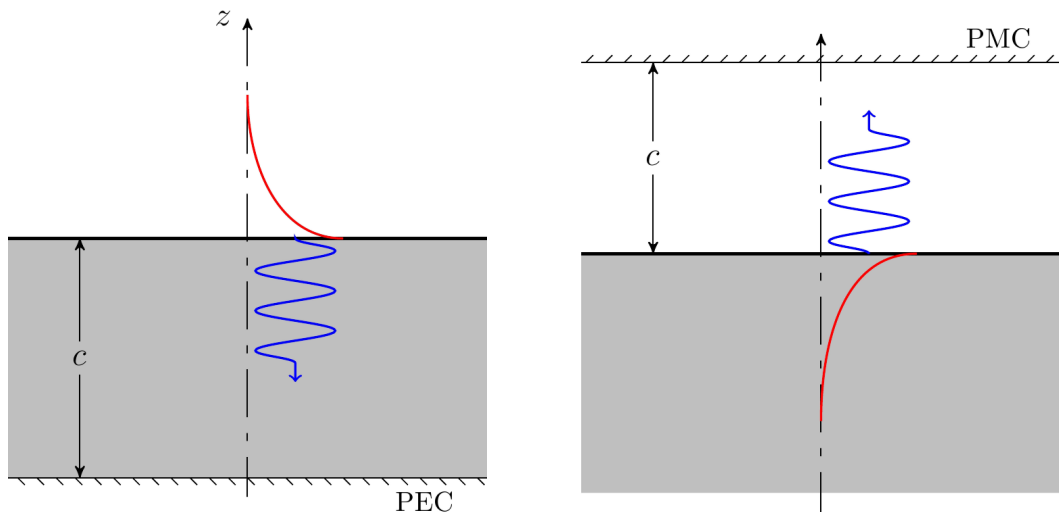


Figure 6.4: Two kinds of modes are supported in the truncated half space. They are corresponding to the two branches of the eigenvalues in Fig. 6.3.

mode supported in the corresponding region. To find the expansion coefficients, $C_{mi}^{(1)}$, $C_{mi}^{(2)}$ and D_{mi} , we impose the appropriate continuity conditions that govern the fields at the radial $\rho = b$ between region 1 and region 2 as follows.

6.2.2 Continuity at the Radial Interface

In order to set up the matrix equation to solve the expansion coefficients, we approximate above infinite series as a summation over finite number of terms, N_i . The source coefficients, $C_{mi}^{(0)}$, which can be derived from the expansion of the coil field in the nonconductive region, will be given later. Because the modes are different in each region, the continuity of the tangential magnetic field and the normal component of the magnetic flux density are applied in the weak sense for the cylindrical boundary $\rho = b$ extending from $z = 0$ to $z = h$. Matrix equations for the three sets of unknown coefficients are found by matching $H_z \sin(\kappa_i z)$, $H_\phi \cos(\kappa_i z)$, and $B_\rho \cos(\kappa_i z)$ at the boundary $\rho = b$, integrated between 0 and h . Applying trigonometric function orthogonality relations,

$$\int_0^h \sin(\kappa_j z) \sin(\kappa_i z) dz = \frac{h}{2} \delta_{ij}, \quad (6.17)$$

and

$$\int_0^h \cos(\kappa_j z) \cos(\kappa_i z) dz = \frac{h}{2} \delta_{ij}, \quad (6.18)$$

we obtain the following matrix equations

$$\boldsymbol{\kappa} \left[\mathbf{C}_m^{(0)} + \mathbf{C}_m^{(1)} \right] = \mathbf{M}_s \mathbf{v} \mathbf{C}_m^{(2)}, \quad (6.19)$$

$$im \left[\mathbf{C}_m^{(0)} + \mathbf{C}_m^{(1)} \right] = im \mathbf{M}_c \mathbf{C}_m^{(2)} - \mathbf{M}_r \mathbf{M}_m(\boldsymbol{\gamma} b) \mathbf{D}_m, \quad (6.20)$$

$$\mathbf{M}_m(\boldsymbol{\kappa} b) \mathbf{C}_m^{(0)} + \Lambda_m(\boldsymbol{\kappa} b) \mathbf{C}_m^{(1)} = \mathbf{M}_c \mathbf{M}_m(\mathbf{v} b) \mathbf{C}_m^{(2)} + im \mathbf{M}_r \mathbf{D}_m. \quad (6.21)$$

where functions $\Lambda_m(z)$ and $\mathbf{M}_m(z)$ are defined in (4.51). The bold symbols $\mathbf{C}_m^{(0)}$, $\mathbf{C}_m^{(1)}$, and $\mathbf{C}_m^{(2)}$ are column vectors of expansion coefficients, whereas \mathbf{u} , \mathbf{v} , $\boldsymbol{\gamma}$, $\mathbf{M}_m(\boldsymbol{\kappa} b)$, etc. are $N_i \times N_i$ diagonal matrices. Other matrices in (6.19)-(6.21), \mathbf{M}_s , \mathbf{M}_c and \mathbf{M}_r , have elements defined by

$$\mathbf{M}_s[i, j] = \frac{2}{h} \left[\int_0^c \frac{v_j \sin(\alpha_j z)}{\alpha_j \cos(\alpha_j c)} \sin(\kappa_i z) dz + \int_c^h \frac{\cos[v_j(h-z)]}{\sin[v_j(h-c)]} \sin(\kappa_i z) dz \right], \quad (6.22)$$

$$\mathbf{M}_c[i, j] = \frac{2}{h} \left[\int_0^c \frac{\cos(\alpha_j z)}{\cos(\alpha_j c)} \cos(\kappa_i z) dz + \int_c^h \frac{\sin[v_j(h-z)]}{\sin[v_j(h-c)]} \cos(\kappa_i z) dz \right], \quad (6.23)$$

$$\mathbf{M}_r[i, j] = \frac{2}{h} \int_0^c \cos(\kappa_i z) \cos(\beta_j z) dz. \quad (6.24)$$

Evaluating the integrals with the relationship (6.15) leads to the results as

$$\mathbf{M}_s[i, j] = \frac{2k^2 v_j}{h(\kappa_i^2 - \alpha_j^2)(\kappa_i^2 - v_j^2)} \left\{ \sin(\kappa_i c) - \frac{\kappa_i \sin(\alpha_j c)}{\alpha_j \cos(\alpha_j c)} \cos(\kappa_i c) \right\}, \quad (6.25)$$

$$\mathbf{M}_c[i, j] = \frac{2k^2 \kappa_i}{h(\kappa_i^2 - \alpha_j^2)(\kappa_i^2 - v_j^2)} \left\{ \sin(\kappa_i c) - \frac{\kappa_i \sin(\alpha_j c)}{\alpha_j \cos(\alpha_j c)} \cos(\kappa_i c) \right\}, \quad (6.26)$$

and

$$\mathbf{M}_r[i, j] = \frac{c}{h} \{ \text{sinc}[(\kappa_i + \beta_j)c] + \text{sinc}[(\kappa_i - \beta_j)c] \}, \quad (6.27)$$

where the sinc function is defined as

$$\text{sinc}(x) = \frac{\sin(x)}{x}. \quad (6.28)$$

From (6.25) and (6.26), we know that matrix \mathbf{M}_s has a similar structure as \mathbf{M}_c .

We can solve for the expansion coefficients, $C_{mi}^{(1)}$, $C_{mi}^{(2)}$ and D_{mi} , using the matrix equations (6.19)–(6.21) for a given source coefficient $C_{mi}^{(0)}$. However, because the matrix equations tend to be potentially ill-conditioned in our method, special procedure is adopted to get a stable solution. The discussion will be given in Section 6.4.

6.2.3 Impedance Change near a Borehole Opening

It has been shown, using reciprocity theorem, that coil impedance change due to an induced current can be calculated using an integral over a surface enclosing the coil [82]. Taking the surface to be a cylinder with radius b and expressing the integrand in terms of magnetic scalar potentials gives

$$\Delta Z = \frac{\omega}{\mu_0 I^2} \int_0^h \int_{-\pi}^{\pi} \left[\psi^{(1)} \frac{\partial \psi^{(0)}}{\partial \rho} - \psi^{(0)} \frac{\partial \psi^{(1)}}{\partial \rho} \right]_{\rho=b} b d\phi dz. \quad (6.29)$$

By substituting for $\psi^{(0)}$ and $\psi^{(1)}$ from (6.11) and (6.12) into (6.29) and using the Wronskian

$$I'_m(z)K_m(z) - I_m(z)K'_m(z) = \frac{1}{z}, \quad (6.30)$$

we get the general expression for the impedance change of a coil in a borehole and a truncated domain

$$\Delta Z = \frac{i\omega\pi h}{\mu_0 I^2} \sum_{m=-\infty}^{\infty} \sum_{i=1}^{\infty} \frac{C_{mi}^{(0)} C_{mi}^{(1)}}{I_m(\kappa_i b) K_m(\kappa_i b)}, \quad (6.31)$$

where $C_{mi}^{(0)}$ is given by (D.11) for the case of a rotary coil and (D.14) for the case of an bobbin coil except it should have an extra factor $K_m(\kappa_i b)$ included. The coefficients, $C_{mi}^{(1)}$, are determined from (6.19)-(6.21).

The differential bobbin coil consists of two separate bobbin coils with opposite current excitation is also considered here, Fig. 6.5. The source coefficients for the differential bobbin coil can be constructed using the addition theorem. Assuming the coils have the same size and the separation between these two coils is d_0 , the source coefficients for this differential bobbin coil can be expressed as

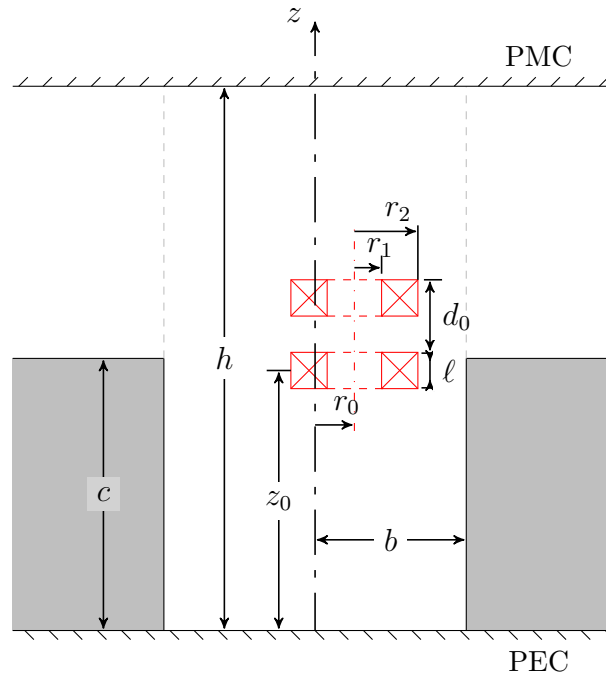


Figure 6.5: A differential bobbin coil at the opening of a borehole in a conductor.

$$\begin{aligned}
C_{mi}^{(0)} &= C_{mi}^{(10)} - C_{mi}^{(20)} \\
&= \frac{8\mu_0\nu I}{h\kappa_i^3} \Phi(\kappa_i r_2, \kappa_i r_1) K_m(\kappa_i b) I_m(\kappa_i r_0) \sin\left(\frac{\kappa_i \ell}{2}\right) \sin\left(\frac{\kappa_i d_0}{2}\right) \cos(\kappa_i z_0^d). \quad (6.32)
\end{aligned}$$

Here, z_0^d is the axial position of the probe center. Coefficients, $C_{mi}^{(10)}$ and $C_{mi}^{(20)}$, represent the source coefficients for each coil. This completes the determination of the source coefficients for a differential bobbin coil.

The impedance change of a differential coil can be written as

$$\Delta Z = \frac{\omega\pi h}{\mu_0 I^2} \sum_{m=-\infty}^{\infty} \sum_{i=1}^{\infty} \frac{[C_{mi}^{(10)} - C_{mi}^{(20)}] [C_{mi}^{(11)} + C_{mi}^{(21)}]}{I_m(\kappa_i b) K_m(\kappa_i b)}, \quad (6.33)$$

where $C_{mi}^{(11)}$ is the reflection coefficients due to one of the coils and $C_{mi}^{(12)}$ due to another one. From reciprocity theorem, we know that

$$C_{mi}^{(10)} C_{mi}^{(21)} = C_{mi}^{(20)} C_{mi}^{(11)}. \quad (6.34)$$

By substituting it into (6.33), we have

$$\begin{aligned}
\Delta Z &= \frac{\omega\pi h}{\mu_0 I^2} \sum_{m=-\infty}^{\infty} \sum_{i=1}^{\infty} \frac{C_{mi}^{(10)} C_{mi}^{(11)} - C_{mi}^{(20)} C_{mi}^{(21)}}{I_m(\kappa_i b) K_m(\kappa_i b)} \\
&= \Delta Z^{(1)} - \Delta Z^{(2)}. \quad (6.35)
\end{aligned}$$

Therefore, the impedance change of a differential probe can also be easily obtained from the results of a single coil by subtracting the impedance change at one position from the one at another position and the distance between these two positions is d_0 . These two methods are equivalent to each other.

6.3 Incident Field Calculation

As mentioned before, we need to compute the eddy current density inside the conductor as the incident field for the crack modeling with volume element method. Once the expansion coefficients are calculated, Fourier transform of the electric field in conductive region ($0 \leq z \leq c$

and $\rho \geq b$) can be calculated as from (6.2)

$$\tilde{E}_{\rho m}(\rho, z) = \omega \left(\frac{vm}{\rho} \tilde{W}_{am} + \frac{\partial^2 \tilde{W}_{bm}}{\partial \rho \partial z} \right), \quad (6.36)$$

$$\tilde{E}_{\phi m}(\rho, z) = \omega \left(-\frac{\partial \tilde{W}_{am}}{\partial \rho} + \frac{vm}{\rho} \frac{\partial \tilde{W}_{bm}}{\partial z} \right), \quad (6.37)$$

$$\tilde{E}_{zm}(\rho, z) = \omega \left(\frac{\partial^2}{\partial z^2} + k^2 \right) \tilde{W}_{bm}. \quad (6.38)$$

Eddy current in the conductor is given by $\mathbf{J} = \sigma \mathbf{E}$ and, therefore, the expression for each component is given by

$$\tilde{J}_{\rho m}(\rho, z) = -\omega \sigma \sum_{i=1}^{\infty} \frac{m K_m(v_i \rho)}{\rho K_m(v_i b)} \frac{\sin(\alpha_i z)}{\alpha_i \cos(\alpha_i c)} C_{mi}^{(2)} + \frac{v}{k^2} \frac{K'_m(\gamma_i \rho)}{K_m(\gamma_i b)} \beta_i \gamma_i \sin(\beta_i z) D_{mi}, \quad (6.39)$$

$$\tilde{J}_{\phi m}(\rho, z) = -\omega \sigma \sum_{i=1}^{\infty} \frac{K'_m(v_i \rho)}{K_m(v_i b)} \frac{v_i \sin(\alpha_i z)}{\alpha_i \cos(\alpha_i c)} C_{mi}^{(2)} + \frac{vm}{\rho k^2} \frac{K_m(\gamma_i \rho)}{K_m(\gamma_i b)} \beta_i \sin(\beta_i z) D_{mi}, \quad (6.40)$$

$$\tilde{J}_{zm}(\rho, z) = -\frac{1}{\mu_0} \sum_{i=1}^{\infty} \frac{K_m(\gamma_i \rho)}{K_m(\gamma_i b)} \gamma_i^2 \sin(\beta_i z) D_{mi}. \quad (6.41)$$

The expansion coefficients, $C_{mi}^{(2)}$ and D_{mi} , are calculated from (6.19)-(6.21).

6.4 Discussion on the Ill-Conditioned Matrices

One of the improvements in the current method is that we introduced the normalizing factor, $\cos(\alpha_i c)$ for $0 \leq z \leq c$ and $\sin[v_i(h - c)]$ for $c \leq z \leq h$ in (6.13). Without these normalizing factors, the matrices \mathbf{M}_s and \mathbf{M}_c have a large condition number. For example, in the case we will present later, the order of magnitude of these condition numbers is around 10^{20} . The inverse of these matrices is required to solve the matrix equations. This might cause an inaccuracy of the final results [120]. We can reduce these large condition numbers into 10^3 with the normalizing factors in (6.13).

In general, we choose a relatively large truncation range h and make $c = h/2$ so that the truncation boundaries have slight influence on the final results. However, there is a numerical issue associated with these parameter choices when we try to solve the matrix equations (6.19)-(6.21). Unlike \mathbf{M}_s and \mathbf{M}_c , matrix \mathbf{M}_r still has an extremely large condition number even after normalizing factor is introduced. Here, \mathbf{M}_r is only related to \mathbf{D}_m . It is not stable to solve \mathbf{D}_m

directly from this ill-conditioned matrix system, although we could obtain correct solutions for $\mathbf{C}_m^{(1)}$ and $\mathbf{C}_m^{(2)}$ by solving (6.19)-(6.21). Therefore, it is sufficient to get the impedance change from above solution, but it fails for the incident field calculation in which the coefficient \mathbf{D}_m is needed.

By relating the TE and TM modes in the conductive region, we utilize another boundary condition at the borehole surface to overcome this ill-conditioned problem. We can find the relationship between expansion coefficients $\mathbf{C}_m^{(2)}$ and \mathbf{D}_m based on the boundary condition that normal component of eddy current inside the conductor should be zero at the borehole interface $\rho = b$ for $0 \leq z \leq c$. We obtain a different matrix equation by integrating $E_\rho \sin(\beta_i z)$ between 0 and c at the boundary $\rho = b$. By applying

$$\int_0^c \sin(\beta_j z) \sin(\beta_i z) dz = \frac{c}{2} \delta_{ij}, \quad (6.42)$$

we get the matrix equation

$$i\beta \mathbf{M}_m(\gamma b) \mathbf{D}_m = -mk^2 \mathbf{M}_t \mathbf{C}_m^{(2)}, \quad (6.43)$$

where the elements of matrix \mathbf{M}_t is defined as

$$M_t[i, j] = \frac{2}{c} \int_0^c \frac{\cos(\alpha_j z)}{\cos(\alpha_j c)} \cos(\beta_i z) dz. \quad (6.44)$$

Once $\mathbf{C}_m^{(2)}$ is solved, \mathbf{D}_m can be easily obtained from (6.43) without inverting any ill-conditioned matrix. Substituting all the coefficients into (6.39)-(6.41), we can obtain the incident field accurately.

6.5 Numerical Algorithm for Complex Eigenvalue Calculation

6.5.1 Complex Eigenvalues

In order to ensure that numerical results are accurate, a reliable method for computing complex eigenvalues satisfying (6.15) is needed [121]. Some of the algorithms which work well for the real root search might not be suitable here. However, there are still several ways to calculate the eigenvalues numerically for a complex equation like $f(z) = 0$.

The first one is to extend the bisection method to the complex roots. For an equation defined on the real domain, a zero is located in an interval, in which the function has opposite signs at the two ends. For a complex function $f(z)$, the phase of the function can be considered and the cross point of four quadrants should be the zero point, Fig. 6.6. The other way is to calculate the reciprocal of $f(z)$ and observe the magnitude of function $1/f(z)$. The point with infinite large value is the zero location. Applying these two methods to our eigenvalue problem, Fig. 6.7 shows the order of magnitude of function $1/|f(z)|$ and the phase plot of $f(z)$. These two methods can be used to find the root through visualization. To get the accurate eigenvalues, we have to resort to other methods.

6.5.2 Newton-Raphson Method

Most of the root search method requires the initial values. As discussion in Section 6.2.1, we can get a good initial guess by considering two limiting cases depending on the value of c . One is from the eigenvalues satisfying if $\cos[v_i(h - c)] = 0$ and another one is the eigenvalues from $\cos(\alpha_i c) = 0$. The limiting cases generate two sets of eigenvalues, in one set the values are real and positive and the other set starts close to k on the complex plane and tends toward

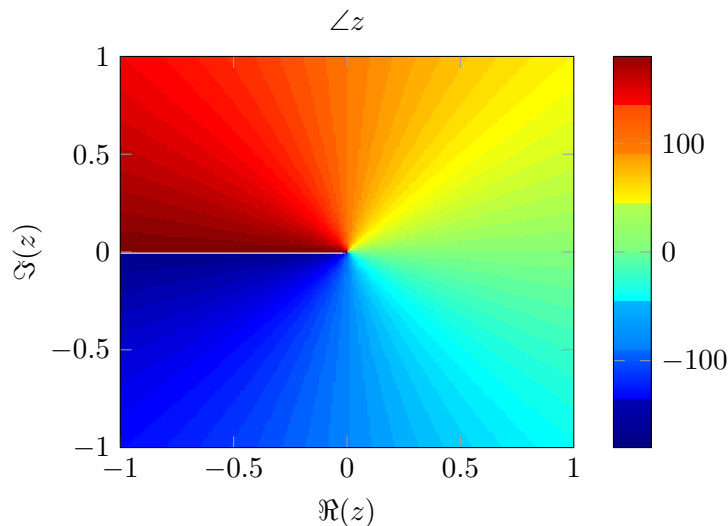


Figure 6.6: The phase of the function $f(z) = z$ on the complex plane. The phase of a complex function can be used to search the root of corresponding equation.

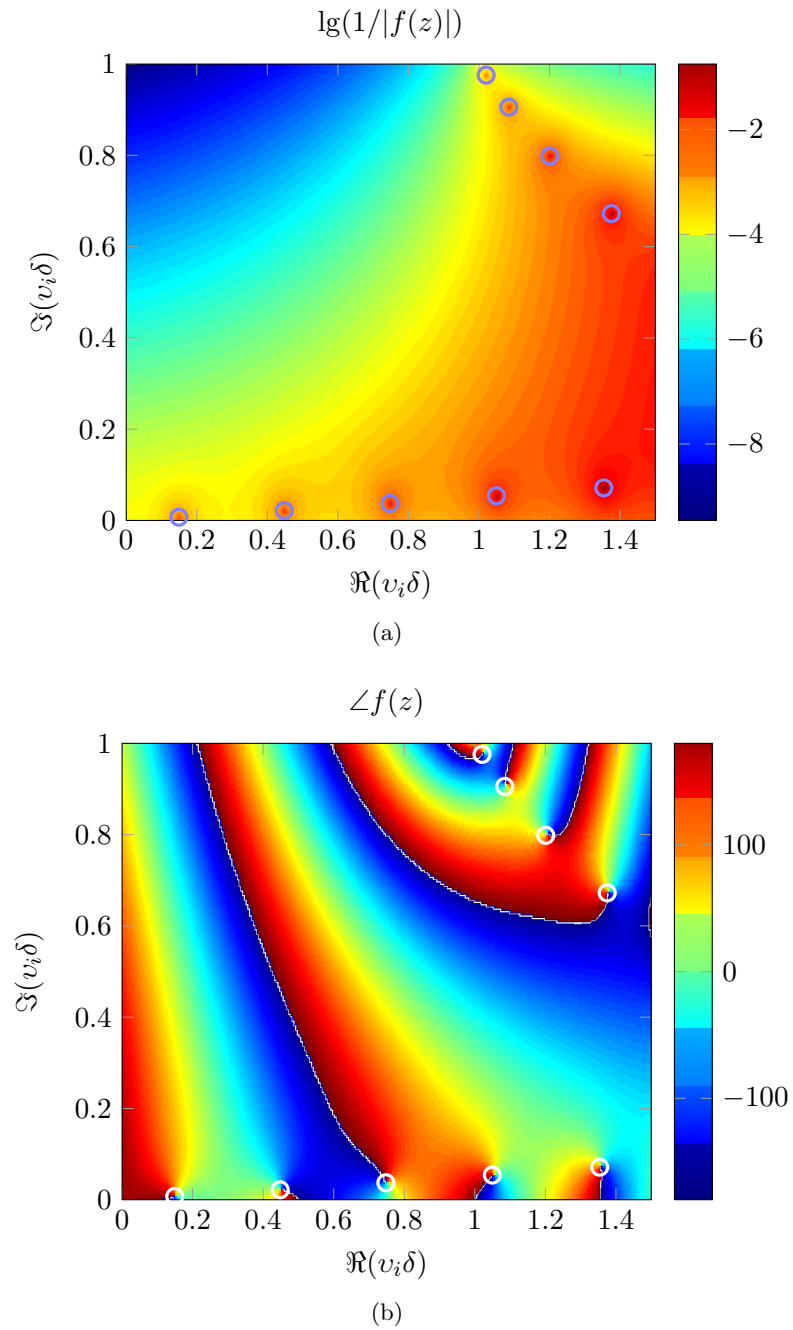


Figure 6.7: The order of magnitude of the function $1/|f(z)|$ (a) and the phase of function $f(z)$ (b) for the eigenvalue problem discussed in this chapter.

κ_i , Fig. 6.3. At intermediate values of c one gets a hybridization of the two sets in which one set is dominant depending on whether c is large or small. With these initial guess, the Newton-Raphson method can be applied to our problem. Newton-Raphson method does not require the derivative of the function, which makes the method much easier to apply.

6.5.3 Lyness Algorithm

Another robust method for locating initial estimate of the q_i is one based on a procedure given by Delves and Lyness [122]. The method has been applied to the eigenvalue calculation for the eddy-current interaction with a right-angle conductive wedge [31]. The key step uses Cauchy's theorem to test whether a pole or several poles of a given function lies in a prescribed region of the complex plane. By finding the poles of a function, we could implicitly locate the reciprocal of zeros. Thus if C is a closed contour in the complex plane which dose not pass through a zero of $f(z)$, using Cauchy's theorem, we can have that

$$\sigma_n = \frac{1}{2\pi i} \oint_C z^n \frac{f'(z)}{f(z)} dz = \sum_{i=1}^N \nu_i^n, \quad n = 1, 2, \dots, N \quad (6.45)$$

where $f(z)$ is an analytic function inside and on the contour C enclosing region R and the summation is over the enclosed poles. In addition, ν_i^n are the zeros of $f(z)$ in R raised to the n -th power. The path integral, evaluated for $n = 0$ gives the number of zeros of $f(z)$ enclosed by contour C

$$\sigma_0 = \frac{1}{2\pi i} \oint_C \frac{f'(z)}{f(z)} dz = \sum_{i=1}^N \nu_i^0 = N. \quad (6.46)$$

A numerical integration inevitably gives rise to errors but we only need compute with sufficient accuracy to identify unambiguously the integer N . It is best to work with at most a few poles in each region, say three or fewer, and if N exceeds the chosen limit, we can simple shrink the region R to capture fewer poles. One strategy that may be adapted is to choose a region of integration small enough that there is only one pole in it. Then it is easy to locate it accurately.

If there are several poles in R and the number of poles N can be obtained from σ_0 , we only need to calculate $\sigma_1, \sigma_2, \dots, \sigma_N$ to locate them by constructing the N -th order polynomial $P(z)$ [123]. For example, if $N = 1$ we have

$$P(z) = z - \sigma_1,$$

with a root ν_1 , whereas if $N = 2$ we have

$$P(z) = z^2 - \sigma_1 z + \frac{\sigma_1^2 - \sigma_2}{2},$$

with roots ν_1 and ν_2 . One can find the roots of higher order polynomials via a number of available techniques but they tend to decrease in efficiency and accuracy as N increases. The polynomial $P(z)$ does not approximate the function $f(z)$, it simply has the same roots as the function in R . Hence, we actually replace the problem of finding the zeros for a given analytic function $f(z)$ in region R with the one of finding the zeros of a given polynomial $P(z)$ in the same region. The above method allows us to find several roots simultaneously, thus avoiding the need to isolate zeros which may be difficult when they are close together or tightly grouped in the complex plane.

For borehole edge, all the eigenvalues are located in the area between the dashed horizontal line and the real axis in Fig. 6.3, we employ the above scheme and search the area by dividing it into subareas with a trapezoidal or rectangular shape as appropriate. In each subarea we calculate the complex roots by computing the repeated integrals of (6.45) along its bounding path. The procedure continues up to a certain maximum $\Re\{\alpha_i\}$ or when the maximum set number of eigenvalues has been reached. The path integrals need not be computed with great accuracy since they are used to compute initial estimates of the zeros prior to refinement using the Newton-Raphson routine.

6.6 Results

6.6.1 Coil Impedance Change at Borehole Opening

We compute both coil impedance change and incident fields using MATLAB for a rotary coil near the borehole edge. The parameters are listed in Table 6.1. Similar truncation criterion for h and N_i is used to ensure the accuracy of the results. Usually 60 terms in the series expansion are used in both orders and modes. The variation of normalized impedance change of a rotary coil as a function of axial position at a fixed frequency $f = 10$ kHz is shown in Fig. 6.8. The normalizing factor is the isolated coil reactance $X_0 = \omega L_0$, where the self-inductance L_0 is

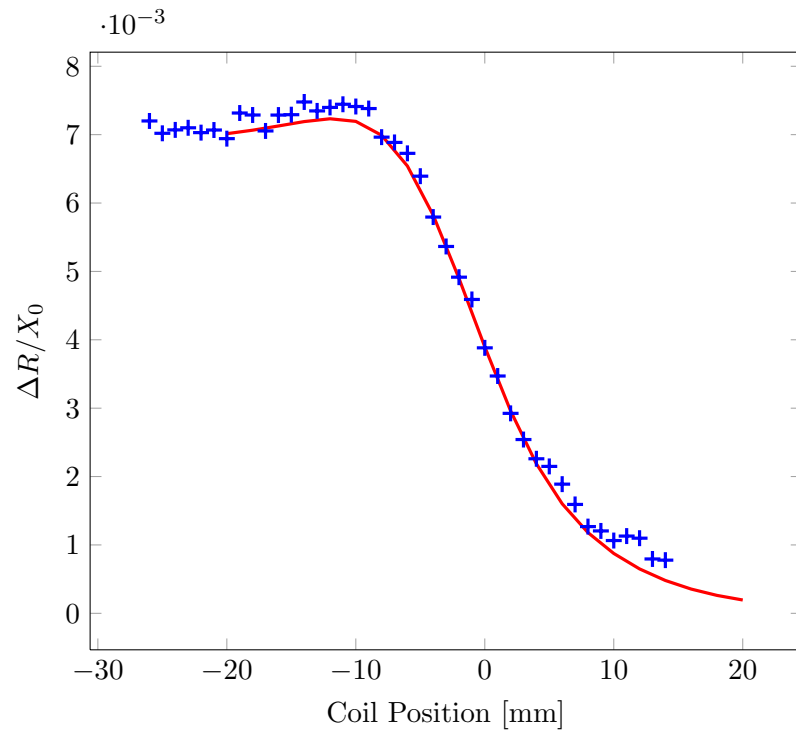
Table 6.1: Coil and borehole parameters for a coil around the opening of a borehole. The configurations are shown in Fig. 6.2 for a rotary coil and Fig. 6.5 for a differential bobbin coil, respectively.

Coil	
Inner radius (r_1)	6.95 mm
Outer radius (r_2)	9.35 mm
Length (ℓ)	6.70 mm
Number of turns (N)	335
Lift-off for rotary coil ($b - x_2$)	7.67 mm
Offset for bobbin coil (r_0)	4.1 mm
Test Specimen	
Borehole radius (b)	20 mm
Conductivity (σ)	24.36 MS/m
Relative permeability (μ_r)	1
Other Parameters	
Frequency (f)	10 kHz
Skin depth at 10 kHz (δ)	1.02 mm
Isolated coil induction (L_0)	1.745 mH

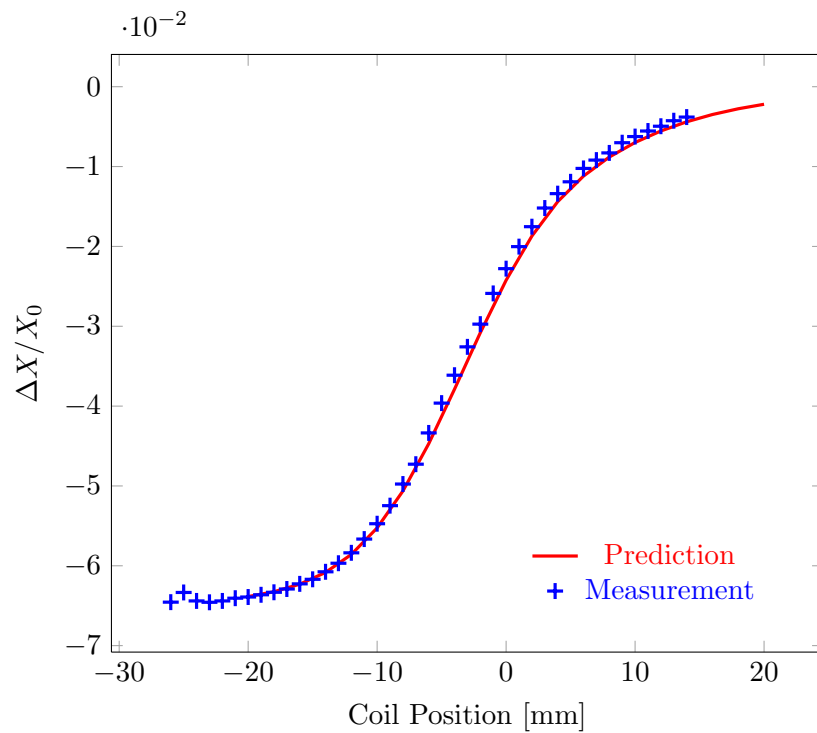
1.754 mH. The prediction shows a good agreement with the experimental measurement as before. The measurements were conducted by Rob Ditchburn of DSTO, Melbourne, Australia.

The impedance change of an offset bobbin coil and a differential probe near the borehole edge are also computed. In order to check our theory, we compared the prediction with the measurements done by Ditchburn. The variation of normalized impedance change as a function of axial position at $f = 10$ kHz is shown in Fig. 6.9. The coil parameters are listed in Table 6.1.

Based on the results for a single bobbin coil, the impedance change of a differential probe with coil separation $d_0 = 10$ mm is calculated at four different frequencies as the probe scans along the axial direction, Fig. 6.10. The differential signal goes to zero when the differential coil far away from the borehole edge or at the depth of the borehole. For a fixed frequency, the impedance change varies dramatically when the coil is near the borehole edge. At low frequency with large skin depth the impedance changes slowly as the coil is moved along the axial direction, while the coil impedance varies faster at high frequency. The same results could be obtained using both of the approaches mentioned in Section 6.2.3.

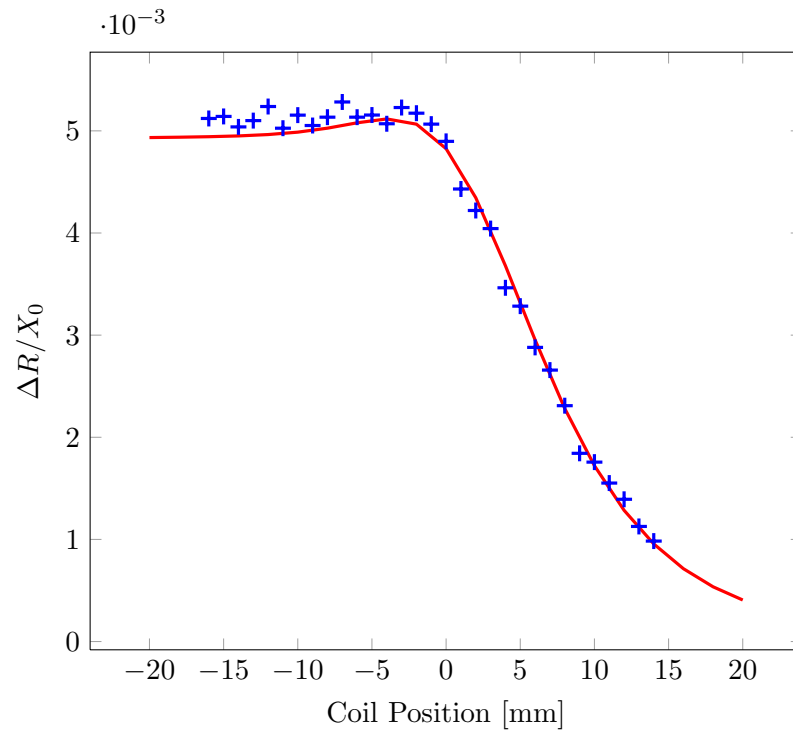


(a)

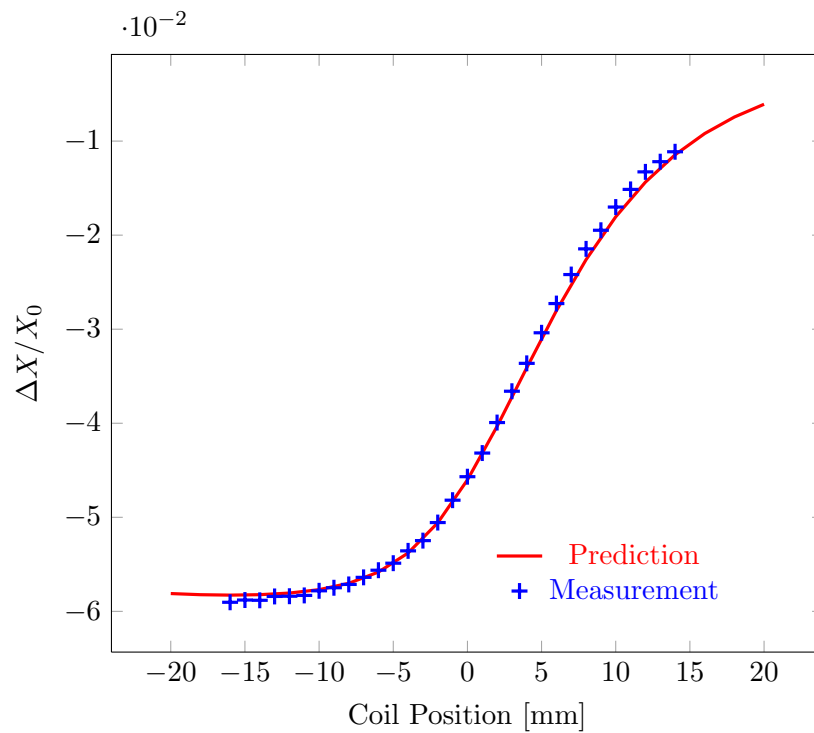


(b)

Figure 6.8: Coil resistance change (a) and reactance change (b) of a rotary coil as a function of the axial position. The experiments were conducted at 10 kHz.



(a)



(b)

Figure 6.9: Variation of the normalized resistance change (a) and reactance change (b) of an bobbin coil as a function of the axial position with respect to the edge of the borehole opening at a fixed frequency 10 kHz.

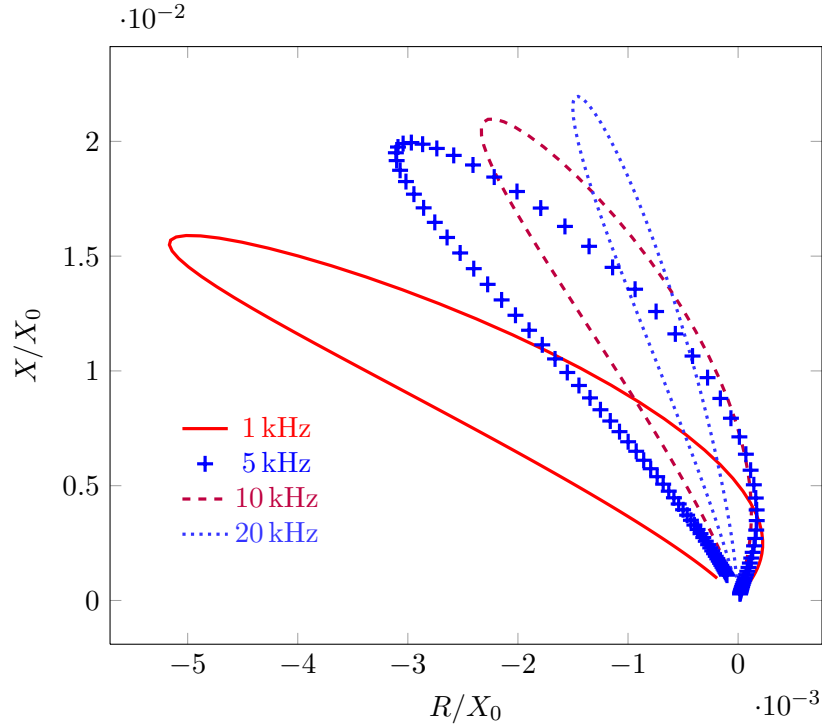


Figure 6.10: Normalized impedance plane plot for a differential probe around the edge of borehole at four different frequencies, 1 kHz, 5 kHz, 10 kHz, and 20 kHz.

6.6.2 Current Distribution around a Borehole Edge

Eddy current distribution inside the conductor is presented in Figs. 6.11 and 6.12. Figure 6.12 shows the azimuthal component of eddy-current density for three coils positions on the plane $\phi = 0^\circ$: 9.35 mm, 0 mm, and -9.35 mm. The operating frequency is 500 Hz. The result shows how the eddy-current distribution changes and the amplitude decreases as the coil moves away from the edge. In order to verify the boundary conditions, Fig. 6.11 is used to show the radial, and axial components of the eddy current density at the plane $\phi = 0^\circ$ for the coil position $z_0 = c$ with $f = 500$ Hz. Apparently, the normal component of the current is getting to zero as the point approaches to the conductor boundary for both $z = c$ and $\rho = b$ surface, respectively.

The computation time for each coil position is only a few seconds and it could be further reduced by using more efficient functions to evaluate the source coefficients, $\mathbf{C}_m^{(0)}$ for the rotary coil.

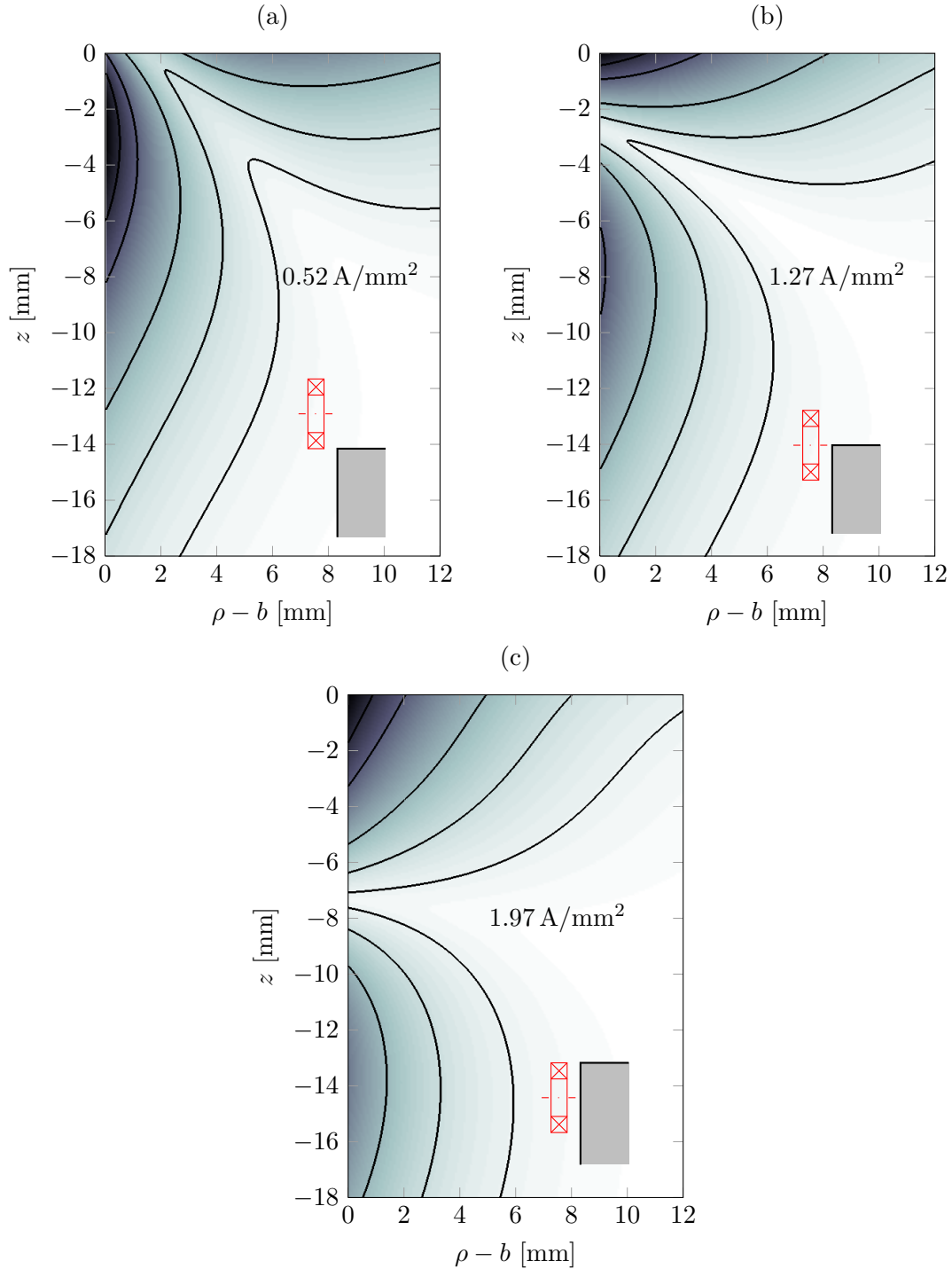


Figure 6.11: Amplitude contours of azimuthal component of eddy-current density for three coil positions at the $\phi = 0^\circ$ plane: 9.35 mm (a), 0 mm (b), and -9.35 mm (c). The numbers in each graph show the maximum amplitude. The frequency is 500 Hz .

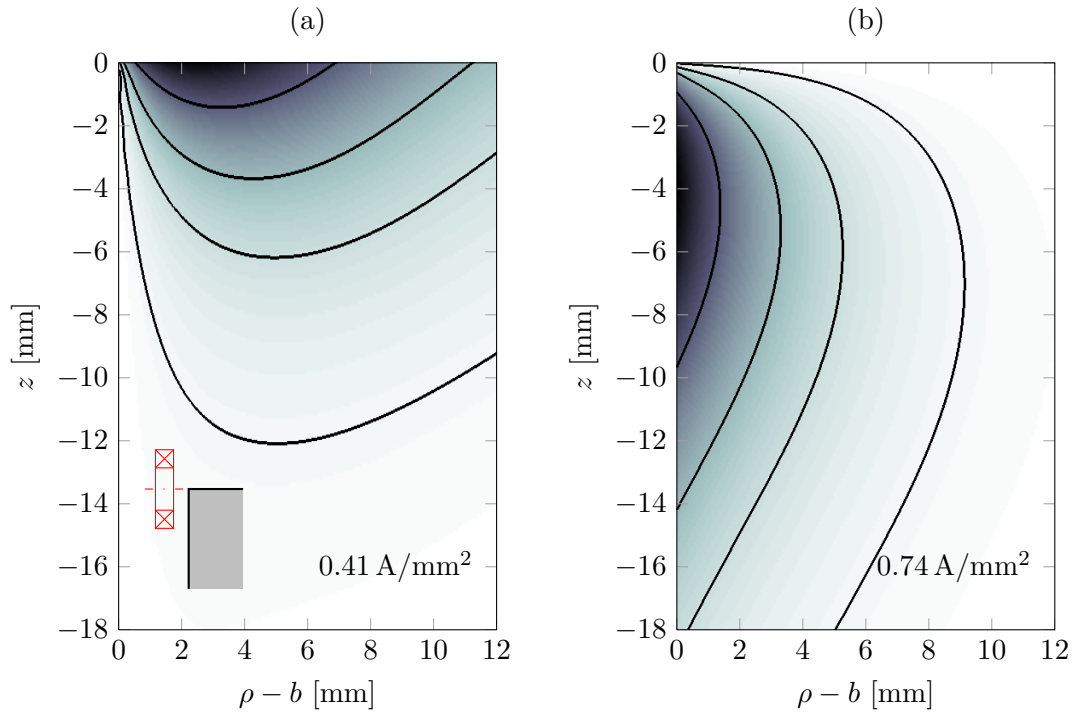


Figure 6.12: Amplitude contours of radial (a) and axial (b) component of eddy-current density at the $\phi = 0^\circ$ plane. The coil located is at the edge of the conductor. The numbers in each graph show the maximum amplitude. The frequency is 500 Hz.

6.7 Summary

The interaction of a coil with the opening of a borehole is formulated using TREE method. To get a stable solution for the current fields, the problem is reformulated with an improved closed-form expression so that the final matrix equations have a small condition number. The zero order term is eliminated by adopting different truncation boundary conditions. We investigate the matrix property of the matrix equations in our method to make sure the correction of the final results.

Numerical algorithms are discussed for the calculation of the complex eigenvalues used in the formulation. The impedance change due to a rotary coil and a bobbin coil is computed and the results are compared with experimental measurements. Good agreement is obtained. The current distribution is plotted to verify the boundary conditions. The eddy-current fields calculated in this chapter can be used as the incident field in the corresponding crack problem. The fields are also can be used as the incident field for the thin skin theory, a different method

which is potentially efficient for the crack calculation.

CHAPTER 7. COIL IMPEDANCE CHANGE DUE TO CORNER CRACKS

The impedance change of an induction coil due to cracks around the opening of a borehole is formulated in this chapter. The basic crack model is the same as that demonstrated in Chapter 4. The current field calculated from Chapter 6 can be used as the incident field for this crack problem. In boerhole model, the configuration is homogeneous in the axial direction and the situation is different for this problem, in which the medium becomes inhomogeneous in the axial direction and eigenvalues don't have simple forms. In order to derive the Green's function for a point source around the opening of a borehole, we combine the crack model presented in Chapter 4 and the approach developed in Chapter 6. The reflection coefficients have to be modified to take care the wave interaction with two surfaces which intersect with each other. In our method, this is an important step for the coil signal estimation of the fastener inspection. The theoretical model is developed, even though we have not completed the program so far. Here, we present the derivation of the Green's function used in the volume integral method. The associated difficulties of the problem are discussed at the end.

7.1 Introduction

The coil impedance change due to a crack around the opening of a borehole is considered, Fig. 7.1. A longitudinal crack lies near the borehole open end. The conductor has the permeability of free space, μ_0 and the conductivity, σ_0 . A coil, which carries a current varying as the real part of $Ie^{-\omega t}$, introduces the alternating magnetic field into the cracked conductor. The incident field calculation is provided in the last chapter. For this configuration, the crack model is the same as before and we only derive the Green's kernel used in the volume element

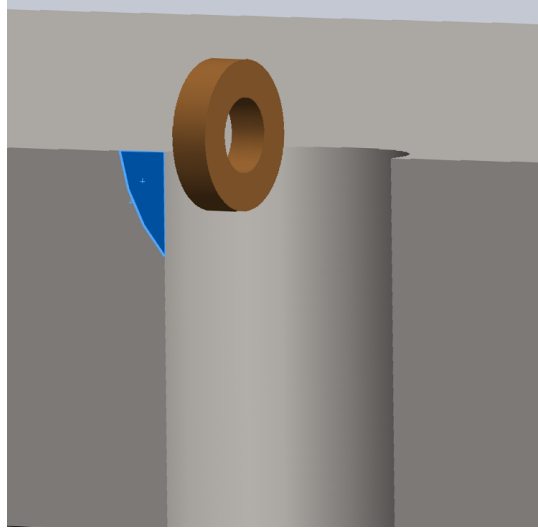


Figure 7.1: A rotary pancake coil is used to inspect a crack near the opening of a borehole.

method for a point source around the boerhole opening.

We have presented the use of scalar decomposition for crack problems in Chapter 4 and the same formulation is used here. For convenience, the time factor $\exp(-i\omega t)$ is suppressed and the fields and potential variables are all expressed in terms of the Fourier series

$$W(\rho, \phi, z) = \sum_{m=-\infty}^{\infty} \tilde{W}_m(\rho, z) e^{im\phi}. \quad (7.1)$$

For the source free region, the magnetic field has a scalar representation like

$$\mathbf{H} = \nabla \times \nabla \times (\hat{z}W_a) + k^2 \nabla \times (\hat{z}W_b), \quad (7.2)$$

and the electric field can be expressed as

$$\mathbf{E} = i\omega\mu[\nabla \times (\hat{z}W_a) + \nabla \times \nabla \times (\hat{z}W_b)], \quad (7.3)$$

where $k^2 = i\omega\mu\sigma_0$. From (7.2), the Fourier transform of the magnetic fields is given by

$$\tilde{H}_{\rho m} = \frac{\partial^2 \tilde{W}_{am}}{\partial \rho \partial z} + k^2 \frac{im}{\rho} \tilde{W}_{bm}, \quad (7.4)$$

$$\tilde{H}_{\phi m} = \frac{im}{\rho} \frac{\partial \tilde{W}_{am}}{\partial z} - k^2 \frac{\partial \tilde{W}_{bm}}{\partial \rho}, \quad (7.5)$$

$$\tilde{H}_{zm} = \left(\frac{\partial^2}{\partial z^2} + k^2 \right) \tilde{W}_{am}, \quad (7.6)$$

and, from (7.3), Fourier transform of the electric fields has the form

$$\tilde{E}_{\rho m} = i\omega\mu \left(\frac{im}{\rho} \tilde{W}_{am} + \frac{\partial^2 \tilde{W}_{bm}}{\partial \rho \partial z} \right), \quad (7.7)$$

$$\tilde{E}_{\phi m} = -i\omega\mu \left(\frac{\partial \tilde{W}_{am}}{\partial \rho} - \frac{im}{\rho} \frac{\partial \tilde{W}_{bm}}{\partial z} \right), \quad (7.8)$$

$$\tilde{E}_{zm} = i\omega\mu \left(\frac{\partial^2}{\partial z^2} + k^2 \right) \tilde{W}_{bm}. \quad (7.9)$$

The Green's function, which satisfies

$$(\nabla^2 + k^2) \begin{bmatrix} G_{aa} & G_{ab} \\ G_{ba} & G_{bb} \end{bmatrix} = - \begin{bmatrix} 1 & 0 \\ 0 & 1 \end{bmatrix} \delta(\mathbf{r} - \mathbf{r}'), \quad (7.10)$$

is needed in the volume integral calculation. The related functions $U_{ij}(\mathbf{r}|\mathbf{r}')$ is defined as

$$G_{ij}(\mathbf{r}|\mathbf{r}') = -\nabla_t^2 U_{ij}(\mathbf{r}|\mathbf{r}') \quad i, j = a, b \quad (7.11)$$

In order to derive the dyadic Green's kernel used in (4.29), the scalar Green's function is determined first. The TREE method is applied in the axial direction as before and the same truncation boundary conditions are imposed at $z = 0$ and $z = h$, as listed in Table 4.2.

For a homogeneous truncated domain, the scalar Green's functions are given in (4.35) and (4.36). The Green's functions for a dipole point source in a truncated borehole are developed in (4.40) by considering the coupling of TE and TM modes due to the borehole interface. Here, we continue our discussion from the scalar Green's function for a current dipole point source in a half-space conductor.

7.2 Scalar Green's Function for a Half Space

Let's consider a point source inside a half-space conductor. The domain is truncated at with PEC condition at $z = 0$ and PMC condition at $z = h$. The interface between the conductor and free space is located at $z = c$, Fig. 7.2. In this problem, TE and TM modes are independent to each other. With axial truncation, the method introduced in Chapter 6 are used here to satisfy the continuity of the fields at the interface, $z = c$.

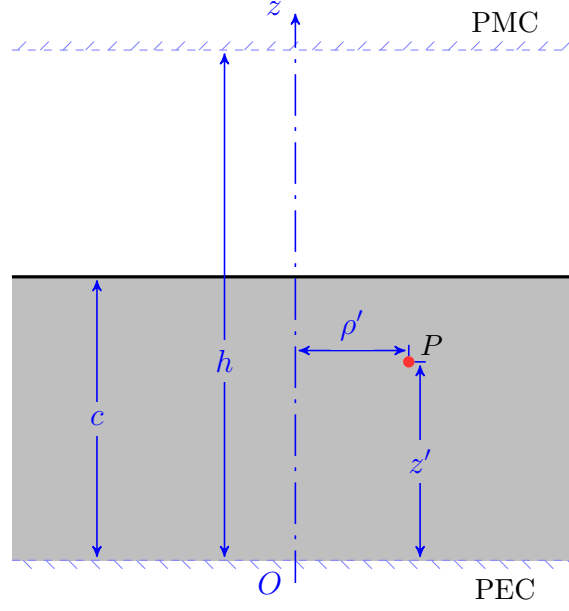


Figure 7.2: A point source in a truncated half space.

Thus, the Green's function corresponding to the TE mode can be written as

$$G_a^{(H)} = \sum_{m=-\infty}^{\infty} e^{im(\phi-\phi')} \sum_{i=1}^{\infty} \tilde{G}_0(\rho, \rho', v_i) \sin(\alpha_i z') \begin{cases} \sin(\alpha_i z) A_{mi} & 0 \leq z \leq c \\ \cos[v_i(h-z)] A_{mi} \xi_i & c \leq z \leq h \end{cases} \quad (7.12)$$

where A_{mi} and ξ_i are the coefficients to be determined and α_i and v_i satisfy

$$v_i^2 = \alpha_i^2 - k^2. \quad (7.13)$$

The eigenvalues, v_i and α_i , are determined by applying boundary conditions at the interface $z = c$. The continuity of B_z at $z = c$ gives

$$\sin(\alpha_i c) = \xi_i \cos[v_i(h-c)], \quad (7.14)$$

and the continuity of H_ϕ at $z = c$ implies

$$\alpha_i \cos(\alpha_i c) = \xi_i v_i \sin[v_i(h-c)]. \quad (7.15)$$

Combining (7.13)–(7.15), the eigenvalues, α_i , are found by solving this complex transcendental equation

$$v_i \sin[v_i(h-c)] \sin(\alpha_i c) - \alpha_i \cos[v_i(h-c)] \cos(\alpha_i c) = 0. \quad (7.16)$$

This equation is similar to that in (6.15) and the same numerical methods mentioned in Section 6.5 can be used to solve the equation. Once the eigenvalues are calculated, ξ_i can be determined from (7.14) or (7.15).

The coefficients in (7.12) are found by using a set of functions for the half space defined as

$$\psi_\ell(z) = \begin{cases} \sin(p_\ell z) & 0 \leq z \leq c \\ \xi_\ell \cos[q_\ell(h-z)]/\sqrt{\mu_r} & c \leq z \leq h \end{cases} \quad (7.17)$$

and these functions have the orthogonal property

$$\int_0^h \psi_i(z)\psi_j(z) dz = \frac{h_i}{2} \delta_{ij}, \quad (7.18)$$

where

$$h_i = c + \frac{\xi_i^2}{\mu_r}(h-c) + \frac{k^2 \sin(2\alpha_i c)}{2\alpha_i q_i^2}. \quad (7.19)$$

Substituting (7.12) into (7.10), applying the orthogonality property of $e^{im\phi}$ and (7.18), we can show that

$$G_a^{(H)} = \sum_{m=-\infty}^{\infty} e^{im(\phi-\phi')} \sum_{i=1}^{\infty} \frac{1}{\pi h_i} I_m(v_i \rho_{<}) K_m(v_i \rho_{>}) \sin(\alpha_i z') \begin{cases} \sin(\alpha_i z) & 0 \leq z \leq c \\ \xi_i \cos[v_i(h-z)] & c \leq z \leq h \end{cases} \quad (7.20)$$

Compared with the scalar Green's function for the homogeneous domain, the TM Green's kernel for a half space ($0 < z < c$) takes the form

$$G_b^{(H)} = \frac{1}{\pi c} \sum_{m=-\infty}^{\infty} e^{im(\phi-\phi')} \sum_{i=1}^{\infty} I_m(\gamma_i \rho_{<}) K_m(\gamma_i \rho_{>}) \cos(\beta_i z) \cos(\beta_i z'), \quad (7.21)$$

where $\gamma_i^2 = \beta_i^2 - k^2$ and $\beta_i = (2i-1)\pi/2c$.

Equations (7.20) and (7.21) give the scalar Green's function for a point source in the half space. To derive the Green's kernel for the Borehole opening, these two functions are modified by adding the effect of fields migration from an interface at $\rho = b$.

7.3 Point Source around the Opening of a Borehole

In borehole model, reflection terms are introduced to the homogeneous Green's kernel to represent the field migration from the cylindrical interface and the TE and TM modes are

coupled due to the continuity of the fields at the interface. However, the eigenmodes, due to the truncation in the axial direction, are independent to each other. For the borehole opening, the modes represented by eigenvalues, v_i in the half-space solution are also coupled due to the boundary conditions at these two intersecting surfaces.

By introducing the coupling between the modes supported by the truncated half space, the scalar Green's function for a point source near the opening of a borehole can be derived in the similar procedure as that from homogeneous unbounded domain to the borehole structure.

Consider a point source in the conductor is located outside of the cylindrical plane $\rho = \rho_s$, Fig. 7.3. The continuity conditions at the plane $z = c$ are satisfied by matching the fields for the half space. The fields inside the borehole are matched with the fields outside the borehole at $\rho = b$. Fourier transform of the TE potential inside the borehole ($\rho < b$) can be expressed as

$$\tilde{W}_{am}^{(1)} = \sum_{i=1}^{\infty} \frac{I_m(\kappa_i \rho)}{I_m(\kappa_i b)} \sin(\kappa_i z) C_{mi}^{(1)}. \quad (7.22)$$

The Fourier transform of the TM potential for the same region, inside the borehole, can be

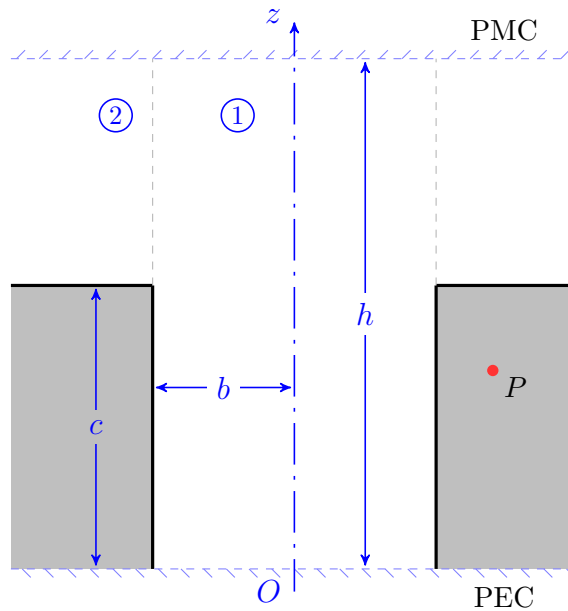


Figure 7.3: A point source around the opening of a borehole. The domain is truncated in the axial direction.

written as

$$\tilde{W}_{bm}^{(1)} = \sum_{i=1}^{\infty} \frac{I_m(\kappa_i \rho)}{I_m(\kappa_i b)} \cos(\kappa_i z) D_{mi}^{(1)}. \quad (7.23)$$

For the region $b < \rho < \rho_s$, the TE potential has the form

$$\tilde{W}_{am}^{(2)} = \sum_{i=1}^{\infty} \left[\frac{I_m(v_i \rho)}{I_m(v_i b)} C_{mi}^{(H)} + \frac{K_m(v_i \rho)}{K_m(v_i b)} C_{mi}^{(2)} \right] \begin{cases} \sin(\alpha_i z) & 0 < z < c \\ \xi_i \cos[v_i(h-z)] & c < z < h \end{cases} \quad (7.24)$$

and the TM potential for the conductive region ($b < \rho < \rho_s$ and $0 < z < c$) can be written as

$$\tilde{W}_{bm}^{(2)} = \sum_{i=1}^{\infty} \left[\frac{I_m(\gamma_i \rho)}{I_m(\gamma_i b)} D_{mi}^{(H)} + \frac{K_m(\gamma_i \rho)}{K_m(\gamma_i b)} D_{mi}^{(2)} \right] \cos(\beta_i z). \quad (7.25)$$

where the coefficients, $C_{mi}^{(H)}$ and $D_{mi}^{(H)}$, are determined by the solution in the half-space problem for a given source.

The unknown coefficients in (7.22)–(7.25), $C_{mi}^{(1)}$, $C_{mi}^{(2)}$, $D_{mi}^{(1)}$, and $D_{mi}^{(2)}$, can be found by enforcing the continuity of tangential magnetic fields and normal magnetic flux across the cylindrical interface $\rho = b$. For a specific order m , the TE and TM modes are coupled with each other and so do the modes represented by the eigenvalues. Therefore, for the given source coefficients, other coefficients can be expressed in the form

$$\begin{bmatrix} C_{mi}^{(1)} \\ D_{mi}^{(1)} \end{bmatrix} = \sum_{\ell=1}^{\infty} \begin{bmatrix} T_{mi\ell}^{(aa)} & T_{mi\ell}^{(ab)} \\ T_{mi\ell}^{(ba)} & T_{mi\ell}^{(bb)} \end{bmatrix} \begin{bmatrix} C_{m\ell}^{(H)} \\ D_{m\ell}^{(H)} \end{bmatrix}, \quad (7.26)$$

and

$$\begin{bmatrix} C_{mi}^{(2)} \\ D_{mi}^{(2)} \end{bmatrix} = \sum_{\ell=1}^{\infty} \begin{bmatrix} \Gamma_{mi\ell}^{(aa)} & \Gamma_{mi\ell}^{(ab)} \\ \Gamma_{mi\ell}^{(ba)} & \Gamma_{mi\ell}^{(bb)} \end{bmatrix} \begin{bmatrix} C_{m\ell}^{(H)} \\ D_{m\ell}^{(H)} \end{bmatrix}, \quad (7.27)$$

for each order m . Here the matrix multiplication represents the coupling between TE and TM fields and the summation represents the eigenmode coupling. Identifying $\tilde{W}_m(\mathbf{r}|\mathbf{r}')$ with $\tilde{U}_m(\mathbf{r}|\mathbf{r}')$, the source coefficients can be obtained from the corresponding Green's function, $\tilde{G}^{(H)}$.

The source coefficients in (7.26) and (7.27) are found from (7.20) and (7.21) as

$$C_{m\ell}^{(H)} = -\frac{\sin(\alpha_\ell z')}{\pi h_\ell v_i^2} I_m(v_\ell b) K_m(v_\ell \rho'), \quad (7.28)$$

and

$$D_{m\ell}^{(H)} = -\frac{\cos(\beta_\ell z')}{\pi c \gamma_i^2} I_m(\gamma_\ell b) K_m(\gamma_\ell \rho'). \quad (7.29)$$

In order to construct the Green's kernel for an internal source, only $C_{mi}^{(2)}$ and $D_{mi}^{(2)}$ are needed and the (7.27) can be expressed as

$$\begin{bmatrix} \mathbf{C}_m^{(2)} \\ \mathbf{D}_m^{(2)} \end{bmatrix} = \begin{bmatrix} \mathbf{\Gamma}_m^{(aa)} & \mathbf{\Gamma}_m^{(ab)} \\ \mathbf{\Gamma}_m^{(ba)} & \mathbf{\Gamma}_m^{(bb)} \end{bmatrix} \begin{bmatrix} \mathbf{C}_m^{(H)} \\ \mathbf{D}_m^{(H)} \end{bmatrix}, \quad (7.30)$$

where $\mathbf{C}_m^{(2)}$, $\mathbf{D}_m^{(2)}$ etc. are column vectors with length N_i and $\mathbf{\Gamma}_m^{(aa)}$ etc. are $N_i \times N_i$ matrices, or as

$$\begin{bmatrix} C_{mi}^{(2)} \\ D_{mi}^{(2)} \end{bmatrix} = \begin{bmatrix} \mathbf{\Gamma}_{mi}^{(aa)} \cdot \mathbf{C}_m^{(H)} + \mathbf{\Gamma}_{mi}^{(ab)} \cdot \mathbf{D}_m^{(H)} \\ \mathbf{\Gamma}_{mi}^{(ba)} \cdot \mathbf{C}_m^{(H)} + \mathbf{\Gamma}_{mi}^{(bb)} \cdot \mathbf{D}_m^{(H)} \end{bmatrix}, \quad (7.31)$$

where $\mathbf{\Gamma}_{mi}^{(aa)}$ is the i -th row of $\mathbf{\Gamma}_m^{(aa)}$. Here, We have truncated all the infinite summation into N_i terms.

We construct an expression for $U_{aa}(\mathbf{r}|\mathbf{r}')$ by identifying it with W_a in (7.24) for the case where the $C_{mi}^{(2)}$ arise from a TE source only as represented by the coefficients $C_{mi}^{(H)}$. For $U_{ab}(\mathbf{r}|\mathbf{r}')$, $U_{ba}(\mathbf{r}|\mathbf{r}')$, and $U_{bb}(\mathbf{r}|\mathbf{r}')$, we proceed in the similar way. Thus in the form of (7.24) and (7.25) we write

$$U_{aa}(\mathbf{r}|\mathbf{r}') = \sum_{m=-\infty}^{\infty} e^{im(\phi-\phi')} \sum_{i=1}^{\infty} \sin(\alpha_i z) \left[\frac{I_m(v_i \rho)}{I_m(v_i b)} C_{mi}^{(H)} + \frac{K_m(v_i \rho)}{K_m(v_i b)} \mathbf{\Gamma}_{mi}^{(aa)} \cdot \mathbf{C}_m^{(H)} \right], \quad (7.32)$$

$$U_{ab}(\mathbf{r}|\mathbf{r}') = \sum_{m=-\infty}^{\infty} e^{im(\phi-\phi')} \sum_{i=1}^{\infty} \sin(\alpha_i z) \frac{K_m(v_i \rho)}{K_m(v_i b)} \mathbf{\Gamma}_{mi}^{(ab)} \cdot \mathbf{D}_m^{(H)}, \quad (7.33)$$

$$U_{ba}(\mathbf{r}|\mathbf{r}') = \sum_{m=-\infty}^{\infty} e^{im(\phi-\phi')} \sum_{i=1}^{\infty} \cos(\beta_i z) \frac{K_m(\gamma_i \rho)}{K_m(\gamma_i b)} \mathbf{\Gamma}_{mi}^{(ba)} \cdot \mathbf{C}_m^{(H)}, \quad (7.34)$$

$$U_{bb}(\mathbf{r}|\mathbf{r}') = \sum_{m=-\infty}^{\infty} e^{im(\phi-\phi')} \sum_{i=1}^{\infty} \cos(\beta_i z) \left[\frac{I_m(\gamma_i \rho)}{I_m(\gamma_i b)} D_{mi}^{(H)} + \frac{K_m(\gamma_i \rho)}{K_m(\gamma_i b)} \mathbf{\Gamma}_{mi}^{(bb)} \cdot \mathbf{D}_m^{(H)} \right], \quad (7.35)$$

for the conductive region.

The first term in (7.32) and (7.35) occurs in the half-space solution and can be separated from the additional terms that arise in the quarter space solution as follows

$$\begin{bmatrix} U_{aa} & U_{ab} \\ U_{ba} & U_{bb} \end{bmatrix} = \begin{bmatrix} U_a^{(H)} & 0 \\ 0 & U_b^{(H)} \end{bmatrix} + \begin{bmatrix} U^{aa} & U^{ab} \\ U^{ba} & U^{bb} \end{bmatrix}, \quad (7.36)$$

for $\mathbf{r} \neq \mathbf{r}'$. For example, the TE potential due to a TM source in (7.33) can be written as

$$U_{ab} = U^{ab} = -\frac{1}{\pi c} \sum_{m=-\infty}^{\infty} e^{im(\phi-\phi')} \sum_{i=1}^{\infty} \frac{K_m(v_i \rho)}{\gamma_i^2 K_m(v_i b)} \sin(\alpha_i z) \sum_{\ell=1}^{\infty} \mathbf{\Gamma}_{mi\ell}^{(ab)} I_m(\gamma_\ell b) K_m(\gamma_\ell \rho') \cos(\beta_\ell z'). \quad (7.37)$$

The coefficients in the forgoing expansions are determined using the interface conditions at the surface $\rho = b$ to ensure the continuity of tangential magnetic fields and the continuity of normal magnetic flux. The following integrals are applied to the fields in region 1 and 2

$$\begin{aligned} & \frac{1}{h\pi} \int_0^{2\pi} e^{-im\phi} \int_0^h \sin(\kappa_i z) H_z \, d\phi \, dz, \\ & \frac{1}{h\pi} \int_0^{2\pi} e^{-im\phi} \int_0^h \cos(\kappa_i z) H_\phi \, d\phi \, dz, \\ & \frac{1}{h\pi} \int_0^{2\pi} e^{-im\phi} \int_0^h \cos(\kappa_i z) B_\rho \, d\phi \, dz, \end{aligned}$$

at $\rho = b$. These conditions, applied in the weak sense, give respectively

$$\boldsymbol{\kappa}^2 \mathbf{C}_m^{(1)} = \mathbf{M}_p \mathbf{v}^2 \left[\mathbf{C}_m^{(H)} + \mathbf{C}_m^{(2)} \right], \quad (7.38)$$

$$im\boldsymbol{\kappa} \mathbf{C}_m^{(1)} = im\boldsymbol{\kappa} \mathbf{M}_p \left[\mathbf{C}_m^{(H)} + \mathbf{C}_m^{(2)} \right] - k^2 \mathbf{M}_r \left[\Lambda_m(\boldsymbol{\gamma}b) \mathbf{D}_m^{(H)} + M_m(\boldsymbol{\gamma}b) \mathbf{D}_m^{(2)} \right], \quad (7.39)$$

$$\boldsymbol{\kappa} \Lambda_m(\boldsymbol{\kappa}b) \mathbf{C}_m^{(1)} = \boldsymbol{\kappa} \mathbf{M}_p \left[\Lambda_m(\mathbf{v}b) \mathbf{C}_m^{(H)} + M_m(\mathbf{v}b) \mathbf{C}_m^{(2)} \right] + imk^2 \mathbf{M}_r \left[\mathbf{D}_m^{(H)} + \mathbf{D}_m^{(2)} \right], \quad (7.40)$$

where the coefficient matrices, such as $\boldsymbol{\kappa}$ and $\Lambda_m(\boldsymbol{\kappa}b)$, are diagonal matrices, and matrices \mathbf{M}_p and \mathbf{M}_r are defined as follows

$$\mathbf{M}_p[i, j] = \frac{2}{h} \left[\int_0^c \sin(\alpha_j z) \sin(\kappa_i z) \, dz + \xi_j \int_c^h \cos[v_j(h-z)] \sin(\kappa_i z) \, dz \right], \quad (7.41)$$

and

$$\mathbf{M}_r[i, j] = \frac{2}{h} \int_0^c \cos(\kappa_j z) \cos(\beta_i z) \, dz. \quad (7.42)$$

Thus, the matrix element \mathbf{M}_p is given by

$$\mathbf{M}_p[i, j] = \frac{2k^2}{h(\kappa_i^2 - \alpha_j^2)(\kappa_i^2 - v_j^2)} \{ \alpha_j \cos(\alpha_j c) \sin(\kappa_i c) - \kappa_i \sin(\alpha_j c) \cos(\kappa_i c) \}, \quad (7.43)$$

and \mathbf{M}_r is the same as that in (6.27) .

Eliminate $\mathbf{C}_m^{(1)}$ in (7.38)–(7.40) gives

$$im \left[\mathbf{A}_1 - \mathbf{A}_2 \right] \left[\mathbf{C}_m^{(H)} + \mathbf{C}_m^{(2)} \right] = -\mathbf{K} \left[\Lambda_m(\boldsymbol{\gamma}b) \mathbf{D}_m^{(H)} + M_m(\boldsymbol{\gamma}b) \mathbf{D}_m^{(2)} \right], \quad (7.44)$$

$$\Lambda_m(\boldsymbol{\kappa}b) \mathbf{A}_1 \left[\mathbf{C}_m^{(H)} + \mathbf{C}_m^{(2)} \right] - \mathbf{A}_2 \left[\Lambda_m(\mathbf{v}b) \mathbf{C}_m^{(H)} + M_m(\mathbf{v}b) \mathbf{C}_m^{(2)} \right] = im\mathbf{K} \left[\mathbf{D}_m^{(H)} + \mathbf{D}_m^{(2)} \right]. \quad (7.45)$$

Here, we have defined

$$\mathbf{A}_1 = \mathbf{M}_p \mathbf{v}^2, \quad \mathbf{A}_2 = \boldsymbol{\kappa}^2 \mathbf{M}_p, \quad \text{and} \quad \mathbf{K} = k^2 \boldsymbol{\kappa} \mathbf{M}_r. \quad (7.46)$$

Combining (7.44) and (7.45), we find

$$\begin{aligned} & \{ \mathbf{K} \mathbf{M}_m(\gamma b) \mathbf{K}^{-1} [\Lambda_m(\boldsymbol{\kappa} b) \mathbf{A}_1 - \mathbf{A}_2 \mathbf{M}_m(\boldsymbol{\nu} b)] - m^2 [\mathbf{A}_1 - \mathbf{A}_2] \} [\mathbf{C}_m^{(H)} + \mathbf{C}_m^{(2)}] \\ &= \mathbf{K} \mathbf{M}_m(\gamma b) \mathbf{K}^{-1} \mathbf{A}_2 [\Lambda_m(\boldsymbol{\nu} b) - \mathbf{M}_m(\boldsymbol{\nu} b)] \mathbf{C}_m^{(H)} - \imath m \mathbf{K} [\Lambda_m(\gamma b) - \mathbf{M}_m(\gamma b)] \mathbf{D}_m^{(H)}, \end{aligned} \quad (7.47)$$

and

$$\begin{aligned} & \{ m^2 \mathbf{K} - [\Lambda_m(\boldsymbol{\kappa} b) \mathbf{A}_1 - \mathbf{A}_2 \mathbf{M}_m(\boldsymbol{\nu} b)] [\mathbf{A}_1 - \mathbf{A}_2]^{-1} \mathbf{K} \mathbf{M}_m(\gamma b) \} [\mathbf{D}_m^{(H)} + \mathbf{D}_m^{(2)}] \\ &= \imath m \mathbf{A}_2 [\Lambda_m(\boldsymbol{\nu} b) - \mathbf{M}_m(\boldsymbol{\nu} b)] \mathbf{C}_m^{(H)} \\ & \quad + [\Lambda_m(\boldsymbol{\kappa} b) \mathbf{A}_1 - \mathbf{A}_2 \mathbf{M}_m(\boldsymbol{\nu} b)] [\mathbf{A}_1 - \mathbf{A}_2]^{-1} \mathbf{K} [\Lambda_m(\gamma b) - \mathbf{M}_m(\gamma b)] \mathbf{D}_m^{(H)}. \end{aligned} \quad (7.48)$$

Finally, compared with (7.30), the reflection matrices $\Gamma_m^{(aa)}$ and $\Gamma_m^{(ab)}$ are obtained from (7.47) for any order m . Similarly, $\Gamma_m^{(ba)}$ and $\Gamma_m^{(bb)}$ are obtained from (7.48).

For the solution of the zeroth order, $m = 0$, the TE and TM modes are decoupled and (7.47) reduces to the following form

$$[\Lambda_0(\boldsymbol{\kappa} b) \mathbf{A}_1 - \mathbf{A}_2 \mathbf{M}_0(\boldsymbol{\nu} b)] [\mathbf{C}_0^{(H)} + \mathbf{C}_0^{(2)}] = \mathbf{A}_2 [\Lambda_0(\boldsymbol{\nu} b) - \mathbf{M}_0(\boldsymbol{\nu} b)] \mathbf{C}_0^{(H)}. \quad (7.49)$$

Thus,

$$\Gamma_0^{(aa)} = [\Lambda_0(\boldsymbol{\kappa} b) \mathbf{A}_1 - \mathbf{A}_2 \mathbf{M}_0(\boldsymbol{\nu} b)]^{-1} \mathbf{A}_2 [\Lambda_0(\boldsymbol{\nu} b) - \mathbf{M}_0(\boldsymbol{\nu} b)] - \mathbf{I}. \quad (7.50)$$

If c is approaching to h , then

$$\alpha_i = \beta_i = \kappa_i, \quad \gamma_i^2 = \nu_i^2 = \kappa^2 - k^2,$$

and \mathbf{A}_1 , \mathbf{A}_2 , and \mathbf{K} become diagonal matrices

$$\mathbf{A}_1 = \gamma^2 \mathbf{I}, \quad \mathbf{A}_2 = \kappa^2, \quad \mathbf{K} = k^2 \boldsymbol{\kappa}.$$

Equations (7.47) and (7.48) become

$$\begin{aligned} & \{ m^2 k^2 - \mathbf{M}_m(\gamma b) [\boldsymbol{\kappa}^2 \mathbf{M}_m(\gamma b) - \gamma^2 \Lambda_m(\boldsymbol{\kappa} b)] \} [\mathbf{C}_m^{(H)} + \mathbf{C}_m^{(2)}] \\ &= [\Lambda_m(\gamma b) - \mathbf{M}_m(\gamma b)] \left\{ \boldsymbol{\kappa}^2 \mathbf{M}_m(\gamma b) \mathbf{C}_m^{(H)} - \imath m k^2 \boldsymbol{\kappa} \mathbf{D}_m^{(H)} \right\}, \\ & \{ m^2 k^2 - \mathbf{M}_m(\gamma b) [\boldsymbol{\kappa}^2 \mathbf{M}_m(\gamma b) - \gamma^2 \Lambda_m(\boldsymbol{\kappa} b)] \} [\mathbf{D}_m^{(H)} + \mathbf{D}_m^{(2)}] \\ &= [\Lambda_m(\gamma b) - \mathbf{M}_m(\gamma b)] \left\{ \imath m \boldsymbol{\kappa}^2 \mathbf{C}_m^{(H)} + [\boldsymbol{\kappa}^2 \mathbf{M}_m(\gamma b) - \gamma^2 \Lambda_m(\boldsymbol{\kappa} b)] \mathbf{D}_m^{(H)} \right\}. \end{aligned}$$

These reflection matrices calculated from (7.47) and (7.48) agree with (4.53) in the borehole model.

7.4 Dyadic Green's Function for a Longitudinal Crack

Like what we did in Section 4.5, operating $\hat{\phi} \cdot \mathcal{G}(\mathbf{r}|\mathbf{r}') \cdot \hat{\phi}$ on dyadic Green's function defined in (4.28), we get the dyadic Green's kernel for a longitudinal crack near a borehole edge

$$G_{\phi\phi}^{(\Gamma)}(\mathbf{r}|\mathbf{r}') = \frac{\partial^2 U^{aa}}{\partial \rho \partial \rho'} - \frac{1}{k^2 \rho'} \frac{\partial^3 U^{ab}}{\partial \rho \partial \phi' \partial z'} - \frac{1}{\rho} \frac{\partial^3 U^{ba}}{\partial \phi \partial z \partial \rho'} + \frac{1}{k^2 \rho \rho'} \frac{\partial^4 U^{bb}}{\partial \phi \partial z \partial \phi' \partial z'}. \quad (7.51)$$

and we can evaluate those terms in (7.51) using the decomposition given in (7.36) as

$$\frac{\partial^2 U^{aa}}{\partial \rho \partial \rho'} = -\frac{1}{\pi} \sum_{m=-\infty}^{\infty} e^{im(\phi-\phi')} \sum_{i=1}^{\infty} \frac{1}{v_i} \sin(\alpha_i z) \frac{K'_m(v_i \rho)}{K_m(v_i b)} \Gamma_{mi}^{(aa)} \cdot \tilde{\mathbf{U}}_m^a, \quad (7.52)$$

$$\frac{1}{k^2 \rho'} \frac{\partial^3 U^{ab}}{\partial \rho \partial \phi' \partial z'} = -\frac{i}{\pi c k^2 \rho'} \sum_{m=-\infty}^{\infty} m e^{im(\phi-\phi')} \sum_{i=1}^{\infty} \frac{v_i}{\gamma_i^2} \sin(\alpha_i z) \frac{K'_m(v_i \rho)}{K_m(v_i b)} \Gamma_{mi}^{(ab)} \cdot \tilde{\mathbf{U}}_m^b, \quad (7.53)$$

$$\frac{1}{\rho} \frac{\partial^3 U^{ba}}{\partial \phi \partial z \partial \rho'} = \frac{i}{\pi \rho} \sum_{m=-\infty}^{\infty} m e^{im(\phi-\phi')} \sum_{i=1}^{\infty} \frac{\beta_i}{v_i^2} \sin(\beta_i z) \frac{K_m(\gamma_i \rho)}{K_m(\gamma_i b)} \Gamma_{mi}^{(ba)} \cdot \tilde{\mathbf{U}}_m^a, \quad (7.54)$$

$$\frac{1}{k^2 \rho \rho'} \frac{\partial^4 U^{bb}}{\partial \phi \partial z \partial \phi' \partial z'} = -\frac{1}{\pi c k^2 \rho \rho'} \sum_{m=-\infty}^{\infty} m^2 e^{im(\phi-\phi')} \sum_{i=1}^{\infty} \frac{\beta_i}{\gamma_i^2} \sin(\beta_i z) \frac{K_m(\gamma_i \rho)}{K_m(\gamma_i b)} \Gamma_{mi}^{(bb)} \cdot \tilde{\mathbf{U}}_m^b, \quad (7.55)$$

where elements of $\tilde{\mathbf{U}}_m^a$ and $\tilde{\mathbf{U}}_m^b$ are given by

$$\tilde{U}_{m\ell}^a = \frac{v_\ell}{h_\ell} I_m(v_\ell b) K'_m(v_\ell \rho') \sin(\alpha_\ell z'), \quad (7.56)$$

$$\tilde{U}_{m\ell}^b = \beta_\ell I_m(\gamma_\ell b) K_m(\gamma_\ell \rho') \sin(\beta_\ell z'). \quad (7.57)$$

By integrating the kernel in (7.51) over a crack cell, the reflection matrix element in the volume integral equation can be calculated. The matrix element of half-space kernel is given in Appendix C. This completes the derivation of the matrix elements used in our method to evaluate the current dipole source over the crack region.

7.5 Discussion and Summary

A MATLAB code is written based on above crack model and some tests are under way. The problem we currently have is the ill-conditioned matrix in (7.47) and (7.48). The reflection matrix is calculated by inverting the matrix on the left-hand side of these two equations. However, like what we stated in Chapter 6, these two matrices have large condition numbers and the reflection matrix becomes inaccurate after we invert these matrices. One of the solutions is

to construct the matrix equations by eliminating other unknown coefficients, not the coefficients $\mathbf{C}_m^{(1)}$. The investigation of the matrix properties is still in progress.

The reflection matrices are calculated for each order. Apparently, the summation in the matrix element calculation has slow convergence due to the hyper-singularity around the bore-hole edge. That means we need large number of orders and modes. Inverting the full matrix is time-consuming. Therefore, we are also considering other methods with some approximations to accelerate the computation speed, such as the thin skin theory.

CHAPTER 8. CONCLUSION

In this dissertation, we have presented several EC problems solved in cylindrical polar coordinates: cracks near an infinitely long borehole, longitudinal cracks in a tube, and impedance change of coils around the opening of a borehole. The fields are expressed in terms of scalar TE and TM potentials. To solve the crack problems, the crack is equivalent to a current dipole source distributed over the crack region. Dyadic Green's functions for a point source in these structures are derived to construct an electric integral equation and the dipole density is solved using the volume element method. The incident field associated with a given coil source can be also derived using the similar approach. Finally, the coil signals are obtained based the dipole density using the reciprocity theorem. The comparison between the results from the crack model and the experimental measurements shows a good agreement for all the cases.

As discussed at the beginning of this dissertation, each problem has different physical meaning and mathematical background. The methods and concepts are extended from simple models to the complicated problems. With appropriate modification, this systematic approach could be further applied to the other similar structures, such as cracks near holes in a plate. On the other hand, the results for a complicated geometry can be verified by considering some special cases in which the problem can be reduced to the simple structures, like what we did in the tube and borehole models. The transient eddy current problems could be solved by applying Laplace transformation with the spectrum approaches derived in this work.

The TREE method is applied to all the problems. Series expansion is introduced according to the given truncation boundary conditions. The expansion coefficients are found by matching the fields at the interfaces. In TREE method, each expansion function is related to the different eigenmode supported in the corresponding structure. For simple geometries, the eigenvalues have simple forms, as in the case of the infinitely long borehole and tube. For more complicated

geometrical shape, such as the coil at the opening of a borehole, both the series form and the eigenvalues have to be extended into a broad concept. Due to the hyper-singularity at the borehole opening, the matrix equations tend to be ill-conditioned. It is critical to have a better way to solve these matrix equations.

We only applied the axial truncation in this dissertation. It is also possible to make the truncation in the radial direction for some problems. The choice of the truncation strategy depends on the problem configuration. With radial truncation, the mode coupling due to a cylindrical interface should be considered in the eigenvalues, instead of the expansion coefficients. Therefore the eigenvalue calculation becomes even more important.

The numerical issues related to our crack models are also interesting topics, such as the analysis of the complex zeros for a given function, the series convergence in a complicated multiple summation and the convergence acceleration techniques. We believe, with better method, it is possible to further speed up the whole calculation.

There are still lots of work related to the fastener problem. One is how to deal with the boundary conditions along a curved surface. The other one is to obtain an approximation solution using thin crack theory to accelerate the calculation at high frequency. The details about the hyper-singularity at the borehole edge also need further investigation.

**APPENDIX A. USEFUL MATHEMATICAL FORMULAS IN
CYLINDRICAL COORDINATE SYSTEM**

Mathematical Identities

Vector Identities

$$\nabla \times \nabla \psi = 0,$$

$$\nabla \cdot \nabla \times \mathbf{A} = 0,$$

$$\nabla \cdot (\psi \mathbf{A}) = \mathbf{A} \cdot \nabla \psi + \psi \nabla \cdot \mathbf{A},$$

$$\nabla \times \nabla \times \mathbf{A} = \nabla \nabla \cdot \mathbf{A} - \nabla^2 \mathbf{A}.$$

Integral Identities

Stokes' theorem

$$\oint_C \mathbf{A} \cdot d\mathbf{l} = \int_S \nabla \times \mathbf{A} \cdot d\mathbf{s}.$$

Divergence theorem

$$\oint_S \mathbf{A} \cdot d\mathbf{s} = \int_V \nabla \cdot \mathbf{A} \, dv.$$

First Green's identity

$$\oint_V (\phi \nabla^2 \psi + \nabla \phi \cdot \nabla \psi) \, dv = \oint_S \phi \nabla \psi \cdot d\mathbf{s}.$$

Second Green's identity

$$\oint_V (\phi \nabla^2 \psi - \psi \nabla^2 \phi) \, dv = \oint_S (\phi \nabla \psi - \psi \nabla \phi) \cdot d\mathbf{s}.$$

Scalar Decomposition

In cylindrical coordinate system, we define

$$\nabla_t \equiv \nabla - \hat{z}\partial/\partial z.$$

Therefore,

$$\begin{aligned}\nabla_t^2 &= \nabla^2 - \partial^2/\partial z^2, \quad \nabla \times \hat{z} = \hat{\rho}\frac{1}{\rho}\frac{\partial}{\partial\phi} - \hat{\phi}\frac{\partial}{\partial\rho}, \\ \nabla \times \nabla \times \hat{z} &= -\hat{z}\nabla_t^2 + \frac{\partial}{\partial z}\nabla_t, \\ \nabla \times \mathcal{I}\nabla_t^2 &= -(\nabla \times \hat{z})(\nabla \times \nabla \times \hat{z}) + (\nabla \times \nabla \times \hat{z})(\nabla \times \hat{z}), \\ \mathcal{I} &= \hat{z}\hat{z} + \frac{\nabla_t\nabla_t}{\nabla_t^2} + \frac{\nabla \times \hat{z}\nabla \times \hat{z}}{\nabla_t^2}, \\ \nabla\nabla &= \nabla_t\nabla_t + (\nabla_t\hat{z} + \hat{z}\nabla_t)(\hat{z} \cdot \nabla) + \hat{z}\hat{z}(\hat{z} \cdot \nabla)^2.\end{aligned}$$

Gradient, Divergence, Curl and Laplacian

The gradient, divergence, curl, and laplacian defined in cylindrical coordinate are as follows.

$$\begin{aligned}\nabla\psi &= \frac{\partial\psi}{\partial\rho}\hat{\rho} + \frac{1}{\rho}\frac{\partial\psi}{\partial\phi}\hat{\phi} + \frac{\partial\psi}{\partial z}\hat{z}, \\ \nabla \cdot \mathbf{A} &= \frac{1}{\rho}\frac{\partial}{\partial\rho}(\rho A_\rho) + \frac{1}{\rho}\frac{\partial A_\phi}{\partial\phi} + \frac{\partial A_z}{\partial z}, \\ \nabla \times \mathbf{A} &= \left(\frac{1}{\rho}\frac{\partial A_z}{\partial\phi} - \frac{\partial A_\phi}{\partial z}\right)\hat{\rho} + \left(\frac{\partial A_\rho}{\partial z} - \frac{\partial A_z}{\partial\rho}\right)\hat{\phi} + \frac{1}{\rho}\left(\frac{\partial(\rho A_\phi)}{\partial\rho} - \frac{\partial A_\rho}{\partial\phi}\right)\hat{z}, \\ \nabla^2\psi &= \frac{1}{\rho}\frac{\partial}{\partial\rho}\left(\rho\frac{\partial\psi}{\partial\rho}\right) + \frac{1}{\rho^2}\frac{\partial^2\psi}{\partial\phi^2} + \frac{\partial^2\psi}{\partial z^2}.\end{aligned}$$

Assume a vector field is defined as

$$\mathbf{B} = \nabla \times \nabla \times (\hat{z}W_a) + k^2\nabla \times (\hat{z}W_b),$$

where both TE and TM potentials satisfy Helmholtz equation. Then the components of the vector field \mathbf{B} are

$$\begin{aligned}B_\rho &= \frac{\partial^2 W_a}{\partial\rho\partial z} + \frac{k^2}{\rho}\frac{\partial W_b}{\partial\phi}, \\ B_\phi &= \frac{1}{\rho}\frac{\partial^2 W_a}{\partial\phi\partial z} - k^2\frac{\partial W_b}{\partial\rho}, \\ B_z &= \left(k^2 + \frac{\partial^2}{\partial z^2}\right)W_a.\end{aligned}$$

APPENDIX B. BOBBIN COIL ABOVE A HALF-SPACE CONDUCTOR

Bobbin coil above a half-space conductor is a classical problem in EC NDE, which have been completely solved in terms of a closed-form integral using magnetic vector potential theory. Here, we compare the integral form with the series solution for this problem. It is a good example to understand the idea of TREE method.

The solution of a circular filament in free space is given first, and then the coil solution is presented. Both integral form and series form are discussed.

Circular Filament in Free Space

In order to obtain the solution of a coil field in free space, the field of a single current loop, a filament, is given first. The magnetic vector potential, \mathbf{A} , is used to formulate the fields. It is clear that only azimuthal component, A_ϕ , exists if the coil is placed along z axis. Assume the radius of the filament is ρ_0 and it is located at $z = z_0$ in the cylindrical coordinate system. An AC current with magnitude I is flowing in the filament.

Filament Field in Integral Form

The Bessel function of the first kind is chosen to express the field based on the fact that it is regular on the axis and vanishes as ρ goes to infinity. By using Hankel transform, the integrand can be found from the jump of the magnetic field at $z = z_0$. The solution has the form

$$A_\phi(\rho, z) = \frac{\mu_0 I \rho_0}{2} \int_0^\infty J_1(\kappa \rho_0) J_1(\kappa \rho) e^{-\kappa |z - z_0|} d\kappa. \quad (\text{B.1})$$

The eigenvalue κ varies continuously from zero to infinity and, thus, the solution involves a continuous spectrum of eigenvalues.

An alternative field expression can be derived with Fourier cosine transformation in the axial direction. The whole domain of the problem can be divided into two regions at the circularly cylindrical surface passing the filament which is in the plane $z = z_0$. The modified Bessel functions and cosine function are used to represent the field. Therefore, the complete form could be found using Fourier cosine transformation and then apply discontinuity condition to the magnetic field. Finally, the magnetic vector potential of a current loop is given by

$$A_\phi(\rho, z) = \frac{\mu_0 I \rho_0}{\pi} \int_0^\infty I_1(v\rho_<) K_1(v\rho_>) \cos[v(z - z_0)] dv. \quad (\text{B.2})$$

where $\rho_>$ is the greater of ρ and ρ_0 . Similarly, $\rho_<$ is the lesser of ρ and ρ_0 . It is clear that the solution is finite at the axis and goes to zero as ρ increases.

Filament Field in Series Form

As stated in Chapter 2, the series solution can be obtained with the aid of TREE method. The problem domain can be truncated in the axial direction or in the radial direction. Eigenvalues are discretized due to truncation and two kinds of classical series expansion, Fourier series and Fourier-Bessel series, are used to represent the field, respectively. The solution with axial truncation is given in Appendix D.

With radial truncation, the solution can be expressed in terms of Fourier-Bessel series. The domain is truncated at $\rho = b$. The truncation condition is chosen as PMC, $\mathbf{B}_t = \mathbf{0}$ at $\rho = b$. Bessel functions are used to construct the solution and zeros of Bessel functions are the eigenvalues. In order to find the expansion coefficients, we need the orthogonality properties for the zeros of Bessel functions. The final expression can be written as

$$A_\phi(\rho, z) = \sum_{s=1}^{\infty} \frac{I \rho_0}{\kappa_s [b J_1'(\kappa_s b)]^2} J_1(\kappa_s \rho_0) J_1(\kappa_s \rho) e^{-\kappa_s |z - z_0|}, \quad (\text{B.3})$$

where eigenvalues κ_s are positive zeros of $J_1(\kappa b)$. Compared with (B.1), the discrete spectrum of eigenvalues is involved in (B.3). However, the field behavior is similar and the fields exponentially decay in the axial direction and vanish as ρ goes to infinity.

The magnetic vector potential, \mathbf{A} , is calculated using (B.3) and the equipotential lines are plotted in Fig. B.1.

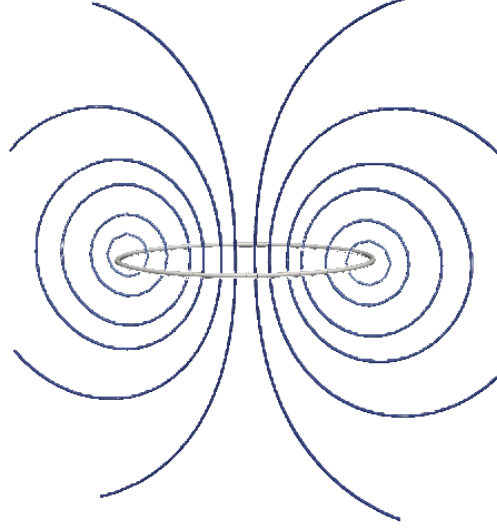


Figure B.1: Equipotential lines of the magnetic vector potential, \mathbf{A} on a plane passing through the axis of the filament.

Coil with Rectangular Cross Section in Free Space

The coil field is obtained using superposition principle from corresponding filament field.

Coil Field in Integral Form

As shown in Fig. B.2, the coil has a rectangular cross section with inner radius r_1 and outer radius r_2 . Its electric field is given by integrating the filament field over the rectangular cross section as

$$E_{\phi}^{(0)}(\rho, z) = \nu \int_{r_1}^{r_2} \int_{z_c - \ell/2}^{z_c + \ell/2} E_{\phi}(\rho, z) d\rho_0 dz_0, \quad (\text{B.4})$$

where E_{ϕ} is the filament field, ν is turns density of the coil.

Substituting (B.1) into (B.4), the coil field is given by

$$E_{\phi}^{(0)}(\rho, z) = \frac{i\omega\mu_0\nu I}{2} \int_0^{\infty} \frac{1}{\kappa^3} \chi(\kappa r_1, \kappa r_2) F(\kappa, z) J_1(\kappa\rho) d\kappa, \quad (\text{B.5})$$

where functions $F(\kappa, z)$ and $\chi(\alpha_1, \alpha_2)$ are defined as

$$\begin{aligned}
F(\kappa, z) &= \kappa \int_{z_c - \ell/2}^{z_c + \ell/2} e^{-\kappa|z - z_0|} dz_0 \\
&= \begin{cases} 2e^{-\kappa(z - z_c)} \sinh(\kappa\ell/2) & z > z_c + \ell/2 \\ 2 \{1 - e^{-\kappa\ell/2} \cosh[\kappa(z - z_c)]\} & z_c + \ell/2 \leq z \leq z_c - \ell/2 \\ 2e^{\kappa(z - z_c)} \sinh(\kappa\ell/2) & z < z_c - \ell/2 \end{cases} \quad (\text{B.6})
\end{aligned}$$

and

$$\begin{aligned}
\chi(\alpha_1, \alpha_2) &= \int_{\alpha_1}^{\alpha_2} x J_1(x) dx \\
&= \frac{\pi}{2\alpha} [J_1(\alpha) \mathbf{H}_0(\alpha) - J_0(\alpha) \mathbf{H}_1(\alpha)] \Big|_{\alpha_1}^{\alpha_2}. \quad (\text{B.7})
\end{aligned}$$

Here \mathbf{H}_ν are the Struve functions.

Coil Field in Series Form

Similarly, the same idea can be applied to the series form (B.3) and we have

$$E_\phi^{(0)}(\rho, z) = \sum_{s=1}^{\infty} \frac{\omega \nu I}{\kappa_s^4 [b J_1'(\kappa_s b)]^2} \chi(\kappa_s r_1, \kappa_s r_2) F(\kappa_s, z) J_1(\kappa_s \rho). \quad (\text{B.8})$$

The electric field is calculated using (B.8) and the field on the plane passing through the axis of the coil is shown in Fig. B.2.

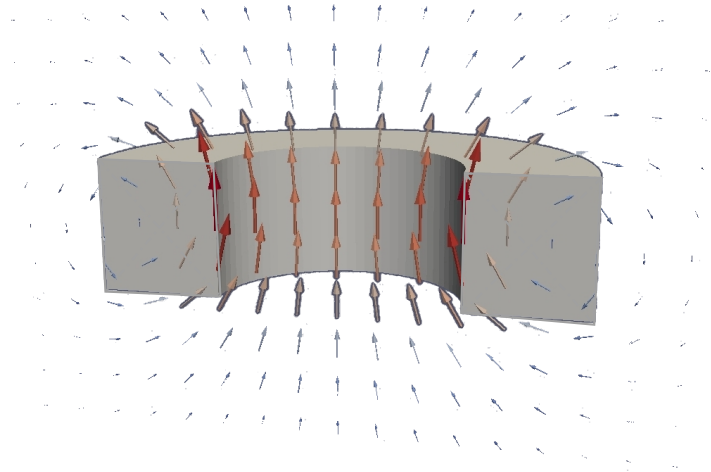


Figure B.2: Magnetic field of a coil with rectangular cross section in free space.

Self-Inductance of an Isolated Coil in Free Space

The self-inductance of this rectangular coil can be derived based on the definition of the voltage. The voltage induced by electric field \mathbf{E} in a length of wire is

$$V = - \int_C \mathbf{E} \cdot d\ell, \quad (\text{B.9})$$

where the path integral C is along the wire. For a coil with rectangular cross section, the impedance of an isolated coil is

$$Z_0 = \frac{V}{I} = -2\pi\nu^2 \int_{r_1}^{r_2} \int_{z_c-\ell/2}^{z_c+\ell/2} \rho_0 E_\phi^{(0)}(\rho, z) d\rho_0 dz_0. \quad (\text{B.10})$$

By substituting (B.5) to (B.10), the self-inductance is obtained as

$$L = \frac{Z_0}{i\omega} = 2\pi\mu_0\nu^2 \int_0^\infty d\kappa \chi^2(\kappa r_1, \kappa r_2) \kappa^{-6} (\kappa\ell + e^{-\kappa\ell} - 1). \quad (\text{B.11})$$

Bobbin Coil above a Half-Space Conductor

For the incident field of a bobbin coil above a conductive half space, the formula is obtained by introducing a reflection coefficient due to the presence of the conductor.

Electric Field for a Coil above a Half-Space Conductor

The electric field of a bobbin coil above a half space can be written as

$$E_\phi(\rho, z) = \frac{i\omega\mu_0\nu I}{2} \int_0^\infty \mathcal{J}(\kappa) [e^{\kappa z} - \Gamma(\kappa)e^{-\kappa z}] J_1(\kappa\rho) d\kappa, \quad (\text{B.12})$$

where $\Gamma(\kappa)$ is the reflection coefficient due to the presence of the conductor and have the form

$$\Gamma(\kappa) = \frac{\lambda - \kappa}{\lambda + \kappa}. \quad (\text{B.13})$$

Here $\lambda^2 = \kappa^2 + k^2$. This reflection coefficient is found from the continuity of the tangential electric and magnetic fields at the interface of the conductor.

The magnitude of electric field in the conductor, which is proportional to the eddy-current density, is shown in Fig. B.3.

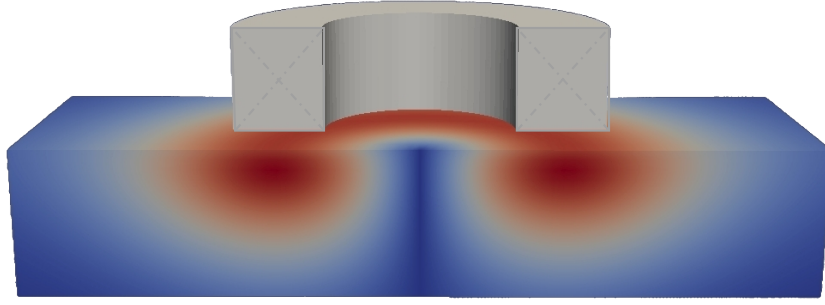


Figure B.3: Distribution of eddy-current density for a cylindrical coil above a half space.

Impedance Change due to a Conductive Half Space

The impedance change of the coil due to a half-space conductor can be calculated from the induced electric field due to eddy currents in the conductor. The impedance change of the coil is given by

$$\Delta Z = -\frac{2\pi\nu^2}{I^2} \int_{z_c-\ell/2}^{z_c+\ell/2} \rho_0 E_\phi^{(ec)}(\rho, z) d\rho_0 dz_0, \quad (\text{B.14})$$

where $E^{(ec)}$ is the electric field due to the induced eddy current, i.e. the second term in (B.12) and the final solution is

$$\Delta Z = -i\pi\omega\mu_0\nu^2 \int_0^\infty d\kappa \frac{\chi^2(\kappa r_2, \kappa r_1)}{\kappa^6} \Gamma(\kappa) (e^{-\kappa z_1} - e^{-\kappa z_2})^2. \quad (\text{B.15})$$

APPENDIX C. COIL IMPEDANCE CHANGE DUE TO CRACKS IN A HALF-SPACE CONDUCTOR

TREE method provides a fast approach to solve the coil impedance change due to a crack in a half-space conductor. Theodoulidis, Poulakis, and Dragogias use a double truncation strategy to express the Green's function in terms of a double summation [124]. We summarize their solutions here for reference. The Green's function is divided into a term due to a point source in unbounded domain and a term due to the reflection. The same crack model is used in this work. The schematic is the same as Fig. 4.8.

Unbounded Domain Kernel

Assume the source point is at the origin in Cartesian coordinate, then the scalar Green's function in homogeneous domain can be written as

$$G_0(\mathbf{r}|\mathbf{r}') = \frac{e^{ikR}}{4\pi R}, \quad R = \sqrt{x^2 + y^2 + z^2}. \quad (\text{C.1})$$

For a crack perpendicular to the x -axis, the unbounded domain kernel is

$$\begin{aligned} G_{xx}^{(0)} &= \left(1 + \frac{1}{k^2} \frac{\partial^2}{\partial x^2}\right) G_0(\mathbf{r}|\mathbf{r}') \\ &= \frac{e^{ikR}}{4\pi k^2 R} \left(k^2 + \frac{ik}{R} - \frac{1 + k^2 x^2}{R} - \frac{3ikx^2}{R^3} + \frac{3x^2}{R^4}\right). \end{aligned} \quad (\text{C.2})$$

Thus, the corresponding matrix element in volume integral method is given by

$$M^{(0)} = k^2 \int_0^{\Delta x} \int_{y-\Delta y/2}^{y+\Delta y/2} \int_{z-\Delta z/2}^{z+\Delta z/2} G_{xx}^{(0)} dx dy dz. \quad (\text{C.3})$$

If the source is far away from the source point, this triple integral is easy to compute. For the singular source point, the following coordinate variable transformation is introduced to

overcome the hypersingularity of the diagonal terms in the matrix. By letting

$$y = r \cos \varphi, \quad z = r \sin \varphi, \quad (\text{C.4})$$

we have

$$M^{(0)} = \frac{k^2}{\pi} \int_0^{\Delta x} dx \left[\int_0^{\varphi_1} d\varphi \frac{r_y^2 (1 - ikR_y) e^{ikR_y}}{R_y^3} + \int_0^{\pi/2 - \varphi_1} \frac{r_z^2 (1 - ikR_z) e^{ikR_z}}{R_z^3} \right], \quad (\text{C.5})$$

where

$$r_y = \frac{\Delta y}{2 \cos \varphi}, \quad r_z = \frac{\Delta z}{2 \cos \varphi}, \quad (\text{C.6})$$

and

$$R_y = \sqrt{x^2 + r_y^2}, \quad R_z = \sqrt{x^2 + r_z^2}, \quad \varphi_1 = \arctan \frac{\Delta y}{\Delta z}. \quad (\text{C.7})$$

Reflection Matrix Element

The reflection term can be obtained by applying the TREE method. The domain is truncated in x direction from 0 to h_x and in y direction from 0 to h_y , assume the source dipole is located at $x_0 = h_x/2, y_0 = h_y/2, z_0 = 0$. The reflection term can be written as

$$G_{xx}^{(\Gamma)} = \frac{2}{h_x h_y} \sum_{i=1}^{\infty} \sum_{j=1}^{\infty} \frac{e^{\lambda_{ij}(z+z_0)}}{\kappa_{ij}^2 \lambda_{ij}} \left(k^2 v_j^2 \frac{\lambda_{ij} - \kappa_{ij}}{\lambda_{ij} + \kappa_{ij}} - u_i^2 \lambda_{ij}^2 \right) \sin(u_i x) \sin(u_i x_0) \sin(v_j y) \sin(v_j y_0), \quad (\text{C.8})$$

with

$$u_i = \frac{2i-1}{2h_x} \pi, \quad v_j = \frac{2j-1}{2h_y} \pi, \quad (\text{C.9})$$

and $\lambda^2 = \kappa^2 - k^2$. Integrating over a single crack cell, the following terms are needed in the matrix element calculation.

$$\int_{z_0 - \Delta z/2}^{z_0 + \Delta z/2} e^{\lambda_{ij} z_0} dz_0 = \frac{2e^{\lambda_{ij} z_0}}{\lambda_{ij}} \sinh \left(\lambda_{ij} \frac{\Delta z}{2} \right), \quad (\text{C.10})$$

$$\frac{1}{\Delta x} \int_{x_0}^{x_0 + \Delta x} \sin(u_i x_0) dx_0 = \frac{2}{u_i \Delta x} \sin \left(\frac{u_i \Delta x}{2} \right) \sin \left[u_i \left(x_0 + \frac{\Delta x}{2} \right) \right], \quad (\text{C.11})$$

and

$$\int_{y_0 - \Delta y/2}^{y_0 + \Delta y/2} \sin(v_j y_0) dy_0 = \frac{2}{v_j} \sin \left(\frac{v_j \Delta y}{2} \right) \sin(v_j y_0). \quad (\text{C.12})$$

APPENDIX D. COILS INSIDE A BOREHOLE

The impedance change of a coil inside a borehole has been solved in integral form by Burke and Theodoulidis in 2004 [83] and in series form in 2007 [93]. Here, a different series form with the same truncation boundary conditions used before is given as a reference. This solution is used as the incident field calculation for the crack model.

Consider a coil inside a borehole in the absence of cracks, Fig. D.1. The problem has been stated in Chapter 4. The truncation conditions are the same as the ones we imposed before. The Fourier series representation of TE and TM potentials for the region between the coil and the cylindrical interface can be written as

$$\tilde{W}_{am}^{(0)} = \sum_{i=1}^{\infty} \sin(\kappa_i z) K_m(\kappa_i \rho) C_{mi}^{(0)}, \quad (\text{D.1})$$

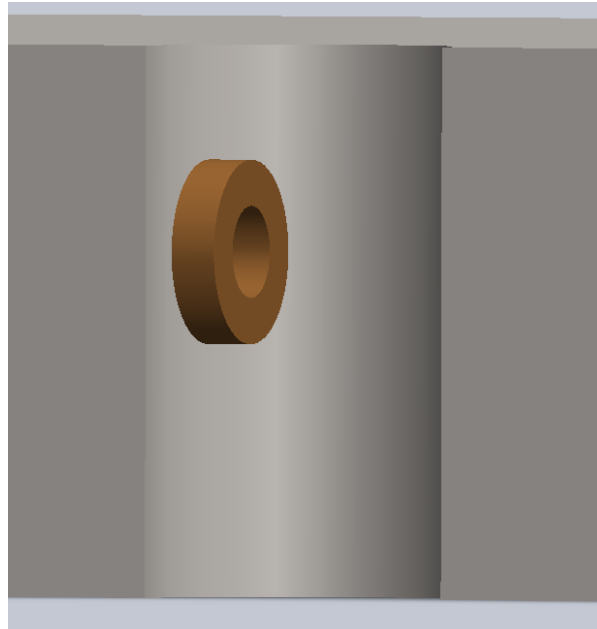


Figure D.1: A rotary coil inside a borehole.

due to the source and

$$\tilde{W}_{am}^{(1)} = \sum_{i=1}^{\infty} \sin(\kappa_i z) I_m(\kappa_i \rho) C_{mi}^{(1)}, \quad (\text{D.2})$$

due to the reflection. The TE and TM potentials representing the fields in the conductive region are expressed as

$$\tilde{W}_{am}^{(2)} = \sum_{i=1}^{\infty} \sin(\kappa_i z) K_m(\gamma_i \rho) C_{mi}^{(2)}, \quad (\text{D.3})$$

and

$$\tilde{W}_{bm}^{(2)} = \sum_{i=1}^{\infty} \cos(\kappa_i z) K_m(\gamma_i \rho) D_{mi}^{(2)}, \quad (\text{D.4})$$

where eigenvalues $\kappa_i = (2i - 1)\pi/2h$ and $\gamma_i^2 = \kappa_i^2 - k^2$.

By imposing the continuity conditions of magnetic fields at the interface $\rho = b$, we can determine the unknown coefficients as follows.

$$C_{mi}^{(1)} = \Gamma_{mi}^{aa} C_{mi}^{(0)}, \quad C_{mi}^{(2)} = T_{mi}^{aa} C_{mi}^{(0)}, \quad D_{mi}^{(2)} = T_{mi}^{ba} C_{mi}^{(0)}, \quad (\text{D.5})$$

where

$$\begin{aligned} \Gamma_{mi}^{aa} &= -\frac{K_m(\kappa_i b)}{I_m(\kappa_i b)} \{ \mu_r k^2 m^2 - M_m(\gamma_i b) [\mu_r \kappa_i^2 M_m(\gamma_i b) - \gamma_i^2 M_m(\kappa_i b)] \} \Delta_m^{-1}, \\ T_{mi}^{aa} &= \frac{\mu_r \kappa_i^2 M_m(\gamma_i b)}{I_m(\kappa_i b) K_m(\gamma_i b) \Delta_m}, \quad T_{mi}^{ba} = \frac{im \kappa_i \mu_r}{I_m(\kappa_i b) K_m(\gamma_i b) \Delta_m}. \end{aligned} \quad (\text{D.6})$$

Δ_m has been introduced in (4.54).

The impedance change of an induction coil inside the borehole is given by

$$\begin{aligned} \Delta Z &= \frac{i\omega}{\mu_0 I^2} \int_0^h \int_{-\pi}^{\pi} \left[\psi^{(1)} \frac{\partial \psi^{(0)}}{\partial \rho} - \psi^{(0)} \frac{\partial \psi^{(1)}}{\partial \rho} \right]_{\rho=b} b \, d\phi \, dz \\ &= \frac{i\omega \pi h}{\mu_0 I^2} \sum_{m=-\infty}^{\infty} \sum_{i=1}^{\infty} \kappa_i^2 C_{mi}^{(0)} C_{mi}^{(1)}, \end{aligned} \quad (\text{D.7})$$

where ψ is the magnetic scalar potential defined in (6.5).

The incident field distribution is required in the crack problem and the general expressions for the eddy current density components in the conductor are

$$J_{\rho} = i\omega\sigma \sum_{m=-\infty}^{\infty} e^{im\phi} \sum_{i=1}^{\infty} \sin(\kappa_i z) \left[\frac{im}{\rho} K_m(\gamma_i \rho) C_{mi}^{(2)} - \kappa_i \gamma_i K'_m(\gamma_i \rho) D_{mi}^{(2)} \right], \quad (\text{D.8})$$

$$J_{\phi} = -i\omega\sigma \sum_{m=-\infty}^{\infty} e^{im\phi} \sum_{i=1}^{\infty} \sin(\kappa_i z) \left[\gamma_i K'_m(\gamma_i \rho) C_{mi}^{(2)} + \frac{im}{\rho} \kappa_i K_m(\gamma_i \rho) D_{mi}^{(2)} \right], \quad (\text{D.9})$$

$$J_z = -i\omega\sigma \sum_{m=-\infty}^{\infty} e^{im\phi} \sum_{i=1}^{\infty} \gamma_i^2 \cos(\kappa_i z) K_m(\gamma_i \rho) D_{mi}^{(2)}. \quad (\text{D.10})$$

The source coefficients, $C_{mi}^{(0)}$ are determined by expressing the TE potential in the absence of conductors. There is no TM component involved for a coil in free space and TE potential satisfies Laplace equation. The field of a filament loop is equivalent to that of an infinitesimally thin magnetic shell at the surface bounded by the filament [94]. The potential expression of a filament is found by applying the Green's second theorem to the surface enclosing the magnetic disk. Finally, according to the superposition principle, the coil field is obtained by integrating over the rectangular cross section of the coil and the coefficients are

$$C_{mi}^{(0)} = -\frac{4\nu\mu_0 I \cos 9\kappa_i z_0}{\pi h \kappa_i^4} \sum_{n=-\infty}^{\infty} \Psi_{m-n}(\kappa x_2, \kappa x_1) \Xi_n(\kappa r_2, \kappa r_1), \quad (\text{D.11})$$

where

$$\Psi_m(\alpha_1, \alpha_2) = \int_{\alpha_1}^{\alpha_2} I_m(x) dx, \quad (\text{D.12})$$

and

$$\Xi_n(\alpha_1, \alpha_2) = n \sin(n\pi/2) \int_{\alpha_1}^{\alpha_2} \int_0^\nu \frac{1}{\xi} I_n(\xi) \sin \sqrt{\nu^2 - \xi^2} d\xi d\nu. \quad (\text{D.13})$$

The same approach can be used to determine the source coefficients for a bobbin coil. The solution is

$$C_{mi}^{(0)} = -\frac{4\nu\mu_0 I}{h\kappa_i^3} \chi(\kappa_i r_1, \kappa_i r_2) I_m(\kappa_i r_0) \sin(\kappa_i z_0) \sin\left(\frac{\kappa_i \ell}{2}\right), \quad (\text{D.14})$$

where χ is defined in (B.7).

APPENDIX E. BOUNDARY INTEGRAL EQUATION FOR EDDY-CURRENT PROBLEMS WITH DIRICHLET BOUNDARY CONDITION

A paper published in Journal of Nondestructive Evaluation¹

Hui Xie^{2,3,4}, Jiming Song^{2,5}, Ming Yang², Norio Nakagawa³

Abstract

A boundary integral equation (BIE) is developed for the eddy-current (EC) problems with Dirichlet boundary condition by considering the difference between the field without cracks and the one with cracks. Once the field and its normal derivative are given for the structure in the absence of cracks, normal derivative of the scattered field on the surface can be calculated by solving this integral equation numerically. For infinite-domain problems, this equation is more efficient than the conventional BIE due to a smaller computational region needed. Four kinds of two-dimensional EC problems have been solved using this integral equation. The surface impedance for different cases is presented in this paper. Numerical results are compared with analytical solutions and published numerical results. There are good agreements between them. Also, this concept can be extended to three-dimensional problems with other boundary conditions.

¹This work was supported in part by the National Science Foundation CAREER Grant ECS-0547161 and in part by Harpole-Pentair Assistant Professorship at Iowa State University.

²Department of Electrical and Computing Engineering, Iowa State University, Ames, IA 50011, USA.

³Center for Nondestructive Evaluation, Iowa State University, Ames, IA 50011, USA.

⁴Primary researcher and author.

⁵Primary researcher and corresponding author, e-mail: jisong@iastate.edu.

Introduction

Boundary element method (BEM) is one of widely used numerical approaches for solving eddy-current (EC) problems due to its high efficiency and the ability to handle complex geometries [6]. With different boundary integral formulations, this approach has been applied to many kinds of EC problems to investigate the eddy-current interaction with cracks [69, 70, 68]. In contrast, other numerical methods, such as finite element method (FEM) and volume integral method, are very expensive to analyze EC problems due to the need of dealing with high conductivity at low frequency. Besides this, BEM is applicable not only to the problems with bounded region but also to the infinite-domain problems.

The key part of BEM is to find appropriate boundary integral equations (BIEs). For various EC problems, different BIEs should be derived to take the advantage of crack models. The ideal crack is a mathematical model which is defined as a surface crack of infinitesimal thickness. The BEM has been applied to this crack model for different inclination in a uniform applied field by Kahn [65]. Nonetheless, only the sum of the surface impedance on both sides of the ideal crack could be solved using Kahn's equation. The v-groove crack model in a nonuniform field was also investigated in that work. Beyond this, the ideal crack can be modeled as a current dipole layer on the crack surface and the radiated field can be viewed as being generated by this dipole layer because of zero thickness. An electric field integral equation (EFIE) has been formulated to find the dipole density for the ideal crack [40, 74]. In addition, BIEs for the magnetic vector potential have been developed using an complicated integral kernel with a weaker singularity than that of the EFIE approach [42]. By combining the variational method with BEM, Nakagawa et al. have studied the effect of crack closure, which may produce weak but finite electrical contacts inside the thin crack [125]. However, these BIEs are only valid for the thin crack model, in which crack thickness is quite small compared with other dimensions and the skin depth.

On the other hand, the ideal crack model, due to its simple geometric structure, has been analytically investigated in some EC problems. For a deep crack, this model involves eddy-current interaction with the sharp tip and the square corner. Kahn et al. have analytically solved the

semi-infinite crack problem, which is a special case of the thin crack model, with modification of Sommerfeld's diffraction theory and the square corner problem with image theory [33]. An approximate closed form solution for a long, surface-breaking crack has been obtained using the Wiener-Hopf technique by Harfield and Bowler [46]. A infinitely long conducting cylinder with a radial crack has also been analyzed in terms of a series of Bessel functions by Spal and Kahn [34].

In order to efficiently solve more general EC problems for both bounded and infinite region with less number of unknowns, a BIE for the magnetic field is proposed in this paper. The formulation is based on the solution for the structure in the absence of cracks. In combination with the method of moments (MoM), this integral equation can be solved numerically. The proposed BIE provides an easier way to truncate the unbounded computational domain without adding any extra hypothetical boundaries. Here, the crack models mentioned above, including thin crack and v-groove crack models, are used to examine this approach.

Formulation

General Formulation

For the sake of simplicity, two-dimensional (2D) EC problems with surface crack are considered. Assume the conductor is nonmagnetic material, which has the permeability of free space μ_0 and the conductivity σ . A uniform magnetic field H_0 , which has only a z component, is applied to the crack as shown in Fig. E.1. Here, time factor $e^{-\omega t}$ is suppressed. In the conductor, total magnetic field $H(\boldsymbol{\rho})$ satisfies the scalar Helmholtz equation

$$(\nabla^2 + k^2)H(\boldsymbol{\rho}) = 0, \quad (\text{E.1})$$

where $k^2 = \omega\mu_0\sigma$. The corresponding BIE can be written as

$$\int_S dS(\boldsymbol{\rho}') G(\boldsymbol{\rho}, \boldsymbol{\rho}') \frac{\partial H(\boldsymbol{\rho}')}{\partial n'} = H(\boldsymbol{\rho}) + H_0 \int_S dS(\boldsymbol{\rho}') \frac{\partial G(\boldsymbol{\rho}, \boldsymbol{\rho}')}{\partial n'},$$

where \boldsymbol{n} is the normal direction of the boundary surface, S , and $G(\boldsymbol{\rho}, \boldsymbol{\rho}')$ is the Green's function for 2D Helmholtz wave equation, which is given by

$$G(\boldsymbol{\rho}, \boldsymbol{\rho}') = \frac{i}{4} H_0^{(1)}(k|\boldsymbol{\rho} - \boldsymbol{\rho}'|),$$

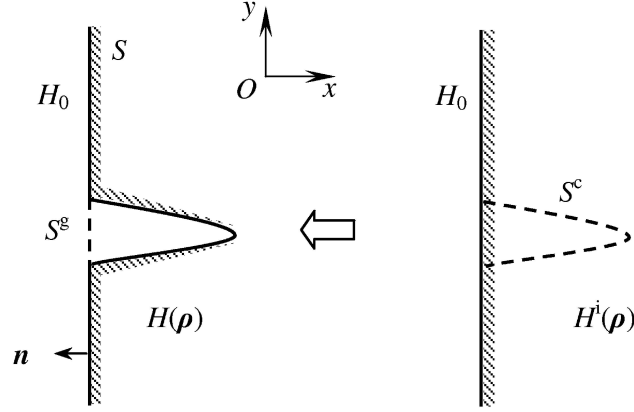


Figure E.1: Schematic configuration of the surface crack problems with uniform applied field, H_0 . $H^i(\boldsymbol{\rho})$ is the incident magnetic field in the absence of cracks. S^c and S^g represent crack surface and “gap” surface, respectively.

where $H_0^{(1)}(z)$ is the Hankel function of the first kind of zero order. If $\boldsymbol{\rho}$ approaches the surface S , (E.2) has the following form

$$\int_S dS(\boldsymbol{\rho}') G(\boldsymbol{\rho}, \boldsymbol{\rho}') \frac{\partial H(\boldsymbol{\rho}')}{\partial n'} = \frac{1}{2} H_0 + H_0 \int_S dS(\boldsymbol{\rho}') \frac{\partial G(\boldsymbol{\rho}, \boldsymbol{\rho}')}{\partial n'}.$$

Here, all integrals in (E.2) are based on principal values. This equation is referred to as the conventional BIE in the following discussion. For the problems with infinite domain, the integral should be performed over the whole surface S (including crack surface S^c) when (E.2) is solved. Several extra long enough hypothetical boundaries should be needed to truncate the computational domain if numerical methods are applied to this equation.

Now let us rewrite the total magnetic field as

$$H(\boldsymbol{\rho}) = H^i(\boldsymbol{\rho}) + H^s(\boldsymbol{\rho}), \quad (\text{E.2})$$

where $H^i(\boldsymbol{\rho})$ is the incident magnetic field, the field in the absence of the crack, and $H^s(\boldsymbol{\rho})$ is the magnetic field scattered by the crack. The incident field also satisfies (E.2) except only for the surface without cracks. Therefore, the BIE for the scattered field, $H^s(\boldsymbol{\rho})$, can be derived by combining (E.2) and the BIE for the incident magnetic field

$$\int_S dS(\boldsymbol{\rho}') G(\boldsymbol{\rho}, \boldsymbol{\rho}') \frac{\partial H^s(\boldsymbol{\rho}')}{\partial n'} = H^{\text{inc}}(\boldsymbol{\rho}) + \int_{S^c - S^g} dS(\boldsymbol{\rho}') \left[H_0 \frac{\partial G(\boldsymbol{\rho}, \boldsymbol{\rho}')}{\partial n'} - G(\boldsymbol{\rho}, \boldsymbol{\rho}') \frac{\partial H^i(\boldsymbol{\rho}')}{\partial n'} \right],$$

where

$$H^{\text{inc}}(\boldsymbol{\rho}) = \begin{cases} \frac{1}{2}H_0 - H^i(\boldsymbol{\rho}) & \boldsymbol{\rho} \in S^c \\ 0 & \boldsymbol{\rho} \in S \text{ except } S^c \end{cases} \quad (\text{E.3})$$

and the subscript of the integral on the right hand side of (E.3), $S^c - S^g$, represents subtracting the integral over S^g from that over S^c . The “gap” region S^g is the surface without cracks excluding the part which overlaps with the whole surface S , as shown in Fig. E.1. The right hand side of (E.3) just involves a smaller computational region compared with (E.2) and its value goes to zero when the point $\boldsymbol{\rho}$ is far away from the crack region. To solve (E.3), we only need to truncate the computational domain without adding any extra boundaries. Apparently, it is more efficient and faster than using (E.2) to solve EC problems. More detailed discussion is given in Section E.

Ideal Crack

As stated above, the ideal crack, which acts as a perfect barrier to the flow of eddy current, has infinitesimal thickness. Thus, only the sum of the fields on opposite sides of the crack, $H_+^s - H_-^s$, can be solved. Here, subscripts, \pm , refer to limiting values approaching each side of the crack surface S^\pm , as shown in Fig. E.2. The integral over surface S^g is equal to zero due to the infinitesimal thickness. Finally, (E.3) can be reduced to

$$\int_{S^c} G \frac{\partial(H_+^s - H_-^s)}{\partial n'} dS + \int_{S \text{ except } S^c} G \frac{\partial H^s}{\partial n'} dS = \begin{cases} H_0 - H^i(\boldsymbol{\rho}) & \boldsymbol{\rho} \in S^c \\ 0 & \boldsymbol{\rho} \in S \text{ except } S^c \end{cases} \quad (\text{E.4})$$

which is the same as the formulation derived by Kahn [65]. Notice that half of H_0 is added to $H^{\text{inc}}(\boldsymbol{\rho})$ in (E.3) for the point over the crack surface S^c , because the contribution from the point on the opposite side of the crack, which introduces another principal value, should be considered when crack thickness goes to zero.

The concept we demonstrate in this paper is similar to the one mentioned in [65]. The problems discussed here, however, are more general and the surface impedance on both sides of the thin crack can be calculated separately. That is the reason why (E.3) can be reduced

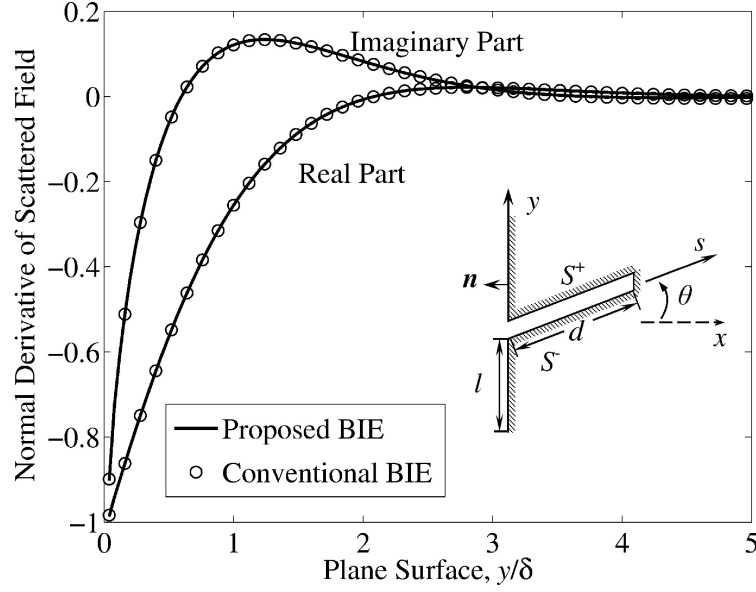


Figure E.2: Normal derivative of the scattered field on the plane surface for a perpendicular crack ($\theta = 0^\circ$) with depth $d = 4\delta$. Values are normalized by the surface impedance for the half-space conductor. Numerical results calculated from proposed (*solid line*) and conventional (*circle*) BIEs are shown. Inset: configuration of the thin crack in a half-space conductor (Surface S^+ and S^- are the upper and lower surfaces of the crack, respectively).

to (E.4) for the ideal crack model, in which the surface impedance on both sides of the crack should be calculated together.

Numerical Results

The proposed BIE is discretized into matrix equation by virtue of the MoM [106]. Pulse basis and point-matching (collocation) method are used in our code. Matrix element is evaluated with standard six-point Gaussian quadrature rule [109] or the one incorporating logarithmic singularities [107]. Based on the given incident field, $H^i(\rho)$, and its normal derivative, $\partial H^i/\partial n$, our program is implemented allowing for arbitrary surface crack in the conductor with simple structure, such as a half-space plane, an infinitely long cylinder, or a thin metal sheet. Four kinds of two-dimensional EC problems are tested in our work: a thin crack or a v-groove crack in the half-space conductor and a surface crack in the conducting cylinder or the quarter-space conductor. Normal derivative of the scattered field $\partial H^s/\partial n$ is calculated first from (E.3). Then

normal derivative of the total field $\partial H/\partial n$, which is proportional to the surface impedance due to the uniform applied magnetic field, is obtained by adding the contribution from the incident field $\partial H^i/\partial n$ together according to (E.2).

In order to verify our formulation and program, a thin crack in the half-space conductor is examined first. The configuration is briefly summarized in the inset of Fig. E.2. The depth of the crack is d and the angle between the crack surface and the normal of the plane surface is θ . All the lengths are normalized by the skin depth δ . The incident field for the half-space conductor is $H^i(\rho) = H_0 e^{ikx}$. In our implementation, the tip of the thin crack is modeled as one single element.

Figure E.2 shows the normal derivative of scattered field over the plane surface for the case with $d = 4\delta$ and $\theta = 0^\circ$. Numerical results calculated from the conventional BIE with domain truncation are also plotted for comparison. Results are normalized by the surface impedance for the half-space conductor, $-ikH_0$. Curves in Fig. E.2 clearly indicate the eddy-current interaction with a square corner can extend to about 2.5δ . Thus, at least a range of 5δ is needed to separate the mutual influence between two neighbor corners. In solving the conventional BIE, the solution domain should be truncated to a $10 \times 15\delta^2$ rectangle to ensure the correctness of the results for this case. As a result, the evaluation of integrals in (E.2) should be implemented over a length of about 58δ , but 18δ is enough for the proposed BIE. This means a large computational region and a lot of extra unknowns should be required if the conventional BIE with domain truncation, which introduces several corners to truncate the infinite region, is used to solve this kind of problems. Computational region, however, can be just confined to the region one needs without adding any hypothetical boundaries using (E.3). The number of unknowns and CPU time also can be significantly decreased.

The error due to domain truncation should be considered if the proposed BIE is used to solve infinite-domain problems. For the same case ($d = 4\delta, \theta = 0^\circ$), the results with different truncated lengths are compared. Here, truncated length l denotes the distance from truncated boundary to the crack, as shown in Fig. E.2. By choosing the result with $l = 20\delta$ as a reference, absolute errors for corresponding point with different truncated lengths are illustrated in Fig. E.3. The accuracy is improved when the truncated length increases. Because of domain

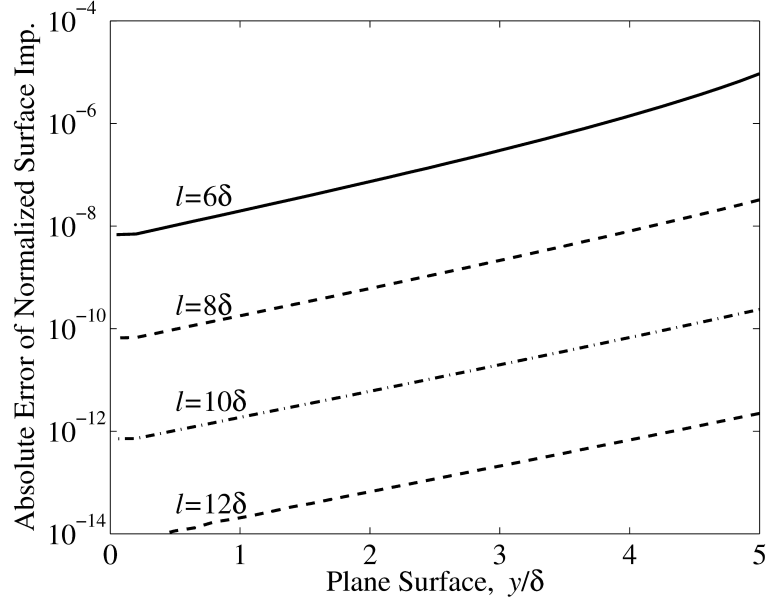


Figure E.3: Absolute error in the normalized surface impedance, $\frac{\partial H}{\partial n}/(-ikH_0)$, on the plane surface for different truncated length l ($d = 4\delta$, $\theta = 0^\circ$). The result with $l = 20\delta$ is chosen as the reference.

truncation, the error for the points close to the truncated boundary is greater than those close to the crack.

Figure E.4 shows a comparison of the normalized surface impedance, $\frac{\partial H}{\partial n}/(-ikH_0)$, on the crack surface calculated from (E.3) and Kahn's results [65] for the same case as that of Fig. E.2 with $\theta = 0^\circ$. In our program, surface impedance on each side of the thin crack is calculated separately. Then the average of them is taken to compare with Kahn's results. Due to the symmetry of this structure, surface impedance on the upper crack surface S^+ and the lower one S^- are the same as their average value. These numerical results are also compared with analytical solutions for two limiting cases: infinitely deep crack (for $2.5 < s/\delta < 4$) and a square corner (for $0 < s/\delta < 2$) [33]. There are good agreements when the crack is deep enough so that contributions from tip and corner can be separated with each other. When the crack depth is relatively small, they can not be treated separately. So the analytical solution of these two limiting cases should not to be used to check the numerical results. Nonetheless, results calculated from the conventional BIE can be used to make a comparison. Our numerical results also have good agreements with Kahn's [65] for cases with $d = \delta$ or 0.5δ . It should be

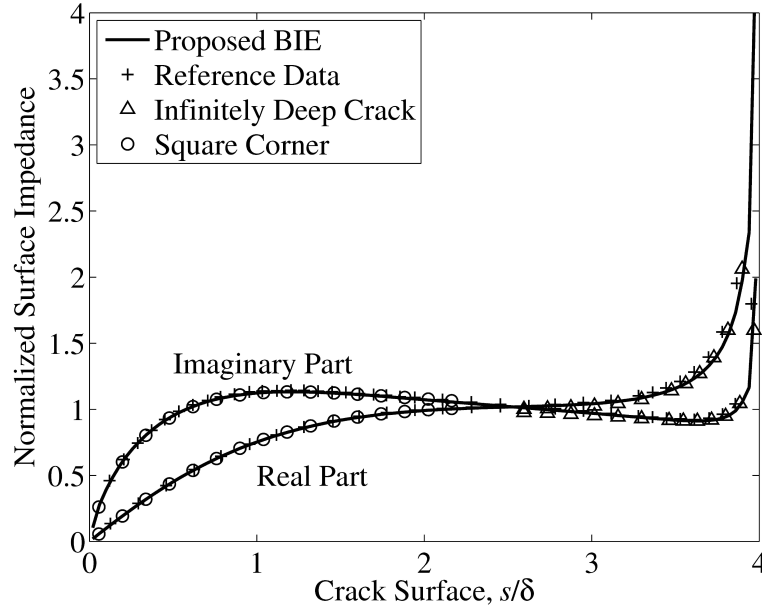
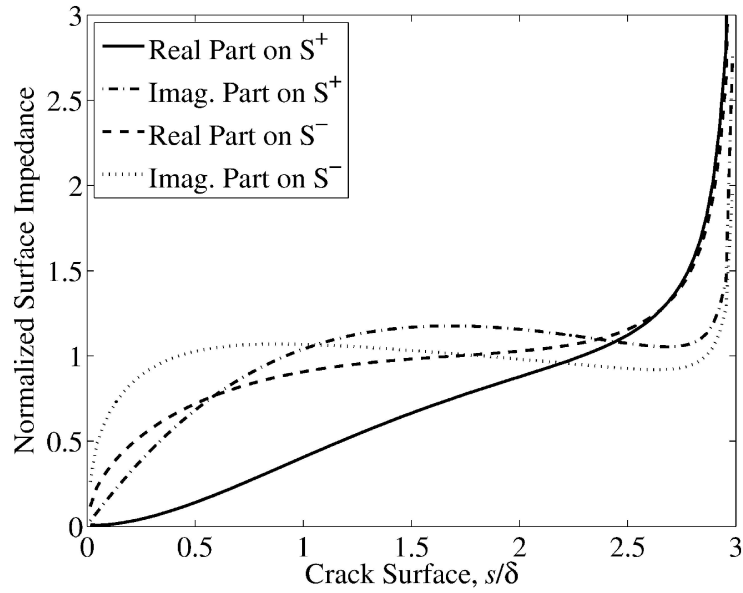


Figure E.4: Normalized surface impedance on the crack surface for a perpendicular crack with depth $d = 4\delta$. The results (*solid line*) are calculated using the proposed BIE. Kahn's results [65] for the ideal crack (*plus sign*) are plotted. The analytical solution for the infinitely deep crack (*triangle*) and square corner (*circle*) are also shown for comparison.

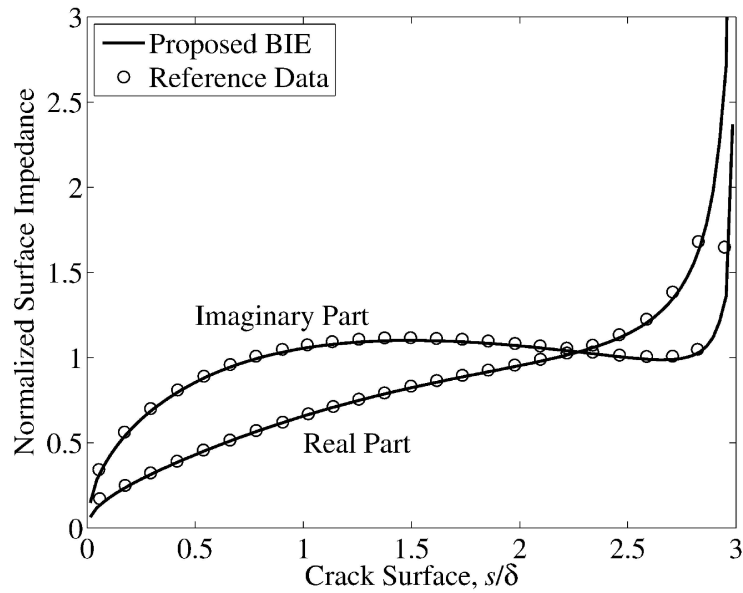
noticed that our results come from the thin crack model, while the ideal crack model was used in Kahn's calculation.

Figures E.5 and E.6 show the normalized surface impedance for the case with $d = 3\delta$ and $\theta = 30^\circ$. Fig. E.5(a) shows the surface impedance on both sides of the crack separately. Different current distribution can be observed due to the asymmetrical structure. The change of eddy current becomes more rapid around the sharp corner. Fig. E.5(b) shows the average of surface impedances on both sides for each sampling point. Kahn's results [65] for the ideal crack with same depth are also plotted for comparison. Again, the slight difference between them comes from the different crack models used, i.e. the difference between the thin crack and the ideal crack. Fig. E.6 shows the normalized surface impedance over the plane surface compared with Kahn's results [65]. It is clear to see the disturbance of eddy current stretches out further in the positive y -direction, which is the direction of the crack inclination.

For the second comparison, a v-groove crack in the half-space conductor is considered to check the terms associated with the integral over "gap" surface S^g in (E.3). The configuration



(a)



(b)

Figure E.5: Normalized surface impedance over the crack surface for a crack with $d = 3\delta$ and $\theta = 30^\circ$. The results on both sides of the crack (a) and the average value of them (b) are plotted. Also Kahn's results [65] for the ideal crack (*circle*) are shown in (b).

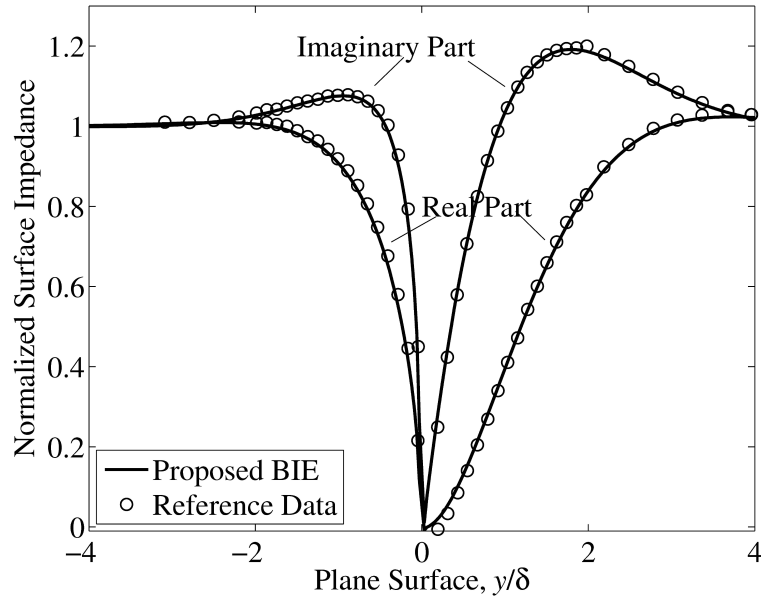
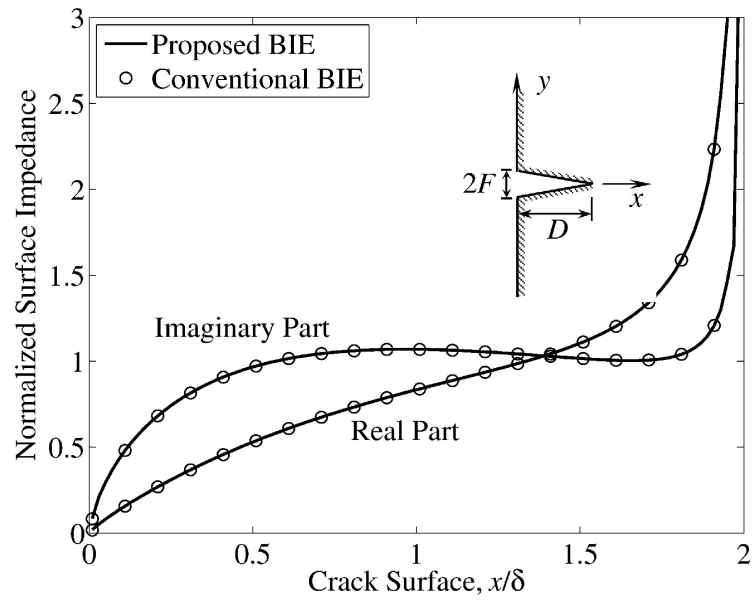


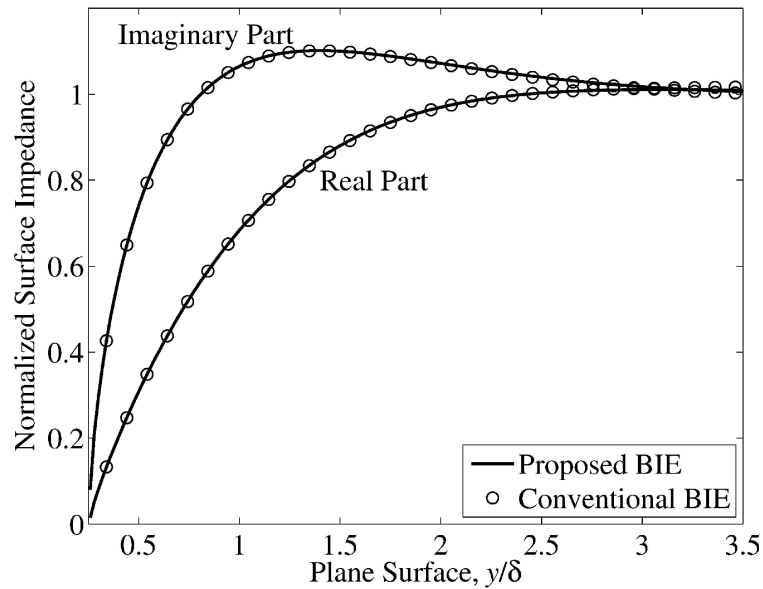
Figure E.6: Comparison of results from Kahn (*circle*) [65] and the proposed BIE (*solid line*) for the normalized surface impedance on the plane surface: $d = 3\delta$ and $\theta = 30^\circ$.

is illustrated in Fig. E.7(a). The depth of the crack is D and the half width of the opening is F . Incident field is the same as that for the preceding structure. Fig. E.7 shows the normalized surface impedance over both the crack surface and the plane surface for the case with $D = 2\delta$ and $F = 0.25\delta$. Numerical results are compared with those obtained from the conventional BIE with large enough truncated domain. A length of 45δ is needed for this calculation with the conventional BIE, whereas one-quarter of this length is sufficient for the proposed equation. The improvement of the efficiency is obvious.

Another example we use is a thin crack in the infinitely long, conducting cylinder, as shown in Fig. E.8. The radius of the cylinder a and the depth of the crack d are equal to the skin depth. A single element is used to model the tip of the crack, which is the same as that for the half-space conductor. Fig. E.8 shows a comparison between numerical and analytical results for the surface impedance on both crack surface and cylinder surface. The value is normalized by the surface impedance for a conducting cylinder in the absence of cracks. Analytical solution is calculated from equations given in [34]. Due to limited computational region, the efficiency of proposed BIE is the same as that of the conventional BIE.



(a)



(b)

Figure E.7: Normalized surface impedance on both crack surface (a) and plane surface (b) for a v-groove crack with depth $D = 2\delta$ and half-opening $F = 0.25\delta$. The results calculated from proposed (*solid line*) and conventional (*circle*) BIEs are shown for comparison.

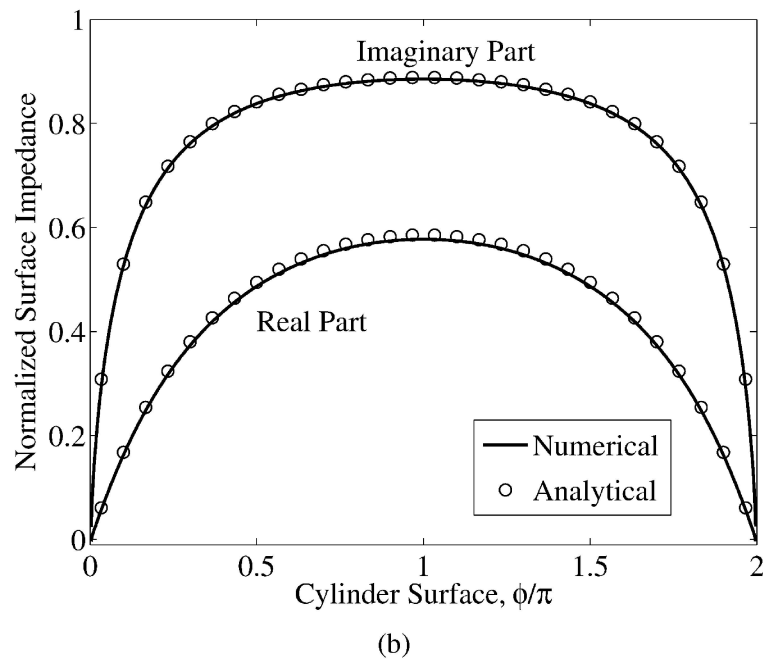
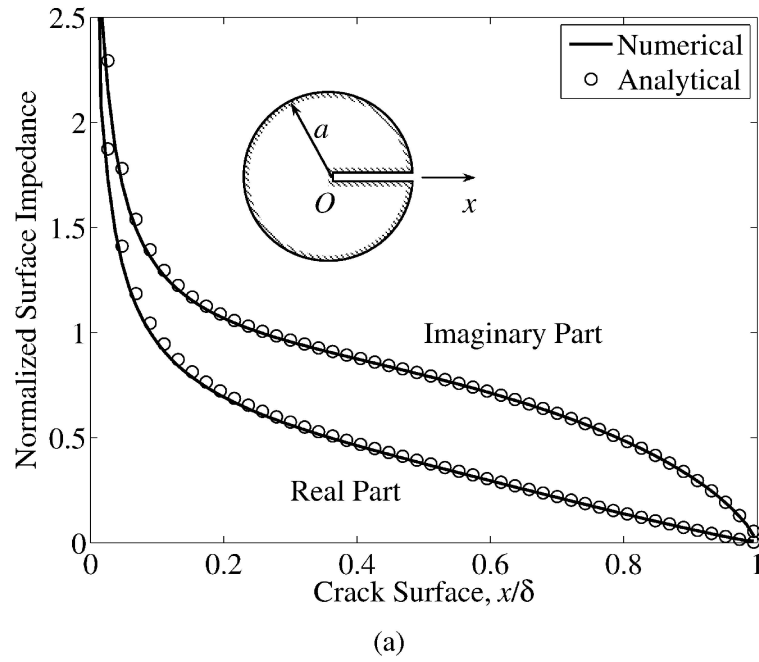


Figure E.8: Comparison of numerical result (*solid line*) and analytical solution (*circle*) for the normalized surface impedance on both crack surface (a) and cylinder surface (b), $d = a = 1\delta$.

Finally, numerical results for a thin crack in the quarter-space conductor with different depth are shown in Fig. E.9. The angle between crack surface and horizontal plane is θ . The incident field and its normal derivative used in (E.3) are solved analytically by image theory [33]. Again, comparisons are made with the results calculated from the conventional BIE. The results for a crack in the half-space conductor with the same inclination angle ($\theta = 45^\circ$) are also plotted. It is reasonable to see the results agree well with each other when the crack depth is long enough ($d = 8\delta$ is used here) as shown in Figs. E.9(a) and E.9(b), whereas the effect on account of square corner can be observed when the crack becomes shorter as illustrated in Figs. E.9(c) and E.9(d). Fig. E.9(d) indicates about 3δ should be considered to separate the interaction between two neighbor corners and roughly $8 \times 8\delta^2$ truncated area should be included for the conventional BIE. Therefore, a length of 10δ for the proposed equation is still much smaller than that for the conventional BIE.

The number of unknowns N assigned in the above infinite-domain cases are listed in Table E.1. The inverse matrix is obtained using the direct solver. The matrix-filling time, as well as the memory requirement are proportional to the square of the number of unknowns, $O(N^2)$, assuming the incident field can be directly calculated using analytical solution. As can be seen from this table, the advantage of the proposed BIE is obvious.

Table E.1: Number of unknowns computed in five infinite-domain cases.

Number of unknowns, N	Conventional BIE	Proposed BIE
Thin crack in half space (Fig. E.2, $d = 4\delta$, $\theta = 0^\circ$)	870	270
Thin crack in half space (Fig. E.2, $d = 3\delta$, $\theta = 30^\circ$)	810	195
V-groove crack in half space (Fig. E.7(a), $F = 0.25\delta$, $D = 2\delta$)	675	180
Thin crack in quarter space (Fig. E.9(a), $d = 8\delta$, $\theta = 45^\circ$)	960	480
Thin crack in quarter space (Fig. E.9(a), $d = 3\delta$, $\theta = 45^\circ$)	570	150

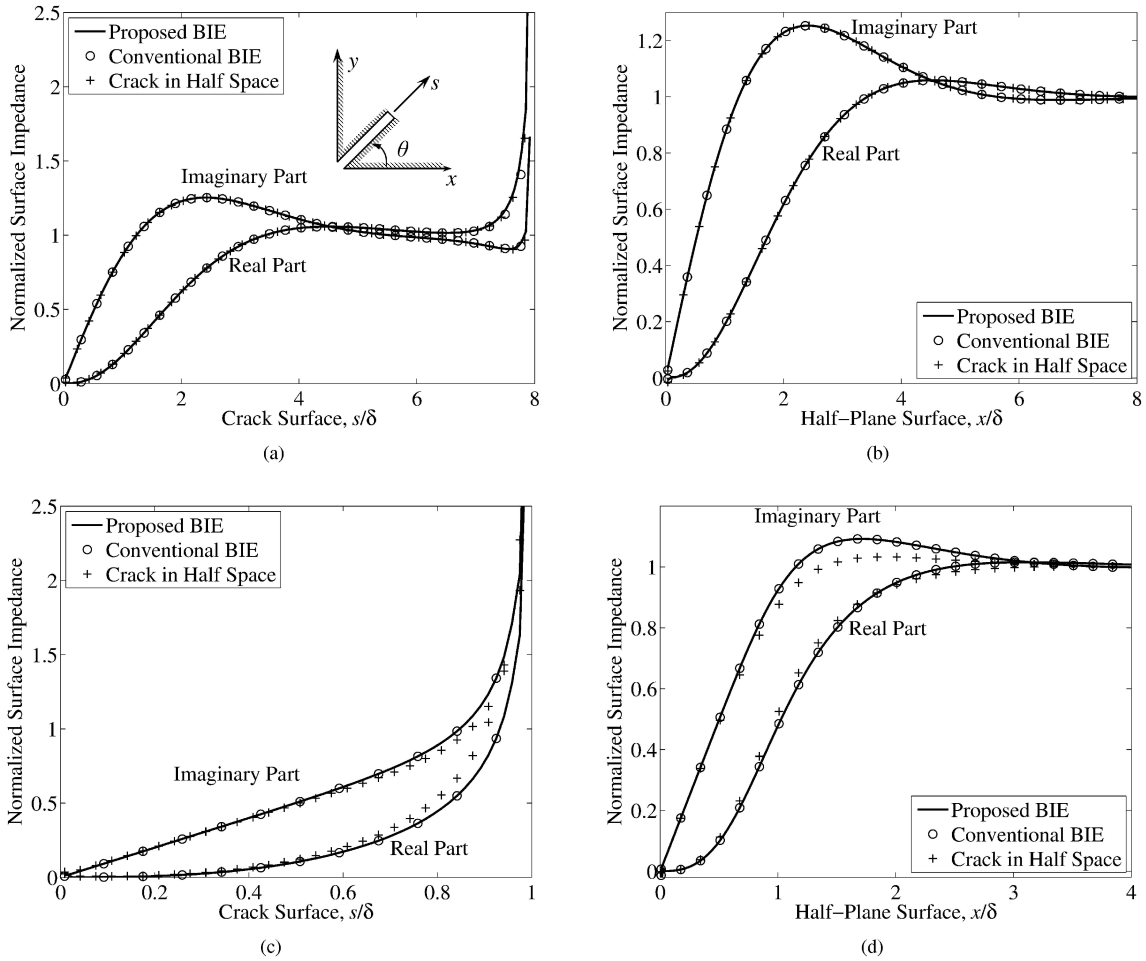


Figure E.9: Normalized surface impedance of cases with $d = 8\delta$, $\theta = 45^\circ$ (a, b) and $d = \delta$, $\theta = 45^\circ$ (c, d). Numerical results from proposed (*solid line*) and conventional (*circle*) BIEs are shown. The results for the surface crack in a half-space conductor with same inclination angle (*plus sign*) are also plotted.

Conclusion

A BIE has been proposed to solve two-dimensional EC problems for the given incident field and its normal derivative. The formulation, implemented with the MoM, has been validated with analytical results and published numerical data for different kinds of 2D structures. This approach not only can be used to solve infinite-domain problems without adding any hypothetical boundaries, but also is more efficient than the conventional BIE because of a smaller computational domain needed. In addition, surface impedance on each side of the thin crack can be calculated separately through our proposed BIE. It is certainly helpful to understand the interaction between eddy current and cracks. Despite the EC problems over a finite computational domain can not be accelerated with this approach, the computational speed for the infinite-domain problem can be improved a lot without too much extra programming effort.

Although the structures discussed in this paper pertain to two-dimensional EC problems with Dirichlet boundary condition, the concept described here can be similarly applied to three-dimensional structures and other boundary conditions to reduce the number of unknowns. However, the incident field without cracks $H^i(\boldsymbol{\rho})$ in (E.2) needs to be calculated using numerical method for the problems with complex geometric boundary.

BIBLIOGRAPHY

- [1] C. Hellier and M. Shakinovsky, *Handbook of Nondestructive Evaluation*, 2nd ed. McGraw-Hill Professional, 2012.
- [2] N. Bowler, "Eddy current nondestructive evaluation," unpublished.
- [3] C. A. Balanis, *Advanced Engineering Electromagnetics*. John Wiley & Sons, 1989.
- [4] R. Albanese and G. Rubinacci, "Formulation of the eddy-current problem," *IEE Proc.-A*, vol. 137, no. 1, pp. 16–22, Jan. 1990.
- [5] E. Kriezis, T. Tsiboukis, S. Panas, and J. Tegopoulos, "Eddy currents: theory and applications," *P. IEEE*, vol. 80, no. 10, pp. 1559–1589, Oct. 1992.
- [6] B. A. Auld and J. C. Moulder, "Review of advances in quantitative eddy current nondestructive evaluation," *J. Nondestruct. Eval.*, vol. 18, no. 1, pp. 3–36, 1999.
- [7] J. S. Knopp, J. C. Aldrin, and P. Misra, "Considerations in the validation and application of models for eddy current inspection of cracks around fastener holes," *J. Nondestruct. Eval.*, vol. 25, no. 3, pp. 123–137, Sept. 2006.
- [8] J. S. Knopp, J. C. Aldrin, and K. V. Jata, "Computational methods in eddy current crack detection at fastener sites in multi-layer structures," *Nondestruct. Test. Eva.*, vol. 24, no. 1–2, pp. 103–120, 2010.
- [9] S. Paillard, G. Pichenot, M. Lambert, and H. Voillaume, "Eddy current modelling for fasteners inspection in aeronautic," in *ECNDT 2006 Proc.* Berlin: Eur. NDT, Sept. 2006, pp. 1–8.

- [10] S. Paillard, G. Pichenot, M. Lambert, and H. Voillaume, "Eddy current modelling for inspection of riveted structures in aeronautics," in *Stud. Appl. Electromag.*, 2007, vol. 28, pp. 25–32.
- [11] P. R. Underhill and T. W. Krause, "Eddy current analysis of mid-bore and corner cracks in bolt holes," *NDT & E Int.*, vol. 44, no. 6, pp. 513–518, 2011.
- [12] C. V. Dodd and W. E. Deeds, "Analytical solutions to eddy-current probe-coil problems," *J. Appl. Phys.*, vol. 39, no. 6, pp. 2829–2838, 1968.
- [13] S. K. Burke, "Eddy-current inspection of cracks in a multilayer conductor," *J. Appl. Phys.*, vol. 67, no. 1, pp. 465–476, 1990.
- [14] J. W. Luquire, W. E. Deeds, and C. V. Dodd, "Alternating current distribution between planar conductors," *J. Appl. Phys.*, vol. 41, no. 10, pp. 3983–3991, 1970.
- [15] L. Yong, T. P. Theodoulidis, and T. G. Yun, "Magnetic field-based eddy-current modeling for multilayered specimens," *IEEE Trans. Magn.*, vol. 43, no. 11, pp. 4010–4015, Nov. 2007.
- [16] J. W. Luquire, W. E. Deeds, and C. V. Dodd, "Axially symmetric eddy currents in a spherical conductor," *J. Appl. Phys.*, vol. 41, no. 10, pp. 3976–3982, 1970.
- [17] T. P. Theodoulidis and E. Kriezis, "Coil impedance due to a sphere of arbitrary radial conductivity and permeability profiles," *IEEE Trans. Magn.*, vol. 38, no. 3, pp. 1452–1460, May 2002.
- [18] C. V. Dodd, C. C. Cheng, and W. E. Deeds, "Induction coils coaxial with an arbitrary number of cylindrical conductors," *J. Appl. Phys.*, vol. 45, no. 2, pp. 638–647, 1974.
- [19] T. Okita and T. Takagi, "Impedance analysis of circular coils on double-structured axisymmetrical cylinders with different conductivities and permeabilities," *Eur. Phys. J.-Appl. Phys.*, vol. 52, no. 1, p. 10801, 2010.
- [20] R. E. Beissner and M. J. Sablik, "Theory of eddy currents induced by a nonsymmetric coil above a conducting half-space," *J. Appl. Phys.*, vol. 56, no. 2, pp. 448–454, 1984.

- [21] S. K. Burke, "Impedance of a horizontal coil above a conducting half-space," *J. Phys. D Appl. Phys.*, vol. 19, no. 7, pp. 1159–1173, 1986.
- [22] S. K. Burke and M. E. Ibrahim, "Mutual impedance of air-cored coils above a conducting plate," *J. Phys. D Appl. Phys.*, vol. 37, no. 13, pp. 1857–1868, 2004.
- [23] T. P. Theodoulidis, "Analytical model for tilted coils in eddy-current nondestructive inspection," *IEEE Trans. Magn.*, vol. 41, no. 9, pp. 2447–2454, Sept. 2005.
- [24] T. P. Theodoulidis, "Model of ferrite-cored probes for eddy current nondestructive evaluation," *J. Appl. Phys.*, vol. 93, no. 5, pp. 3071–3078, Mar. 2003.
- [25] T. P. Theodoulidis, "Application of the eigenvalues method in eddy current NDE: A model of eddy current ferrite-cored probes," in *Stud. Appl. Electromag.*, ser. VII, G. Dobmann, Ed., 2006, pp. 164–170.
- [26] S. K. Burke, "Eddy-current induction in a uniaxially anisotropic plate," *J. Appl. Phys.*, vol. 68, no. 7, pp. 3080–3090, 1990.
- [27] J. Zhou and W. D. Dover, "Electromagnetic induction in anisotropic half-space and electromagnetic stress model," *J. Appl. Phys.*, vol. 83, no. 3, pp. 1694–1701, Feb. 1998.
- [28] T. P. Theodoulidis, *Eddy current canonical problems (with applications to nondestructive evaluation)*. Tech Science Press, 2006.
- [29] T. P. Theodoulidis and E. Kriezis, "Series expansions in eddy current nondestructive evaluation models," *J. Mater. Process. Tech.*, vol. 161, no. 1-2, pp. 343–347, 2005.
- [30] T. P. Theodoulidis and J. R. Bowler, "Eddy current coil interaction with a right-angled conductive wedge," *P. Roy. Soc. A-Math. Phys.*, vol. 461, no. 2062, pp. 3123–3139, 2005.
- [31] T. P. Theodoulidis and J. R. Bowler, "Interaction of an eddy-current coil with a right-angled conductive wedge," *IEEE Trans. Magn.*, vol. 46, no. 4, pp. 1034–1042, Apr. 2010.

- [32] J. R. Bowler and T. P. Theodoulidis, "Coil impedance variation due to induced current at the edge of a conductive plate," *J. Phys. D Appl. Phys.*, vol. 39, no. 13, pp. 2862–2868, July 2006.
- [33] A. H. Kahn, R. Spal, and A. Feldman, "Eddy-current losses due to a surface crack in conducting material," *J. Appl. Phys.*, vol. 48, no. 11, pp. 4454–4459, Nov. 1977.
- [34] R. Spal and A. H. Kahn, "Eddy currents in a conducting cylinder with a crack," *J. Appl. Phys.*, vol. 50, no. 10, pp. 6135–6138, Oct. 1979.
- [35] A. M. Lewis, "Electromagnetic methods for NDE of metal fatigue cracks: practical techniques and theoretical models," *Nondestruct. Test. Eva.*, vol. 6, no. 6, pp. 389–409, May 1992.
- [36] S. K. Burke and L. R. F. Rose, "Interaction of induced currents with cracks in thin plates," *P. Roy. Soc. Lond. A Mat.*, vol. 418, no. 1854, pp. 229–246, 1988.
- [37] N. Harfield, Y. Yoshida, and J. R. Bowler, "Low-frequency perturbation theory in eddy-current non-destructive evaluation," *J. Appl. Phys.*, vol. 80, no. 7, pp. 4090–4100, 1996.
- [38] T. P. Theodoulidis and J. R. Bowler, "Eddy-current interaction of a long coil with a slot in a conductive plate," *IEEE Trans. Magn.*, vol. 41, no. 4, pp. 1238–1247, Apr. 2005.
- [39] J. R. Bowler and S. A. Jenkins, "Validation of three dimensional eddy-current probe-flaw interaction model using analytical results," *IEEE Trans. Magn.*, vol. 26, no. 5, pp. 2085–2088, Sept. 1990.
- [40] J. R. Bowler, "Eddy-current interaction with an ideal crack. I. The forward problem," *J. Appl. Phys.*, vol. 75, no. 12, pp. 8128–8137, 1994.
- [41] J. R. Bowler, S. A. Jenkins, L. D. Sabbagh, and H. A. Sabbagh, "Eddy-current probe impedance due to a volumetric flaw," *J. Appl. Phys.*, vol. 70, no. 3, pp. 1107–1114, 1991.
- [42] J. R. Bowler, Y. Yoshida, and N. Harfield, "Vector-potential boundary-integral evaluation of eddy-current interaction with a crack," *IEEE Trans. Magn.*, vol. 33, no. 5, pp. 4287–4294, Sept. 1997.

- [43] N. Harfield and J. R. Bowler, "Analysis of eddy-current interaction with a surface-breaking crack," *J. Appl. Phys.*, vol. 76, no. 8, pp. 4853–4856, 1994.
- [44] A. M. Lewis, D. H. Michael, M. C. Lugg, and R. Collins, "Thin-skin electromagnetic fields around surface-breaking cracks in metals," *J. Appl. Phys.*, vol. 64, no. 8, pp. 3777–3784, 1988.
- [45] J. R. Bowler and N. Harfield, "Evaluation of probe impedance due to thin-skin eddy-current interaction with surface cracks," *IEEE Trans. Magn.*, vol. 34, no. 2, pp. 515–523, Mar. 1998.
- [46] N. Harfield and J. R. Bowler, "Solution of the two-dimensional problem of a crack in a uniform field in eddy-current non-destructive evaluation," *J. Phys. D Appl. Phys.*, vol. 28, no. 10, pp. 2197–2205, Oct. 1995.
- [47] N. Harfield and J. R. Bowler, "Theory of thin-skin eddy-current interaction with surface cracks," *J. Appl. Phys.*, vol. 82, no. 9, pp. 4590–4603, Oct. 1997.
- [48] J. R. Bowler and N. Harfield, "Thin-skin eddy-current interaction with semielliptical and epicyclic cracks," *IEEE Trans. Magn.*, vol. 36, no. 1, pp. 281–291, Jan. 2000.
- [49] H. Sabbagh, "A model of eddy-current probes with ferrite cores," *IEEE Trans. Magn.*, vol. 23, no. 3, pp. 1888–1904, May 1987.
- [50] C. S. Antonopoulos, T. D. Tsiboukis, and E. E. Kriezis, "Field calculation in single- and multilayer coaxial cylindrical shells of infinite length by using a coupled $T - \Omega$ and boundary element method," *IEEE Trans. Magn.*, vol. 28, no. 1, pp. 61–66, Jan. 1992.
- [51] F. Buvat, G. Pichenot, D. Premel, D. Lesselier, M. Lambert, H. Voillaume, and J. P. Choffy, "Eddy-current modeling of ferrite-cored probes," in *Rev. Prog. Q.*, D. O. Thompson and D. E. Chimenti, Eds., vol. 24, no. 1, 2005, pp. 463–470.
- [52] T. Nakata, N. Takahashi, K. Fujiwara, K. Muramatsu, and Z. G. Cheng, "Comparison of various methods for 3-D eddy current analysis," *IEEE Trans. Magn.*, vol. 24, no. 6, pp. 3159–3161, Nov. 1988.

- [53] A. Ptchelintsev and B. de Halleux, "Two-dimensional finite element model for a long rectangular eddy current surface coil," *Rev. Sci. Instrum.*, vol. 71, no. 2, pp. 571–576, Feb. 2000.
- [54] Z. Badics, Y. Matsumoto, K. Aoki, F. Nakayasu, M. Uesaka, and K. Miya, "An effective 3-D finite element scheme for computing electromagnetic field distortions due to defects in eddy-current nondestructive evaluation," *IEEE Trans. Magn.*, vol. 33, no. 2, pp. 1012–1020, Mar. 1997.
- [55] O. Bíró and K. Preis, "Finite element analysis of 3-D eddy currents," *IEEE Trans. Magn.*, vol. 26, no. 2, pp. 418–423, Mar. 1990.
- [56] T. Nakata, N. Takahashi, and K. Fujiwara, "Efficient solving techniques of matrix equations for finite element analysis of eddy currents," *IEEE Trans. Magn.*, vol. 24, no. 1, pp. 170–173, Jan. 1988.
- [57] O. Bíró, "Edge element formulations of eddy current problems," *Comput. Methods Appl. M.*, vol. 169, no. 3-4, pp. 391–405, 1999.
- [58] J. R. Bowler, "Eddy current calculations using half-space Green's functions," *J. Appl. Phys.*, vol. 61, no. 3, pp. 833–839, 1987.
- [59] S. E. Barlow, "Alternative electrostatic Green's function for a long tube," *J. Appl. Phys.*, vol. 94, no. 9, pp. 6221–6222, Nov. 2003.
- [60] J. R. Bowler, "Time domain half-space dyadic Green's functions for eddy-current calculations," *J. Appl. Phys.*, vol. 86, no. 11, pp. 6494–6500, Dec. 1999.
- [61] J. R. Bowler and F. Fu, "Time-domain dyadic Green's function for an electric source in a conductive plate," *IEEE Trans. Magn.*, vol. 42, no. 11, pp. 3661–3668, Nov. 2006.
- [62] N. Bowler, "Analytical solution for the electric field in a half space conductor due to alternating current injected at the surface," *J. Appl. Phys.*, vol. 95, no. 1, pp. 344–348, Jan. 2004.

- [63] D. M. Mckirdy, "Recent improvements to the application of the volume integral method of eddy current modeling," *J. Nondestruct. Eval.*, vol. 8, no. 1, pp. 45–52, 1989.
- [64] D. D. Reis, M. Lambert, and D. Lesselier, "Eddy-current evaluation of three-dimensional defects in a metal plate," *Inverse Probl.*, vol. 18, no. 6, pp. 1857–1871, 2002.
- [65] A. H. Kahn, "Boundary integral equation methods for two-dimensional models of crack-field interactions," *J. Nondestruct. Eval.*, vol. 7, no. 1–2, pp. 3–14, June 1988.
- [66] W. Rucker and K. Richter, "Calculation of two-dimensional eddy current problems with the boundary element method," *IEEE Trans. Magn.*, vol. 19, no. 6, pp. 2429–2432, Nov 1983.
- [67] C. Dezhi, K. R. Shao, S. Jianni, and Y. Weili, "Eddy current interaction with a thin-opening crack in a plate conductor," *IEEE Trans. Magn.*, vol. 36, no. 4, pp. 1745–1749, July 2000.
- [68] R. E. Beissner, "Boundary element model of eddy current flaw detection in three dimensions," *J. Appl. Phys.*, vol. 60, no. 1, pp. 352–356, 1986.
- [69] D. Zheng, "Three-dimensional eddy current analysis by the boundary element method," *IEEE Trans. Magn.*, vol. 33, no. 2, pp. 1354–1357, Mar. 1997.
- [70] K. R. Shao, K. D. Zhou, and J. D. Lavers, "Boundary element analysis method for 3-D eddy current problems using the second order vector potential," *IEEE Trans. Magn.*, vol. 27, no. 5, pp. 4089–4092, Sept. 1991.
- [71] H. Tsuboi and M. Tanaka, "Three-dimensional eddy current analysis by the boundary element method using vector potential," *IEEE Trans. Magn.*, vol. 26, no. 2, pp. 454–457, Mar. 1990.
- [72] Y. Yoshida and J. R. Bowler, "Vector potential integral formulation for eddy-current probe response to cracks," *IEEE Trans. Magn.*, vol. 36, no. 2, pp. 461–469, Mar. 2000.
- [73] K. Ishibashi, "Eddy current analysis by boundary element method utilizing impedance boundary condition," *IEEE Trans. Magn.*, vol. 31, no. 3, pp. 1500–1503, May 1995.

- [74] P. Beltrame and N. Burais, "Generalization of the ideal crack model in eddy-current testing," *IEEE Trans. Magn.*, vol. 40, no. 2, pp. 1366–1369, Mar. 2004.
- [75] M. Yang, J. Song, Z. Chen, and N. Nakagawa, "A fast multipole boundary integral equation method for two-dimensional diffusion problems," in *Rev. Prog. Q.*, D. O. Thompson and D. E. Chimenti, Eds., vol. 894, Mar. 2007, pp. 294–301.
- [76] M. Yang, J. Song, and N. Nakagawa, "Fast multipole solutions for diffusive scalar problems," in *Rev. Prog. Q.*, D. O. Thompson and D. E. Chimenti, Eds., vol. 975, Feb. 2008, pp. 305–312.
- [77] H. Xie, J. Song, M. Yang, and N. Nakagawa, "Boundary integral equation for eddy-current problems with Dirichlet boundary condition," *J. Nondestruct. Eval.*, vol. 29, no. 4, pp. 214–221, 2010.
- [78] L. Gong, R. Hagel, K. Zhang, and R. Unbehauen, "Solution of the 3D helmholtz equation with eddy currents in cylindrical coordinates by longitudinal components," *IEEE Trans. Magn.*, vol. 28, no. 2, pp. 1154–1157, Mar. 1992.
- [79] R. Grimberg, E. Radu, O. Mihalache, and A. Savin, "Calculation of the induced electromagnetic field created by an arbitrary current distribution located outside a conductive cylinder," *J. Phys. D Appl. Phys.*, vol. 30, no. 16, pp. 2285–2291, Aug. 1997.
- [80] R. Grimberg, E. Radu, A. Savin, and S. Chifan, "The calculation of the electromagnetic field created by an arbitrary current distribution placed in the proximity of a multi-layer conductive cylinder; application to thickness determination for metallic coatings on wires," *J. Phys. D Appl. Phys.*, vol. 32, no. 7, pp. 832–840, Apr. 1999.
- [81] T. P. Theodoulidis, C. S. Antonopoulos, and E. E. Kriezis, "Analytical solution for the eddy current problem inside a conducting cylinder using the second order magnetic vector potential," *COMPEL*, vol. 14, no. 4, pp. 45–48, 1995.
- [82] T. P. Theodoulidis, "Analytical modeling of wobble in eddy current tube testing with bobbin coils," *Res. Nondestruct. Eval.*, vol. 14, no. 2, pp. 111–126, Feb. 2002.

- [83] S. K. Burke and T. P. Theodoulidis, "Impedance of a horizontal coil in a borehole: a model for eddy-current bolthole probes," *J. Phys. D Appl. Phys.*, vol. 37, no. 3, pp. 485–494, Feb. 2004.
- [84] N. M. Sakaji, "Force and eddy currents in a solid conducting cylinder due to an eccentric circular current loop," *J. Phys. D Appl. Phys.*, vol. 33, no. 18, pp. 2239–2248, 2000.
- [85] S. K. Burke, R. J. Ditchburn, and T. P. Theodoulidis, "Impedance of curved rectangular spiral coils around a conductive cylinder," *J. Appl. Phys.*, vol. 104, no. 1, p. 014912, July 2008.
- [86] R. J. Ditchburn, S. K. Burke, and M. Posada, "Eddy-current nondestructive inspection with thin spiral coils: Long cracks in steel," *Journal of Nondestructive Evaluation*, vol. 22, pp. 63–77, 2003.
- [87] A. Skarlatos and T. P. Theodoulidis, "Impedance calculation of a bobbin coil in a conductive tube with eccentric walls," *IEEE Trans. Magn.*, vol. 46, no. 11, pp. 3885–3892, Nov. 2010.
- [88] T. P. Theodoulidis, N. V. Kantartzis, T. D. Tsiboukis, and E. E. Kriezis, "Analytical and numerical solution of the eddy-current problem in spherical coordinates based on the second-order vector potential formulation," *IEEE Trans. Magn.*, vol. 33, no. 4, pp. 2461–2472, July 1997.
- [89] J. R. Bowler and T. P. Theodoulidis, "Eddy currents induced in a conducting rod of finite length by a coaxial encircling coil," *J. Phys. D Appl. Phys.*, vol. 38, no. 16, pp. 2861–2868, Aug. 2005.
- [90] H. Sun, J. R. Bowler, and T. P. Theodoulidis, "Eddy currents induced in a finite length layered rod by a coaxial coil," *IEEE Trans. Magn.*, vol. 41, no. 9, pp. 2455–2461, Sept. 2005.

- [91] S. K. Burke, J. R. Bowler, and T. P. Theodoulidis, "An experimental and theoretical study of eddy-current end effects in finite rods and finite length holes," in *Rev. Prog. Q.*, D. O. Thompson and D. E. Chimenti, Eds., vol. 820, no. 1. AIP, 2006, pp. 361–368.
- [92] T. P. Theodoulidis, "End effect modelling in eddy current tube testing with bobbin coils," *Int. J. Appl. Electrom.*, vol. 19, no. 1-4, pp. 207–212, 2004.
- [93] T. P. Theodoulidis and J. R. Bowler, "Eddy current modeling of coils in boreholes," in *Rev. Prog. Q.*, D. O. Thompson and D. E. Chimenti, Eds., vol. 894, Mar. 2007, pp. 233–240.
- [94] T. P. Theodoulidis and J. R. Bowler, "Impedance of an induction coil at the opening of a borehole in a conductor," *J. Appl. Phys.*, vol. 103, no. 2, p. 024905, 2008.
- [95] R. Grimberg, L. Udpa, A. Savin, R. Steigmann, and S. S. Udpa, "Inner-eddy-current transducer with rotating magnetic field, experimental results: application to nondestructive examination of pressure tubes in phwr nuclear power plants," *Res. Nondestruct. Eval.*, vol. 16, no. 2, pp. 65–77, Apr. 2005.
- [96] R. Grimberg, L. Udpa, A. Savin, R. Steigmann, and S. S. Udpa, "Inner-eddy-current transducer with rotating magnetic field: theoretical model, forward problem," *Res. Nondestruct. Eval.*, vol. 16, no. 2, pp. 79–100, 2005.
- [97] A. Skarlatos, G. Pichenot, D. Lesselier, M. Lambert, and B. Duchene, "Numerical modeling of eddy current nondestructive evaluation of ferromagnetic tubes via an integral equation approach," in *Stud. Appl. Electromag.*, A. Tamburrino, Y. Melikhov, Z. Chen, and L. Udpa, Eds., 2008, vol. 31, pp. 225–230.
- [98] V. Monebhurrun, D. Lesselier, and B. Duchene, "Evaluation of a 3-D bounded defect in the wall of a metal tube at eddy current frequencies: the direct problem," *J. Electromagnet. Wave.*, vol. 12, no. 3, pp. 315–347(33), 1998.
- [99] S. K. Burke, "A thin-skin model for eddy-current NDE of cracks in a borehole," in *Stud. Appl. Electromag.*, 2011, vol. 35, pp. 36–43.

- [100] D. Chen, K. R. Shao, and J. D. Lavers, "Very fast numerical analysis of benchmark models of eddy-current testing for steam generator tube," *IEEE Trans. Magn.*, vol. 38, no. 5, pp. 2355–2357, Sept. 2002.
- [101] G. Micolau, G. Pichenot, D. Premel, D. Lesselier, and M. Lambert, "Dyad-based model of the electric field in a conductive cylinder at eddy-current frequencies," *IEEE Trans. Magn.*, vol. 40, no. 2, pp. 400–409, Mar. 2004.
- [102] J. R. Bowler, T. P. Theodoulidis, H. Xie, and Y. Ji, "Evaluation of eddy-current probe signals due to cracks in fastener holes," *IEEE Trans. Magn.*, vol. 48, no. 3, pp. 1159–1170, 2012.
- [103] C.-T. Tai, *Dyadic Green Functions in Electromagnetic Theory*, ser. Electromagnetic Waves, D. G. Dudley, Ed. IEEE Press, 1993.
- [104] L. B. Felsen and N. Marcuvitz, *Radiation and Scattering of Waves*, D. G. Dudley, Ed. IEEE Press, 1972.
- [105] G. N. Watson, *A Treatise on the Theory of Bessel Functions*. Cambridge University Press, 1922.
- [106] R. F. Harrington, *Field Computation by Moment Methods*. New York: Macmillan, 1968.
- [107] J. A. Crow, "Quadrature of integrands with a logarithmic singularity," *Math. Comput.*, vol. 60, pp. 297–302, 1993.
- [108] M. Abramowitz and I. A. Stegun, Eds., *Handbook of Mathematical Functions with Formulas, Graphs, and Mathematical Tables*. Govt. Print. Off., 1972.
- [109] W. H. Press, S. A. Teukolsky, W. T. Vetterling, and B. P. Flannery, *Numerical Recipes in Fortran: The Art of Scientific Computing*. Cambridge University Press, 1992.
- [110] C. Brezinski, "Convergence acceleration during the 20th century," *J. Comput. Appl. Math.*, vol. 122, no. 1-2, pp. 1–21, Oct. 2000.

- [111] N. Kinayman and M. I. Aksun, “Comparative study of acceleration techniques for integrals and series in electromagnetic problems,” in *Digest AP-S*, vol. 2, June 1995, pp. 1037–1040.
- [112] J. Song, “Midpoint summation: A method for accurate and efficient summation of series appearing in electromagnetics,” *IEEE Antenn. Wirel. Lett.*, vol. 9, pp. 1084–1087, Nov. 2010.
- [113] J. R. Mosig and A. Alvarez Melcon, “The summation-by-parts algorithm—a new efficient technique for the rapid calculation of certain series arising in shielded planar structures,” *IEEE T. Microw. Theory*, vol. 50, no. 1, pp. 215–218, Jan. 2002.
- [114] T. K. Sarkar and O. Pereira, “Using the matrix pencil method to estimate the parameters of a sum of complex exponentials,” *IEEE Antenn. Propag. M.*, vol. 37, no. 1, pp. 48–55, Feb. 1995.
- [115] T. P. Theodoulidis, “Developments in efficiently modelling eddy current testing of narrow cracks,” *NDT & E Int.*, vol. 43, no. 7, pp. 591–598, 2010.
- [116] L. Xing, “Rapid calculation of eddy current field Green’s function using the matrix pencil method,” *NDT & E Int.*, vol. 42, no. 2, pp. 85–91, 2009.
- [117] S. K. Burke, “A benchmark problem for computation of ΔZ in eddy-current nondestructive evaluation (NDE),” *J. Nondestruct. Eval.*, vol. 7, no. 1, pp. 35–41, 1988.
- [118] W. C. Chew, *Waves and Fields in Inhomogeneous Media*, ser. Electromagnetic Waves. Wiley-IEEE Press, Feb. 1999.
- [119] D. J. Harrison, L. D. Jones, and S. K. Burke, “Benchmark problems for defect size and shape determination in eddy-current nondestructive evaluation,” *J. Nondestruct. Eval.*, vol. 15, no. 1, pp. 21–34, Mar. 1996.
- [120] J. W. Demmel, *Applied Numerical Linear Algebra*. Philadelphia: SIAM, 1997.

- [121] K. Weigelt, "Solution of complex eigenvalue equations as used in the analytical solution of eddy-current problems of coupled regions," *J. Magn. Magn. Mater.*, vol. 83, no. 1-3, pp. 501–505, 1990.
- [122] L. M. Delves and J. N. Lyness, "A numerical method for locating the zeros of an analytic function," *Math. Comput.*, vol. 21, no. 100, pp. 543–560, Oct. 1967.
- [123] J. N. Lyness, "Numerical algorithms based on the theory of complex variable," in *Proceedings of the 1967 22nd national conference*. New York: ACM, 1967, pp. 125–133.
- [124] T. P. Theodoulidis, N. Poulakis, and A. Dragogias, "Rapid computation of eddy current signals from narrow cracks," *NDT & E Int.*, vol. 43, no. 1, pp. 13–19, 2010.
- [125] N. Nakagawa, V. G. Kogan, and G. Bozzolo, "Effect of crack closure on eddy current signals," in *Rev. Prog. Q.*, D. O. Thompson and D. E. Chimenti, Eds., vol. 7A, 1988, pp. 173–179.

BIOGRAPHICAL SKETCH

Hui Xie was born December 7, 1982 in Baiyin, Gansu Province, China. He received the Bachelor of Science in Electrical Engineering from Zhejiang University in 2005 and the Ph.D. from Iowa State University in 2012. He has served as a Research Assistant in Center for nondestructive Evaluation and Teaching Assistant in the Department of Electric and Computer Engineering at Iowa State University. He is currently a Post Doctoral Scientist in the Math and Modeling Department at Schlumberger-Doll Research.